POLYMER NANOCOMPOSITES BASED ON AMORPHOUS COPOLYESTER AND ORGANO–INORGANIC NANOFILLERS: A STRUCTURE AND PROPERTY STUDY

Thesis submitted to the

UNIVERSITY OF PUNE

for the degree of

DOCTOR OF PHILOSOPHY (Ph.D.)

in

CHEMISTRY

by

Rajendra A. Kalgaonkar

Polymer Science and Engineering Division

National Chemical Laboratory (NCL)

Pune – 411008

INDIA

April 2007

Dedicated to my beloved Family

CERTIFICATE

Certified that the work incorporated in the thesis, "**POLYMER NANOCOMPOSITES BASED ON AMORPHOUS COPOLYESTER AND ORGANO–INORGANIC NANOFILLERS: A STRUCTURE AND PROPERTY STUDY",** submitted by Mr. Rajendra A. Kalgaonkar was carried out by the candidate under my supervision. Such material as has been obtained from other sources has been duly acknowledged in the thesis.

(Dr. (Mrs.) Jyoti P. Jog)

Research Guide

Polymer Science and Engineering Division

National Chemical Laboratory,

Pune- 411008.

DECLARATION

I hereby declare that the work presented in the thesis entitled "**POLYMER NANOCOMPOSITES BASED ON AMORPHOUS COPOLYESTER AND ORGANO–INORGANIC NANOFILLERS: A STRUCTURE AND PROPERTY STUDY",** submitted for Ph. D. Degree in Chemistry to the University of Pune, has been carried out under the supervision of Dr. (Mrs.) Jyoti P. Jog at the Polymer Science and Engineering Division, National Chemical Laboratory, Pune. The work is original and has not been submitted in part or in full by me for any degree or diploma to this or any other University.

April 2007 (**Rajendra A. Kalgaonkar**)

Pune

ACKNOWLEDGEMENTS

During the course of my thesis work there were many people who were instrumental in helping me. I would like to thank all those people who made this thesis possible and an enjoyable experience for me.

My foremost thanks go to my research advisor Dr. Jyoti P. Jog for her patience, encouragement and for allowing me freedom to pursue my interests and learn how to learn. Under her guidance I not only learned how to conduct research, but also how to communicate my ideas. I have learned a great deal from interacting with her.

It is my honour to acknowledge Dr. S. Sivaram, Director, NCL, for giving me an opportunity to work in this prestigious research institution. I will be forever grateful to him for introducing me to the wonderful world of polymer nanocomposites. I consider myself extremely privileged to have got the opportunity to associate with him.

I would like to thank Dr. M. G. Kulkarni, Head, Polymer Science and Engineering Division and Dr. B. D. Kulkarni, Head, Chemical Engineering and Process Development Division, for their cooperation.

I am extremely grateful to Dr. Ashish Lele for his valuable suggestions, support and kind cooperation, which has broadened my experience. I would like to thank Dr. Sanjeev Tambe whose comments, and suggestions were invaluable to my research. Thanks also to Drs. C. Ramesh, P. R. Rajmohanan, S. D. Pradhan, Mrs. S. D. Kulkarni, C. R. Rajan, U. Natarajan, M. V. Badigar, and U. K. Kharul. I am also thankful to Harshavardhan Pol, E. Deendayalan, and Sanjay Shukla from the Polymer Processing Center, Mr. A. B. Gaikwad (SEM facility), Mr. R. S. Gholap, Purv Purohit (TEM facility), and Mr. U. V. Dhawale for their cooperation. Many thanks are due to the Administrative staff, Library staff, Engineering Services, Stores and Purchase for their cooperation. My sincere thanks to Deenanath Bharati for his help.

My heartfelt thanks go to my friends Vivek Borkar and Aniruddha Dhupe whose help during the course of this work was invaluable. This work would not have been possible without continued support and input from friends and colleagues. I am grateful to members of JPJ group, both past and present for their friendship, teamwork, collaborations, and discussions: Santosh Wanjale, Dr. L. Priya, Prashant Patil, Chetan Chanmal, M. Dhanalaxmi, Amol Ridhore, Sachin Punde, Yashodhan Gokhale, Sateesh Peddini, Pravin Kodgire, Dr. Nabi Saheb, Dr. Neelima Bulakh, and Sangeeta

Hambir. I would like to especially thank Santosh for his support, help and friendship. I was very fortunate to be able to work with you.

Many thanks are also due to my friends Subramanyam, Yogesh Bhole, Santosh Kumbharkar, Harshada, Shubhangi, Snehalata, Girish, Shailesh, and Vipin for their help.

I sincerely thank my colleagues and all the members of Polymer Science and Engineering Division, for their cooperation, and for providing me with an excellent working ambience during the course of this work.

I greatly acknowledge the financial assistance from Council of Scientific and Industrial Research (CSIR) for providing a research fellowship for carrying out the doctoral work.

I am forever indebted to my parents, from whom I learned a great deal, my grandmother, my wife and best friend, Sarika, and my sister Smriti. Their infallible love and support has always been my strength. Their patience and sacrifice will remain my inspiration throughout my life. I am grateful to the Purohit family for their continued support, encouragement and love, which has meant a lot to me. Finally, I thank my son Soham, the greatest joy that has enlightened my life.

TABLE OF CONTENTS

CHAPTER 2: LITERATURE

CHAPTER 3: MATERIALS AND EXPERIMENTAL TECHNIQUES

CHAPTER 4: PETG/LAYERED SILICATE NANOCOMPOSITES

CHAPTER 5: PETG20A NANOCOMPOSITES

CHAPTER 6: PETGCNT NANOCOMPOSITES

CHAPTER 7: CONCLUSIONS AND RECOMMENDATIONS

LIST OF PUBLICATIONS

ABSTRACT

The unique properties of nanocomposites which not only make them obvious technology materials, but also provide a convenient macroscopic system to study fundamental scientific issues concerning confined and tethered polymers, have sparked the attention of material developers. Studying the formation, structure and dynamics of polymer nanocomposites can lead to a better understanding of organic–inorganic hybrids, polymers in confined environment or at a solid interface. It is in this context that the work presented in this thesis has been undertaken to investigate novel polymer nanocomposites based on amorphous polyester and two types on nanofillers viz. layered silicates:– inorganic nanofillers having one dimension in nanoscale and carbon nanotubes:– organic nanofillers having two dimensions in nanoscale.

In polymer/clay nanocomposites better dispersion of clay layers in the polymer matrix can be achieved by organic modification of the mobile surface cations, rendering the clay surface hydrophobic, thereby facilitating the delamination of the clay layers into nanoscale platelets by the polymer chains. The nano size of the clay layers in the polymer matrix, results in markedly improved mechanical, thermal, optical and physico-chemical properties as compared to pristine polymer. Depending on the structure of the dispersed nanoclay, polymer/clay nanocomposites can be classified into: *Intercalated nanocomposites* that are formed when a single (or sometimes more) extended polymer chain is intercalated (sandwiched) between the silicate layers. The result is a well–ordered multilayer structure of alternating polymeric and inorganic layers. *Exfoliated or delaminated nanocomposites*, which are obtained when the silicate layers are completely and uniformly dispersed in the continuous polymer matrix. In practice a combination of these two structures is obtained.

In case of carbon nanotubes (CNTs) their covalent functionalization can improve the dispersion in polymer matrix. However, when a polar polymer is used as the matrix phase, unmodified CNTs can be dispersed uniformly to facilitate formation of percolated filler superstructure that leads to better property performance, as shown in this thesis. Incorporation of CNTs in the polymer matrix may lead to two types of nanocomposites. One in which the CNTs are agglomerated, bundled or entangled together, leading to many defects in the composite, and limiting the efficiency of the nanotubes to improve

the polymer matrices. Second type of polymer/CNT nanocomposites consist of well dispersed or aligned nanotubes in the polymer matrix, which predominantly influence the mechanical and functional property performance of these nanocomposites.

Poly(ethylene glycol-co-cyclohexane-1,4-dimethanol terephthalate) (PETG) nanocomposites based on two grades of PETG, six organically modified layered silicates and CNTs were fabricated by melt blending technique using a twin screw extruder and an internal batch mixer. The microstructure of the nanocomposites was characterized by wide angle X–ray diffraction (WAXD, while the morphology was investigated by transmission electron microscopy (TEM) and scanning electron microscopy (SEM). Relaxation dynamics of the nanocomposites over a wide range of frequencies and temperatures was investigated using dynamic mechanical thermal analysis (DMTA) and dielectric relaxation spectroscopy (DRS). This was correlated to the microstructure using rheology, WAXD, TEM and SEM.

Because of the hydrophilic nature of pristine clay, the formation of a thermodynamically homogeneous mixture of clay with hydrophobic polymers at molecular level is difficult. A typical way to enhance the interaction between the clay and the polymer is to use organic molecules having long hydrocarbon chains to modify clay, resulting into increased interlayer spacing. The effect of molecular size and molecular structure of the intercalant used to modify the hydrophilic nature of the layered silicates, on the structure and viscoelastic properties of the PETG/clay nanocomposites was investigated. Furthermore, the effect of modifier concentration on the properties of the nanocomposites is also discussed. It was demonstrated that the concentration, molecular size and the molecular structure of the intercalant molecule used to modify the clay have a critical role to play in property enhancement of polymer/layered silicate nanocomposites. They govern the extent of intercalation of the polymer in the clay gallery space. Specific comparisons were made between various PETG/layered silicate nanocomposites depending on the CEC of the layered silicate and concentration of the intercalant to address these effects. Microstructural investigation indicated that, larger the size of the intercalant molecule lower is the polymer chain intercalation in the clay galleries. In addition, it was shown that the modifier concentration governs intercalation of the polymer chains in the clay interlayer. Furthermore, it was observed that presence of

favorable specific interactions between the polymer and the intercalant facilitate more polymer chains to infiltrate the clay galleries. The amount of polymer chains present in the confined state between the clay galleries govern the property performance of polymer nanocomposites. Thus, these nanocomposites showed higher storage modulus as compared to those with lower amounts of intercalation. It was also observed that the damping decreased which is as a result of confinement of polymer in the clay inter layer. Finally it was shown that the amount of polymer present in the confined environment governs the rheological response of the nanocomposite. The solid–like behavior in the nanocomposites was strongly dependent of the amount of the intercalated polymer.

Structural investigations of PETG20A nanocomposite confirmed the formation of intercalated nanocomposites. Accelerated relaxation dynamics of the α–process was observed from the DRS study. Only one relaxation was identified in pure PETG at $T > T_g$, whereas two relaxation modes (α and Maxwell–Wagner–Sillars (MWS)) were retrieved from the nanocomposite data. MWS is an interfacial polarization, which is observed in heterogeneous systems and arises due to blocking of mobile charge carriers on a mesoscopic scale. The dielectric data was fitted reasonably well to the semi–empirical Havriliak–Negami (HN) equation. A clear effect of clay loading on ac conductivity was observed with significant increase in conductivity which was attributed to the ability of the clay platelets to facilitate ion transfer through the inter– and intra–regions of the silicate galleries. DMTA showed that the dynamic storage modulus of the nanocomposites increases over the entire range of temperatures studied, with increasing clay content. A direct comparison made between the DRS and the DMTA results showed excellent agreement in the accelerated α relaxation dynamics of PETG on addition of 20A clay. In melt rheology, viscosity and moduli were found to increase on incorporation of clay into PETG.

PETGCNT nanocomposites were prepared using PETG and CNTs at three different CNT loadings of 3, 5, and 7 wt%. The storage modulus of the nanocomposites increased tremendously with increasing CNT content as compared to pure PETG especially in the rubbery regime. The effectiveness of MWCNTs as nano fillers was explained by considering the relative modulus (E'_r). The increase in the modulus was attributed to the formation of a percolated CNT network. Furthermore, from the loss

modulus (E'') peak, it was observed that the T_g of PETGCNT nanocomposites exceeds that of pure PETG because of restricted mobility of the polymeric chains in the nanocomposites due to the presence of the filler network. The significant decrease in the tan δ values with increase in the CNT content indicates the existence of the constrained amorphous phase. These results corroborated the presence of a CNT filler network as a major mechanism of reinforcement in PETGCNT nanocomposites. The linear rheological measurements showed an increase in the storage, loss moduli and the complex viscosity of the nanocomposites with CNT loading. Through a series of rheological analyses such as the presence of finite yield stress, crossover frequency of G' and G'', shape of the Cole–Cole plots, the frequency independence of tan δ and the van Gurp–Palmer plots that are widely accepted in literature to be able to identify the rheological percolation, it was shown that the solid–like behavior of PETGCNT nanocomposites is indeed due to the presence of a percolating MWCNT network. Additionally, non–linear rheological study was also used to describe the presence of percolating MWCNT network in these nanocomposites. DRS study was used to complement the rheological analysis. Finally, a comparison of the responses of both rheological and electrical properties was presented. Although both were related to the formation of a percolating network superstructure of the filler, the responses showed different percolation threshold in rheological and dielectric measurements.

Signature of the Candidate | Signature of the Research Guide

Rajendra A. Kalgaonkar | Dr. (Mrs.) Jyoti P. Jog

NOMENCLATURE

CEC	Cation Exchange Capacity (meq $100g^{-1}$)
CHDM	1,4–Cyclohexanedimethanol
CNT	Carbon Nanotube
DMTA	Dynamic Mechanical Thermal Analysis
DRS	Dielectric Relaxation Spectroscopy
DSC	Differential Scanning Calorimeter
HDT	Heat Distortion Temperature
MMT	Montmorillonite
MWCNT	Multi Walled Carbon Nanotube
MWS	Maxwell–Wagner–Sillars
NMR	Nuclear Magnetic Resonance
PETG	Poly(ethylene glycol–co–cyclohexane-1,4–dimethanol terephthalate)
PLS	Polymer Layered Silicate
SAXS	Small Angle X–ray Scattering
SEM	Scanning Electron Microscope
SWCNT	Single Walled Carbon Nanotube
TEM	Transmission Electron Microscope
TGA	Thermogravimetric Analysis
WAXD	Wide Angle X–ray Diffraction
WAXS	Wide Angle X–ray Scattering
XRD	X–ray Diffraction

LIST OF SYMBOLS

T_g	Glass transition temperature	°C
E'	Elastic storage modulus	Pa
E''	Elastic loss modulus	Pa
E'_r	Relative modulus	
G^*	Shear complex modulus	Pa
G'	Shear storage modulus	Pa
G''	Shear loss modulus	Pa
ω	Frequency	rad s^{-1}
η^*	Complex viscoesity	Pa s
η'	Dynamic viscosity	Pa s
η''	Loss viscosity	Pa s
η	Steady shear viscosity	Pa s
$\dot{\gamma}$	Shear rate	s^{-1}
δ	Phase angle	°
ε^*	Complex dielectric permittivity	
ε'	Dielectric constant	
ε''	Dielectric loss	
σ'	Conductivity	S/cm
σ_{ac}	ac Conductivity	S/cm
σ_{dc}	dc Conductivity	S/cm
E_A	Activation energy	eV
k_B	Boltzmann constant	eV/K
F_{max}	Peak frequency	Hz
F^0	pre–exponential factor	

LIST OF FIGURES

LIST OF TABLES

CHAPTER 1

INTRODUCTION

This chapter provides the necessary background relevant to the contents of the thesis, the motivation behind this work, as well as the objectives of this work. The overview of PETG and the nanofillers used in this work, viz. layered silicates, and CNTs is presented with respect to their types, classification and structure. Methods for fabrication of polymer nanocomposites and the applications of these materials are also described.

1.1 Motivation

Material science has been a subject of intense interest for thousands of years. Prehistorically Egyptians and Sumerians used charcoal for reduction of copper, zinc and tin ores in the manufacture of bronze. The primary driving forces behind materials research today are similar to those of thousands of years ago, as scientists strive for stronger, tougher, lighter and efficient materials that aim to raise the comfort of life in general, all at a lowest possible price. Over the past decade nanocomposites; two–phase materials where one of the phases has at least one dimension in the range of 1–100 nanometers (10^{-9}m) range, have been the subject of tremendous interest. The term "nanocomposite" is commonly used in two distinct areas of material science, viz. ceramics and polymers. However, nanocomposites based on polymers will only be considered here. The unique properties of nanocomposites which not only make them obvious technology materials, but also provide a convenient macroscopic system to study fundamental scientific issues concerning confined and tethered polymers, have sparked the attention of material developers. Studying the formation, structure and dynamics of polymer nanocomposites can lead to a better understanding of organic–inorganic hybrids, polymers in confined environment or at a solid interface. It is in this context that the work presented here has been undertaken to investigate novel polymer nanocomposites based on amorphous polyester and two types on nanofillers viz. layered silicates (one dimension in nanoscale) and carbon nanotubes (two dimensions in nanoscale). We begin the thesis by briefly introducing the polymer nanocomposites. In this chapter the necessary background relevant to the contents of this thesis is provided. We also discuss the overall objectives of this work and the structure of this thesis.

1.2 Background

1.2.1 Polymer Composites

For years, composite materials have been recognized as measure replacements over conventional materials including, metals, metal alloys, wood, ceramics and polymers. Many kinds of composite materials are developed today, and are classified based on their reinforcement and matrix. Based on the type of reinforcement used, there are particle reinforced composites, fiber reinforced composites and structural composites.

Based on the matrix used there are metal–matrix composites, ceramic–matrix composites and polymer–matrix composites.

Polymer–matrix composites are prepared by mixing polymers with inorganic filler materials such as reinforcing fibers (e.g. glass, carbon, aramid, etc.) and particulate solids (e.g. talc, carbon black, calcium carbonate, mica, etc.). Such composites exhibit physical properties synergistically derived from both the organic and inorganic components, e.g. they show superior mechanical properties and higher heat deflection temperature compared to the pristine polymers while maintaining processibilty.[1] Based on the application it is necessary to design the appropriate composite system.

However, the enhancement in property performance of polymer composites is achieved at the expense of optical clarity, surface gloss and also leads in many cases to an increased part weight. This is because conventional polymer composites require higher filler loadings (typically ≥ 20 wt%) for achieving significant property improvement. The replacement of traditional composites with a new class of more effective composites that use nanofillers have attracted considerable interest both technologically as well as academically.

1.2.2 Polymer Nanocomposites

Advent of nanoscience and nanotechnology has continuously provided the impetus pushing for the development of materials with fascinating properties and rich variety of applications. Polymer nanocomposites represent a new class of materials based on reinforcement of polymeric materials using organo–inorganic nanofillers. These nanocomposites show remarkable property improvements as compared to virgin polymers and that too at low filler loadings compared to conventional microcomposites. There are three types of nanofillers:

1. Nano particles which comprise of particles having all three dimensions in nanometer range e.g., semiconductor, metal nanoparticles, colloidal dispersion of polymers etc.[2,3]
2. Two dimensional nanofillers wherein two dimensions of the filler are in nanometer scale e.g. nano tubes and cellulose whiskers that have the third dimension larger, forming elongated structures.[4,5]

3. The third type of nanofillers corresponds to the case in which there is only one dimension on a nanolevel. Examples are layered silicates or clays, which are platelet shaped.

The work presented in this dissertation is focused on polymer nanocomposites incorporated with two types of nanofillers, viz. nanoclays (inorganic nanofiller) and carbon nanotubes (organic nanofillers). Thus, polymer nanocomposites comprising of nanofillers having one and two dimensions in nano scale are investigated.

1.3 Why use Nanofillers?

In conventional polymer composites many fillers with dimensions in micrometer range have been extensively used to enhance the property performance of polymers. Indeed, properties of polymers can be tailored by changing the filler loading, shape and size of the filler particles. A further improvement in the properties of polymers can be achieved by using fillers with larger aspect ratio. It is logical to anticipate that the dispersion of fillers, with dimensions in nanometer scale having very large aspect ratio, surface area and stiffness, in the polymer matrix could lead to even larger property improvements. These nanofillers include carbon nanotubes (CNT) and clays. Furthermore, the very small size and thickness of the filler means that a single gram contains over a million individual particles. Thus, the important advantage that these nanocomposites have is the various property enhancements are all achieved at very low filler content of ≤5 vol%. Hence, the cost, clarity and polymer processability are maintained. This is in contrast to typical filled grades of polymer composites where the filler content of 30–40 vol% is required to bring about similar enhancement in the properties.[6,7] Improvement in strength, stiffness and toughness are primary characteristics of organo–inorganic nanocomposites.[8–12] Desirable property performance such as barrier properties, thermal stability, moisture stability, solvent resistance and fire retardancy usually accompany the reinforcement benefit.[9,10,13] As a result of nanofiller incorporation, nanocomposites are finding applications in those areas in which conventional composites are being used.

1.4 Layered Silicates

Layered silicate minerals are hydrous aluminum silicates and are generally classified as phyllosilicates, or layered silicates. These consist of natural clays like montmorillonite, hectorite, and saponite as well as synthetic clays such as magadite, mica, laponite, flourohectorite, etc. Natural clays are most commonly formed either by the in situ alteration of volcanic ash or by the hydrothermal alteration of volcanic rocks. Bentonite is a rock, which consists of commonly known Smectite or Montmorillonite group clays as major component and auxiliary minerals such as kaolin, quartz, gypsum, iron ore etc. Sodium or calcium bentonite is not itself a mineral name, but more correctly, it is Smectite clay composed primarily of the mineral Montmorillonite having sodium or calcium ions as its predominant cations. Smectite or Montmorillonite group clays are further classified into two sub–groups, viz. trioctahedral and dioctahedral Smectite clays. Montmorillonite, Beidilite and Nontronite are trioctahedral Smectite clays whereas Hectorite and Saponite are dioctahedral Smectite clays.

Clays are hydrated silicates of Al, Mg, K and Fe and other non clay minerals. The particles of clay are very fine in size, plate like in shape and have very large specific surface areas that are chemically active. Clay minerals usually consist of various physical combinations of tetrahedral and octahedral sheets. The tetrahedral sheet is composed of Si^{4+} and oxygen. Al^{3+}, Fe^{3+} may substitute Si^{4+} laving negatively charged tetrahedral sheet behind. Octahedral sheet is composed of Al^{3+}, Fe^{3+}, Mg^{2+} and Fe^{2+} cations and O^{2-}, OH^{-} and F^{-} anions. Substitution of bivalent cations for trivalent cations and univalent cations for bivalent cations or unfilled octahedral sheet layer sites leave behind the net negative charge. The two octahedral layers are joined by tetrahedral oxygen. Depending upon the number of sheets present, there are three type clays.

1. 1:1 type: In this type one tetrahedral (T) and one octahedral (O) sheet is present. This TO package has basal spacing of 0.7 nm. e.g. kaolinite, serpentine
2. 2:1 type: In this type two tetrahedral (T) and one octahedral (O) sheets are present. The oxygen atoms of two tetrahedral sheets are projected into octahedral sheet. This TOT package has basal spacing of 1.0 nm. e.g. pyrophyllite, talc, montmorillonite

3. Mixed layer type: mixed layer clays are combination of minerals. It may contain equal proportions or dominated by one mineral. The arrangement of the component mineral may be random, short range ordered or long range ordered.

The commonly used layered silicates in polymer nanocomposites, like the better known members of the group talc and mica, belong to the general family of 2**:**1 layered- or phyllosilicates. Their crystal structure consists of layers made up of two silica tetrahedral fused to an edge-shared octahedral sheet of either aluminum of magnesium hydroxide. Stacking of the layers leads to a regular van der Waals gap between the layers called the interlayer or gallery. Isomorphic substitution within the layers generates negative charges that are normally counterbalanced by cations residing in the interlayer space.

Among these layered silicates, montmorillonite is particularly attractive as reinforcement for the polymer/clay nanocomposites because, it is environmentally friendly, readily available in large quantities with relatively low cost and its intercalation chemistry is well understood. Montmorillonite is a three–layer mineral, formed by stacking of several layers of tetrahedron and octahedron sheets, electrostatically held together by isomorphic interlayer cations. As the electrostatic attraction is low, exposure to polar fluids such as water will cause the formation of a monomolecular layer of water between the silicate layers. The basis behind bentonite swelling is that the several layers of water dipoles can form into weak "stacked" tetrahedral structures, causing the silicate layers to separate this is termed intercrystalline swelling. Purity and quality of bentonite will vary, as per the depositional environment and subsequent weathering processes and also differs by region and deposit.

The lattice structure of montmorillonite clays comprises of an octahedral Alumina sheet, sandwiched between two tetrahedral Silica sheets. The structural details of montmorillonite are given in Figure 1.1. A single crystal lattice of Montmorillonite is negatively charged owing to the isomorphism substitution mainly in the octahedral layer (e.g. Mg^{2+} for Al^{3+}). The negative charge of the lattice is balanced by the exchangeable cations, which are held in the interlayer space of the clay. The exchangeable cations can

be sodium and/or calcium ions, which can be replaced by suitable organic or inorganic cations.

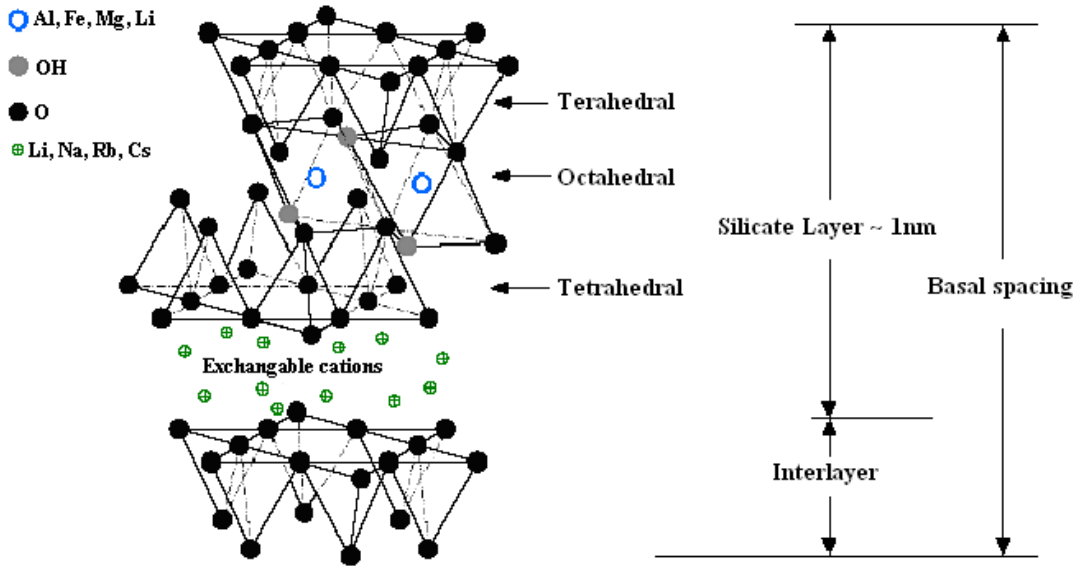

Figure 1.1 Structure of montmorillonite[14]

The idealized unit cell formula of sodium form of montmorillonite is $Na_{0.67}$ $[Al_{3.33}Mg_{0.67}]$ $[Si_8]$ O_{20} $(OH)_4$ in which one of every 6–octahedral Al^{3+} has been replaced by Mg^{2+}. The charge deficit is 0.67 esu per unit cell, or 0.67 equivalent charge per 734 g (formula weight) of clay. This gives value of 91.3 milliequivalents (meq) charge deficit in layer per 100 g of clay. This deficiency of charge must be balanced by equal quantity of cation charge at its surface for electrical neutrality. The maximum amount of any one cation that can be taken up by particular clay is constant and is known as the cation exchange capacity (CEC) or Base Exchange Capacity (BEC) of that clay. The amount is expressed in meq per 100 g of dry clay. CEC varies from 80–100 depending up on the substituted cation. Due to isomorphous substitution for M^{3+} by M^{2+} and M^{2+} by M^{+} in its structure, bentonite clay has unique nature of cation exchange and adsorption capacity. The

adsorption efficiency of bentonite is enhanced several folds after purification and/or modification. Applicability of these properties is known for a very long time in terms of decolorizing edible oils, clarification of alcoholic beverages and removal of grease from raw wool.

1.4.1 Organomodification of Clays

The Smectite clay possesses a large surface area (~ 750 m^2/g). In order to utilize their high surface area efficiently, the chemical modification of such clays is necessary. During modification the exchangeable interlamellar cations are replaced by the other cations, inorganic or organic, present in the external environment. This can be achieved by several methods and the modified products obtained can be classified into various categories including acid–treated clays, pillared clays, and nanoclays. Of particular interest in polymer/clay nanocomposites are nanoclays.

Nanoclays are complexes derived from clay–organic reactions. The clays used are Smectite group clays, generally montmorillonite or Hectorite. These clays are hydrophilic and accessible to intercalation. Therefore, they are liable to intercalate organics through ion–exchange and/or adsorption when reacted with organic compounds and to be transformed to hydrophobic or organophilic nature. The organophilicity is ascribed to the interlamellar surface coverage with organics. Owing to the organophilic nature, the modified clays are named organophilic–clays or organo–clays.

Despite ignorance of scientific basis of such interaction process, the uptake of certain organic compounds by clays has been known for a very long time, being the basis of wide use of clays. For such utilities clays are generally named "bleaching or Fuller's earth".

Complex forming compounds may be classified into the following groups:

1. Uncharged polar organic compounds (Neutral organic compounds).
2. Negatively charged organic compounds (Acidic organic compounds).
3. Positively charged organic compounds (Basic organic compounds).

The nanoclays of particular interest with respect to usage of clay as a nanofiller in polymer composites are prepared by modification of clay using positively charged organic compounds. This class includes the organic compounds like quaternary ammonium

compounds (quaternaries), amines, alkaloids, purines, nucleosides, proteins, etc. The properties and end use of clays modified by such organic bases are largely dependent on the organic compound adsorbed by the clays.

1.4.2 Structure and Properties of Organomodified Clays

The organomodified clays are prepared by reacting more voluminous organic onium cations with the montmorillonite clay. The reaction results in the exchange of relatively small sodium ions with organic counter ions. This ion–exchange results in to increase of the clay interlayer space, enabling organic cation chains to move in between them and secondly, the surface properties of each clay sheet are changed from being hydrophilic to hydrophobic.

During the cation exchange reaction the organic cations could either replace the inorganic cations or neutralize the hydrogen ions at clay surfaces.[15–17] Hendricks concluded from his work that the adsorption of organic cations by clays is influenced both by electrostatic (columbic) and Van der Waals attractive forces.[18] Grim et. al. found that in case of organic cations having relatively small size the maximum amount adsorbed did not go beyond the CEC of the clays, even when a large excess of the organic ion was present in the solution.[19] Under similar conditions larger organic ions were taken up in the excess of the CEC because of the influence of Van der Waals forces on the adsorption of large organic cations by clays. Similar findings were reported by Cowan and White using isotherms for the adsorption of a homologous series of primary n–alkyl ammonium ions from ethyl (C_2) to tetradecylammonium (C_{14}) by sodium montmorillonite.[20] Vansant and Uytterhoeven concluded that apart from Van der Waals forces of organic cations, the combination of variation in hydration status of the cations and electrostatic interactions between cation and clay surface played an important role in adsorption of n–alkyl ammonium ions on Na–montmorillonite.[21] On interaction with clay particles cationic portion of positively charged organic salts are accommodated in the interlayer space of clay crystals by replacing inorganic cations initially present. The interaction between the clay platelets and organic cations results in the replacement of Na^+ cations by organic cation moieties, which leads to the increase in the basal spacing. Barrer et. al. found this increment to be directly related to the amount of organic cations present after the ion

exchange.[22] Jordan studied montmorillonite complexes with primary n–alkyl ammonium ions of varying chain length (from C_3 to C_{18}).[23] He concluded that the basal spacing values were constant at 1.36 nm for C_3 to C_{10} and 1.76 nm for C_{10} onwards. Further, when the cation area was smaller than half of the area per exchange site, the amine cation adsorbed on one surface was found to be fitted into the gaps between the cations lying on opposing surface to form monolayer complexes but when the area of the cation was greater than half the area per exchange position interpenetration of this kind could not be realized and double layer complexes formed (e.g. for n–hexadecyl ammonium). Jordan et. al.[24] using XRD evidenced following results for a long chain cation such as n–octadecyl ammonium: (a) the formation of double layer complexes when the amounts of cations adsorbed were equivalent to the exchange capacity, (b) the alkyl chain in double–layer complex stands at an angle to the silicate layer at amounts adsorbed higher than the CEC, and (c) at still higher amounts adsorbed, the chains were found reoriented into near–vertical positions with respect to the surface giving rise to a close packed arrangement which allows extensive Van der Waals interactions between adjacent alkyl chains to be established. Greene–Kelly have reported similarly for pyridinium and its derivatives in montmorillonite.[25] Thus, besides being dependent on the alkyl chain length of the cation and the charge on the mineral layer, the arrangement of intercalated n–alkyl ammonium/pyridinium ions and/or molecules is also influenced by the amount of the cations and/or molecules adsorbed which ultimately depend on the amount of the compound reacted. The orientation of alkyl ammonium ions between the clay aggregates has been investigated by Lagaly.[26] He has reported that besides the formation of paraffin–type structures of chains in all–trans conformation, aggregates of chains containing gauche–conformations are commonly observed. More recently molecular dynamics simulations have provided insights in to the packing orientation of alkyl ammonium surfactant chains in the clay interlayers.[27] It was observed that a disordered liquid–like arrangement of the alkyl chains was preferred in the clay gallery. In this disordered state the alkyl chains do not remain flat, but instead, overlap and co–mingle with the adjacent onium ions in the opposing layers within the galleries. Krikorian and Pochan have reported the significance of the molecular conformations of the surfactant used in the nanoclays, on the morphology of the nanocomposites.[28,29] They showed that presence of less ordered and

more gauche conformation of the surfactant, which is a manifestation of reduced packing density of the clay interlayer, resulted in an exfoliated nanocomposite. Whereas, in nanoclays, which had more ordered, trans conformations, characteristic of tightly packed environment a predominantly intercalated morphology of the nanocomposites was reported.

1.5 Carbon Nanotubes

Carbon nanotubes (CNTs) were first reported by Ijima[30] in 1991, and the first polymer nanocomposites using CNTs as a filler were reported in 1994 by Ajayan et. al.[31] CNTs are classified into single–walled nanotubes (SWCNT), multi–walled nanotubes (MWCNT) and carbon nanofibers (CNF). MWCNTs were the first types of CNTs to be reported which comprise of a number of graphene layers coaxially rolled together to form a cylindrical tube. Ijima was also the first to isolate SWCNTs with a diameter of just 1–2 nm in 1993.[32] In 1997, bundles of aligned SWCNTs were first synthesized by Smalley's group.[33] CNTs possess high flexibility, low mass density, and a large aspect ratio. CNTs have a unique combination of mechanical, electrical, and thermal properties that make them excellent candidates to substitute or complement conventional nano fillers in fabrication of multifunctional polymer nanocomposites.[34,35] CNTs are stronger than steel, lighter than aluminum and more conductive than copper. It has been shown by theoretical and experimental studies that CNT Young's modulus is greater than 1 TPa and they posses tensile strength up to 180 GPa.[36,37]

1.5.1 Structure of Carbon Nanotubes

A CNT is an allotrope of carbon along with diamond, graphite, and fullerenes. CNTs are long cylinders of covalently bonded carbon atoms. SWNT with a diameter of 1–2 nm consists of a single graphene sheet (graphene is a single atomic layer of carbon atoms in sp^2 arrangement) wrapped into a cylindrical shape, and hemispherical caps seal both ends of the tube. The carbon atoms in the cylinder have partial sp^3 character that increases as the radius of curvature of the cylinder decreases. Rolled up sheets of graphene form the tube of the nanotube molecule as shown in Figure 1.2. The MWCNTs comprise of a number of graphene layers coaxially rolled together to form a cylindrical

tube. Each carbon atom within the atomic layer of a graphene sheet is covalently bonded to three neighboring carbon atoms. Three sp^2 orbitals on each carbon form σ–bonds to three other carbon atoms. One 2p orbital remains unhybridized on each carbon; these orbitals are perpendicular to the plane of the carbon ring combine to form the π–bonds. The atomic interactions between the neighboring layers are the van der Waals forces. The outer diameter of the MWCNTs is about 3–10 nm. A special case of MWCNT is double–wall carbon nanotubes (DWCNT) that consist of two concentric graphene cylinders. DWCNTs are expected to exhibit higher flexural modulus than SWCNTs due to the two walls and higher toughness than regular MWCNTs due to their smaller size.[38]

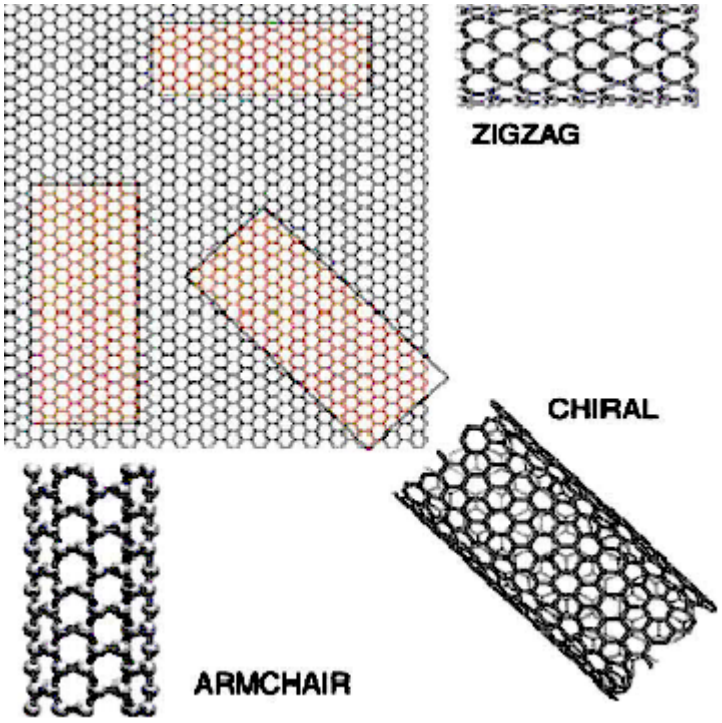

Figure 1.2 Schematic diagram of how a hexagonal lattice of graphene can be rolled up to form a carbon nanotube[39]

1.5.2 Production Methods of Carbon Nanotubes

CNTs can mainly be produced by arc discharge, chemical vapor decomposition (CVD) and laser ablation. Ijima used the arc discharge method while preparing CNTs for the first time.[30] In that process two graphite rods are connected to a power supply with a

gap in the order of a millimeter. A current of 100 amps passes through the rods causing the carbon to vaporize into hot plasma some of which recondenses in the form of nanotubes. The tubes produced are of high quality with few defects. Adding metal catalysts to the rod and changing the temperature allows production of both SWCNTs and MWCNTs. The disadvantages of this method are low yield (around 30%), and short tubes (50 microns or less).

Chemical Vapor Deposition (CVD) is a technique where a substrate is placed in an oven at ~ 600 ºC. A carbon feed gas such as methane is slowly added, and as the gas decomposes it recombines as nanotubes. A porous catalyst can be used to increase efficiency and growth position control. While this method can produce high yields, these nanotubes are often riddled with defects and consequently have much lower tensile strength than arc discharge tubes.

Laser Ablation is a very costly method that produces SWCNTs by focusing a laser on graphite target in an Argon atmosphere. This gives a typical yield of around 70% and varying the furnace temperature gives the great advantage of diameter control.

None of the methods can be tuned to yield a nanotube with a specific chirality although much research is focused in this area. Instead a range of chiralities is produced along with graphitic or catalyst impurities. However it is believed that CVD might offer more control over the length and structure of the produced nanotubes, and the process appears scalable to industrial quantities.

1.6 Fabrication of Polymer Nanocomposites

Fabrication methods of polymer nanocomposites have overwhelmingly focused on improving nanofiller dispersion, because better nanofiller dispersion in the polymer matrices has been found to improve properties. As this thesis focuses on two nanofillers, viz. layered silicates and CNTs, we will focus or discussion on fabrication of polymer nanocomposites pertaining to these nanofillers only. Throughout this thesis the terms “polymer nanocomposites” and “nanofillers” are freely used to describe polymer nanocomposites based only on layered silicates and CNTs.

The techniques of solution blending, in situ polymerization, and melt blending are widely applied to produce polymer nanocomposites. Melt blending is commercially the most viable method of preparation.

1.6.1 Solution Blending

This is one of the most common routes for preparation of polymer nanocomposites. In this technique suitable solvents are used to disperse the nanofiller followed by dissolving the polymer in the same solvent and mixing the two at room temperature or elevated temperature. Finally the nanocomposite is recovered by precipitating or casting a film. Although this is an advantageous method on lab scale it is difficult to apply the solution blending method in industry due to the problems associated with the use of large quantities of solvent.

1.6.2 In situ Polymerization

This is a conventional process of synthesizing polymer nanocomposites especially those based on thermoset polymers. The nanofiller is first dispersed in the monomer. As with solution blending fuctionalization of the nanofiller improves its initial dispersion in the liquid monomer and consequently in the nanocomposites. This step requires a certain amount of time, which is governed by the polarity of the monomer molecules, surfactant molecules in the nanofiller, and the dispersion temperature. This is followed by the initiation of the reaction. Note that as polymerization progresses and the viscosity of the medium increases, the extent of in situ polymerization reactions may be limited.

1.6.3 Melt Blending

Melt blending consists of blending a molten thermoplastic with the nanofiller in order to optimize the polymer–nanofiller interactions. It is a promising approach for forming nanocomposites that would greatly expand the commercial opportunities of this technology. The polymer chains have a significant loss of conformational entropy during the intercalation. The proposed driving force for this mechanism is the important enthalpic contribution of the polymer/nanofiller interactions during the blending and annealing steps. In melt intercalation process, rheological and thermodynamic characters

of the materials are important parameters that affect the degree of dispersion and properties of the final nanocomposites. Generally the degree of dispersion of the nanofiller in the polymer matrix is governed by matrix viscosity, average shear rate, and mean residence time in the mixing process. Additionally the compatibility of the polymer with the nanofiller also governs the degree of dispersion of the nanofiller. Polar polymers are found to be more compatible with the nanofillers as compared to their nonpolar counterparts. Thus, in polar polymers such as polyamides, PMMA, etc. a more uniform dispersion of the nanofiller is observed than that observed in polyolefins. Functionalization of either the polymer or the nanofiller also enhances the compatibility between the two, thus maximizing the dispersion of the nanofiller in the polymer matrix.

1.7 Types of Polymer Nanocomposites

In polymer/clay nanocomposites better dispersion of clay layers in the polymer matrix can be achieved by organic modification of the mobile surface cations, rendering the clay surface hydrophobic, thereby facilitating the delamination of the clay layers into nanoscale platelets by the polymer chains. The nano size of the clay layers in the polymer matrix, results in markedly improved mechanical, thermal, optical and physico–chemical properties as compared to pristine polymer. Depending on the structure of the dispersed nanoclay, polymer/clay nanocomposites can be classified into three main types. This depends on the nature of the components used including polymer matrix, clay and organic cation. If the polymer cannot intercalate between the silicate sheets, a microcomposite is obtained. The phase–separated composite that is obtained has the same properties as traditional microcomposites. Beyond this traditional class of polymer–filler composites, two types of nanocomposites can be obtained: ***Intercalated structures*** are formed when a single (or sometimes more) extended polymer chain is intercalated (sandwiched) between the silicate layers. The result is a well–ordered multilayer structure of alternating polymeric and inorganic layers. ***Exfoliated or delaminated structures*** are obtained, when the silicate layers are completely and uniformly dispersed in the continuous polymer matrix. The delamination configuration is of particular interest because it maximizes the polymer–clay interactions, making the entire surface of the layers available for the polymer. This should lead to the most significant changes in

mechanical and physical properties. A schematic of the types of possible structure formations in polymer/clay composites is depicted in Figure 1.3.

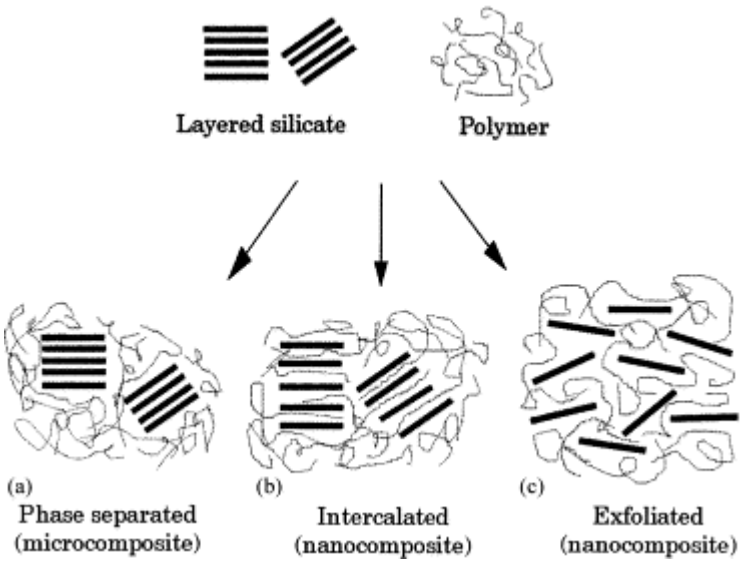

Figure 1.3 Schematic representation of possible structure formation in polymer/clay nanocomposites

Due to their large aspect ratios, CNTs are recognized to agglomerate and entangle easily during processing of the nanocomposites, leading to poor mechanical performance. In case of MWCNTs their covalent functionalization can improve the dispersion in polymer matrix. However, when a polar polymer is used as the matrix phase, unmodified MWCNTs can be dispersed uniformly to facilitate formation of percolated filler superstructure that leads to better property performance, as shown in this thesis. Incorporation of MWCNTs in the polymer matrix may lead to two types of nanocomposites. One in which the MWCNTs are agglomerated, bundled or entangled together, leading to many defects in the composite, and limiting the efficiency of the nanotubes to improve performance of the polymer matrices. Second type of polymer/CNT nanocomposites consist of well dispersed or aligned nanotubes in the polymer matrix, which predominantly influence the mechanical and functional property performance of these nanocomposites.[40,41]

1.8 Applications of Polymer Nanocomposites

The potential use of polymer nanocomposites seems to have by far a much wider and many application fields. Applications of polymer nanocomposites using different polymer matrices and nanofillers are based on their improved mechanical properties (tensile strength and Young's modulus), improved heat/dimensional stability and enhanced barrier to water, hydrocarbon and gas (particularly oxygen) permeation.

Toyota, in late 1980's was the first company to develop and commercialize polymer/clay nanocomposites. They used nylon 6 as the matrix phase and montmorillonite as the clay filler for a timing–belt cover in one of their car models, which became the first commercial polymer nanocomposite.[42] This nanocomposite exhibited unprecedented mechanical properties. The flexural strength was doubled whereas flexural modulus increased by almost four folds and the tensile strength and modulus were almost doubled at clay loading of <5%. Since then nanocomposites are gradually gaining acceptance in the mainstream polymer industry finding applications in automotive to packaging sector.

Unitika Co. of Japan developed Nylon 6 nanocomposite (Nylon M2350) using synthetic clay as reinforcement during polymerization. Nylon M2350 has been used by Mitsubishi Motors for an engine cover on its GDI models, where the nanocomposite is said to offer a 20% weight reduction and excellent surface finish (Figure 1.4a).

Recently, General Motors along with partners Southern Clay Products, Basell (Former Montel), and Blackhawk Automotive Plastics, presented the first automotive exterior application, a step assist for 2002 *GMC Safari* and *Chevrolet Astro* vans, based on polypropylene/clay nanocomposite, that aids users in stepping into and out of the vehicle (Figure 1.4b).[43,44] According to the executive director of science for GM Research and Development, the parts made of nanocomposite material cost, on a volume–basis, about as much as conventional thermoplastic olefins (because, of course, less filler is needed to manufacture them) guaranteeing a lighter–weight component and in turn, a more fuel–efficient vehicle.

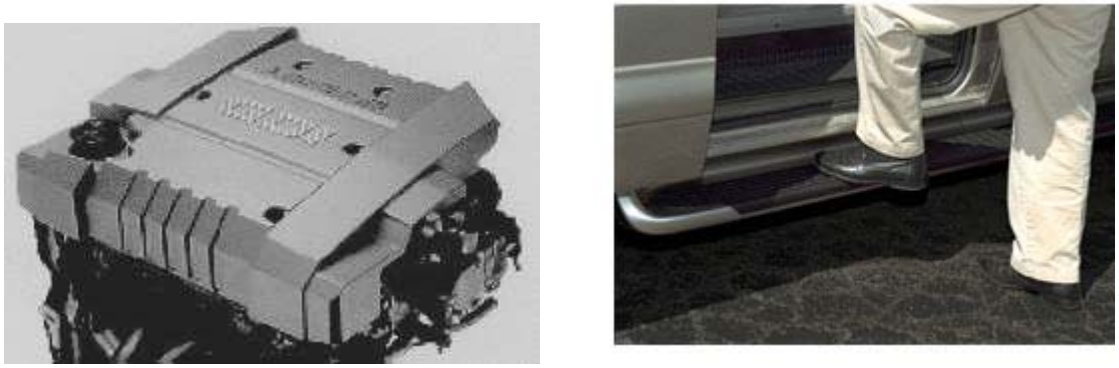

(a) **(b)**

Figure 1.4 Polymer nanocomposites for structural applications

Bayer AG, Germany developed nylon 6 nanocomposites for transparent barrier film packaging. Bayer is marketing two grades of nanocomposites, Durethan LPDU 601–1 and LPDU 601–2, which in comparison to neat nylon offers decrease in the Oxygen Transmission Rate (OTR) by 50%. The nanocomposites are made in the reactor using nano-clay from Nanocor.

New applications of polymer/clay nanocomposites are nowadays envisaged by automotive industrials for a next commercialization: PP/clays for bodywork with anti-scratch properties (Dow Plastics/Magma); acetal/clays for ceiling lights (Showa Denko); PP/clays for panes of doors, consoles and interior decoration (Ford, Volvo) due to aesthetics, recyclable and lightness properties; nylon/clays for bumpers with enhanced mechanical and lightness properties (Toyota); nylon/clays for fuel reservoir with airtightness properties (Ube America), etc.

Honeywell claims that nylon 6 with 2% nanoclay has three times the oxygen barrier of straight nylon 6, and 4% nanoclay confers a six-fold improvement.[45–47] The passive barriers are the clay particles, which make the oxygen transmission inside the composite more difficult. Additionally they also conduct the oxygen molecules to specific oxygen–captors. In this way, the clay incorporation limits the oxygen transmission up top 15–20% of the value found in the pure polymer.

Nanocor and Mitsubishi Gas Chemical Company developed the MXD6 high barrier semi-aromatic nylons in nanocomposite form. Its barrier properties are said to be

superior to EVOH and its processing characteristics are ideal for multilayer films, bottles and thermoformed containers (see Figure 1.5a).[48]

InMat Inc. has developed several applications for their nanocomposite coatings, especially in tennis balls, that conserve the internal pressure for a long time. Figure 1.5b shows the Wilson tennis balls, provided with a double core.[49]

(a) **(b)**

Figure 1.5 Polymer nanocomposites for barrier applications

Very few commercial products based on CNTs and polymers exist in the market at present. The only major commercial product based on CNTs in the market for the past decade that is based on polymer/CNT composite that is designed primarily to improve electrical conductivity that facilitates electrostatic painting of automotive mirrors.

The current suppliers of polymer nanocomposites are listed in Table 1.1. It is observed that a wide range of polymer matrices including PP, TPO, EVA, acetal, polycarbonate, biodegradable polylactic acid (PLA), and polyaniline are used. However, the nanofiller used is predominantly layered silicates. But new generation of nanofillers based on CNTs suggest an important growth in polymer nanocomposite market in the near future.

Table 1.1 Overview of polymer nanocomposite market[a]

Supplier & Tradename	Matrix Resin	Nanofiller	Target Application
Bayer AG (Durethan LPDU)	Nylon 6	Layered Silicates	Barrier films
Clariant	PP	Layered Silicates	Packaging
Creanova (Vestamid)	Nylon 12	CNTs	Electrically conductive
GE Plastics (Noryl GTX)	PPO/Nylon	CNTs	Automotive painted parts
Honeywell (Aegis)	Nylon 6, Barrier Nylon	Layered Silicates	Multi-purpose bottles and film
Hyperion	PETG, PBT, PPS, PC, PP	Layered Silicates	Electrically conductive
Kabelwerk Eupen of Belgium	EVA	Layered Silicates	Wire & cable
Nanocor (Imperm)	Nylon 6, PP Nylon MDX6	Layered Silicates	Multi-purpose molding PET beer bottles
Polymeric Supply	Unsaturated polyester	Layered Silicates	Marine, transportation
RTP	Nylon 6, PP	Layered Silicates	Multi-purpose, electrically conductive
Showa Denko (Systemer)	Nylon 6, Acetal	Layered Silicates, Mica	Flame retardance, Multi-purpose
Ube (Ecobesta)	Nylon 6, 12, Nylon 6, 66	Layered Silicates	Multi-purpose Auto fuel systems
Unitika	Nylon 6	Layered Silicates	Multi-purpose
Yantai Haili Ind., Commerce of China	UHMWPE	Layered Silicates	Earthquake-resistant pipe

[a] Source: Bins & Associates, Sheboygan, WI, USA

1.9 Research Objectives

The primary objective of this thesis is to fabricate novel polymer nanocomposites based on PETG using two different commercially available nanofillers viz. organically modified layered silicates and MWCNTs, via melt compounding technique (Henceforth MWCNTs will also be abbreviated as CNTs unless mentioned otherwise). Evaluate the effect of their structure on the viscoelastic properties both in solid and melt state as well as on the dynamics of the nanocomposites as studied by dynamic mechanical analysis and dielectric relaxation spectroscopy and correlate these with the property performance of PETG.

The specific objectives of this dissertation were:

- To fabricate nanocomposites based on PETG and organo–inorganic nanofiller viz. organically modified montmorillonite and CNTs.
- To study the effect of the modifier concentration on the structure and viscoelastic properties of the nanocomposites.
- To study the effect of the intercalant molecular size and molecular structure on the structure and viscoelastic properties of the nanocomposites.
- To study the effect of clay concentration on the dynamics of the nanocomposites using DMTA and DRS, and to correlate this to the nanocomposite morphology through WAXD, TEM and rheology.
- To gather an understanding of the microstructure–property linkages in PETGCNT nanocomposites by studying the reinforcement effect of CNTs on the structure and viscoelastic properties of the nanocomposites both in solid as well as melt state.

The following techniques have been used to characterize the nanocomposites:

- Microstructure of nanocomposite by wide angle X–ray diffraction (WAXD).
- Dispersion of clay in PETG by transmission electron microscopy (TEM).
- Nano–morphology CNT based PETG nanocomposites by scanning electron microscopy (SEM).
- Thermal stability by thermogravimetric Analysis (TGA).
- Solid–state viscoelastic properties by dynamic mechanical thermal analysis (DMTA).

- Melt state viscoelastic properties by using a strain–controlled rheometer.
- Relaxation dynamics over a wide range of frequencies and temperatures using dielectric relaxation spectroscopy (DRS).

1.10 Structure of the Thesis

The studies reported in this thesis are concentrated on fabrication of novel amorphous copolyester nanocomposites based on organo–inorganic nanofillers using melt compounding technique. The entire thesis is presented in seven chapters, the contents of which are spread in such a manner so as to gather an understanding of the microstructure–property relationships in these nanocomposites.

Chapter 1 provides the necessary background relevant to the contents of the thesis, the motivation behind this work, as well as the objectives of this work. The overview of PETG and the nanofillers used in this work, viz. layered silicates, and CNTs is presented with respect to their types, classification and structure. Methods for fabrication of polymer nanocomposites and the applications of these materials are also described. This chapter also discusses the objectives of the present work and the structure of the thesis.

Chapter 2 provides a detailed literature search on different polymer nanocomposites. It describes the contribution of various researchers towards synthesis, characterization, and property improvements achieved in polymer nanocomposites based on layered silicates and CNTs. The properties and applications of PETG are also described.

Chapter 3 presents details of the materials used in this study and the experimental techniques used for characterization. The materials used in this study are polymer nanocomposites based on two grades of amorphous copolyester (Eastar 6763 and Eastar GN071) and six different organically modified layered silicates, and CNTs.

Chapter 4 reports the effect of molecular size and molecular structure of the intercalant used to modify the hydrophilic nature of the layered silicates, on the structure and viscoelastic properties of the nanocomposites prepared using PETG (Eastar 6763) and six different organically modified clays. Furthermore, the effect of modifier concentration on the properties of the nanocomposites is also discussed.

Chapter 5 describes the effect of clay concentration on the structure and properties of PETG/clay nanocomposites prepared using PETG (grade Eastar GN071) and organophilic clay (Cloisite 20A) at different clay loadings. In this study, dynamics of the nanocomposites are investigated over a broad range of temperatures and frequencies using DRS and DMTA and related to their nanomorphology through WAXD, TEM, and rheology.

Chapter 6 focuses on fabrication of PETG based CNT nanocomposites using simple melt processing technique, and understanding their viscoelastic properties through a series of experiments performed under various conditions of sinusoidal deformations. Both linear as well as non–linear rheological studies are discussed. To gather a better understanding between microstructure–property relationships of the nanocomposites, the electrical conductivity, and complex permittivity of the nanocomposites are also described.

Finally in chapter 7 the overall conclusions of this thesis are summarized along with recommendations for future research work.

REFERENCES

1. T. J. Pinnavaia, *Science* **220(4595)** 365 (1983)
2. N. Herron, D. L. Thorn, *Adv. Mater.* **10** 1173 (1998)
3. E. Ruckenstein, Y. N. Yuan, *Polymer* **38** 3855 (1997)
4. W. Helbert, J. Y. Cavaille, A. Dufresne, *Polym. Compos.*, **17** 604 (1996)
5. P. Hajji, J. Y. Cavaille, V. Favier, C. Gauthier, G. Vigier, *Polym. Compos.* **17** 612 (1996)
6. P. Walter, D. Mader, P. Reichert, R. Mülhaupt, *J. Macromol. Sci. Pure. Appl. Chem.* **36A** 1613 (1999)
7. L. E. Nielsen in: Mechanical Properties of Polymers and Composites; Marcel Dekker, New York (1974)
8. A. Usuki, Y. Kojima, M. Kawasumi, A. Okada, Y. Fukushima, T. Kurauchi, O. Kamigatio, *J. Mater. Res.* **8** 1179 (1993)
9. K. Yano, A. Usuki, A. Okada, T. Kurauchi, O. Kamigatio, *J. Polym. Sci. Part A: Polym. Chem.* **31** 2493 (1993)

10. P. B. Messersmith, E. P. Giannelis, *Chem. Mater.* **6** 1719 (1994)
11. A. Okada, A. Usuki, *Mater. Sci. Eng.: C* **3** 109 (1995)
12. T. Lan, T. J. Pinnavaia, *Chem. Mater.* **6** 2216 (1994)
13. J. W. Gilman, *Appl. Clay. Sci.* **15** 31 (1999)
14. E. P. Giannelis, R. Krishnamoorti, E. Manias, *Adv. Polym. Sci.* **138** 107 (1999**)**
15. S. W. Bailey in: The status of clay mineral structures, *Clay and Clays Minerals Proc.* 14th Nat Conf, Berkley, California, Pergamon Press (1966)
16. D. J. Greenland, R. H. Laby, J. P. Quirk, *Trans. Faraday Soc.* **61** 2013 (1965)
17. H. Van Olphen in: An Introduction to Clay Colloids Chemistry, John Wiley & Sons Inc. New York (1977)
18. S. B. Hendricks, *J. Phys. Chem.* **45** 65 (1941)
19. R. E. Grim, W. H. Allaway, F. L. Cuthbert, *J. Am. Ceram. Soc.* **30** 137 (1947)
20. C. T. Cowan, D. White, *Trans. Faraday Soc.* **54** 691 (1958)
21. E. F. Vansant, J. B. Uytterhoeven, *Clay Clay Miner.* **20** 47 (1972)
22. R. M. Barrer, K. Brummer, *Trans. Faraday Soc.* **59** 959 (1963)
23. J. W. Jordan, *J. Phys. Colloid Chem.* **53** 294 (1949)
24. J. W. Jordan, B. J. Hook, C. M. Finlayson, *J. Phys. Colloid Chem.* **54** 1196 (1950)
25. R. Greene–Kelly, *Trans. Faraday Soc.* **51** 412 (1955)
26. G. Lagaly, *Solid State Ionics* **22** 43 (1986)
27. E. Hackett, E. Manias, E. P. Giannelis, *J. Chem. Phys.* **108** 7410 (1998)
28. V. Krikorian, D. J. Pochan, *Chem. Mater.* **15** 4317 (2003)
29. V. Krikorian, D. J. Pochan, *Macromolecules* **38** 6520 (2005)
30. S. Ijima, *Nature (London)* **354**, 56 (1991)
31. P. M. Ajayan, O. Stephan, C. Colliex, D. Trauth, *Science* **265**, 1212 (1994)
32. S. Iijima, T. Ichihashi, *Nature* **364**, 737 (1993)
33. I. Y. Boris, R. E. Smalley, *Am. Sci.* **85** 324 (1997)
34. C. A. Cooper, R. J. Young, M. Halsall, *Compos. Part A–Appl. S* **32A** 401 (2001)
35. G. Gao, T. Cagin, W. A. Goddard III, *Nanotechnology* **9** 184 (1998)
36. T. Uchida, S. Kumar, *J. Appl. Polym. Sci.* **98** 985 (2005)
37. A. Dee Heer Walt, *MRS Bull.* **29** 281 (2004)
38. M. Monthioux, *Carbon* **40** 1809 (2002)

39. M. Dresselhaus, G. Dresselhaus, P. Eklund, R. Saito, *Phys. World* **January** (1998)
40. L. Jin, C. Bower, O. Zhou, *Appl. Phys. Lett.* **73**, 1197 (1998)
41. E. S. Choi, J. S. Brooks, D. L. Eaton, M. S. Al – Haik, M. Y. Hussaini, H. Garmestani, D. Li, K. Dahmen, *J. Appl. Phys.* **94**, 6034 (2003)
42. T. Kurauchi, A. Okada, T. Nomura, T. Nishio, S. Saegusa, and R. Deguchi in: Nylon 6–clay hybrid–synthesis, properties and application to automotive timing belt cover, *SAE Technical Paper Series 910584* International Congress and Exposition, Detroit (1991)
43. www.scprod.com
44. www.composite.about.com
45. http://www.azom.com/details.asp?ArticleID=921
46. http://metunanocomposite.tripod.com/applicat/
47. K. Nakamura, K. Nakamura, *PCT Int. Appl. WO2004054802* **26** (2004)
48. http://www.nanocor.com/techpapers.asp: Multilayer containers featuring nano-nylon MDX6 barrier layers with superior performance and clarity, Mitsubishi Gas Chemical Inc. and Nanocor presentation at Nova-Pack (2003)
49. http://www.InMat.com

CHAPTER 2

LITERATURE

This chapter provides a detailed literature search on different polymer nanocomposites. It describes the contribution of various researchers towards synthesis, characterization, and property improvements achieved in polymer nanocomposites based on layered silicates and CNTs. The properties and applications of PETG are also described. The chapter is mainly divided into three parts which review the polymer layered silicate nanocomposites, CNT nanocomposites, and PETG, respectively.

2.1 Polymer Layered Silicate Nanocomposites

2.1.1 Synthesis of Polymer Layered Silicate Nanocomposites

Polymer layered silicate (PLS) nanocomposites can be synthesized by solution blending, in situ polymerization, and melt blending as reported in chapter 1. In 1992 Aranda et. al. showed that poly (ethylene oxide) (PEO)/montmorillonite nanocomposites can be prepared by dissolving PEO in a suitable solvent which also swells the montmorillonite.[1] Various polymer–clay nanocomposites, using polymers like poly(vinyl acetate),[2] polyethylene (PE),[3] PEO,[4] polycaprolactone (PCL),[5] poly(lactic acid) (PLA),[6] syndiotactic–polystyrene,[7] and poly(methyl methacrylate) (PMMA)[8] have been synthesized using this route. Although no studies involving measurements of the nanocomposite properties after a certain period of time (in order to study the aging behavior of the nanocomposite) is reported, it is believed that once the clay is dispersed by a certain distance from the neighboring platelet so that no Van der Waals interactions are present, the clay layers would not collapse back and deteriorate the properties.

In 1988 Okada et. al. from Toyota Motor Company (Japan) filed the first US patent (#4739007) for the development of nylon/clay nanocomposites by in situ polymerization route. The approach they took was to modify natural Na–montmorillonite by cation exchanging it with ammonium cations of various ω–amino acids [$H_3N^+(CH_2)_{n-1}COOH$, n = 2, 3, 4, 5, 6, 7, 8, 11, 12, and 18]. Montmorillonite cation exchanged with 12–aminolauric acid was used for nanocomposite preparation by *in situ* polymerization of ε–caprolactam in presence of the cation exchanged clay. This nanocomposite exhibited unprecedented mechanical properties. The flexural strength was doubled whereas flexural modulus increased by almost four folds and the tensile strength and modulus were almost doubled at a clay loading of <5%. Since then various exfoliated polymer–clay nanocomposites, using polymers like polystyrene (PS),[9] epoxy,[10–14] poly (ethylene terepthalate) (PET),[15,16] PE,[17–21] PMMA,[22] PCL,[23] polycarbonate (PC),[24,25] polypropylene (PP),[26,27] poly(dimethyl siloxane),[28] polyamide,[29–32] polyimide (PI),[33] etc., have been synthesized by this route. Thus it may be inferred that in situ polymerization often leads to exfoliated nanocomposites. However, the exact reason behind this phenomenon remains elusive. There are extensive reports of exfoliated nanocomposites synthesized by in situ polymerization method where the catalyst is anchored on the clay surface. PLS

nanocomposites synthesized by this route has a portion of polymer chains tethered to the clay surface.[18,34–36] In this case monomers diffuse into the clay gallery to react chemically at this growth site; the growing polymer chain physically pushes the platelets apart by volume expansion to cause exfoliation.

In 1993, Giannelis et. al. showed that PLS nanocomposites can be developed by melt blending the polymer and an organically modified layered silicate in a twin–screw extruder.[37] Vaia et. al described this technique and gave a general explanation for the driving forces for this process.[38–40] Improved intercalation was observed by using conventional processing techniques like extrusion. Cho et. al. showed that melt processing technique can be an effective method to achieve exfoliation and dispersion of the silicate layers in nylon 6 matrix.[41] Moreover, comparable properties to those achieved by in situ polymerization are possible in nanocomposites prepared by melt processing for optimally compatibilized PLS systems. Diffusion and shear stress during melt blending also affect the degree of dispersion and exfoliation. A layer by layer pealing mechanism has been proposed for exfoliated PLS nanocomposites prepared using a co–rotating twin screw extruder. Fornes et. al. suggested various roles of shear stress in the melt–compounding process, including breaking silicate particles and dispersing them into stacks of silicate platelets or tactoids.[42,43] Also, the stress can shear the silicate tactoids into smaller stacks of silicate platelets, or even peal individual platelets apart, a process which allows polymer chains to diffuse into the silicate gallery. The various factors that affect the dispersion of clays in PLS nanocomposites are discussed in more details in the following section. Many commercially important PLS nanocomposites have been synthesized using the melt blending technique. Some examples are nylons[42–44], PET,[45] PE,[46,47] PP,[48–50] PCL,[51,52] poly(butylenes terephthalate) (PBT),[53], ethylene vinyl alcohol (EVOH),[54] PC,[13] etc.

If technically possible, melt compounding could be significantly more economical and simple than in situ polymerization processes. This approach would allow nanocomposites to be formulated directly using conventional extruders and mixers as needed without the necessary involvement of resin producers. Indeed in many commercially important polymers, solution intercalation or in situ polymerization techniques are difficult to implement on an industrial scale, because a suitable solvent–

polymer system is not always available and also an additional step of solvent removal is involved.[55,56] Being environmentally friendly and cost effective, the development of the melt blending route brought PLS nanocomposites closer to commercialization.

2.1.2 Factors Affecting Dispersion of Clay Platelets

2.1.2.1 Molecular Weight of Polymer

Fornes et. al proposed a model for explaining the mechanism of exfoliation of clay layers, from an initially present stack of clay layers, by the stepwise skewing of the clay platelets, followed by peeling, one–by–one, of the silicate layers off the silicate stack under the influence of shear forces.[42] A schematic of the skewing/peeling and diffusion mechanism as proposed by Fornes et. al. is shown in Figure 2.1. The intercalation/exfoliation of clay platelets was shown to be a combination of two mechanisms 1) the breaking up of large clay stacks into smaller stacks of fewer and fewer clay platelets under the influence of large shear forces (Figure 2.1a), and 2) the diffusion of the polymer molecules into the clay galleries (Figure 2.1b). They also showed that higher the molecular weight of the polymer matrix, higher was its melt viscosity; greater was the stress exerted on the stack of clay platelets and lesser was the number of platelets left in the stack.

Although the mechanism of intercalation/exfoliation by breaking of large clay crystals into smaller ones (Figure 2.1a) and then peeling of each platelet one after one seems possible, the bending of the ends of clay layers (Figure 2.1b) in order to allow the intercalation of polymer chains seems unlikely. Most likely the whole clay platelets at the top and at the bottom of a clay crystal would just separate out one after another by skewing under the influence of shear force since this would require less energy than that required for bending the ends of the clay layers and hence their ionic bonds with the neighboring platelets.

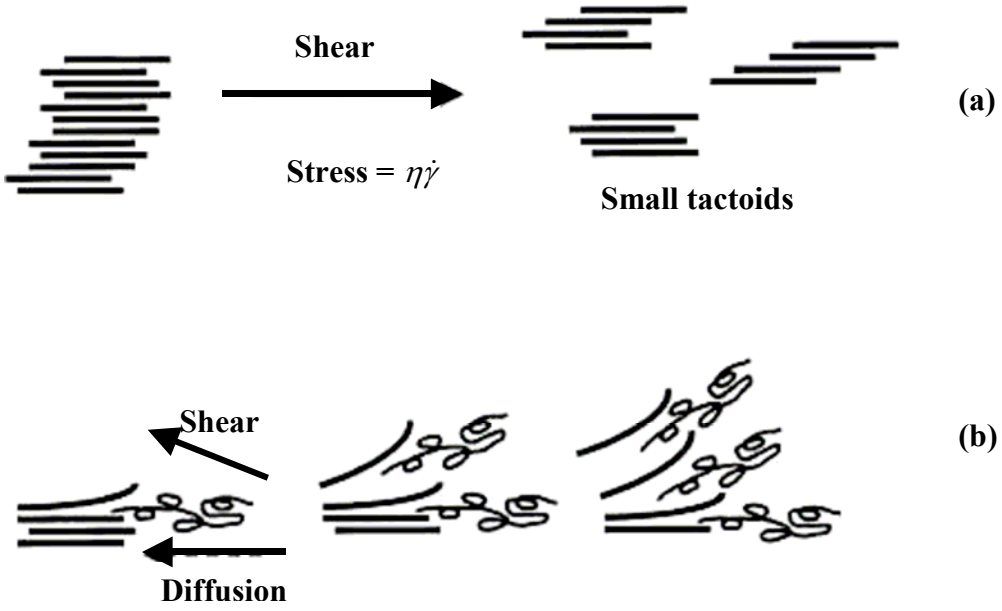

Figure2.1 Schematic of clay exfoliation during melt mixing of nanocomposites[42]

Increase in the molecular weight decreases the diffusion of polymer chains ($D \sim 1/M^2$)[57] into the clay galleries and hence should decrease the rate of hybrid formation. Thus, in a nanocomposite system, the rate of hybrid formation depends on the type of mechanism, which dominates. For example, Ishida et. al.[58] observed a decrease in the degree of intercalation/exfoliation on increase in the molecular weight of the base resin for PLS nanocomposites based on epoxy, PS, etc. They prepared the nanocomposites by manually mixing the polymer melt and clay. Due to the lower degree of shear involved, the mechanism of the diffusion of polymer chains dominated the intercalation process and hence the degree of intercalation/exfoliation decreased with the increase in molecular weight. Fornes et. al.[42] observed an increase in the degree of intercalation/exfoliation with increasing molecular weight in nylon/clay nanocomposites. The nanocomposites were made by extruding a mixture of polymer and clay through a twin–screw extruder. Due to the higher degree of shear involved the breakup of large stacks into smaller ones took place and hence increased the rate of hybrid formation. Thus the molecular weight

of the base resin affects the rate of hybrid formation by two different mechanisms and the actual rate depends on the combinatory effect of both the mechanisms.

2.1.2.2 Thermodynamics of Intercalation Process

Vaia et. al.[59,60] proposed a mean–field model to explain the intercalation of polymer molecules in an organically modified clay. They proposed that changes taking place in both entropy and enthalpy by the addition of clay into the polymer matrix play an important role in determining the degree of intercalation/exfoliation in the nanocomposite system.

From an entropic point of view they proposed that the intercalation of polymer chains in the clay gallery decreases its entropy due to polymer confinement and thus decreases the overall entropy, and thus the free energy, of the system, which is unfavorable for further polymer intercalation. But they also proposed that this decrease in entropy can be balanced by the increase in entropy of the alkyl–ammonium chains on the surface of the clay layers due to increased gallery height. The increase in the entropy depends on the gallery height, which in turn depends on the interlayer packing density of the alkyl ammonium (aliphatic) chains. Interlayer packing density is the number of aliphatic chains of the surfactant present per unit area of the surface of the silicate layer. At very low packing densities the aliphatic chains display mono/bilayer arrangement while at very high packing densities they display solid–like fully extended arrangement.[60,61]

At both low and very high packing density the aliphatic chains have comparatively less conformational freedom and thus the total entropy increase is not high enough to balance the decrease in entropy by polymer confinement and is thus unfavorable for polymer intercalation. At intermediate range of packing densities the chains adopt pseudo–trilayer arrangements, which have comparatively higher conformational freedom and thus balance the decrease in entropy by polymer confinement, resulting in a net entropy change near zero. Thus the hybrid formation by melt intercalation now depends on the enthalpic interactions between the polymer and clay surfaces which can be increased by polymer and clay surface functionalization. By experiments they also showed that the outcome of polymer intercalation depends on the

silicate functionalization and constituent polar interactions between the clay and the polymer.[60]

Balazs and coworkers[62] have investigated the thermodynamic factors affecting the hybrid formation. They have suggested that the interaction between the polymer and the treated clay surface decides the type of composite formed. If the interaction parameter (χ), between the polymers and surface of the treated clay, is less than zero and length of polymer chains is large, then the probability of forming an intercalated hybrid is maximum. From thermodynamic point of view, increasing the attractive interaction between the polymer and surfactants promotes formation of exfoliated structures. But the kinetic behavior of interpenetrating of interpenetrating polymers can hinder formation of exfoliated structures. They have provided design criteria for synthesizing exfoliating agents. The polymer must contain a fragment that is highly attracted to surface and thus promotes the miscibility. In addition it should contain a longer segment that is not attracted to the sheets and will attempt to push layers apart. Once separated, these blocks will stearically hinder the surfaces from coming into closer contact. They have suggested that use of a mixture of functionalized and non–functionalized polymers for the melt can also lead to exfoliated morphologies.[63] Miscibility can also be enhanced between organically modified clay and polymers with higher number of branches, due to the compactness of the macromolecules.[64] They have also shown a bare surface and a surface with too many tethered surfactants are both unfavorable for forming hybrids. This also suggests that there is an optimal grafting density, which depends on the specific value of χ between the polymer and surfactant.[65]

2.1.2.3 Polymer–Clay Interaction

As explained in the earlier section it was shown by Vaia et. al.[60] that functionalization of the clay surfaces is very critical for polymer intercalation into the clay galleries. Presence of functional groups on the surface of the clay layers easily intercalate polar polymers but do not favor intercalation of non–polar polymers like PE and PP. Addition of a compatibilizer like maleated polyolefin oligomer increases the interaction between the clay surface and the non–polar polymer. This increase in

interaction originates from the strong hydrogen bonding between the maleic anhydride (MA) groups and the oxygen atoms on the clay surfaces.[66]

Increased interaction between the two, acts as a driving force for the intercalation of the compatibilizer into the clay galleries. The bulky nature of the maleated polyolefin oligomer increases the clay–spacing and decreases the interactions between the clay layers which in turn favor the intercalation of the base resin (PE/PP). Increasing the polarity of the compatibilizer increases the interactions between the clay and the polymer and hence the degree of intercalation/exfoliation.[60]

2.1.2.4 Processing Conditions

Dennis et. al. have reported on the effects of the melt processing conditions on the exfoliation of PLS nanocomposites based on polyamide 6.[44] It was shown that various factors including the residence time in the extruder and the intensity of shear control the dispersion of clay in the polymer matrix. They found that the degree of clay dispersion was maximized by the backmixing in a co–rotating twin–screw extruder.

2.1.3 Structure and Morphology

2.1.3.1 X–ray Diffraction

X–ray diffraction (XRD) has been traditionally used to evaluate the structure of PLS nanocomposites. Due to the periodic arrangement of the silicate layers, with periodicity of 1–4 nm and the presence of high atomic number species in the interlayers, the choice of XRD in determining the interlayer spacing is obvious. The finite layer expansion in the case of intercalated nanocomposites leads to the emergence of a new set of basal planes, which can be identified. Study of the relative position, shape and intensity of the basal reflections can identify the nanocomposite structure. For an intercalated structure, the d_{001} characteristic peak tends to shift to lower angle regime due to the expansion of the basal spacing. Although the layer spacing increases, there still exists an attractive force between the silicate layers to stack them in an ordered structure. In contrast, no peaks are observed in the XRD pattern of exfoliated polymer nanocomposites due to loss of the structural registry of the layers. The absence of Bragg diffraction peaks in the nanocomposites may indicate that the clay has been completely

exfoliated or delaminated.[60] However, in the absence of registry, as in an exfoliated or a delaminated nanocomposite, as well as in a disordered nanocomposite, XRD does not provide definite information regarding the structure of the nanocomposite. The absence of Bragg diffraction peaks in a XRD scan should not be used as the sole evidence for formation of an exfoliated hybrid. Morgan and Gilman[67] and Eckel et al.[68] pointed out that XRD analysis alone can lead to false interpretations of the extent of exfoliation. Several factors such as clay dilution, peak broadening and preferred orientation make XRD characterization of polymer nanocomposites susceptible to errors. Clay dilution and peak broadening can yield false result that exfoliation has occurred. Conversely, preferred orientation effects can result in the false conclusion that exfoliation has not occurred.

Small angle X–ray scattering (SAXS) is also used as a technique to analyze PLS nanocomposites. Bafna et al have used 2 dimensional simultaneous SAXS and wide angle X–ray scattering (WAXS) measurements to determine the 3 dimensional orientations of the polymer and clay in the polymer nanocomposites.[69]

2.1.3.2 Transmission Electron Microscopy

Transmission electron microscopic (TEM) observation is needed to confirm formation of exfoliated nanocomposites.[68] XRD does not yield the information relating to the spatial distribution of the silicate in the polymer matrix because all its data are averaged over the whole regions of the specimen. On the other hand, transmission electron microscopy (TEM) can provide useful information in a localized area on the morphology, structure and spatial distribution of the dispersed phase of the nanocomposites. Vaia et al. indicated that the features of the local microstructures from TEM give useful detail to the overall picture that can be drawn from the XRD results.[38] Thus XRD and TEM techniques are regarded as complementary to each other for materials characterization of the clay–polymer nanocomposites.

2.1.4 Nanocomposite Properties

2.1.4.1 Thermal Stability

The first report on the enhanced thermal stability of a PLS nanocomposite was based on PMMA/clay nanocomposites.[70] The intercalated PMMA between the clay layers exhibited resistance to thermal degradation under conditions that would otherwise completely degrade pure PMMA. Thermogravimetric analysis revealed that both linear and cross–linked PMMA intercalated into clay galleries have 40–50 °C higher decomposition temperature. The stability of the PMMA nanocomposite was attributed not only to its different structure but also to restricted thermal mobility of the PMMA chains in the clay gallery.

Many reports concerning the improved thermal stability of PLS nanocomposites have been recently published.[71–73] The nanocomposites exhibits a significant delay in weight loss that may be due to the barrier effect caused by both the volatile thermooxidation decomposition products to the gas and oxygen from the gas phase to the polymer. According to Gilman et. al. this barrier effect increases during volatilization due to the reassembly of the reticular of the silicate on the surface.[74] The role of clay in the nanocomposite structure may be the main reason for the difference in TGA results of these systems compared to the previously reported systems. The clay acts as a heat barrier, which enhances the overall thermal stability of the system, as well as assist in the formation of char after thermal decomposition. In the early stages of thermal decomposition, the clay would shift the decomposition to higher temperature. After that, this heat barrier effect would result in a reverse thermal stability. In other words, the stacked silicate layers could hold accumulated heat that could be used as a heat source to accelerate the decomposition process, in conjunction with the heat flow supplied by the outside heat source.

2.1.4.2 Coefficient of Thermal Expansion

Liang et. al. observed a significant decrease in the coefficient of thermal expansion (CTE) of poly(ether imide) (PEI) by addition of clay to it.[75] The CTE of PEI decreased from 2.37×10^{-5} K^{-1} for PEI to 1.33×10^{-5} K^{-1} for PEI containing 10 wt%

organically modified clay. They propose the reduced segmental motion of the PEI matrix by addition of clay to it as the reason for the decrease in the CTE.

Yoon et. al. studied the thermal expansion behavior of nylon–6/clay nanocomposites.[76] TEM analysis showed that the clay layers were exfoliated in the polymer matrix. They studied the coefficient of thermal expansion for injection molded Izod bars. They observed a decrease in the CTE along the flow direction (FD) and the transverse direction (TD) when compared to nylon–6 containing no clay. They observed that the CTE decreases more along the FD than along the TD and was attributed to the anisotropy of the clay platelets. They also showed that nanocomposites made from high molecular weight polymer had higher degree of exfoliation (higher aspect ratio) and thus lower CTE and the nanocomposites made from lower molecular weight polymer had lower degree of exfoliation (lower aspect ratio) and thus higher CTE even though it was lower than the base resin.

2.1.4.3 Barrier Properties

Generally, PLS nanocomposites are characterized by dramatic reduction in gas and liquid permeabilities, and at the same time, the solvent uptake decreases accordingly. This improvement in the barrier properties can be attributed to the creation of a tortuous path on incorporation of clay in the polymer matrix that retards the progress of the gas molecule through the resin matrix as shown in Figure 2.2. Dramatic decrease in the water vapor transmission has been reported in poly(urethane urea)/clay nanocomposites.[77] Oxygen gas permeability has been measured for PLA/clay nanocomposites by Sinha Ray et. al.[78] The oxygen gas transmission reduces dramatically from 200 for pure PLA to about 50 $O_2TR/ml.mm.m^{-2}.day^{-1}.MPa^{-1}$ in the nanocomposites. The data was analyzed using Nielsen theoretical expression allowing prediction of gas permeability as a function of the length and width of the filler particles as well as their volume fraction in the polymer matrix.[79]

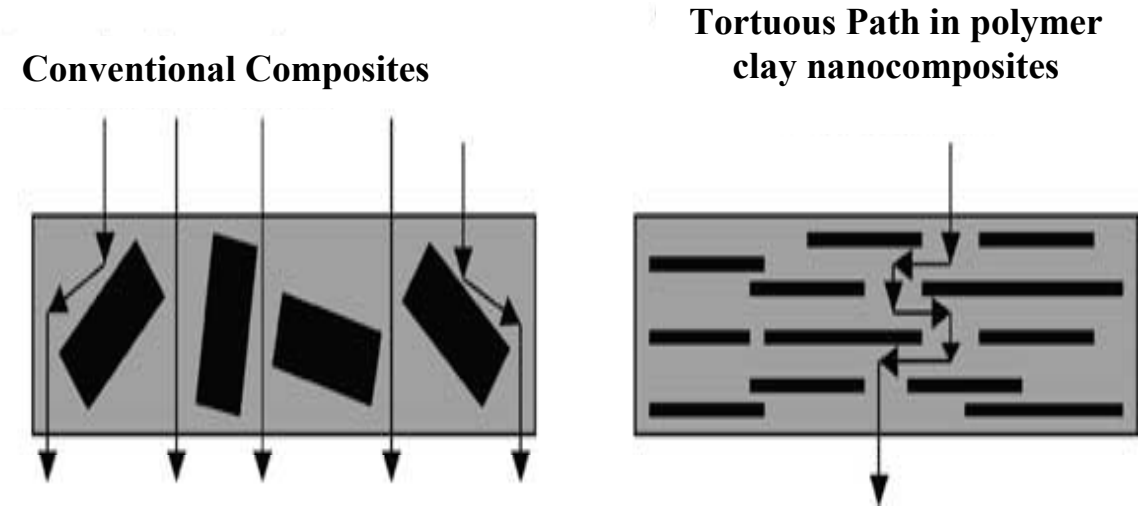

Figure 2.2 Schematic of tortuous path for barrier property enhancement in polymer clay nanocomposites

2.1.4.4 Flame Retardancy

The potential flame retardant properties of PLS nanocomposites were first reported in a 1976 Unitika patent application on nylon–6/clay nanocomposites.[80] However, it was only recently that a more detailed evaluation of the flammability properties of these materials was reported.[37] Recent work done by Gilman et. al. using cone calorimetry and radioactive gasification experiments, has shown improved flammability behavior of a number of PLS nanocomposites.[73,74,81] The flammability properties of layered silicate based nanocomposites with different polymers viz. PP, PS, nylon–6, and epoxies show dramatic reduction in flammability.[82] The reduced flammability in the nanocomposites was attributed to the response of a high–performance carbonaceous–char layer, which builds up on the outer surface during combustion. This surface–char has a high concentration of clay that insulates the underlying material by becoming a mass transport barrier slowing the oxygen supply as well as the escape of the decomposition products during combustion.

2.1.4.5 Optical Clarity

Although layered silicates are microns in lateral dimensions, they are just 1 nm thick. Thus when single clay layers are dispersed in a polymer matrix the resulting nanocomposite is optically clear in visible region. At the same time, there is a loss of intensity in the UV region (for $\lambda < 300$ nm), mostly due to scattering of the clay particles. This loss of intensity mainly occurs due to intercalated/immiscible tactoids, whereas exfoliated clay layers do not seem to contribute. There is no marked decrease in the clarity due to nano–dispersed fillers compared to that of the neat filled polymer. This behavior is generally observed by UV/vis transmittance for films with thickness of ~ 0.1–3 mm of PLS nanocomposites, based on PVA and PP.[2,83]

2.1.4.6 Dynamic Mechanical Properties

Dynamic mechanical thermal analysis (DMTA) is an important tool to study the structure–property relationships in polymer composites. DMTA probes essentially the relaxations in polymers, thereby providing a method to understand the mechanical behavior and the molecular structure of these materials under various conditions of stress and temperature. It is generally observed that the addition of organic layered silicates increases the storage modulus of the nanocomposites. Hasegawa et. al. reported the mechanical properties of PP/clay nanocomposites prepared using MA modified PP oligomer as a compatibilitzer.[84] The storage moduli values observed for PP/clay nanocomposites were found to be higher than those of pure PP upto 130 °C. The relative storage moduli of PP/clay nanocomposite to those of pure PP were studied to understand the effect of clay hybridization. These values were found to be relatively small below glass transition temperature (T_g) of PP, however above T_g they drastically increased and then decreased to melt. This tendency was emphasized more strongly as clay layers were more uniformly dispersed in the PP matrix. While the relative storage moduli of poorly dispersed clay layers was found to be relatively small and almost independent of temperature. Jog et al have reported that the PP/clay nanocomposites exhibit higher storage modulus (increase of about 56 %) than neat PP over the entire temperature range studied (-40 to 120 °C).[85,86] The loss modulus that corresponds to the dissipation of the energy shows a peak at about 11 °C for PP, which corresponds to the glass transition

temperature of PP. In PP/clay nanocomposites, this peak is not well defined. It was thus concluded that the cooperative relaxation of PP in the nanocomposites becomes weak due to the restricted mobility of the chains in presence of the clay layers.

Tyan et al first observed an increase in T_g in the case of PI.[87] Messersmith et. al. observed an increase in T_g as well as broadening of peak as measured by DMTA in epoxy nanocomposites, which they have attributed to the hindered relaxational mobility in polymer segments near the surface.[88] Similar increase in T_g is observed in nanocomposites of PCL,[52] PU,[89] PI,[90–92] PMMA,[93–95] PS,[96] PP,[97–102] and poly(vinyl chloride).[103] This increase in T_g has been ascribed by most of them to the restriction in segmental motion.[89,97,98] However, not always an increase in T_g is observed in the DMTA results of PLS nanocomposites. Lowering of T_g has been reported for PP/clay[104] nanocomposites and epoxy/clay[105] nanocomposites. The decrease in T_g was attributed to the plasticization of the matrix near the silicate layers by the surfactant chains.

2.1.4.7 Melt Rheology

A rheological study of polymer nanocomposites is of much importance considering their fabrication and final applications. Rheology is a powerful tool, which provides important information on the internal microstructure of the nanocomposites, the state of dispersion of the clay, its orientation and aspect ratio, as well as the effects of particle–particle interactions in clay and particle–polymer interactions on the viscoelastic behavior of the nanocomposites. Therefore, an understanding of the viscoelastic properties of polymer nanocomposites, both in solid and molten state is essential from processability and structure–property point of view.

2.1.4.7.1 Linear Viscoelastic Properties

Linear viscoelastic properties of intercalated and exfoliated PLS nanocomposites, under dynamic oscillatory shear have been examined using various polymers as matrix phase including polyamides,[106–108] PCL,[109–111] PS,[112] polystyrene–polyisoprene block copolymers,[113–116] and PP.[117–120] The most significant results of these works are summarized as:

1. A transition from liquid–like to solid–like rheological behavior for nanocomposites at relatively low silicate loadings is observed with relatively small differences between intercalated and exfoliated systems. Ren et al have attributed the pseudo–solid like behavior observed in the nanocomposites to the physical jamming of the dispersed clay layered silicates formed due to the highly anisotropic nature.[114]
2. The applicability of the principle of time–temperature superposition to prepare viscoelastic master curves, with frequency shift factors comparable to that of the unfilled polymer, is demonstrated.
3. Prolonged application of large amplitude oscillatory shear leads to a significant decrease of the linear viscoelastic modulus and elimination of solid–like behavior of the nanocomposites.

Dynamic oscillatory shear experiments are representative of the durability of the sample under various conditions of vibrations and/or external stress. Galgali et al have studied the rheological response of isotactic PP/clay nanocomposites in presence and absence of the compatibilizer viz. PP–graft–MA.[121] They show that the nanocomposites show a solid–like rheological response at low frequencies, which is completely dependent on the amount of clay loading in the nanocomposites, and is independent of the finer structure of the nanocomposites, i.e. whether they are end–tethered or melt intercalated. They argue that the typical rheological response of the nanocomposites does not arise due to restricted mobility of the confined polymer chains between the clay galleries, but is an effect of the frictional interactions between the clay layers. Further they have shown that beyond the apparent yield stress the zero shear viscosity of the PP/clay nanocomposite containing 7 wt% clay and the compatibilizer drops dramatically by more than 3 orders of magnitude, suggesting that the solid–like behavior of the PP/clay nanocomposites after annealing is due to the formation of a percolating network that strongly resists deformation.

Recently, Abranyi et al reported through rheological investigation that a percolated clay network formations is possible only under certain conditions.[122] Accordingly, at low clay content higher degree of exfoliation is needed to produce the number of silicate layers to form a percolated structure. When the clay content is higher

which increases the number of individual platelets thus the amount of compatibilizer required for the formation of the network is less. To summarize a threshold concentration of PP–graft–MA exists in PP/clay nanocomposites for the formation of the clay network, which depends on the silicate content.

Lele et al studied the rheology–microstructure links in syndiotactic PP/clay nanocomposites using in situ rheo–X–ray measurements of the nanocomposites during shear.[123] The microstructure of the nanocomposite at low strain and shear rates consisted of a percolating three–dimensional network of dispersed clay tactoids. Rheology indirectly indicated that the observed yielding of the material at high stresses might be linked to the orientation of the clay tactoids, which was evidenced using the rheo–X–ray diffraction measurements. The transient experiments showed that the clay tactoids relax their orientation incompletely after cessation of shear. It was observed that the stress relaxation of the matrix chains, which were compatibilized with clay platelets, drive the orientation relaxation in about 10^{-3} s. After this time scale the clay tactoids are jammed and produce a percolating network having a residual orientation and a residual relaxation modulus. In steady shear experiments at shear rates below 10^{-3} s^{-1} the response corresponding to that of a percolating network would be observed while at shear rates above 10^{-3} s^{-1} a yield like response would be observed.

Hoffmann et. al. have studied the effect of types of modifiers used for flouromica on the rheological property of PS/flouromica nanocomposites.[124] Intercalated structure was observed when 2–phenyethylamine (PEA) was used as modifier while for amine terminated polystyrene (AT–PS) an exfoliated structure was observed. It is reported that the time temperature superposition holds for pristine PS as well as for both nanocomposites. The plots of G' vs. the reduced frequency (ωa_T) showed slightly higher values of G' for intercalated nanocomposites prepared using PEA treated fluoromica, while G' for exfoliated nanocomposite prepared using AT–PS showed significant increase in G'. This increase in G' at low frequencies was attributed to the network formation involving assembly of platelets.

2.1.4.7.2 Non–linear Viscoeleastic Properties

PLS nanocomposites based on poly(butylene succinate) studied under steady shear showed enhanced shear viscosity at all shear rates with respect to time, and increase monotonically with increasing silicate loading at a fixed shear rate.[125] However, the intercalated nanocomposites showed strong rheopexy behavior, especially at low shear rates, whereas the neat polymer exhibited a time dependent viscosity at all shear rates. The shear viscosity attains a plateau with increasing shear rates, however the time required to attain this plateau decreases with increasing shear rate. This behavior is explained considering the planar alignment of the clay particles towards flow direction under shear. Krishnamoorti et al[126] observed that the viscosity of hybrids is comparable to that of the matrix viscosity in Polystyrene isoprene nanocomposites, suggesting that the shear flow aligns the clay tactoids.

Polymer nanocomposites always exhibit diversions from the empirical Cox Merz rule, particularly above percolation thresholds,[126] while neat polymers obey the empirical equation, which require that plotting $\eta(\dot{\gamma})$ versus $\dot{\gamma}$ is almost same as plotting the complex viscosity versus ω and is typically applicable for a wide class of polymer melts and solutions.[127] Thus, for $\dot{\gamma} = \omega$ the viscoelastic data should obey the relationship $\eta^*(\omega) = \eta(\dot{\gamma})$. Failures of the Cox–Merz rule have been observed in other systems like polymer–polymer blends,[128] particle filled polymers,[129] liquid crystalline polymers,[130] and fiber reinforced polymer composites.[131,132]

2.1.4.8 Dielectric Relaxation Spectroscopy

Dielectric relaxation spectroscopy (DRS) is a powerful technique for elucidating molecular relaxation as a function of temperature and frequency, which give information of the effects due to intermolecular cooperative motion and hindered dipolar motion. An alternating current external electric field is applied across the sample in a capacitor plate configuration. The polarization is related to applied electric field and it consists of four different dielectric mechanisms (electronic, atomic, orientation or dipolar and ionic polarization).

Kanapitsas et. al. have investigated the molecular mobility of exfoliated epoxy resin/clay nanocomposites in relation to micro–morphology by DRS.[133] They observed that the large–scale heterogeneity, characteristic of the epoxy matrix is suppressed in the nanocomposites and replaced by small–scale heterogeneity related to the presence of silicate layers. At temperatures lower than 150 °C the overall molecular mobility in the nanocomposites was decreased as compared to that of the matrix polymer. These observations were understood in terms of increased free volume, due to loosened segmental packing in chains confined to nano–volumes and of tethering of the chains to the silicate platelets. This provides an explanation for the observed increased thermal stability of in the PLS nanocomposites.

Online monitoring of the relaxation behavior of molten nylon/clay nanocomposites showed only one relaxation (identified as α relaxation) in molten nylon, while the nanocomposites produced two relaxations [identified as α relaxation and Maxwell–Wagner–Sillars interfacial polarization (MWS)].[134] MWS was ascribed to the conducting ions in a polymer/filler mixture and relaxation properties were dependent on the microstructure of the filler. The MWS relaxation was an order of magnitude greater in intensity than that of the α relaxation.

PP–graft–MA/clay nanocomposites prepared using two organically modified clays were investigated using DRS.[135] In contrast to pure PP, PP–graft–MA showed a dielectrically active relaxation process which can be attributed to localized fluctuations of the polar maleic anhydride groups. Its relaxation rate exhibited unusual temperature dependence, which was ascribed to a redistribution of water molecules in the polymer matrix. In the nanocomposites the relaxation process shifted to higher frequencies up to 3 orders of magnitude as compared to the unfilled polymer, which indicated enhanced molecular mobility in the interfacial regions. Further the nanocomposites showed additional high temperature process due to MWS polarization. The time constant of this process provided additional information on dispersion and delamination of clay platelets.

Recently Page et. al. studied DRS behavior of sodium montmorillonite with a series of polymers. For all systems three relaxation modes were observed.[136] The normal and segmental processes were assigned to motions of polymer chains outside the clay particles. However the relaxation strengths of these processes were much higher than

those in the pure polymers due to enhancement of the internal field by presence of the clay. The α_S' process was only observed in the nanocomposites and below the T_g of the corresponding polymer. This process was attributed to the segmental motions of the intercalated polymer chain.

2.2 Polymer Carbon Nanotube Nanocomposites

2.2.1 Synthesis of Polymer Carbon Nanotube Nanocomposites

In chapter 1 the various methods used for fabrication of polymer nanocomposites have been discussed. The most common method to prepare polymer/CNT nanocomposites is to mix the nanotubes and the polymer in a suitable solvent followed by evaporating the solvent and casting of a film. An early example of polymer/CNT nanocomposite prepared by solution blending is based on polyhydroxyaminoether (PHAE)/CNT nanocomposites.[137] In this work CNT were sonicated in chloroform for 1 h, followed by dissolution of the PHAE in CNT–chloroform dispersion. Mixing was achieved by sonication for an additional hour. The obtained nanocomposite after drying the suspension, showed reasonably good dispersion of CNTs in the polymer matrix. In the following studies Shaffer and Windle dispersed chemically modified catalytic CNT in water.[138] This was carefully blended with solutions of PVA in water to give nanocomposite dispersions, which could be drop cast to form films with up to 60 % CNTs. Quain et. al.[139] used sonication to disperse catalytic CNT in toluene. This was then blended with a solution of PS, also in toluene. Mixing was achieved by further sonication before casting to form films. Subsequently many groups have utilized this technique.[140] Ruan et al.[141] followed a similar method but used magnetic stirring and sonication to disperse the nanotubes but reflux to mix the nanotubes and polymer.

Polyaniline (PANI)/ CNT nanocomposites were prepared by in situ polymerization.[142] The results revealed the site–selective interaction between the quinoid ring of PANI and CNTs, thus opening the way for charge transfer processes, and improving the electric properties of PANI/CNT composites. Xiao and Zhou deposited polypyrrole (PPY) or poly(3–methylthiophene) PMeT on the surfaces of the CNTs by in situ polymerization.[143] The Faraday effect of the conducting polymer enhances the performance of super–capacitors with CNTs deposited with the conducting polymer.

High performance structural composites based on CNTs and polymer have also been prepared by in situ polymerization. Jia et al. first synthesized PMMA/CNT composites by in situ polymerization of methyl methacrylate monomer with CNTs present.[144] Later, Park et al.,[145] Velasco–Santos et al.,[146] and Jang et al.[147] polymerized in situ PMMA/CNT, and liquid crystalline epoxide (LCE)/CNT composites. For PMMA/CNT composites containing 1 wt% CNT, the storage modulus at 90 °C is increased significantly by 1135 %, and the T_g is raised exceptionally by ~ 40 °C. For LCE/CNT composites containing 1 wt% CNT, the nematic phase temperature of liquid crystalline epoxide (LCE) is decreased. polyamide/CNTs composites have been prepared by in situ hydrolytic polymerization of ε–caprolactam in the presence of pristine and carboxylated nanotubes.[148] ε–Caprolactam monomer was found to form an electron–transfer complex with CNTs giving a homogeneous polymerizable master solution, which facilitates the formation of composites with homogenously dispersed nanotubes.

To summarize, in situ polymerization can be applied for the preparation of almost any polymer nanocomposites containing CNTs, which can be non–covalently or covalently bound to polymer matrix. Non–covalent binding between polymer and nanotube involves physical adsorption and wrapping of polymer molecules through van der Waals and π–π interactions.

In fabrication of polymer/CNT nanocomposites using the melt blending technique, high temperature and high shear forces are deployed to disperse the CNTs in the polymer matrix. This is the most viable technique for current industrial applications of these nanocomposites. This method offers distinct advantages to produce larger volume and low cost composites than in situ polymerization and solution blending techniques. Use of optimum shear forces may impede the tendency of CNTs to form aggregates. McNally et al.[149] and Liu et al.[150,151] used twin–screw melt compounding to prepare the PE/CNT and nylon/CNT nanocomposites. McNally et. al. indicated that CNTs of the PE composites appear to align along the flow direction. This is in contrast to the polymer/CNT composites prepared by solution mixing, where the CNTs tend to be randomly oriented.[149] Similarly, Andrews et al. also reported well dispersed CNTs in PP and PS using shear mixing.[152] Other polymers used to prepare CNT based nanocomposites by melt blending include PC,[153–156] PMMA[157], and PP[158].

2.2.2 Factors Affecting Properties of the Nanocomposites

2.2.2.1 Chemical Functionalization of Nanotubes

Due to the small size of CNTs, there are very strong Van der Waals interactions between the tubes. This will force nanotubes to form bundles. Thus, the advantages of CNTs as fillers cannot be fully achieved unless the CNTs are 'un–bundled'. Recent studies have shown that CNTs can be chemically functionalized with other chemical groups and this facilitates both the CNT dispersion as well as affinity for the polymer matrix.[159,160] Riggs et al.[161] and Lin et al.[162] synthesized polymer grafted CNTs based on acylated CNTs with poly(propionylethylenimine–co–ethylenimine), poly(vinyl acetate–co–vinyl alcohol) and PVA, respectively. They found that PVA grafted CNTs were soluble in PVA solution, PVA/CNT nanocomposite films so–formed are of high optical quality without any observable phase separation. The result indicates that chemical graft functionalization of CNTs by matrix polymer was an effective way to achieve homogeneous dispersion for high–performance polymer/CNT nanocomposites. Cao et al. synthesized dodecylamine grafted CNTs with dodecylamine and acylated CNTs, and found that these grafted CNTs were miscible with polyvinylbutyral caused by the interaction between functional groups in polymer and long dodecylamine chains attached to the ends of CNTs.[163] Also, Hill et al. functionalized CNTs by the grafting reaction between carboxylic acid–bound CNTs and poly(styrene–co–p–(4–(4′–vinylphenyl)–3–oxabutanol)) (PSV).[164] These PSV–grafted CNTs are soluble in common organic solvents and are homogeneously dispersed in the PS matrix. This offers an example for the widely held expectation that the solubility of CNTs will enable the preparation of desirable polymer/CNT nanocomposites.

2.2.2.2 Allignment of Nanotubes in Polymer Matrix

The high aspect ratios of CNTs make them susceptible to orientation. During property investigations possibility of nanotube orientation must be taken into consideration. As with conventional fiber composites, both mechanical properties, such as stiffness and strength, and functional properties, such as electrical, magnetic and optical properties, of polymer/CNT nanocomposites are linked directly to the alignment of carbon nanotubes in the matrix. CNTs can be aligned prior to composite fabrication,

wherein aligned CNTs are incorporated in polymer matrix by in situ polymerization. PMMA and PANI nanocomposites based on aligned CNTs were prepared by infiltrating monomers into CNTs, followed by in situ polymerization.[165,166] The nanocomposite thus formed did not show any alteration in the CNT alignment. CNTs can also be aligned during or after the nanocomposite fabrication by mechanical stretching,[137] spin–casting,[140] wet spinning, melt fiber spinning,[167,168] and electrospinning.[169–172]

2.2.2.3 Formation of Nanotube Network in Polymer Matrix

Formation of a CNT network in a polymer matrix can also affect the various properties of these nanocomposites. Zhou and Seraphin first reported the formation of 2D L – junction, Y – junction, and T – junction CNTs in CNTs prepared by arc discharge method.[173] However, these junctions were limited to 2D and at most 3 way junctions. Later 'H' or 3D junctions were found in CNTs manufactured by CVD method. These junctions are not only important for mechanical properties, but also for electric and thermal applications. Potschke et. al observed a very small scale interwoven lattice of CNTs responsible for the reinforcement effect of the polymer/CNT nanocomposites.[174] Formation CNT network was found to affect the viscoelastic and electrical properties of nanocomposites based on various polymers including polyamides,[175] PMMA,[176] PET,[177] epoxy,[178] PBT,[179] PPY,[180] etc. CNT filled Polyamide 6 nanocomposites have shown an increase of 27% in Young's modulus,[175] while PET/CNT nanocomposites have shown an increase in storage modulus (G') of up to 4 orders of magnitude.[177] Du et. al. have shown an increase storage modulus (G') of up to 2 orders of magnitude in PMMA/SWCNT nanocomposites at a SWCNT loading of 2 wt%.[176]

2.2.3 Morphology

Morphology of polymer/CNT nanocomposites is studied predominantly to understand the fracture mechanisms, and dispersion of nanotubes in polymer matrix. TEM and SEM have been widely employed for this purpose.

2.2.3.1 Transmission Electron Microscopy

Quain et. al. used TEM for characterizing the fracture surface of nanocomposites based on 1 wt% CNTs with PS prepared by solution blending method.[139] They observed that nanotube fracture and pullout is responsible for the failure of the composite. The fracture of CNTs in polystyrene matrix implies that certain load transfer from the polymer to the nanotubes has taken place. However, the pullout of CNTs from the PS matrix indicating that the PS/nanotube interfacial strength is not strong enough to resist debonding of the fillers from the matrix. It is considered that some physical interactions exist at the PS/CNT interface, thereby enabling load transfer from the matrix to the fillers.

Bower et. al. investigated the deformation of aligned carbon nanotubes in polymer matrix.[181] Alignment was achieved by mechanically stretching the composite films above T_g of the polymer and then releasing the load at 300 K. In strained composites buckling was ubiquitously observed in bent nanotubes with large curvatures. Further examination of the fracture surface showed adherence of the polymer to the nanotubes.

2.2.3.2 Scanning Electron Microscopy

Liu et. al. studied the morphology of melt compounded polyamide/CNT nanocomposites using SEM to determine the origins of the mechanical property enhancement in the nanocomposites.[150] They attributed the mechanical property improvements to a better dispersion of CNTs. Further, they observed that the nanotubes are sheathed by several small beads. Such nanotubes bridge the micro–cracks effectively.

Gorga and Cohen investigated the effect of nanotube orientation on the mechanical properties of PMMA/CNT nanocomposites reinforced with 0.1–10 wt% CNTs.[182] On the basis of SEM observations they attributed the significant improvement in the tensile toughness of the nanocomposites to nanotubes oriented in normal to the direction of craze propagation and crack development. Thus, these nanotubes would bridge cracks that developed via craze precursors during tensile tests.

Gong et. al. compared the morphologies of epoxy/CNT based nanocomposites containing CNTs with and without addition of non ionic surfactant.[183] Typically CNTs in the fractured sample without the surfactant appeared to be very long, wavy, and lumped

together. This type of morphology is an indication of highly agglomerated CNTs and weak interactions with the matrix. On the other hand, the CNTs in the fractured sample with surfactant were uniformly distributed and aligned along one direction. Further many nanotubes were terminated and dangled on the surface. This indicates better dispersion of the nanotubes and better load transfer to the nanotubes during the fracture process.

2.2.4 Nanocomposite Properties

2.2.4.1 Thermal and Flammability Properties

Incorporation of CNTs in a polymer matrix could increase the T_g, melting and thermal decomposition of the polymer matrix due to their constraint effect on the polymer segments and chains. Kashiwagi et al.[184] found that the thermal decomposition temperature of PP at peak weight loss in nitrogen was increased by ~12 °C with 2 vol% CNTs. Ge et. al.found that 5 wt% polyacrylonitrile (PAN)/CNT composite showed at 24 °C shift in T_{onset} as compared to that of the neat PAN.[169] A number of mechanisms have been suggested. Dispersed nanotubes might hinder the flux of degradation product and thereby delay the onset of degradation. Polymers near the nanotubes might degrade more slowly, which would shift T_{peak} to higher temperatures. Another possible mechanism attributes the improved thermal stability to the effect of higher thermal conductivity in the nanotube/polymer composites that facilitates heat dissipation within the composite.[185]

Nanotubes can also be used as efficient fire retardant additives in polymer matrices. Flammability properties of melt blended nanocomposites based on ethylene vinyl acetate (EVA) and 2.5 wt% CNT were studied using cone calorimeter.[186] It as observed that CNT significantly reduces the heat release rate compared to virgin EVA.

Incorporation of CNTs could improve the thermal transport properties of polymer composites due to the excellent thermal conductivity of CNTs. It is noted that aligned CNTs will further improve the thermal conductivity. Huang et. al. reported thermal conductivity enhancement in silicon rubber based aligned CNTs.[187] The thermal conductivity of such a composite containing 0.4 vol% (0.3 wt%) aligned CNT is ~115–280 % higher than either the pure polymer or a composite with 0.4 vol% of dispersed CNT. Similarly, Choi et. al have reported that compared to the epoxy/CNT

nanocomposites without an applied magnetic field, the alignment of CNTs under a 25 T magnetic field has lead to a 10 % increase in thermal conductivity.[188]

2.2.4.2 Mechanical Properties

The fiber like structure of CNTs, their low density, high aspect ratio, and extraordinary mechanical properties make them particularly attractive for reinforcement in composite materials. Incorporation of CNTs into a polymer matrix can potentially provide structural materials with dramatically increased modulus and strength. Adding 1 wt% CNTs in the PS/CNT composite films by the solution blending method, results in 36–42 % and 25% improvements in tensile modulus and tensile strength, respectively.[139] Biercuk et al. have observed a monotonic increase of resistance to indentation (Vickers hardness) by up to 3.5 times on adding 2 wt% SWCNTs in epoxy resin.[189] Cadek et al. also found that adding 1 wt% CNTs to PVA increased the modulus and hardness by 1.8 times and 1.6 times, respectively.[190] Ogasawara et. al. performed mechanical analysis on amorphous PI/CNT composite samples.[191] Composites with weight fractions ranging from 3.3 to 14.3 wt%, were tested. The modulus of the composites increased with increasing CNT content. With the 14.3 wt% CNT composite the modulus improved 37 % over the neat polymer but the ultimate tensile strength was decreased by 18 %. In general, inclusion of CNTs in polymer matrices leads to reductions in impact toughness of composites[175,192] and there is an additional effect due to the orientation of the CNTs.[182]

2.2.4.3 Dynamic Mechanical Properties

Velasco–Santos et. al. have incorporated carboxyl functionalized CNTs into PMMA matrix by in situ polymerization to improve the transfer of mechanical load through a chemical bond.[146] The resulting composite with only 1 wt% of functionalized CNTs demonstrated 66 % increase in storage modulus at 40 °C as compared to 50 % in the composite with unfunctionalized CNTs; all increases were measured with respect to the pristine PMMA polymer. In addition, storage modulus for functionalized CNT composites increased by an astonishing factor of 11–fold at 90 °C and T_g was raised by about 40 °C. These composites also showed much higher plasticity than unfunctionalized CNT composites in stress–strain curves.

Shieh et. al.[193] incorporated CNT in crystalline PEO by grafting the CNT surface with PMMA via emulsion reactions and solution mixed PMMA grafted CNT compound with PEO and studied the DMTA properties of the nanocomposites. It was observed that at –100 °C, which was below T_g of neat PEO, the storage modulus of the 20 wt% grafted nanocomposite was improved by 38 % over neat PEO. Below –50 °C, the modulus of the composite apparently increased along with the increasing grafting content up to 20 wt% and no additional benefit was seen in adding another 10 wt% CNT to the composite. The reinforcement effect of the PEO matrix by grafted CNT was claimed to yield moderate increase in the storage modulus.

Sung et al.[194] studied the dynamic mechanical properties of PC/CNT nanocomposites. They observed two tan δ peaks in unannealed samples, which contained higher CNT content (≥ 7 wt%), which was explained by the phase separation morphology model. For nanocomposites with low CNT loadings (≤ 4 wt%) a single tan δ peak was observed. Similarly annealed samples also showed a single broad tan δ peak, which suggested that partially crystalline structure of the nanocomposites was obtained on thermal annealing.

Earlier experimental work on the mechanical properties of carbon nanotube/PVA composites prepared by solution mixing, showed an increase in the stiffness of the material due to the nanotubes, especially at higher temperatures.[138] Effect of interfacial interaction in CNT/epoxy composites has been reported by Gong et al.[183] The role of surfactant in these composites is investigated. DMTA showed that there is significant increase in the T_g and storage modulus of the composites in presence of CNTs with surfactant. Recent work by Sreekumar et al reported DMTA studies on solution spun PAN/SWCNT fibers.[195] The T_g of the polymer increased from ~103 °C to above 143 °C for a nanotube loading of 10 wt%. Further a significant decrease in the magnitude of the tan δ peak followed by broadening towards higher temperatures was observed. This was attributed to the variation in interaction between the polymer and nanotubes. The room temperature modulus of the nanocomposite nearly doubled over that of neat PAN, while the modulus retention at 150 °C was improved by more than an order of magnitude.

2.2.4.4 Electrical Properties

The major commercial application of CNTs, that has already been realized, is their use as conducting fillers in multifunctional polymer composites.[196] Coleman et al.[197] showed that the electric conductivity of poly(p–phenlyenevinylene–co–2,5–dioctoxy–m-phenylenevinylene) polymer could be dramatically increased by up to ten orders of magnitude when 8 wt% CNTs were added, indicative of percolating behavior.[198] Composites containing conducting fillers in insulating polymers become electrically conductive when the filler content exceeds a critical value, known as the percolation threshold. Percolation thresholds as low as 0.002 vol% have been achieved in polymer nanocomposites based on long flexible ropes of aligned CNTs.[199] The percolation threshold of electrical conductivity in polymer/CNT nanocomposites is governed by several CNT characteristics including aspect ratio,[200,201] dispersion,[202] and alignment.[167,203,204]

2.2.4.5 Melt Rheology

Du et. al. studied the rheological response of PMMA/CNT nanocomposites with good nanotube dispersion.[176] At high frequencies, the response is not sensitive to the filler concentration, indicating that the short–range polymer dynamics are not influenced by the nanotubes. In a consistent manner the T_g's of the composites are constant in the absence of strong interfacial bonds and at low nanotube loadings. At low frequencies, the rheological behavior progresses from a liquid–like response to a solid–like response as the nanotube concentration increases.

Mitchell et al. improved dispersion by functionalizing CNTs such that the rheological percolation threshold dropped from 3 wt% when using pristine CNTs to 1.5 wt% in functionalized CNT/PS composites.[205] The values of G' at low frequencies were also higher for the functionalized composites, indicating better load transfer between the nanotube network and the polymer. Within a given system (nanotubes and polymers), the linear viscoelastic response can serve as an indirect qualitative measure of the dispersion state of the nanotubes in the composites, where better dispersion corresponds to higher value of G' or a lower slope. Potschke et. al. found that the rheological percolation

threshold is strongly dependent on temperature.[206] The percolation threshold of PC/CNT nanocomposites decreases from ~5 to 0.5 wt% CNT upon increasing the temperature from 170 to 280 °C.

2.3 Poly(ethylene glycol-co-cyclohexane-1,4-dimethanol terephthalate)

Polyesters and copolyesters are formed from combinations of diacids and diols, the most common being ethylene glycol as the diol and terephthalic acid as the diacid to form polyethylene terephthalate (PET). Further modification of the plastic may be made by introducing other diacids, such as isophthalic acid, or other diols, such as 1,4–cyclohexanedimethanol (CHDM). These modified materials are referred to as 'copolyesters' because of their comonomer content. These modifications are often made to tailor the properties of the material to meet the needs of the end – user and processor.

Poly(ethylene glycol-co-cyclohexane-1,4-dimethanol terephthalate), commonly abbreviated as PETG, is an amorphous copolyester derived from PET modified with CHDM. PETG is a clear, tough, amorphous copolyester that has found wide acceptance in specialty packaging applications due to its high clarity and strength over PET and other resins such as PC and PMMA.[207] PETG offers a range of processing parameters broader than that of normal crystallizable polymers.[208] With a variety of applications including blister packaging, blown film, credit cards, electronic/food packaging, fabricated boxes and sports goods PETG becomes an ideal choice as the nanocomposite matrix phase.

2.3.1 Synthesis of PETG

PETG can be prepared readily via standard melt–phase polycondensation process.[209,210] The diacid can be delivered via transestrification of the dimethyl esters or via direct esterification of the diacids. Numerous conventional catalyst or catalyst combinations can be employed. The use of a catalyst or catalyst combination is important for the manufacture of polyesters via melt–phase process and has been well reported in the literature.[211–215] For preparing PETG, which is amorphous copolyester, useful molecular weight range must be achieved entirely in the melt–phase. This can be a difficult constraint for practical preparation or commercial scale for some compositions where elevated low shear melt viscosities hinder achieving high molecular weight

without the formation of unwanted degradation products. In PETG the composition range of CHDM is controlled between 20–30 mol%, thus resulting in copolyesters, which do not show crystallization peaks when scanned by DSC and are thus considered to be amorphous. PETG has M_n of approximately 26,000 g mol^{-1} and the CHDM to ethylene glycol to terephthalic acid molar ratio in PETG is approximately 1: 2: 3.

The amorphous window of PETG was first published in 1964.[216] This relationship between the composition of CHDM and the copolyester melting point is shown in Figure 2.3. The initial composition for commercialization contained a glycol ratio of around 70 % ethylene glycol and 30 % CHDM. This composition was chosen because it exhibited the slowest rate of crystallization of the glycol compositions.

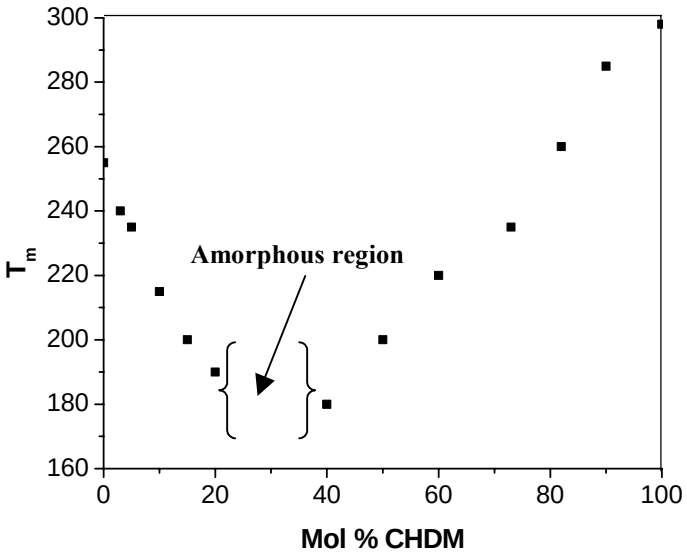

Figure 2.3 Effect of CHDM concentration on the melting point of the copolyesters based on terephthalic acid, ethylene glycol and CHDM[216]

2.3.2 Properties

2.3.2.1 Thermal Properties

PETG retains its thermal stability up to 400 °C beyond which its thermal decomposition is mainly completed in one step with pronounce loss of mass. The

aliphatic backbone in PETG plays a dominant role in controlling the decomposition behavior. 4–methylene–cyclohexanemethanol, 1,4–bis–(methylene)–cyclohexane, and benzoic acid are the characteristic heat decomposition products.[217]

PETG has a T_g of approximately 85 °C as determined by DSC. Because PETG is amorphous a true melting curve and crystallization peak are not observed in the DSC scan.[217] The T_g's of these amorphous copolyesters are lower in comparison with colorless, transparent commercial polymers such as PC, and PMMA. For example, PC has a T_g of 145 °C, and PMMA has a T_g of 100 °C, in contrast to the mid 80 °C range of T_g for PETG.

2.3.2.2 Mechanical Properties

Toughness of PETG as measured by impact resistance and notched Izod values, increases with increasing CHDM content. The T_g and HDT also increase slightly as the CHDM level increases. This is attributed to a decrease in modulus with increasing CHDM level. The role of CHDM in increasing toughness in copolyesters containing PET and poly(1,4–cyclohexylenedimethylene terephthalate) (PCT), has been actively investigated by Yee and coworkers.[218,219] It was observed that PET and copolymers with low content of CHDM showed crazing failure, whereas a transition from crazing to localized shear deformation occurred with increasing CHDM content. With increasing temperature copolymers containing a CHDM linkage showed deformation mode transition from shear deformation to crazing, while no change in the deformation mode was observed in PET. The changes in the deformation behavior were attributed to the conformational transition of cyclohexylene ring.

PETG specimens were subjected to instrumented tensile impact loading in the speed range of 2–3.7 m/s showed that the onset of stress oscillation in the necking phase of PETG is restricted to a given apparent testing frequency (or strain rate) range and depends on both testing conditions and material parameters. It was observed that necking occurred by cold drawing, which was evidenced by the shape recovery of the broken specimens when heated above T_g. Further it was observed that in PETG cold drawing occurs via shear banding and diffuse shear yielding without any orientational crystallization.[220]

2.3.2.3 Chemical Resistance

PETG exhibits good resistance to dilute aqueous solutions of mineral acids, bases, salts, and soaps, and to aliphatic hydrocarbons, alcohols, and a variety of oils. Halogenated hydrocarbons, short chain length ketones, and aromatic hydrocarbons dissolve or swell the copolyester.

2.3.2.4 Dielectric Behavior

PETG has reported dielectric constant values of 2.6 and 2.4 at 1 kHz and 1 MHz, respectively. The volume resistivity of PETG is of the order of 10^{15} Ωcm, while it surface resistivity is 10^{16} Ω/square.

The β relaxation of PETG as investigated by thermally stimulated depolarization currents is found to be at –92.5 °C, is principally due to the motion of polar carboxyl groups. Presence of cyclohexane group between the two methylene groups in PETG does not seem to modify these motions. The α relaxation is considered as the dielectric manifestation of the glass transition and corresponds to cooperative movements of the macromolecules.[221]

2.3.2.5 Barrier Properties

The water–vapor transmission rate of PETG and gas permeability for CO_2 and O_2, of a 250 micron (10–mil) PETG film are 6 g/m^2.24h., and 49 and 10 cm^3.mm/m^2.24h.atm, respectively.

The permeability coefficients of linalool, citral ethyl butyrate, d–limonene, and octanal permeating through permeating through PETG films were measured alone as individual and as a component of a mixture at a temperature of 25 °C and in saturated water vapor. The results were compared with those obtained using low density PE and ionomer films. PETG films were found to be much better barriers against the compounds tested than low density PE and iononmer films.[222]

2.3.3 PETG Composites

PETG is mixed with various fillers in order to achieve specific property improvements.

The ductility of calcium carbonate filled PETG in a uniaxial tensile test was examined as a function of the filler volume fraction.[223] A ductile to quasi brittle transition occurred with increasing filler volume fraction and was from propagation of a stable neck through the entire gauge length of the specimen to fracture in the neck without propagation. It was proposed that when the fracture strain decreases to the draw strain on the polymer the fracture mechanism changes and the fracture strain drops sharply. The effects of different particle size distributions on the ductility of PETG filled with calcium terephthalates and calcium carbonates showed that the critical filler content of the ductile to quasi brittle transition varied from one filler to another.[224]

Fractography of calcium carbonate and calcium terephthalate filled PETG showed five fracture modes defined on the basis of macroscopic stress–strain behavior and were distinguished by certain characteristic features. These features were found to be independent of filler type or content and were characteristic of the fracture mode. The fracture mode changed from ductile (Modes A and B) to quasi brittle (Modes C and D) to brittle (Mode E) with increasing filler content.[225]

The mechanical properties of an orthodontic wire pultruded from S2–glass–reinforced PETG were measured using two experimental devices simulating clinical conditions.[226] It was observed that by adopting certain corrections associated with clamping and shear effects, good agreement between the moduli calculated using rule of mixtures and those measured in clinical tests is achieved. The analytical base developed for prediction of the stiffness of the orthodontic wire for different span/thickness ratios improves the procedure for design of dental appliances.

A maleated impact modifier (TPEg) with polyethylene–octane rubber shell and semicrystalline polymer core was used to toughen PETG.[227] At TPEg loading of 10 % a sharp transition from brittle to super–tough states is observed. The fracture surface of PETG composite with 5 and 10 wt% TPEg loading exhibited slow and fast crack growth region, respectively. The extensive shear yielding matrix in PETG. TPEg (90/10)

dissipates a significant amount of impact energy, and is responsible for the super toughness.

Plain–weave carbon fabric as reinforcement in PETG composites has been specifically designed for deployment in low earth orbit through inflation of compact structures followed by rigidization.[228]

Lamination of glass fiber–reinforced and epoxy based PCB substrate to PETG was achieved by simultaneous surface graft copolymerization of glycidyl methacrylate on argon plasma–pretreated substrate and PETG.[229] The adhesion strength was affected by the plasma pretreatment time of the substrates, the lamination time, and the lamination temperature.

2.3.4 PETG Applications

According to a recent study issued by SRI Consulting, Menlo Park, CA, USA, the demand for polyester resins and compounds in North America in 2003 was 600 million lb/yr. They further break down the polyester market at 60 % PBT (alloys included), 16 % PET, and 22 % copolyesters (of which PETG makes up 80 %).

PETG is useful in a variety of processes and applications because of its clarity, toughness, and good melt strength at processing temperatures. PETG has long been extrusion blow molded into relatively small, simple bottles such as refrigerator containers, and those for packaging shampoos, soaps, detergents, and oils.

PETG is making inroads laboratory flasks and thermoformed containers for rigid medical packaging, and refrigerated/frozen foods. With features such as gloss, transparency, toughness, fast–forming cycles, ease of forming, reusable scrap, radio frequency sealable, and resistance to stress whitening, PETG is ideal for film and sheet extrusion.

REFERENCES

1. P. Aranda, E. Ruiz–Hitzky, *Chem. Mater.* **4** 1395 (1992)
2. K. Strawhecker, E. Manias, *Chem. Mater.* **12** 2943 (2000)
3. H. Jeon, H. Jung, S. Lee, S. Hudson, *Polym. Bull.* **41** 107 (1998)
4. H. Choi, S. Kim, Y. Hyun, M. Jhon, *Macromol. Rapid Commun.* **22** 320 (2001)

5. G. Jimenez, N. Ogata, H. Kawai, T. Ogihara, *J. Appl. Polym. Sci.* **64** 2211 (1997)
6. N. Ogata, S. Kawakage, T. Ogihara, *Polymer* **38** 5115 (1997)
7. C. R. Tseng, J. Y. Wu, H. Y. Lee, F. C. Chang, *Polymer* **42** 10063 (2001)
8. A. Tabtiang, *Polym. Plast. Technol. Eng.* **39** 293 (2000)
9. M. Okamoto, S. Morita, T. Kokata, *Polymer* **42** 2685 (2001)
10. O. Beker, L. Varley, G. P. Simon, *Polymer* **43** 4365 (2002)
11. T. Lan, T. J. Pinnavaia, *Chem. Mater.* **6** 2216 (1994)
12. J. G. Ryu, G. R. Park, S. G. Lyu, J. H. Rhew, G. S. Sur, *Polymer (Korea)* **22** 328 (1998)
13. T. Lan, P. D. Kaviratna, T. J. Pinnavaia, *Polym. Mater. Sci. Eng.* **71** 527 (1994)
14. T. Lan, Z. Wang, H. Shi, T. J. Pinnavaia, *Polym. Mater. Sci. Eng.* **73** 296 (1995)
15. D. Sekelik, E. Stepanov, D. Schiraldi, A. Hiltner, E. Baer, *J. Polym. Sci. Part B: Polym. Phys.* **37** 847 (1999)
16. Y. Ke, C. Long, Z. Qi, *J. Appl. Polym. Sci.* **71** 1139 (1999)
17. T. Gopakumar, J. Lee, M. Kontopoulou, J. Parent, *Polymer* **43** 5483 (2002)
18. Y. Jin, H. Park, S. Im, S. Kwak, *Macromol. Rapid. Commun.* **23** 135 (2002)
19. J. Heinemann, P. Reichert, R. Thomann, R. Mulhaupt, *Macromol. Rapid Commun.* **20** 423 (1999)
20. J. Tudor, L. Willington, D. O'Hare, B. Royan, *Chem. Commun.* **17** 2031 (1996)
21. J. Rong, H. Li, Z. Jing, X. Hong, M. Sheng, *J. Appl .Polym. Sci.* **82** 1829 (2001)
22. M. Okamoto, S. Morita, H. Taguchi, Y. Kim, T. Kataka, H. Tateyama, *Polymer* **41** 3887 (2000)
23. P. B. Messersmith, E. P. Giannelis, *Chem. Mater.* **5** 1064 (1993)
24. X. Huang, S. Lewis, W. J. Brittain, R. A. Vaia, *Macromolecules* **33** 2000 (2000)
25. X. Huang, S. Lewis, W. J. Brittain, R. A. Vaia, *Polym. Prepr.* **41** 589 (2000)
26. K. Weiss, C. Wirth−Pfeifer, M. Hofmann, S. Botzenhardt, H. Lang, K. Bruning, E. Meichel, *J. Mol. Cata. A: Chemical* **182**–**183** 143 (2002)
27. J. Ma, Z. Qi, Y. Hu, *J. Appl. Polym. Sci.* **82** 3611 (2001)
28. S. D. Burnside, E. P. Giannelis, *Chem. Mater.* **7** 1597 (1995)
29. F. Yang, Y. Ou, Z. Yu, *J. Appl. Polym. Sci.* **69** 355 (1998)

30. Y. Kojima, A. Usuki, M. Kawasumi, A. Okada, T. Kurauchi, O. Kamigaito, *J. Polym. Sci. Part A: Polym. Chem.* **31** 1755 (1993)
31. Y. Kojima, A. Usuki, M. Kawasumi, A. Okada, T. Kurauchi, O. Kamigaito, *J. Polym. Sci. Part A: Polym. Chem.* **31** 983 (1993)
32. A. Usuki, M. Kawasumi, Y. Kojima, A. Okada, T. Kurauchi, O. Kamigaito, *J. Mater. Res.* **8** 1174 (1993)
33. K. Yano, A. Usuki, A. Okada, T. Kurauchi, O. Kamigaito, *J. Polym. Sci. Part A: Polym. Chem.* **31** 2493 (1993)
34. C. Liu, T. Tang, Z. Zhao, B. Huang, *J. Polym. Sci. Part A: Polym. Chem.* **40** 1892 (2002)
35. M. W. Weimer, H. Chen, E. P. Giannelis, D. Y. Sogah, *J. Am. Chem. Soc.* **21** 1615 (1999)
36. J. Rong, Z. Jing, H. Li, M. Sheng, *Macromol. Rapid Commun.* **22** 329 (2001)
37. E. P. Giannelis, *Adv. Mater.* **8** 29 (1996)
38. R. A. Vaia, K. D. Jandt, E. J. Kramer, E. P. Giannelis, *Chem. Mater.* **8** 2628 (1996)
39. R. A. Vaia, K. D. Jandt, E. J. Kramer, E. P. Giannelis, *Macromolecules* **28** 8080 (1995)
40. R. A. Vaia, S. Vasudevan, W. Krawiec, L. G. Scanlon, E. P. Giannelis, *Adv. Mater.* **7** 154 (1995)
41. J. W. Cho, D. R. Paul, *Polymer* **42** 1083 (2001)
42. T. D. Fornes, P. J. Yoon, H. Keskkula, D. R. Paul, *Polymer* **42** 9929 (2001)
43. T. D. Fornes, P. J. Yoon, D. R. Paul, *Poly. Mater. Sci. Eng.* **87** 104 (2002)
44. H. R. Dennis, D. L. Hunter, D. Chang, S. Kim, J. L. White, J. W. Cho, D. R. Paul, *Polymer,* **42** 9513 (2001)
45. C. Davis, L. Mathias, J. W. Gilman, D. Schiraldi, J. Shields, P. Trulove, T. Sutto, H. Delong, *J. Polym. Sci. Part B: Polym. Phys.* **40** 2661 (2002)
46. K. Wang, M. Choi, C. Koo, Y. Choi, I. Chung, *Polymer*, **42**, 9819 (2001)
47. C. M. Koo, H. T. Ham, S. O. Kim, K. H. Wang, I. J. Chung, D. C. Kim, W. C. Zin, *Macromolecules* **35** 5116 (2002)
48. A. Usuki, M. Kato, A. Okada, T. Kurauchi, *J. Appl. Polym. Sci.* **63**, 137 (1997)

49. Y. Kurokawa, H. Yasuda, A. Oya, *J. Mater. Sci. Lett.* **15** 1481 (1996)
50. M. Kawasumi, N. Hasegawa, M. Kato, A. Usuki, A. Okada, *Macromolecules,* **30** 6333 (1997)
51. Y. Di. S. Iannace, E. Dimaio, L. Nicolais, *J. Polym. Sci. Part B: Polym. Phys.* **41** 670 (2003)
52. B. Lepoittevin, M. Devalckenaere, N. Pantoustier, M. Alexandre, D. Kubies, C. Calberg, R. Jerome, P. Dubois, *Polymer* **43** 4017 (2002)
53. B. J. Chisholm, R. B. Moore, G. Barber, F. Khouri, A. Hempstead, M. Larsen, E. Olson, J. Kelley, G. Balch, J. Caraher, *Macromolecules* **35** 5508 (2002)
54. N. Artzi, *Polym. Compos.* **22** 710 (2001)
55. C. C. Zeng, *Macromolecules* **34** 4098 (2001)
56. D. Y. Wang, *Chem. Mater.* **14** 3837 (2002)
57. G. Strobl in: The Physics of Polymers; 2nd Edition, Springer–Verlag: Berlin, Heldelberg, New York (1997) pp. 285
58. H. Ishida, S. Cambell, J. Blackwell, *Chem. Mater.* **12** 1260 (2000)
59. R. A. Vaia, E. P. Giannelis, *Macromolecules* **30** 7990 (1997)
60. R. A. Vaia, E. P. Giannelis, *Macromolecules* **30** 8000 (1997)
61. P. LeBaron, Z. Wang, T. Pinnavaia, *Appl. Clay. Sci.* **15** 11 (1999)
62. A. C. Balazs, C. Singh, E. Zhulina, Y. Lyatskaya, *Acc. Chem. Res.* **32**, 651 (1999)
63. V. V. Ginzburg, A. C. Balazs, *Adv. Mater.* **12**, 1805 (2000)
64. C. Singh, A. C. Balazs, *Polym. Inter.* **49** 469 (2000)
65. A. C. Balazs, C. Singh, E. Zhulina, *Macromolecules* **31** 8370 (1998)
66. X. Liu, Q. Wu, *Polymer* **42** 10013 (2001)
67. A. B. Morgan, J. F. Gilman, *J. Appl. Polym. Sci.* **87** 1327 (2003)
68. D. F. Eckel, M. P. Balogh, P. D. Fasulo, W. R. Rodgers, *J. Appl. Polym. Sci.* **93** 1110 (2004)
69. A. Bafna, G. Beaucage, F. Mirabella, S. Mehta, *Polymer* **44** 1103 (2003)
70. A. Blumstein, *J. Polym. Sci.* **A3** 2665 (1965)
71. M. Biswas, S. Sinha Ray, *Adv. Polym. Sci.* **155** 167 (2001)
72. E. P. Giannelis, *Appl. Organomet. Chem.* **12** 675 (1998)
73. J. W. Gilman, *Appl. Clay. Sci.* **15** 31 (1999)

74. J. W. Gilman, T. Ksahiwagi, E. P. Giannelis, E. Manias, S. Lomakin, J. D. Lichtenhan, P. Jones, Flammability Properties of Polymer–Layered Silicate Nanocomposites, in: S. Al–Malaika, A. Golovoy, C. A. Wilkie (Eds.) Chemistry and Technology of Polymer Additives; Blackwell Science: Oxford, England (1999) pp. 249 (Chapter 14)
75. Z. Liang, J. Yin, *J. Appl. Polym. Sci.* **90** 1857 (2003)
76. P. Yoon, T. Fornes, D. R. Paul, *Polymer* **43** 6727 (2002)
77. R. Xu, E. Manias, A. J. Snyder, J. Runt, *Macromolecules* **34** 1989 (2001)
78. S. Sinha Ray, K. Yamada, M. Okamoto, A. Ogami, K. Ueda, *Chem. Mater.* **15** 1456 (2003)
79. L. Nielsen, *J. Macomol. Sci. Part A: Chem.* **A1** 929 (1961)
80. S. Fujiwara, T. Sakamoto, *Kokai Patent Application No. SHO 511976 – 109998* (1976)
81. J. W. Gilman, T. Kashiwagi, J. D. Lichtenhan, *SAMPE J.* **33** 40 (1997)
82. J. W. Gilman, C. L. Jackson, A. B. Morgan, R. Harris, E. Manias, E. P. Giannelis, M. Wuthenow, D. Hilton, S. H. Philips, *Chem. Mater.* **12** 1866 (2000)
83. E. Manias, A. Touny, L. Wu, K. Strawhecker, B. Lu, T. C. Chung, *Chem. Mater.* **13** 3516 (2001)
84. N. Hasegawa, M. Kawasumi, M. Kato, A. Usuki, A. Okada, *J. Appl. Polym. Sci.* **67** 87 (1998)
85. P. Kodgire, R. A. Kalgaonkar, S. S. Hambir, N. N. Bulakh, J. P. Jog, *J. Appl. Polym. Sci.* **81** 1786 (2001)
86. S. S. Hambir, N. N. Bulakh, P. Kodgire, R. A. Kalgaonkar, J. P. Jog, *J. Polym. Sci. Part B: Polym. Phys.* **39** 446 (2001)
87. H. L. Tyan, Y. C. Liu, K. H. Wei, *Chem. Mater.* **11** 1942 (1999)
88. P. B. Messersmith, E. P. Giannelis, *Chem. Mater.* **6** 1719 (1994)
89. K. J. Yao, M. Song, D. J. Hourston, D. Z. Luo, *Polymer* **43** 1017 (2002)
90. H. B. Hsueh, C. Y. Chen, *Polymer* **44** 1151 (2003)
91. T. Agag, T. Koga, T. Takeichi, *Polymer* **42** 3399 (2001)
92. H. L. Tyan, K. H. Wei, T. E. Hsieh, *J. Polym. Sci. Part B: Polym. Phys.* **38** 2873 (2000)

93. Z. Gao, W. Xie, J. M. Hwu, L Wells, W. P. Pan, *J. Therm. Anal. Cal.* **64** 467 (2001)
94. Y. Li, B. Zhao, S. Xi, S. Zhang, *Polym. Inter.* **52**, 892 (2003)
95. P. Meneghetti, S. Qutubuddin, *Langmuir* **20** 3424 (2004)
96. M. Okomoto, S. Morita, H. Taguchi, Y. H. Kim, T. Kokata, H. Tateyama, *Polymer* **41** 3887 (2000)
97. Y. Q. Zhang, J. H. Lee, J. M. Rhee, K. Y. Rhee, *Compos. Sci. Tech.* **64** 1383 (2004)
98. A. B. Morgan, J. D. Harris, *Polymer* **44** 2313 (2003)
99. X. Zhang, M. Yang, Y. Zhao, S. Zhang, X. Dang, X. Liu, D. Wang, D. Xu, *J. Appl. Polym. Sci.* **92** 552 (2004)
100. W. Xu, G. Liang, W. Wang, S. Tang, P. He, W. Pan, *J. Appl. Polym. Sci.* **88** 3225 (2003)
101. M. Zanetti, G. Camino, P. Reichert, R. Mulhaupt, *Macromol. Rapid Commun.* **22** 176 (2001)
102. M. Okamoto, P. H. Nam, P. Maiti, T. Kotaka, T. Nakayama, M. Takada, M. Ohshima, A. Usuki, N. Hasegawa, H. Okamoto, *Nano Lett.* **1** 503 (2001)
103. C. Wan, X. Qiao, Y. Zhang, *Polym. Test.* **22** 453 (2003)
104. X. Liu, Q. Wu, *Polymer* **42** 10013 (2001)
105. A. Yasmin, J. J. Luo, J. L. Abot, I. M. Daniel, *Compos. Sci. Technol.* **66** 2415 (2006)
106. R. Krishnamoorti, E. P. Giannelis, *Macromolecules* **30** 4097 (1997)
107. L.A. Utracki, J. Lyngaae–Jorgensen, *Rheol. Acta* **41** 394 (2002)
108. B. Hoffmann, J. Kressler, G. Stoppelmann, C. Friedrich, G. M. Kim, *Colloid Polym. Sci.* **278** 629 (2000)
109. E. P. Giannelis, R. Krishnamoorti, E. Manias, *Adv. Polym. Sci.* **138** 107 (1999)
110. R. Krishanmoorti, E. P. Giannelis, *Polym. Mater. Sci. Eng.* **75** 46 (1996)
111. R. Krishnamoorti, E. P. Giannelis, *Langmuir* **17** 1448 (2001)
112. B. Hoffmann, C. Dietrich, R. Thomann, C. Friedrich, R. Mulhaupt, *Macromol. Rapid Commun.* **21** 57 (2000)
113. K. M. Lee, C. D. Han, *Macromolecules* **36** 804 (2003)

114. J. Ren, A. S. Silva, R. Krishnamoorti, *Macromolecules* **33** 3739 (2000)
115. J. Ren, R. Krishnamoorti, *Polym. Mater. Sci. Eng.* **82** 264 (2000)
116. C. A. Mitchell, R. Krishnamoorti, *ACS Symposium Series* **804** 159 (2002)
117. M. J. Solomon, A. S. Almusallam, K. F. Seefeldt, A. Somwangthanaroj, P. Varadan, *Macromolecules* **34** 1864 (2001)
118. P. Reichert, B. Hoffmann, T. Bock, R. Thomann, R. Mulhaupt, C. Friedrich, *Macromol. Rapid Commun.* **22** 519 (2001)
119. P. Reichert, H. Nitz, S. Klinke, R. Brandsch, R. Thomann, R. Mulhaupt, *Macromol. Mater. Eng.* **275** 8 (2000)
120. M. J. Solomon, Q. Lu, *Curr. Opin. Colloid In.* **6** 430 (2001)
121. G. Galgali, C. Ramesh, A. K. Lele, *Macromolecules* **34** 852 (2001)
122. A. Abranyi, L. Szazdi, B. Pukanszky Jr, G. J. Vancso, B. Pukanszky, *Macromol. Rapid Commun.* **27** 132 (2006)
123. A. K. Lele, M. Mackley, G. Galgali, C. Ramesh, *J. Rheol.* **46** 1091 (2002)
124. B. Hoffmann, T. Bock, R. Thomann, R. Mulhaupt, C. Friedrich, *Macromol. Rapid Commun.* **22** 519 (2001)
125. S. Sinha Ray, K. Okamoto, M. Okamoto, *Macromolecules* **36** 2355 (2003)
126. R. Krishnamoorti, J. Ren, A. S. Silva, *J. Chem. Phys.* **114** 4968 (2001)
127. J. M. Dealy, K. F. Wissburn, in: Melt Rheology and its role in Plastics Processing: Theory and Applications; Kluwer Academic Publishers, The Netherlands (1999)
128. J. H. Han, C. C. Feng, D. J. Li, C. D. Han, *Polymer* **36** 2451 (1995)
129. N. Nakajima, H. H. Bowermann, W. A. Collins, *J. Appl. Polym. Sci.* **21** 3063 (1977)
130. S. S. Kim, C. D. Han, *Polymer* **35** 95 (1994)
131. R. S. Bailey, A. M. Bellamy, D. J. Groves, D. M. Stocks, R. C. Young, *Theor. Appl. Rheol.* **2** 838 (1992)
132. J. K. Kim, J. H. Song, *J. Rheol.* **41** 1061 (1997)
133. A. Kanapitsas, P. Pissis, R. Kotsilkova, *J. Non–Cryst. Solids* **305** 204 (2002)
134. Y. –H. Lee, A. J. Bur, S. C. Roth, P. R. Start, R. H. Harris, *Polym. Adv. Tech.* **16** 249 (2005)

135. M. Bohning, H. Goering, A. Fritz, K. Brzezinka, G. Turky, A. Schonhals, B. Schartel, *Macromolecules* **38** 2764 (2005)
136. K. A. Page, K. Adachi, *Polymer* **47** 6406 (2006)
137. L. Jin, C. Bower, O. Zhou, *Appl. Phys. Lett.* **73** 1197 (1998)
138. M. S. P. Shaffer, A. H. Windle, *Adv. Mater.* **11** 937 (1999)
139. D. Qian, E. C. Dickey, R. Andrews, T. Rantell, *Appl. Phys. Lett.* **76** 2868 (2000)
140. B. Safadi, R. Andrews, E. A. Grulke, *J. Appl. Polym. Sci.* **84** 2660 (2002)
141. S. L. Ruan, P. Gao, X. G. Yang, T. X. Yu, *Polymer* **44** 5643 (2003)
142. M. Cochet, W. K. Maser, A. Benitor, A. Callejas, M. T. Martinez, J. M. Benoit, J. Schreiber, O. Chauvet, *Chem. Commun.* 1450 (2001)
143. Q. F. Xiao, X. Zhou, *Electrochem. Acta* **48** 575 (2003)
144. Z. J. Jia, Z. J. Wang, C. L. Xu, J. Liang, B. Q. Wei, D. H. Wu, S. W. Zhu, *Mater. Sci. Eng. A: Struct.* **271** 395 (1999)
145. C. Park, Z. Ounaies, K. A. Watson, R. E. Crooks, J. Smith Jr., S. E. Lowther, J. W. Connell, E. J. Siochi, J. S. Harrison, T. L. St. Clair, *Chem. Phys. Lett.* **364** 303 (2002)
146. C. Velasco–Santos, A. L. Martınez–Hernandez, F. T. Fisher, R. Ruoff, V. M. Castano, *Chem. Mater.* **15** 4470 (2003)
147. J. Jang, J. Bae, S. H. Yoon, *J. Mater. Chem.* **13** 676 (2003)
148. C. Zhao, G. Hu, R. Justice, D. W. Schaefer, S. Zhang, M. Yang, C. C. Han, *Polymer* **46** 5125 (2005)
149. T. McNally, P. Potschke, P. Halley, M. Murphy, D. Martin, S. E. Bell, G. P. Brennan, D. Bein, P. Lemoine, J. P. Quinn, *Polymer* **46** 8222 (2005)
150. T. Liu, I. Y. Phang, L. Shen, S. Y. Chow, W. D. Zhang, *Macromolecules* **37** 7214 (2004)
151. W. D. Zhang, L. Shen, I. Y. Phang, T. Liu, *Macromolecules* **37** 256 (2004)
152. R. Andrews, D. Jacques, M. Minot, T. Rantell, *Macromol. Mater. Eng.* **287** 395 (2002)
153. P. Potschke, I. Alig, S. Dudkin, *Polymer* **44** 5023 (2003)
154. P. Potschke, A. R. Bhattacharyya, A. Janke, *Polymer* **44** 8061 (2003)
155. P. Potschke, A. R. Bhattacharyya, A. Janke, *Carbon* **42** 965 (2004)

156. P. Potschke, A. R. Bhattacharyya, A. Janke, H. Goering, *Compos. Interfaces* **10** 389 (2003)
157. Z. Jin, K. P. Pramoda, G. Xu, S. H. Goh, *Chem. Phys. Lett.* **337** 43 (2001)
158. M. –K. Seo, S. –J. Park, *Chem. Phys. Lett.* **395** 44 (2004)
159. A. Hirsch, *Angew. Chem. Int. Ed.41,* **11** 1853 (2002)
160. W. Zhang, S. Ge, Y, Wang, M. H. Rafaliovich, O. Dhez, D. A. Winsett, H. Ade, *Polymer* **44** 2109 (2003)
161. J. E. Riggs, Z. Guo, D. L. Carroll, Y. P. Sun, *J. Am. Chem. Soc.* **122** 5879 (2000)
162. Y. Lin, B. Zhou, K. A. S. Fernando, P. Liu, Y. P. Sun, *Macromolecules* **36** 7199 (2003)
163. L. Cao, H. Z. Chen, M. Wang, J. Z. Sun, *J. Phys. Chem. B* **106** 8971 (2002)
164. D. E. Hill, Y. Lin, A. R. Rao, L. F. Allard, Y. P. Sun, *Macromolecules* **35** 9466 (2002)
165. N. R. Raravikar, L. S. Schadler, A. Vijayaraghavan, Y. Zhao, B. Wei, P. M. Ajayan, *Chem. Mater.* **17** 974 (2005)
166. W. Feng, X. D. Bai, Y. Q. Lian, J. Liang, X. G. Wang, K. Yoshino, *Carbon* **41** 1551 (2003)
167. R. Haggenmueller, H. H. Gommans, A. G. Rinzler, J. E. Fischer, K. I. Winey, *Chem. Phys. Lett.* **330** 219 (2000)
168. R. Haggenmueller, W. Zhou, J. E. Fischer, K. I. Winey, *J. Nanosci. Nanotechno.* **3** 105 (2003)
169. J. J. Ge, H. Hou, Q. Li, M. J. Graham, A. Greiner, D. H. Reneker, F. W. Harris, S. Z. D. Cheng, *J. Am. Chem. Soc.* **126** 15754 (2004)
170. J. Gao, A. Yu, M. E. Itkis, E. Bekyarova, B. Zhao, S. Niyogi, R. C. Haddon, *J. Am. Chem. Soc.* **126** 16698 (2004)
171. H. Hou, J. J. Ge, J. Zeng, Q. Li, D. H. Reneker, A. Greiner, S. Z. D. Cheng, *Chem. Mater.* **17** 967 (2005)
172. F. Ko, Y. Gogotsi, A. Ali, N. Naguib, H. Ye, G. Yang, C. Li, P. Willis, *Ad*v. *Mater.* **15** 1161 (2003)
173. D. Zhou, S. Seraphin, *Chem. Phys. Lett.* **238** (1995)
174. P. Potschke, T. D. Fornes, D. R. Paul, *Polymer* **43** 3247 (2002)

175. O. Meincke, D. Kaempfer, H. Weickmann, C. Friedrich, M. Vathauer, H. Warth, *Polymer* **45** 739 (2004)
176. F. Du, R. C. Scogna, W. Zhou, S. Brand, J. E. Fischer, K. I. Winey, *Macromolecules* **37** 9048 (2004)
177. G. Hu, C. Zhao, S. Zhang, M. Yang, Z. Wang, *Polymer* **47** 480 (2006)
178. C. A. Martin, J. K. W. Sandler, M. S. P. Shaffer, M. –K. Schwarz, W. Bauhofer, K. Schulte, A. H. Windle, *Compos. Sci. Technol.* **64** 2309 (2004)
179. A. Nogales, G. Broza, Z. Roslaniec, K. Schulte, I. Sics, B. S. Hsiao, A. Sanz, M. C. Garcia–Gutierrez, D. R. Rueda, C. Domingo, T. A. Ezquerra, *Macromolecules* **37** 7669 (2004)
180. Y. Long, Z. Chen, X. Zhang, J. Zhang, Z. Liu, *J. Phys. D: Appl. Phys.* **37** 1965 (2004)
181. C. Bower, R. Rosen, L. Jin, J. Han, O. Zhou, *Appl. Phys. Lett.* **74** 3317 (1999)
182. R. E. Gorga, R. E. Cohen, *J. Polym. Sci. Part B: Polym. Phys.* **42** 2690 (2004)
183. X. Gong, J. Liu, S. Baskaran, R. D. Voise, J. S. Young, *Chem. Mater.* **12** 1049 (2000)
184. T. Kashiwagi, E. Grulke, J. Hilding, R. Harris, W. Awad, J. Douglas, *Macromol. Rapid Commun.* **232** 761 (2002)
185. S. T. Huxtable, D. G. Cahill, S. Shenogin, L. Xeu, R. Qzisik, P. Barone, M. Usrey, M. S. Strano, G. Siddons, M. Shim, P. Keblinski, *Nat. Mater.* **2** 731 (2003)
186. G. Beyer, *Fire Mater.* **26** 291 (2002)
187. H. Huang, C. Liu, Y. Wu, S. Fan, *Adv. Mater.* **17** 1652 (2005)
188. E. S. Choi, J. S. Brooks, D. L. Eaton, M. S. Al–Haik, M. Y. Hussaini, H. Garmestani, D. Li, K. Dahmen, *J. Appl. Phys.* **94** 6034 (2003)
189. M. J. Biercuk, M. C. Llaguno, M. Radosavljevic, J. K. Hyun, A. T. Johnson, *Appl. Phys. Lett.* **80** 2767 (2002)
190. M. Cadek, J. N. Coleman, V. Barron, K. Hedicke, W. J. Blau, *Appl. Phys. Lett.* **81** 5123 (2002)
191. T. Ogasawara, Y. Ishida, T. Ishikawa, R. Yokota, *Compos Part A – Appl. S.* **35** 67 (2004)
192. H. Miyagawa, L. T. Drzal, *Polymer* **45** 5163 (2004)

193. Y. –T. Shieh, G. –L. Liu, K. C. Hwang, C. –C. Chen, *Polymer* **46** 10945 (2005)

194. Y. T. Sung, C. K. Kum, H. S. Lee, N. S. Byon, H. G. Yoon, W. N. Kim, *Polymer* **46** 5656 (2005)

195. T. V. Sreekumar, T. Liu, B. G. Min, H. Guo, S. Kumar, R. H. Hauge, R. E. Smalley, *Adv. Mater.* **16** 58 (2004)

196. R. H. Baughman, A. A. Zakhidov, W. A. de Heer, *Science* **297** 787 (2002)

197. J. N. Coleman, S. Curran, A. B. Dalton, A. P. Davey, B. McCarthy, W. Blau, R. C. Barklie, *Phys. Rev.* **B58** R7492 (1998)

198. B. E. Kilbride, J. N. Coleman, P. Fournet, A. Cadek, S. Hutzler, S. Roth, W. J. Blau, *J. Appl. Phys.* **92** 4024 (2002)

199. J. K. W. Sandler, J. E. Kirk, I. A. Kinloch, M. S. P. Shaffer, A. H. Windle, *Polymer* **44** 5893 (2003)

200. J. B. Bai, A. Allaoui, *Compos. Part A – Appl. S.* **34** 689 (2003)

201. M. B. Bryning, M. F. Islam, J. M. Kikkawa, A. G. Yodh, *Adv. Mater.* **17** 1186 (2005)

202. S. Barrau, P. Demont, E. Perez, A. Peigney, C. Laurent, C. Lacabanne, *Macromolecules* **36** 9678 (2003)

203. F. Du, J. E. Fischer, K. I. Winey, *Phys. Rev. B: Condens. Matter,* **72** 121404/1 (2005)

204. J. E. Fischer, K. I. Winey, *J. Polym. Sci. Part B: Polym. Phys.* **41** 3333 (2003)

205. C. A. Mitchell, J. L. Bahr, S. Arepalli, J. M. Tour, R. Krishnamoorti, *Macromolecules* **35** 8825 (2002)

206. P. Potschke, M. Abdul–Goad, I. Alig, S. Dudkin, D. Lellinger, *Polymer* **45** 8863 (2004)

207. S. R. Turner, R. W. Seymour, J. R. Dombroski, Amorphous and Crystalline Polyesters based on 1, 4–Cyclohexanedimethanol; in: J. Scheirs, T. E. Long (Eds.) Modern Polyesters, Wiley: West Sussex, England (2004) pp. 267 (Chapter 7)

208. E. O. Allen, Processing, in: M. D. Baijal (Ed.) Plastic Polymer Science and Technology; Wiley: New York (1982) pp. 271

209. G. A. Akin, S. J. Rush, N. C. Russin, *US Patent 3 271 370* (awarded to Eastman Kodak Company) (1966)
210. C. C. Yau, C. Cherry, *US Patent 5 340 907* (awarded to Eastman Chemical Company) (1994)
211. J. –W. Chen, I. –W. Chen, *J. Polym. Sci. Part A: Polym. Chem.* **37** 1797 (1999)
212. D. E. Kokkalas, D. E. Bikiaris, G. P. Kaarayannidis, *J. Appl. Polym. Sci.* **55** 787 (1995)
213. B. Apicella, M. DiSerio, L. Fiocca, R. Po, E. Santacesaria, *J. Appl. Polym. Sci.* **69** 2423 (1988)
214. R. Bacaloglu, M. Fisch, K. Biesiadsa, *Poly. Eng. Sci.* **38** 1014 (1988)
215. V. Hovnof, *J. Macromol. Sci.* **A15** 503 (1981)
216. R. M. Schulken Jr., R. E. Boy Jr., R. H. Cox, *J. Polym. Sci. Part C: Polym. Symp.* **6** 17 (1964)
217. A. Yu, X. Huang, *J. Appl. Polym. Sci.* **101** 2793 (2006)
218. L. P. Chen, A. F. Yee, E. J. Moskala, *Macromolecules* **32** 5944 (1999)
219. S. –S. Lee, A. F. Yee, *Macromolecules* **36** 6791 (2003)
220. J. Karger – Kocsis, T. Czigany, E. J. Moskala, *Polym. Eng. Sci.* **39** 1404 (1999)
221. M. Kattan, E. Dargent, J. Grenet, *J. Therm. Anal. Calor.* **76** 379 (2004)
222. E. Theodorou, J.S. Paik, *Packag. Technol. Sci.* **5** 21 (1992)
223. S. Bazhenov, J. X. Li, A. Hiltner, E. Baer, *J. Appl. Polym. Sci.* **52** 243 (1994)
224. J. X. Li, A. Silverstein, A. Hiltner, E. Baer, *J. Appl. Polym. Sci.* **52** 255 (1994)
225. J. X. Li, A. Hiltner, E. Baer, *J. Appl. Polym. Sci.* **52** 269 (1994)
226. J. Jandcar, A. T. Dibenedetto, Y. Hadziinikolou, A. J. Goldberg, A. Dianselmo, *J. Mater. Sci. – Mater. M.* **5** 214 (1994)
227. Z. Yu, M. Lei, Y. Ou, G. Yang, *Acta Polym. Sin.* **3** 278 (2000)
228. A. Paesano, D. Cohee, G. R. Palmese, *J. Themoplast. Compos.* **16** 139 (2003)
229. Y. Zhang, K. L. Tan, J. Zhang, C. Q. Cui, T. B. Lim, E. T. Kang, *Int. J. Adhes. Adhes.* **20** 165 (2000)

CHAPTER 3

MATERIALS AND EXPERIMENTAL TECHNIQUES

This chapter details the materials and experimental techniques used for characterization in this study.

3.1 Introduction

This thesis addresses the structure and properties of PETG nanocomposites based on two grades of PETG, six organically modified clays, and carbon nanotubes (CNT) fabricated using the melt blending technique. The different characterization techniques and the materials used in the course of this work are discussed in this chapter. These nanocomposites have been characterized by a host of techniques for their microstructure using X–ray diffraction (XRD), transmission electron microscopy (TEM), and scanning electron microscopy (SEM). The mechanical property enhancements in the nanocomposites have been studied using dynamic mechanical thermal analysis (DMTA). Thermo gravimetric analysis (TGA) is used to elucidate the thermal stability of these nanocomposites. Rheology is an important tool to understand the correlation between the mesostructure of nanocomposites and solid–state properties to create technologically important materials. Linear and non–linear rheological experiments were conducted to elucidate the durability of the nanocomposites structures under various conditions of shear and/or external stress. Dielectric relaxation spectroscopy (DRS) was used to study the effect of nanofillers on the dynamics of the segmental mobility of the polymer chains in the nanocomposites.

3.2 Materials

3.2.1 PETG

The two grades of PETG used in this work are Eastar 6763 and Eastar GN071 (from Eastman Chemical Company, USA). The chemical structure of PETG is shown in Figure 3.1.

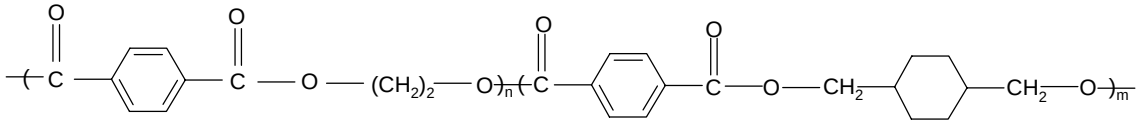

Figure 3.1 Chemical structure of PETG

Both PETGs are amorphous copolyesters and have a similar structure as determined by ^{1}H NMR (see Figure 3.2) Eastar 6763 has been used as the matrix polymer for the nanocomposites described in chapter 4 (PETG/Layered Silicate Nanocomposites),

while Eastar GN071 is used in the nanocomposites described in chapters 5 (PETG20A Nanocomposites) and 6 (PETGCNT Nanocomposites). For convenience both these grades are abbreviated PETG throughout this thesis, unless mentioned otherwise.

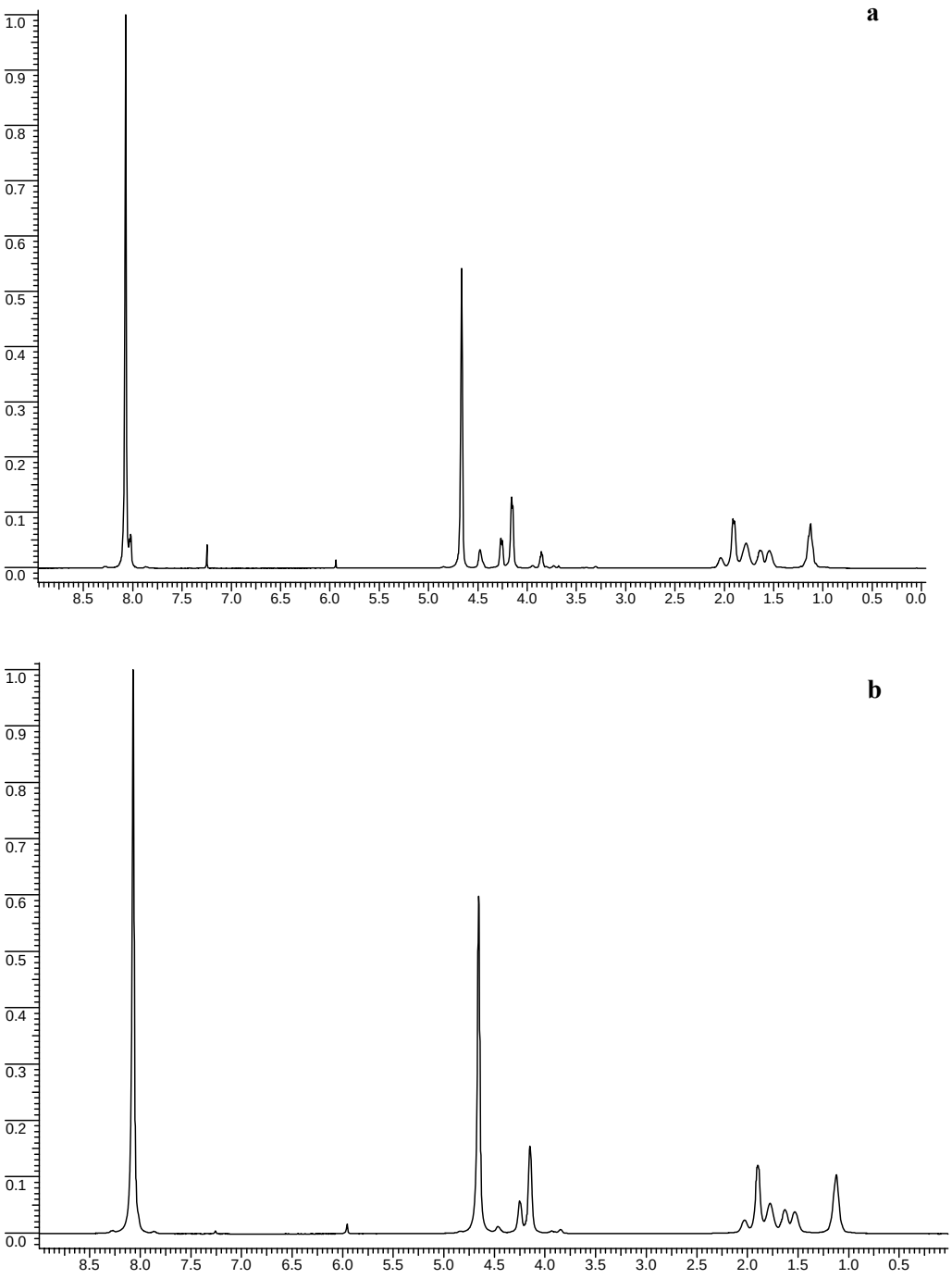

Figure 3.2 ^{1}H NMR of (a) Eastar 6763 and (b) Eastar GN071

Specific property comparison of the two grades of PETG is provided in Table 3.1. It can be clearly observed that the two grades of PETG show almost similar physical properties.

Table 3.1 Property comparison of the two grades of PETG

Property	Eastar 6763	Eastar GN071
Density (g cm^{-3})	1.27	1.27
Thermal Properties		
T_g (°C)	81	82
HDT, at 0.455 MPa (°C)	70	70
HDT, at 1.82 MPa (°C)	64	62
Tensile Properties		
Stress at yield (MPa)	50	50
Stress at break (MPa)	28	30
Elongation at yield (%)	4.3	4.4
Elongation at break (%)	130	180
Flexural Properties		
Flexural modulus (MPa)	2100	2060
Flexural yield strength (MPa)	70	68
Izod Impact Strength[a]		
Notched at 23 °C (J/m)	101	105
Unnotched at 23 °C (J/m)	NB	NB
Notched at -40 °C (J/m)	37	40
Unnotched at -40 °C (J/m)	NB	NB
Dynamic Mechanical Thermal Analysis[b]		
Storage Modulus at 40 °C (Pa)	1.37×10^9	1.16×10^9
Storage Modulus at 85 °C (Pa)	5.46×10^6	1.96×10^7
T_g (Tan δ peak) (°C)	79.12	82.45

[a] NB: no break

[b] experimental data

3.2.2 Layered Silicates

The organically modified montmorillonites (org–MMTs) used are Cloisite 10A (10A), Cloisite 15A (15A), Cloisite 20A (20A), Cloisite 6A (6A), Cloisite 93A (93A), and Cloisite 30B (30B) from Southern Clay Products, USA. All the org–MMTs are based on different tallow compounds containing quaternary ammonium counter ion with the montmorillonite clay. The quaternary ammonium intercalants contained a mixture of alkanes (~65% C18, ~30% C16, ~5% C14) as reported in the product literature. The layered silicates were used as received with no additional purification steps. Details of the org-MMTs used in this study are summarized in Table 3.2.

Table 3.2 Properties of Org–MMT series modified using different intercalant molecules[a]

Org–MMT	The intercalant molecule[b]	CEC (meq $100g^{-1}$ clay)	d–spacing of layered silicate (nm)	% Weight loss		Density (g cm^{-3})
				At Ignition	At 200°C[c]	
10A	DMBHT	125	1.9	39	3	1.90
15A	DMDHT	125	3.2	43	1	1.66
6A	DMDHT	140	3.3	48	1	1.71
20A	DMDHT	95	2.3	38	1	1.77
93A	MDHT	90	2.4	40	1	1.88
30B	MT2EtOH	90	1.8	30	1	1.98

[a] as per company data sheet

[b] DMBHT – Dimethyl benzyl (hydrogenated-tallow); DMDHT – Dimethyl bis(hydrogenated-tallow); MDHT – Methyl bis(hydrogenated-tallow); MT2EtOH – bis(2-hydroxy-ethyl) methyl tallow

[c] experimental data

All the clay samples were used as received without any further purification steps. To ensure that the organic intercalant in the org–MMTs had not degraded at the processing temperature, they were annealed at the processing temperature for at least 5

min (comparable to the processing time). An X-ray diffraction pattern of the annealed sample was obtained and compared with that of the org-MMT as received. The annealed samples did not show any significant changes in the d spacing of the clays. Additionally, percentage weight loss at 200 ^{o}C from thermo gravimetric analysis of the clays was also obtained. The values are listed in Table 3.2. The results clearly prove the thermal stability of all the layered silicates used in this study.

3.2.3 Carbon Nanotubes

Multiwalled carbon nanotubes (henceforth abbreviated as "CNT" unless mentioned otherwise) from Aldrich, produced by CVD method, were used in this work. Typical properties of the CNTs are given in Table 3.3

Table 3.3 Properties of CNTs used for nanocomposite fabrication[a]

Property	Value
Outer Diameter	10–20 nm
Inner Diameter	5–10 nm
Length	0.5-200 μm
Purity	95+%
Melting Point	3652–3697 °C
Density	2.1 g cm^{-3}

[a] as per product data sheet

3.3. Experimental Techniques

3.3.1. X–ray diffraction (XRD)

XRD is one of the primary techniques used to determine the structure of polymer nanocomposites. The three–dimensional structure of nonamorphous materials, such as minerals, is defined by regular, repeating planes of atoms that form a crystal lattice. When a focused X–ray beam interacts with these planes of atoms, a part of the beam is transmitted, a part is absorbed by the sample, a part is refracted and scattered, and a part is diffracted. Diffraction of an X–ray beam by a crystalline solid is analogous to diffraction of light by droplets of water, producing the familiar rainbow. X–rays are

diffracted by each mineral differently, depending on what atoms make up the crystal lattice and how these atoms are arranged.

XRD is a non–destructive analytical characterization technique for identification and quantitative determination of long–range order in various crystalline compounds. The energy of an X-ray photon is related to its wavelength λ and is given by:

$$\varepsilon = h\nu = \frac{hc}{\lambda} \tag{3.1}$$

where h is Planck's constant, ν is the frequency, c is the velocity of light, and ε is energy of the photon. Crystal studies require photon energies in the 10 to 50 KeV range. X–rays are electromagnetic radiation of exactly the same nature as light, but of very much shorter wavelength. The unit of wavelength in the X–ray region is the angstrom (Å) or nanometer (nm), equal to 10^{-10} m and 10^{-9} m, respectively. The X–rays used in diffraction have wavelengths lying in the range of 0.05–0.25 nm, whereas visible light is of the order of 600 nm.[1] X–rays are produced when any electrically charged particle of sufficient kinetic energy decelerates. Electrons are usually used for this purpose, the radiation being produced in an X–ray tube, which contains a source of electrons and two metal electrodes. The high voltage maintained across these electrodes draws the electrons to the anode, or target, which they strike with high velocity. X–rays are produced at the point of impact and radiate in all directions. Most of the kinetic energy of the electrons striking the target is converted into heat, less than 1% being transformed into X–rays.

When the rays coming from the target are analyzed, they are found to contain a mixture of different wavelengths, and the variation of intensity with wavelength is found to depend on the tube voltage. The intensity is zero up to a certain wavelength, called the short wavelength limit (λ_{SWL}), increases rapidly to a maximum then decreases, with no sharp limit on the long wavelength side.

3.3.1.1 Bragg's Law

Figure 3.3 below illustrates interference (constructive) between waves scattering from two adjacent rows of atoms in a crystal. The net effect of scattering from a single row is equivalent to partial reflection from a mirror imagined to be aligned with the row.

Thus, the angle of "reflection" equals the angle of incidence for each row. Interference then occurs between the beams reflecting off different rows of atoms in the crystal.

When X–rays are scattered from a crystal lattice, peaks of scattered intensity are observed which correspond to the following conditions:

1. The angle of incidence = angle of scattering.
2. The path length difference is equal to an integer number of wavelengths.

By finding the wavelengths (λ) that allow the X-rays diffracting from the lower crystal plane to cover the distance from CB to BD and still be in constructive interference with the upper X-rays, Bragg's Law can be upheld. In equation form this is:

$$n\lambda = 2d\sin(\theta) \qquad (3.2)$$

where, n is an integer (1, 2, 3, ……., n), λ the wavelength, d is the distance between atomic planes, and θ the angle of incidence of the X–ray beam and the atomic planes.

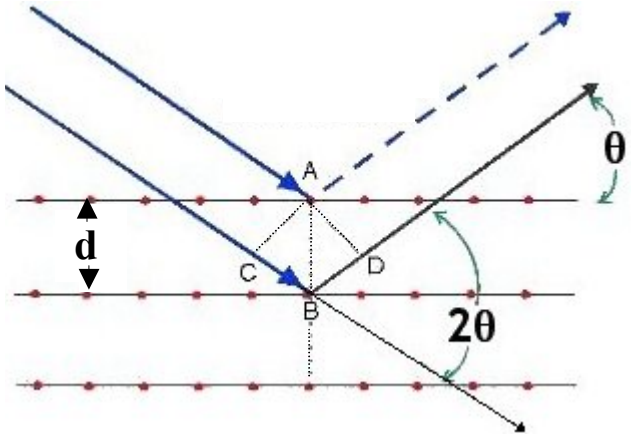

Figure 3.3 A graphical representation of X–ray Radiation Diffracting from crystal planes and what Bragg's law represents

The condition for maximum intensity contained in Bragg's law above allow us to calculate details about the crystal structure, or if the crystal structure is known, to determine the wavelength of the X–rays incident upon the crystal.

A crystal may be defined as a collection of atoms arranged in a pattern that is periodic in 3 dimensions. Crystals are necessarily solids, but not all solids are crystalline. In a perfect single crystal all atoms in the crystal are related either through translational symmetry or point symmetry. Polycrystalline materials are made up of a great number of

tiny single crystals. In powder diffraction method, we can get the information from peak positions, peak intensities, and peak shapes. Deviations from ideal crystallinity, such as finite crystallite size and strain lead to broadening of the diffraction lines.

By analyzing this broadening it is possible to extract information about the microstructure of a material. A perfect crystal would extend in all directions to infinity, so we can say that no crystal is perfect due to its finite size. This deviation from perfect crystallinity leads to a broadening of the diffraction peaks. However, above a certain crystallite size (~ 0.1–1 μm) this type of broadening is negligible. Crystallite size is a measure of the size of a coherently diffracted domain. Due to presence of polycrystalline aggregates crystallite size is not generally the same thing as particle size. In 1918 Scherrer first observed that small crystallite size could give rise to line broadening. He derived a well-known equation for relating the crystallite size to the broadening, which is called the "Scherrer formula".

$$L = \frac{k\lambda}{\beta_0 \cos\theta} \tag{3.3}$$

where, L is the apparent crystallite size, k is Scherrer constant, somewhat arbitrary value that falls in the range 0.87-1, λ is wavelength of the X-ray radiation, β_0 is the half width of the crystalline peak in radians 2θ.

During X–ray diffraction, we measure the angle (θ) by the angle between the arms of the diffractometer as they move. The "n" appears because of the periodicity of the wave and can be any positive integer. We are trying to find the spacing between the lattice planes, d, so the only variable left that we need to control in order to use the Bragg equation is the wavelength (λ) of the X–rays. The target that we use to create the beam controls that variable. Commonly Copper and Molybdenum, which emit X–rays corresponding to a wavelength of 0.154 nm and 0.08 nm, respectively are used as the targets, but other targets are also available which include, Chromium, Iron, Cobalt, and Tungsten.

Powder XRD (X–ray Diffraction) is perhaps the most widely used X–ray diffraction technique for characterizing materials. As the name suggests, the sample is usually in a powdery form, consisting of fine grains of single crystalline material to be

studied. The technique is also widely used for studying particles in liquid suspensions or polycrystalline solids (bulk or thin film materials).

Powder diffraction data can be collected using either transmission or reflection geometry, as shown below (see Figure 3.4). Because the particles in the powder sample are randomly oriented, these two methods will yield the same data. X–ray powder diffraction in the reflection mode (Bragg Brentano Parafocusing geometry)[2,3] is used to characterize the structure of polymer layered silicate nanocomposites. The powder diffraction techniques are based on the established procedures developed for identification and structural characterization of layered minerals.[4]

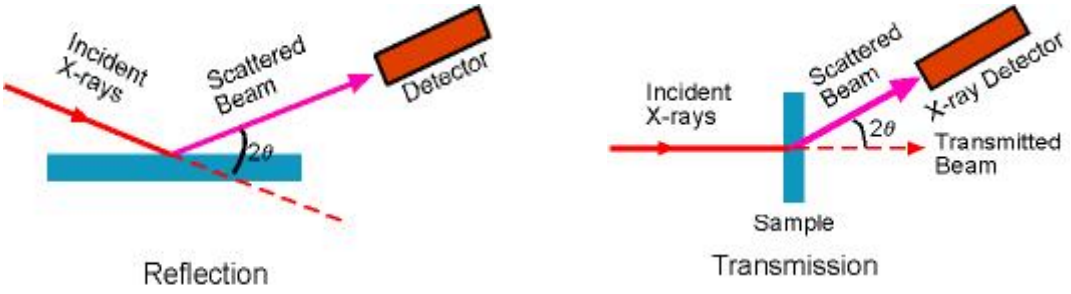

Figure 3.4 Schematic of X–ray diffraction geometries

3.3.2 Transmission Electron Microscopy (TEM)

TEM operates on the same basic principles as the light microscope but uses electrons instead of light. What we can see with a light microscope is limited by the wavelength of light. TEM uses electrons as "light source" and their much lower wavelength makes it possible to get a resolution thousand times better than that with a light microscope. We can see objects to the order of a few nanometers (10^{-9} m). For example, we can study small details in the cell or different materials down to near atomic levels. Therefore, it can be used to confirm results obtained by XRD about the organization of the nano filler morphology in the nanocomposite. The possibility for high magnifications has made the TEM a valuable tool in both medical, biological and materials research.

3.3.2.1 Working Principle

A TEM works much like a slide projector. A projector shines a beam of light through (transmits) the slide, as the structures and objects on the slide affect the light passes through it. These effects result in only certain parts of the light beam being transmitted through certain parts of the slide. This transmitted beam is then projected onto the viewing screen, forming an enlarged image of the slide. TEM works the same way except that they shine a beam of electrons (like the light) through the specimen (like the slide). Whatever part is transmitted is projected onto a phosphor screen for the user to see. A TEM can be divided up into three components, viz. the illuminating system, the objective lens and stage, and the imaging system. Figure 3.5 shows a schematic illustrating the typical parts of a TEM.

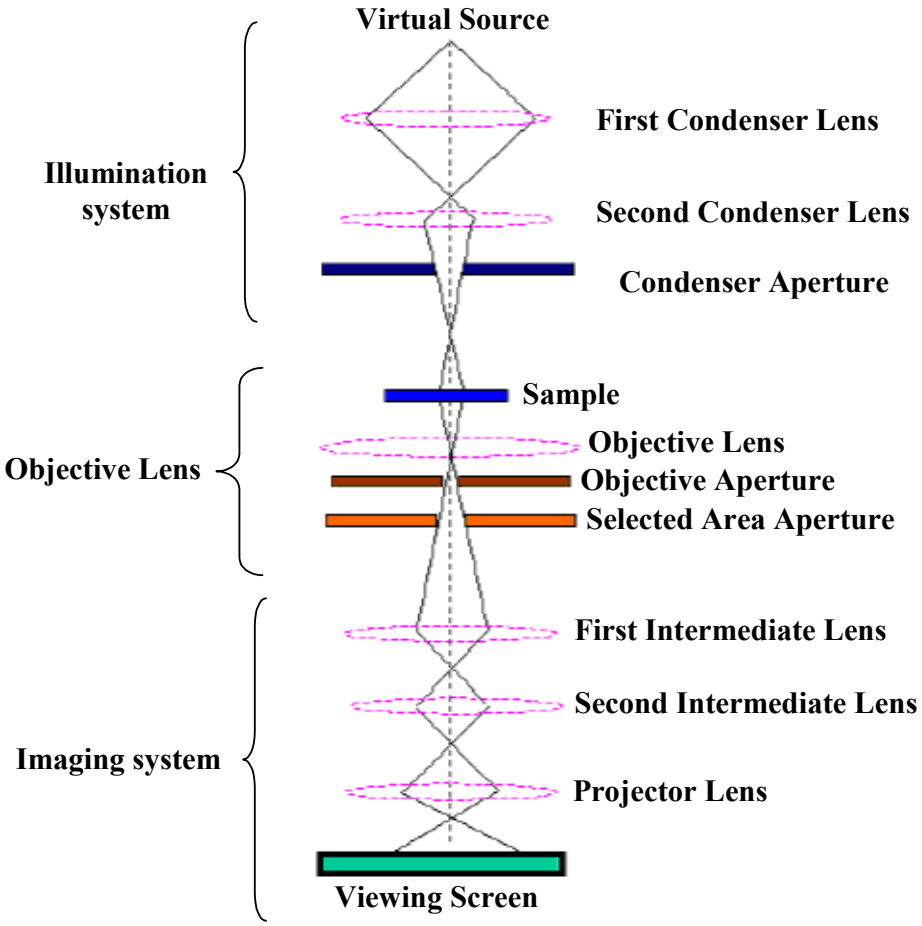

Figure 3.5 Schematic description of a transmission electron microscope

Bright field imaging is an imaging mode in a TEM that uses only unscattered electrons to form the image. Contrast in such an image is entirely due to thickness and density variations in a sample. Unscattered electrons are incident electrons, which are transmitted through the thin specimen without any interaction occurring inside the specimen. The transmission of unscattered electrons is inversely proportional to the specimen thickness. Areas of the specimen that are thicker will have fewer transmitted unscattered electrons and so will appear darker, conversely the thinner areas will have more transmitted and thus will appear lighter. In dark field imaging a single diffracted beam is used to form the image in a TEM. This causes all regions of the specimen that are not of the same crystal structure and orientation as the region which produced the diffracted beam to be represented as very dark in the final image; allowing phase differentiation visually in the TEM.

3.3.2.2 Sample Specifications and Preparation

One of the measure difficulties in obtaining a good TEM image is sample preparation. It is necessary that the TEM specimens are sufficiently thin having the thickness to the order of 100 nm or less. The measurements for polymer nanocomposites are done using the bright field imaging mode. In this mode regions of the sample which are thicker or have higher density will scatter the incident electron beam more strongly and will appear darker in the image as lesser number of electrons will be transmitted. The nano fillers used in this work have a higher density than the polymer. Hence they appear to be darker than the polymer in a TEM image. Thus, if the sample is not sufficiently thin the polymer will also appear darker and this will reduce the contrast of the nano filler. However, due to the high density of the nano fillers it is difficult to cut very thin samples from these nanocomposites. Therefore, the contrast between the nano fillers and the polymer is reduced as the thickness of the sample increases. This phenomenon is termed as “mass–thickness contrast”.

Thin sample specimens for TEM are normally prepared using ultramicrotomy. Properly trimmed samples (of trapezoid shape having its lateral dimensions closer to 1mm) are placed in an arm, which is attached to a motor controlled hand wheel. As the arm moves vertically past the knife, which can be either of glass or diamond, the sample

is cut in the required thickness. These cut sections are collected on water in a boat attached to the knife-edge such that each specimen is lined one after the other. The cut sections are directly transferred to the grids and dried properly before being transferred to the TEM experimental setup.

3.3.3 Scanning Electron Microscopy (SEM)

SEM is designed for direct studying the surfaces of solid objects. By scanning with an electron beam that has been generated and focused by the operation of the microscope, an image is formed in much the same way as a television. SEM gives better resolution and depth of field than optical microscope. For this reason the SEM can produce an image that is a good representation of the three dimensional sample. In this thesis we have used SEM for observing the morphology of the nanocomposites based on CNTs.

3.3.3.1 Operating Principles

The instrument can be simplified into three major sections: a) electron-optical column; b) vacuum system and c) electronics and display system.[5] A tungsten filament is heated to 2700 °K, which produces electrons that are accelerated towards the anode disc. Electrostatic shaping of the electron beam under vacuum gives a beam diameter of about 50 μm. Ultimate performance of the SEM is mainly limited by the diameter of the beam and hence two lenses and condensers demagnify the beam to around 5 nm. The scanning coils deflect this beam and sweep it over the specimen surface. A cathode-ray display tube is scanned synchronously with the electron beam. The brightness of the display tube is modulated by the signal, which arises from the interaction of the beam with the surface element, which is probed. The strength of this signal is translated into image contrast. Secondary electrons, which the beam probe liberates from the specimen surface, are collected and used as the contrast signal. The yield of collected electrons depends on the nature of the specimen surface and on its inclination with respect to the probing beam. Consequently, one obtains pictures with a high perspective appearance.[5]

Figure 3.6 shows a beam of electrons is produced at the top of the microscope by heating of a metallic filament. The electron beam follows a vertical path through the

column of the microscope. It makes its way through electromagnetic lenses, which focus and direct the beam down towards the sample (Figure 3.6). Once it hits the sample, other electrons (backscattered or secondary) are ejected from the sample. Detectors collect the secondary or backscattered electrons, and convert them to a signal that is sent to a viewing screen similar to the one in an ordinary television, producing an image (Figure 3.6).

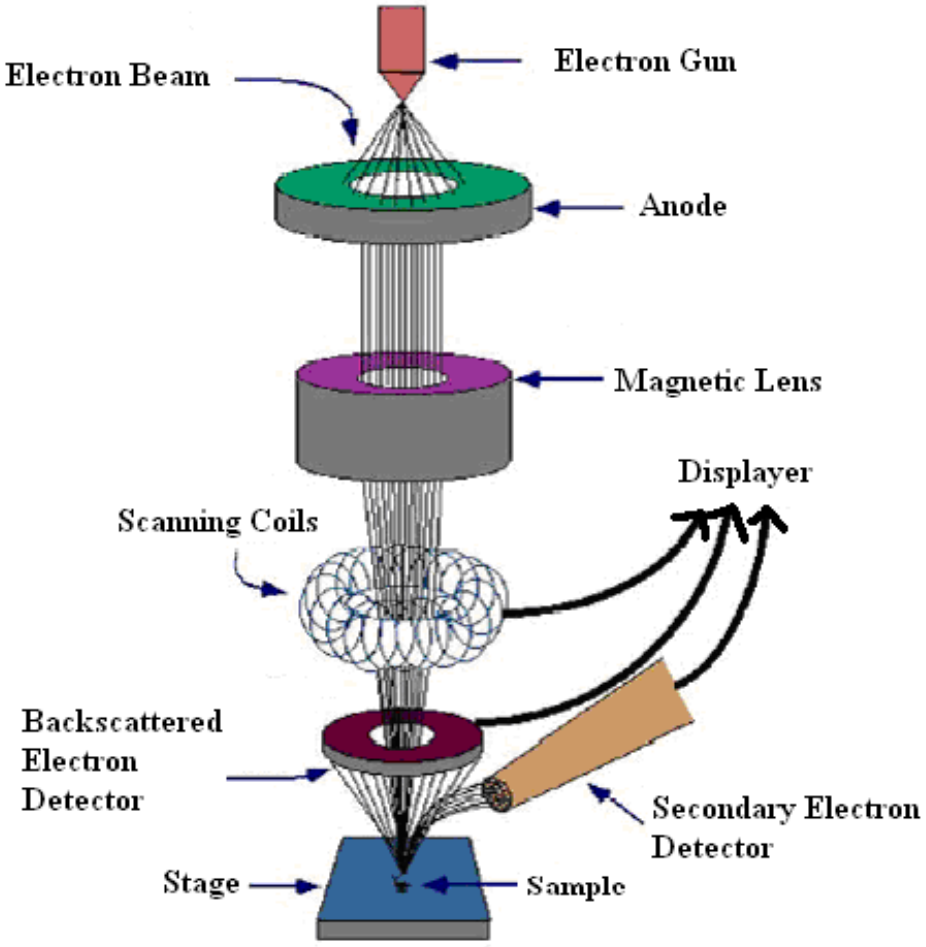

Figure 3.6 Schematic description of a scanning electron microscope

3.3.4 Thermogravimetric Analysis (TGA)

The determination of changes in chemical or physical properties of material as a function of temperature in a controlled atmosphere can be obtained by a thermal analysis. TGA is a good analytical tool to measure thermal decomposition of solids and liquids,

solid–solid and solid–gas chemical reactions, material specification, purity and identification, inorganic solid material adsorption and phase transitions. TGA is based on the measurement of the weight loss of the material as a function of temperature. A simple schematic of TGA instrumentation is shown in Figure 3.7.

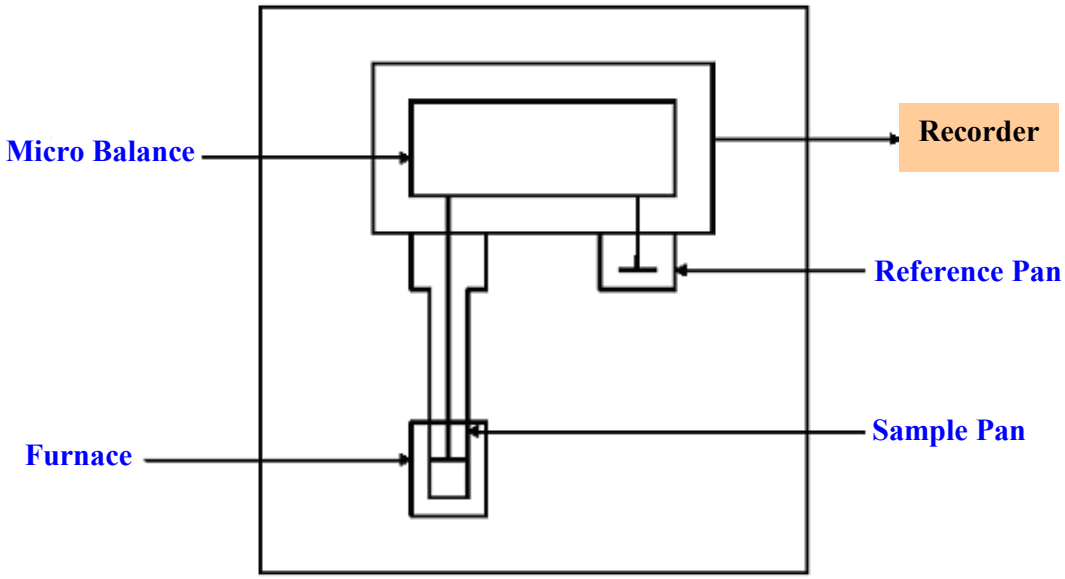

Figure 3.7 Schematic of TGA instrumentation

TGA operates on a null-balance principle, using an electromechanical transducer coupled to a taut-band suspension system. The sensitivity of the balance is 0.1 mg. The microbalance plays a significant role in TGA. During the process of measurement, the change in sample mass affects the equilibrium of the balance. This imbalance is fed back to a force coil, which generates additional electromagnetic force to recover equilibrium. The amount of additional electromagnetic force is proportional to the mass change. During the heating process the temperature may go as high as 1000 °C inside the furnace.

TGA curve provides information concerning the thermal stability of the initial sample, intermediate compounds that may be formed and of the residue if any. In addition to thermal stability, the weight losses observed in TGA can be quantified to predict the pathway of degradation or to obtain compositional information. The

experimental data offer more sophisticated understanding of thermal stability of materials on heating. This ability to obtain measurements at higher temperatures is most useful for inorganic materials such as the nanofillers used in this thesis.

3.3.5 Dynamic Mechanical Thermal Analysis (DMTA)

DMTA is an important tool that provides invaluable insight into the structure–property relationships of polymers. DMTA probes essentially the relationships between the dynamic properties and the structural parameters including molecular weight, molecular orientation, crystallinity, crosslinking, copolymerization, plasticization, etc. under various conditions of stress, temperature, frequency, time, pressure, etc.[6] A wide range of materials can be characterized by DMA regardless of their kind, their physical state, or the form in which they are used. These include thermoplastics, thermosets, elastomers, polymer blends, alloys, composites, adhesives, soft solids like gels, cheese, toothpastes, foams–soft, dry, or rigid, wood, paper, ceramics, metals, etc. From an industry viewpoint the mechanical properties of polymeric materials can be subjected to time, frequency and temperature effects allowing test conditions that simulate the intended application environment. From a research perspective, suitability of innovative materials for new applications can be assessed by considering, modulus, damping, glass transition, softening temperature, rate of cure, degree of cure, viscosity, gelation, sound absorption, impact resistance, and creep.

Films as thin as 5 microns can be studied making DMTA ideal for low sample volume testing. Effects of filler intercalation, particle–particle association and stress/strain curves can be generated for films to a better accuracy than is possible with standard physical testing devices, since the mass and inertia of the clamps is much smaller. The linear and non–linear response of viscoelastic materials as a function of strain are shown in Figure 3.8.

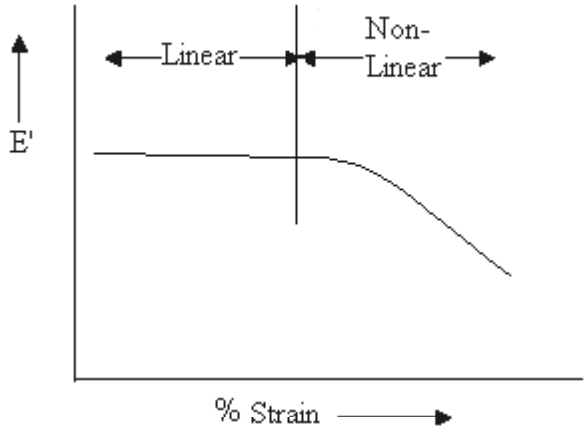

Figure 3.8 Linear and Non–linear response of viscoelastic material

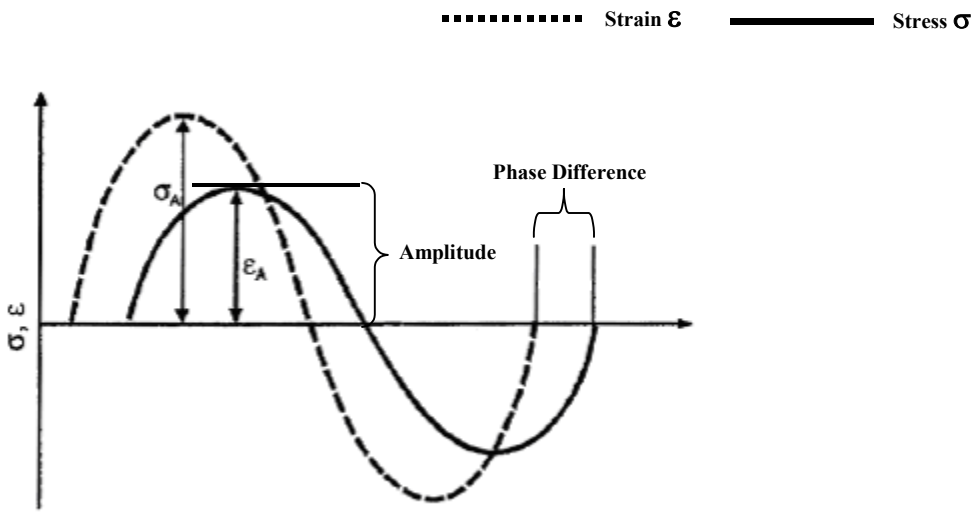

Figure 3.9 Sinusoidal oscillation and response signal of a linear viscoelastic material[9]

The principle of dynamic mechanical test method is to impart a small sinusoidal mechanical strain on to a solid or a viscoelastic liquid and to resolve the stress into real and imaginary components corresponding to elastic and viscous states.[7,8] In viscoelastic studies, the applied force and resulting deformation both vary sinusoidally with time. The strain will also be sinusoidal but will be out of phase with stress. This phase lag results from the time necessary for molecular rearrangements and is associated with the relaxation phenomena (see Figure 3.9). The variation of these components as a function of temperature is used to study the molecular motion in the polymers.

Storage modulus (E') represents the stiffness of a material and is proportional to the maximum amount of elastic energy stored in the material during an oscillating loading cycle. It has nearly the same value as the Young's modulus for low deformations and corresponds to that determined by tensile testing. The storage modulus describes the elastic properties of a material.

Energy dissipated in the material during an oscillating loading cycle is represented by the loss modulus (E''). It is proportional to the energy transformed into heat that cannot be regained. The loss modulus describes the viscous properties of a material. An oscillating stress, σ_A, can be expressed as:

$$\sigma_A = \sigma_0 e^{iwt} \tag{3.4}$$

Due to the loss of energy during the loading cycle the strain, ε_A, in the sample will exhibit a phase shift relative to the applied stress, σ_A, thus

$$\varepsilon_A = \varepsilon_0 e^{i(wt-\delta)} \tag{3.5}$$

The phase angle (δ) represents the phase shift between dynamic stress and dynamic strain in a viscoelastic material that is exposed to a sinusoidal load. The angle δ is expressed in radians. The modulus of the material can therefore be expressed as:

$$E = \frac{\sigma_A}{\varepsilon_A} = \frac{\sigma_0 e^{iwt}}{\varepsilon_0 e^{i(wt-\delta)}} = \frac{\sigma_0 e^{i\delta}}{\varepsilon_0} \tag{3.6}$$

Expressing $e^{i\delta} = Cos\delta + iSin\delta$ yields:

$$E = \frac{\sigma_0}{\varepsilon_0} Cos\delta + i\frac{\sigma_0}{\varepsilon_0} Sin\delta = E' + iE'' \tag{3.7}$$

The ratio between loss modulus and storage modulus described by the loss factor tan δ. This factor is very useful to describe the damping properties of a material. A high tan δ is characteristically for a material with a more non-elastic behavior, while a low value of tan δ is characteristic for a more elastic material.

$$\tan\delta = \frac{E''(\omega)}{E'(\omega)} \tag{3.8}$$

DMTA is about 10 to 100 times more sensitive to changes occurring at the T_g than other thermal technique and is therefore useful to detect a weak T_g.[10] The value for T_g determined by DMTA can differ from that determined using other techniques. Some DMTA operators quote the tan δ peak temperature as T_g while others quote the E'' peak onset or perhaps the onset of the E' drop.

3.3.6 Rheology

Rheology in its broadest sense is the study of the relationships between stress, deformation and flow of matter in a continuous media. Rheology is the science that deals with the study of flow of materials that behave in more complex and unusual manner than ordinary liquids and solids.[11–17] Polymers are viscoelastic fluids, which behave viscous or elastic, depending upon how fast they flow or are deformed in the process. Rheology is very sensitive to very small changes in the polymer structure and thus is an ideal tool for polymer characterization.

Traditionally, the distinction between a liquid and a solid is clear. The response of an ideal solid to deformation may be modelled by Hooke's law. The stress (σ) response is proportional to the imposed strain (γ) and is independent of the strain rate.

$$\sigma = G\gamma \tag{3.9}$$

where, G, which is the proportionality constant, is termed as the shear modulus. It relates to the stiffness of the material or in other words the materials ability to resist deformation. Thus, in a Hookean solid the elastic energy supplied by the deformation is completely conserved. An ideal liquid has a Newtonian viscosity where the stress (σ) response is proportional to the imposed strain rate ($\dot{\gamma}$) and the total strain is irrelevant:

$$\sigma = \eta\dot{\gamma} \tag{3.10}$$

where, η is the coefficient of viscosity. In a Newtonian liquid the energy of deformation is completely dissipated. Complex fluids such as polymers, on application of deformation show behavior that is a combination of both viscous and elastic behavior. Materials, which can be characterized by such behavior, are termed as *viscoelastic materials*.[18]

The quantitative interpretation of the rheological data, obtained with experimental tests, requires description of the rheological response by using mathematical model, providing different parameters with various physical meanings.[18] The rheological models, based on the phenomenological approach, have been developed to achieve maximum agreement between the predicted and experimental rheological properties of matters, by taking into account only the principles of continuum mechanics, regardless of structural characteristics.[19] In the linear theory of viscoelasticity, the differential equations are linear, the ratio of stress to strain is a function of time alone.

The rheological behavior of materials can be determined under oscillatory shear and steady–shear[14]. In steady-shear experiments, the viscosity of the sample is measured as a function of shear rate (over wide range of shear rates) to study the dependence of shear rate of the sample. A constant shear rate is applied and steady shear stress and normal stresses are measured. Normally a Newtonian plateau is observed at low shear rates while as the shear rate increases the viscosity often decreases. However, steady–shear measurements are not very sensitive to the microstructure present in the system. Dynamic rheology, performed under oscillatory shear, is the preferred technique for detecting microstructural features.[14,18] A number of small-deformation experiments are used to measure the linear viscoelastic response of the material.[12,14] When the low–amplitude oscillatory shear technique is used, the sample is subjected to a sinusoidal shear strain, γ, and the resulting shear stress, σ, is measured. As a response of the material to the oscillating strain input, the shear stress will also oscillate sinusoidally at the same oscillation frequency, ω, but in general it will be shifted by the phase angle, δ, (see Figure 3.10).

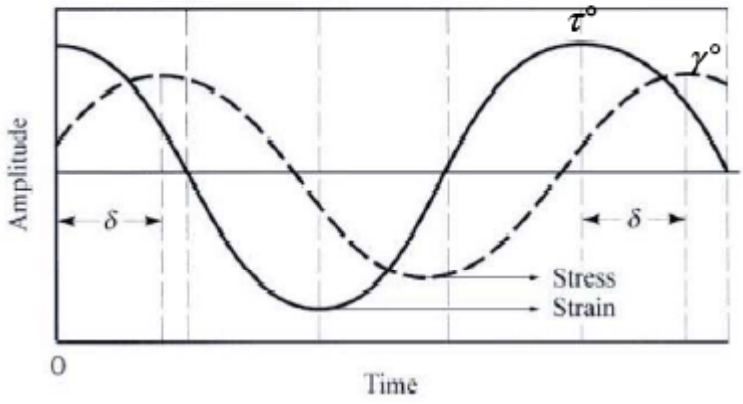

Figure 3.10 An oscillation strain and the stress response for a viscoelastic material

The phase angle δ defining the lag of the stress behind the strain which, is the measured phase lag between the applied stimulus and the response, with respect to the strain wave as described with the following mathematical expressions:[14]

$$\gamma = \gamma_{\circ} \sin \omega t \tag{3.11}$$

$$\sigma = \sigma_{\circ} \sin(\omega t + \delta) \tag{3.12}$$

where $\gamma_{\circ}$ is the shear strain amplitude, and $\sigma_{\circ}$ is the shear stress amplitude.

Within the region of linear viscoelasticity, the resulting stress is also sinusoidal and can be decomposed into an in-phase and an out-of-phase component.[18] At phase angle 0°, the in-phase response, shows that the sample is ideal elastic material, and at phase angle 90°, the out-of-phase response, shows that the sample is ideal viscous material. With viscoelastic materials the phase angle, δ, between the applied stress/strain and the resulting strain/stress is between 0° and 90°. The phase angle is a good indicator of the overall viscoelastic nature of the material.

When the amplitude ratio and the phase angle are measured, the parameters representing viscoelastic behavior can be calculated. In linear viscoelastic regime the resultant linear stress is represented by

$$\sigma(t) = \gamma_{\circ}[G'(\omega)\sin(\omega t) + G''(\omega)\cos(\omega t)] \tag{3.13}$$

The stress component in-phase with the deformation defines the elastic (or storage) modulus G' and is related to the elastic energy stored in the system on deformation.

$$G' = \left(\frac{\sigma}{\gamma}\right)\cos\delta \tag{3.14}$$

The greater the G', the more elastic are the characteristics of the material. The component out–of–phase with the strain gives the viscous (or loss) modulus G'', which is linked to the viscous dissipation of energy in the system.

$$G'' = \left(\frac{\sigma}{\gamma}\right)\sin\delta \tag{3.15}$$

The greater the G'', the more viscous are the characteristics of the material. The storage modulus represents the spring–like deformation in mechanical models, while the loss modulus represents the dashpot–like deformation[12]. The storage modulus, G', and the loss modulus, G'', are the real and the imaginary component of the complex modulus, G^*, respectively,

$$G^* = \frac{\sigma_\circ}{\gamma_\circ} = G' + iG'' = \sqrt{G'^2 + G''^2} \tag{3.16}$$

and the ratio between the dynamic moduli can be written as follows:

$$\frac{G''}{G'} = \tan\delta \tag{3.17}$$

Here $\tan\delta$ is proportional to the ratio of energy dissipated to energy stored and is called the loss factor or damping factor. It is also an indicator of the ratio of viscous to elastic behavior of materials, showing which one is the dominant one. With a $\tan\delta$ value of 1, the elastic and viscous properties of the material are equal. A lower loss factor implies a more elastic structure. Loss factor, $\tan\delta$, is often the most sensitive indicator of various molecular motions within the material.[20]

Similarly, the complex viscosity is defined as

$$\eta^* = \eta' + i\eta'' \tag{3.18}$$

where, η' is the real part and η'' is the imaginary part.

In oscillatory tests, the complex shear modulus, G^* represents the rigidity of the sample, i.e. the resistance to deformation. A schematic representing the typical frequency response of the complex modulus G^* is shown in Figure 3.11.

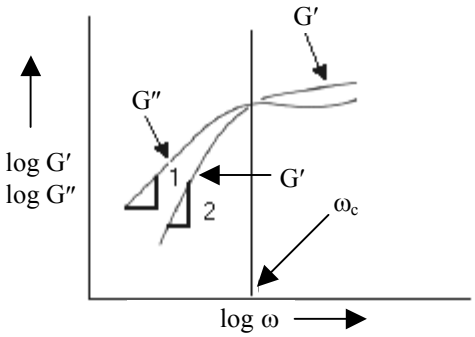

Figure 3.11 Schematic of frequency response of complex modulus for a typical polymer

At low frequencies (terminal region of relaxation), a double logarithmic plot of $G'(\omega)$ and $G''(\omega)$ shows slopes of 2 and 1, respectively, i.e. $G' < G''$, thus, the material behavior is liquid–like. Both G' and G'' increase until the crossover point at some frequency ω_c is reached. The reciprocal of the crossover frequency ω_c is characteristic of the relaxation time of the material. After the crossover frequency, G' reaches a constant value at the intermediate frequencies and is termed as *plateau modulus* ($G' \approx G_N^0$). The *plateau modulus* (G_N^0) is independent of the molecular weight and depends only on the chemical structure of the polymer. Thus, in this region G'' passes through a minimum. At higher frequencies both G' and G'' again increase. The response observed at such high frequencies, which correspond to small time scales, will only be due to small parts of the polymer chains (i.e. few monomeric units).

3.3.7 Dielectric Relaxation Spectroscopy (DRS)

DRS is an extremely effective technique for characterizing the detailed molecular dynamics over large range of time scales. DRS provides information about the segmental

relaxation of a polymer by probing its dielectric properties. DRS is an interesting probe to analyze polymer nanocomposites based on organic–inorganic nanofillers. This is because the segmental motion of the polymer chains is strongly influenced due to the presence of particle–particle and polymer–particle interactions in a composite material. Thus the molecular dynamics of the nanocomposite will be different than that of the bulk homopolymer. DRS technique is sensitive to orientation motions of permanent dipoles and to translational contributions of ions. The reorientation of permanent dipoles causes charge–density fluctuations within the sample. A typical parallel plates sample cell for dielectric analysis is shown in Figure 3.12.

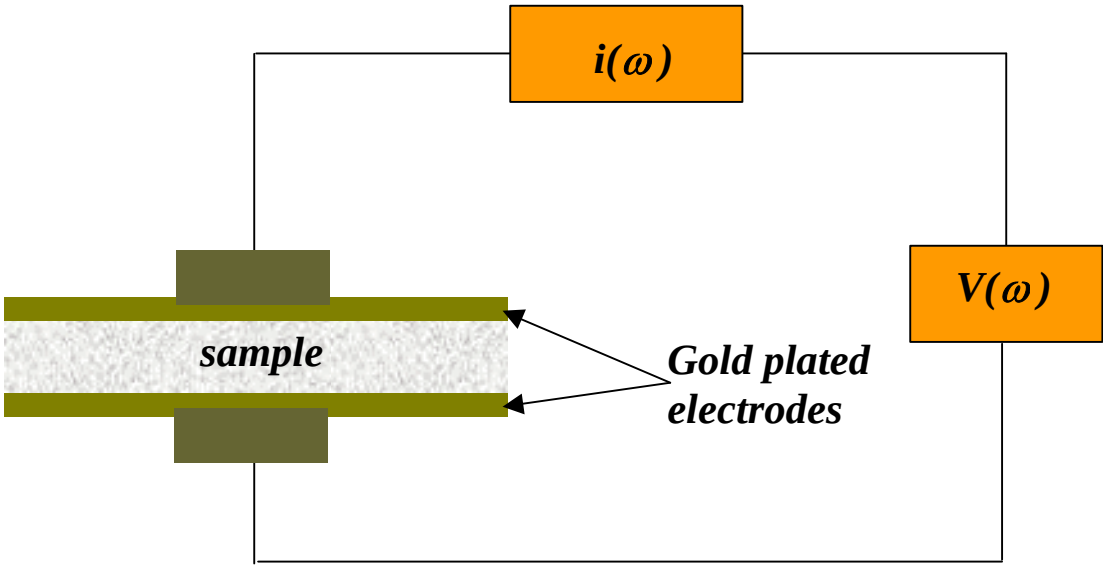

Figure 3.12 Schematic representation of a parallel plates sample test cell for dielectric analysis

A material is said to be dielectric if it has the ability to store energy when an external electric field is applied. When an electric field is applied across the faces of a parallel plate capacitor containing a dielectric, the atomic and molecular charges in the dielectric are displaced from their equilibrium positions and the material is said to be polarized. Several different mechanisms can induce polarization in a dielectric upon application of an external electric field. In polymeric materials the two major polarization mechanisms studied by dielectric relaxation spectroscopy are polarization due to charge migration and polarization due to orientation of permanent dipoles. Each polarization

mechanism has a characteristic relaxation frequency. As the frequency becomes larger, the slower mechanism drops off. This in turn leaves only the faster mechanisms to contribute to the dielectric storage. The dielectric loss factor will correspondingly peak at each critical frequency.

Dielectric measurements are conducted by applying a voltage to electrode interface and measuring the amplitude and the phase shift of the resulting current. The ratio of the output signal to the input perturbation is called the transfer function. If the input signal is the current and the output signal is the voltage, then the transfer function is the system impedance (*Z*). Similarly, if the input signal is the voltage and the output signal is the current then the transfer function is the system admittance (*Y*). In addition to impedance and admittance, there are several other derived quantities that can be obtained from dielectric spectroscopy, including, dielectric permittivity, dielectric modulus, and susceptibility. Since both the amplitude and the phase angle of the output may change with respect to the input values, these quantities are expressed as the complex number. Thus the complex dielectric function (ε^*) is given by

$$\varepsilon^*(\omega) = \varepsilon'(\omega) - i\varepsilon''(\omega) \tag{3.19}$$

where, ε' is the real part, ε'' is the imaginary or loss part, and $i = \sqrt{-1}$. ε^* is defined as factor between an outer alternating electric field $\vec{E}(\omega)$, where ω is the angular frequency of the electric field, f is frequency, $f = \frac{\omega}{2\pi}$ and $\vec{P}(\omega)$ the resulting polarization of the medium. The polarization of the medium (sample) is related to the applied electric field by the following relationship:

$$\vec{P}(\omega) = \left[\varepsilon^*(\omega) - 1\right]\varepsilon_{Vac}\vec{E}(\omega) \tag{3.20}$$

here, ε_{Vac} denotes the permittivity of the sample in vacuum. The complex dielectric function or permittivity of the sample is the property depending on temperature, frequency, pressure and structure. Both ε' and ε'' have direct physical interpretation, i. e. ε' is related to the energy stored in the material and ε'' is proportional to the energy dissipated per cycle. The dielectric loss tangent or the dissipation factor, tan(δ_d) is given by:

$$\tan(\delta_d) = \frac{\varepsilon''(\omega)}{\varepsilon'(\omega)} \tag{3.21}$$

where, δ_d is the phase angle between applied voltage and resulting current. In electro technical characterization of a material the dissipation factor becomes very important.

REFERENCES

1. B. D. Cullity, S. R. Stock, Elements of X–ray Diffraction; 3rd Edition, Prentice Hall: N. J. (2001)
2. D. L. Bish, J. E. Post, Modern Powder Diffraction: Reviews in Mineralogy 20 Edition, Mineralogical Society of America: Washington DC (1989)
3. H. P. Klugg, L. E. Alexander, X–ray diffraction procedures; John Wiley & Sons: U.S.A (1974)
4. G. W. Brindley, G. Brown, Crystal structures of clay minerals and their X-ray identification; Mineralogical Society Monograph number 5 (1984)
5. G. Lawes, Scanning electron microscopy and X–ray microanalysis; John Wiley & Sons (1987)
6. T. Murayama, Dynamic mechanical analysis of polymeric material; Elsevier Scientific Publishing Company (1978)
7. G. C. Ives, J. A. Mead, M. M. Riley, Hand Book of Plastics Test Methods, Iliffe Book Limited, London (1971)
8. N. G. McCrum, B. E. Read, G. Williams, Anelastic and Dielectric Effects in Polymeric Solids, John Wiley & Sons: U.S.A (1967)
9. A. Franck, Viscoelasticity and Dynamic Mechanical Testing, TA Instruments, Application Notes
10. D. W. Clegg, A. A. Collyer, Mechanical Properties of Reinforced Thermoplastics, Elsevier Applied Science, Essex (1986)
11. K. Walters, Rheometry, Chapman and Hall Publication, London (1975)
12. H. A. Barnes, J. F. Hutton, K. Walters, An Introduction to Rheology, Elsevier Scientific Publishers, Amsterdam (1989)
13. D. V. Rogers, K. Walters, Rheological Phenomenon in Focus, Elsevier Scientific Publishers, Amtserdam (1993)

14. C. W. Macosko, Rheology: Principles, Measurements and applications, Wiley – VCH, New York (1994)
15. A. A. Collyer, D. W. Clegg, Rheological Measurements, 2nd Edition, Chapman and Hall Publication, UK (1995)
16. K. E. Gubbins, R. G. Larson, M. A. Barteau, Structure and Rheology of Complex Fluids, Oxford University Press, New York (1999)
17. F. A. Morrison, Understanding rheology, Oxford University Press, New York (2001)
18. J. D. Ferry, Viscoelastic Properties of Polymers, 3rd Edition, John Wiley and Sons, Inc., New York (1980)
19. R. Lapasin, S. Pricl, Rheology of Industrial Polysaccharides: Theory and Applications, Blackie Academic and Professional, London (1995)
20. M. R. Mackley, R. T. J. Marshall, J. B. A. F. Smeulders, *Chem. Eng. Sci.* **49** 2551 (1994)

CHAPTER 4

PETG/LAYERED SILICATE NANOCOMPOSITES

This chapter reports the effect of molecular size and molecular structure of the intercalant used to modify the hydrophilic nature of the layered silicates, on the structure and viscoelastic properties of the nanocomposites prepared using PETG (Eastar 6763) and six different organically modified clays. Furthermore, the effect of modifier concentration on the properties of the nanocomposites is also discussed.

Part of the work presented in this chapter has been published:

1) R. A. Kalgaonkar, J. P. Jog, *J. Polym. Sci. Part: B Polym. Phys.* 41, 3102 – 3113 (2003). 2) R. A. Kalgaonkar, J. P. Jog, *J. Macromol. Sci. Part B – Phys.* B43, 421 – 436 (2004).

4.1 Introduction

Because of the hydrophilic nature of pristine clay, the formation of a thermodynamically homogeneous mixture of clay with hydrophobic polymers at molecular level is difficult. A typical way to enhance the interaction between the clay and the polymer is by exchanging the hydrated cations of the clay interlayer with cationic surfactants having long hydrocarbon chains. It has been widely demonstrated that the cation exchange capacity (CEC) of the layered silicate along with the molecular size and molecular structure of the organic intercalant controls the degree of intercalation of the polymer in the silicate layers. We make specific comparisons between various PETG/layered silicate nanocomposites depending on the CEC of the layered silicate to address these effects. Another way to study the effect of intercalant size on the properties of nanocomposites that is probed in this work is by preparing the nanocomposites using oragnophilic clays consisting of different concentrations of the same intercalant. The present study evolves from the characterization of the nano-structure of the nanocomposite prepared by melt intercalation technique. In this chapter we report a study of effect of concentration, molecular size, and molecular structure of the intercalant on the nano-structure and viscoelastic (solid and melt) properties of PETG/layered silicate nanocomposites prepared from commercially available organically modified montmorillonite layered silicates.

The set of layered silicates used in this study was carefully chosen and placed in pairs or triplets in order to understand the effects of the concentration, molecular size, and molecular structure of the intercalant on the degree of intercalation of the polymer in the clay interlayer. Two pairs were formed between layered silicates, which have a same CEC value but differ in the molecular size or the molecular structure of the alkyl ammonium intercalant, whereas, one triplet represented org–MMTs which were modified using the same intercalant molecule, but differ in intercalant concentration as well as have different d-spacing. The various pairs/triplets, which are used to study the effect of concentration, size, and structure of the intercalant molecule, are illustrated in Table 4.1.

The molecular structure and the nomenclature of the quaternary amine intercalants used to prepare the org–MMTs by cation exchange are given in Figure 4.1.

Here, HT stands for a tallow–based compound in which majority of the double bonds have been hydrogenated and T stands for tallow.

Table 4.1 Pairs/triplets of org–MMTs used in this work to study effects of concentration, size and structure of the intercalant molecule

Type of Effect	Organically Modified Montmorillonites				
Concentration of intercalant molecule	org–MMT 6A	vs.	org–MMT 15A	vs.	org–MMT 20A
Molecular size of intercalant	org–MMT 10A		vs.		org–MMT 15A
Molecular structure of intercalant	org–MMT 30B		vs.		org–MMT 93A

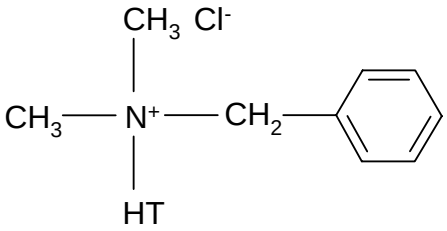

DMBHT used in org–MMT 10A

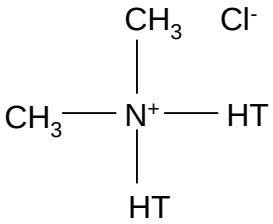

DMDHT used in org–MMT 6A/15A/20A

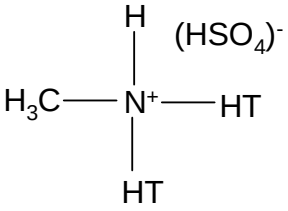

MDHT used in org–MMT 93A

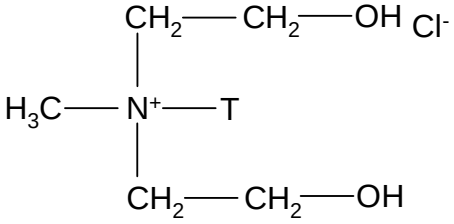

MT2EtOH used in org–MMT 30B

Figure 4.1 Molecular structure and nomenclature of various quaternary amine intercalants used to prepare the org–MMTs by cation exchange

4.2 Experimental

4.2.1 Nanocomposite Fabrication

PETG was melt blended with the org–MMTs using a Berstoff ZE–25 twin screw extruder having co– rotating and intermeshing 25 mm screws having a length to diameter ratio of 41.5. Compounding was carried out at a barrel temperature profile of 170–210 °C using a screw speed of 100 rpm. The residence time inside the extruder was approximately 3.0 min under the processing conditions used in this work. Prior to melt processing, all the materials were dried in an air circulatory oven at 70 °C for 24 h. One composition containing a 5 : 95 ratio in wt% of org-MMT to PETG for each nanocomposite was used in this work. The extruded strands were pelletized and dried at 70 °C for 24 h. The sample coding for PETG/layered silicate nanocomposites is given in Table 4.2

Table 4.2. PETG/layered silicate nanocomposites and their corresponding XRD data

Org-MMT	Sample code for PLS nanocomposite	d_{001} peak of layered silicate d_C (nm)	d_{001} peak of PLS nanocomposite d_{NC} (nm)	$\Delta d = d_{NC} - d_C$ (nm)
10A	PETG10A	1.9	3.6	1.7
15A	PETG15A	3.2	3.6	0.4
6A	PETG6A	3.3	3.5	0.2
20A	PETG20A	2.3	3.6	1.3
93A	PETG93A	2.4	3.3	0.9
30B	PETG30B	1.8	3.8	2.0

4.2.2 Sample Preparation

Samples for X–ray diffraction (XRD), dynamic mechanical thermal analysis (DMTA), and rheology were prepared by compression molding of the extruded

pellets into uniform films of approximately 0.5 and 1 mm thickness. Compression molding was performed using a Carver Press model F–15181 at 210 °C for 3 minutes.

4.2.3 Nanocomposite Characterization

4.2.3.1 Structural Characterization

To elucidate the structure of the clay in the polymer matrix wide–angle X–ray diffraction (WAXD) experiments were performed in reflection mode using a Rigaku Dmax 2500 diffractometer with Cu target and an incident wavelength of 0.1541 nm. The system consisted of a rotating anode generator operated at 40 kV and 150 mA. The samples were uniform thin films of approximately 0.5 mm thickness. The sample holder was an aluminum window on which the compression-molded sample was mounted. Samples were scanned from 2θ = 2 ° to 15 ° at a scan rate of 4.0 °min^{-1}. The basal spacing of MMT was estimated from the d_{001} peak in the XRD pattern.

Transmission electron microscopy (TEM) is used to get a direct evidence of the structure and a definitive description of the spatial correlation. TEM images were observed with a JEOL (JEM 1200 EX) apparatus. The samples for TEM were prepared using a Leica Ultracut UCT microtome. Extruded pellets were placed in an arm, which is attached to a motor controlled hand wheel. As the arm moves vertically past the diamond knife, the sample is cut in the required thickness. These cut sections are collected on water surface, of a boat attached to the knife–edge. The cut sections are directly transferred to the grids and dried properly before being transferred to the TEM experimental setup.

4.2.3.2 Dynamic Mechanical Thermal Analysis (DMTA)

DMTA was used to study the viscoelastic properties of the PETG/layered silicate nanocomposites. A Rheometrics Scientific Dynamic Mechanical Analyzer model IIIE with a rectangular tension/compression fixture was used for this purpose. Sample films used in this study had the dimensions of 0.5 mm thickness and 10 mm width. Temperature ramp experiments were carried out to elucidate viscoelastic properties of PETG/layered silicate nanocomposites. The scans were performed over a temperature range of 35 to 90 °C. The heating rate was 5 °C min^{-1}, frequency was 10 rad s^{-1}, and strain

was 0.05 %. Prior to the tests, all films were dried at least for 6 h in an air circulatory oven at a preset temperature of 70 °C.

4.2.3.3 Melt Rheology

Melt rheological measurements were conducted using a strain controlled rheometer (Rheometric Scientific, ARES). Dynamic oscillatory shear measurements were conducted by using a set of 25 mm diameter parallel plates with a uniform sample thickness of 1 mm. In all the dynamic oscillatory shear measurements, a uniform strain deformation of 1% was set, which is large enough to obtain a reasonable intensity signal at elevated temperature, while it is small enough to avoid nonlinear response. This value was ascertained by conducting strain sweeps to ensure that the data obtained in the dynamic experiments fell into the limits of linear viscoelastic region. The frequency dependence of the dynamic storage modulus (G'), dynamic loss modulus (G''), and dynamic complex viscosity (η^*) was measured in the temperature range of 210–230 °C. To prevent degradation, all the rheological experiments were performed under the protection of nitrogen blanket.

4.3 Results and Discussion

4.3.1 Microstructure

The angular dependence of the scattering intensity is shown in Figure 4.2 for pure Na^+ montmorillonite (a), Cloisite 6A (b), Cloisite 15A (c), and Cloisite 20A (d). The variation in the interlayer spacing of each sample is determined from the angular location of the peaks and Bragg's formula, $n\lambda = 2d \sin\theta$ (where n = 1). The org–MMT 6A shows three distinct peaks at 2θ = 2.6°, 4.7°, and 7.4° corresponding to interlayer spacings of 3.3, 1.8, and 1.2 nm, respectively. It can be noted that Na^+ montmorillonite exhibits a single peak at a 2θ value of about 7.8º corresponding to a basal spacing of about 1.1 nm. The gallery height of org–MMT 6A has increased by about 2.2 nm as is evident from its d_{001} peak. This finite expansion in the gallery height is associated with the organic treatment of the clay using DMDHT. A similar observation can be made in case of diffractograms c and d for Cloisite 15A and Cloisite 20 A, respectively. Clay 15A shows 3 distinct peaks at 2θ values of 2.7, 4.3 and 7.2º corresponding to respective

interlayer spacing of 3.2, 2.0, and 1.2 nm. Thus as compared to Na^+ montmorillonite the increase in the gallery height for clay 15A is 2.1nm. Diffractogram (d) corresponding to clay 20A shows two distinct Bragg's peaks at 2θ values of 3.8 and 7.3º with respective d–spacings of 2.3 and 1.1 nm. Hence, clay 20A shows increase in the gallery height of 1.2 nm as compared to Na^+ montmorillonite. The important point to be noted from the WAXD patterns in Figure 4.2 is that although the type of organic modifier used to increase the wettability of Na^+ montmorillonite is the same viz. DMDHT, still the increase in the gallery heights for these clays differs. These results correspond with the change in the modifier concentration of the clays. Org–MMT 6A, which has the highest values of modifier concentration (47 %) has shown the largest increase in the intergallery spacing of the clay. On the other hand, 20A, which has a modifier concentration of 38 %, shows the least increase in the gallery height.

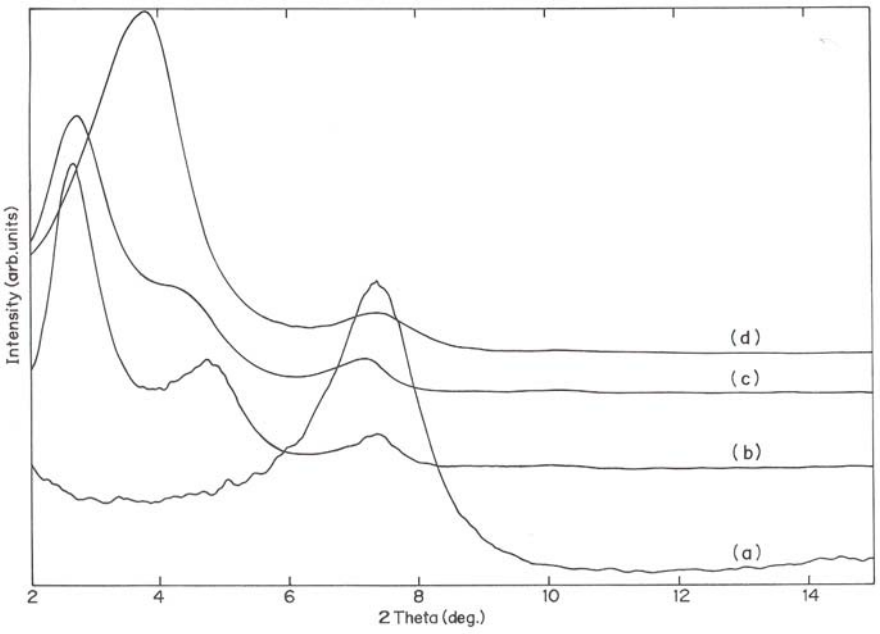

Figure 4.2 X–ray diffraction data for clay and organically modified clays (a) Na^+ montmorillonite, (b) 6A, (c) 15A, and (d) 20A

Similarly the angular dependence of the scattering intensity is shown in Figure 4.3 for pure Na^+ montmorillonite (a), Cloisite 10A (b), Cloisite 93A (c), and Cloisite 30B (d).

The d_{001} peak can be observed at 2θ values of 4.5, 3.6, and 4.8º corresponding to an interlayer distance of 1.9, 2.4, and 1.8 nm, for Clays 10A, 93A and 30B, respectively. The increase in the d spacing by 0.8, 1.3, and 0.7 nm for org-MMTs 10A, 93A and 30B may be attributed to their respective organic treatments.

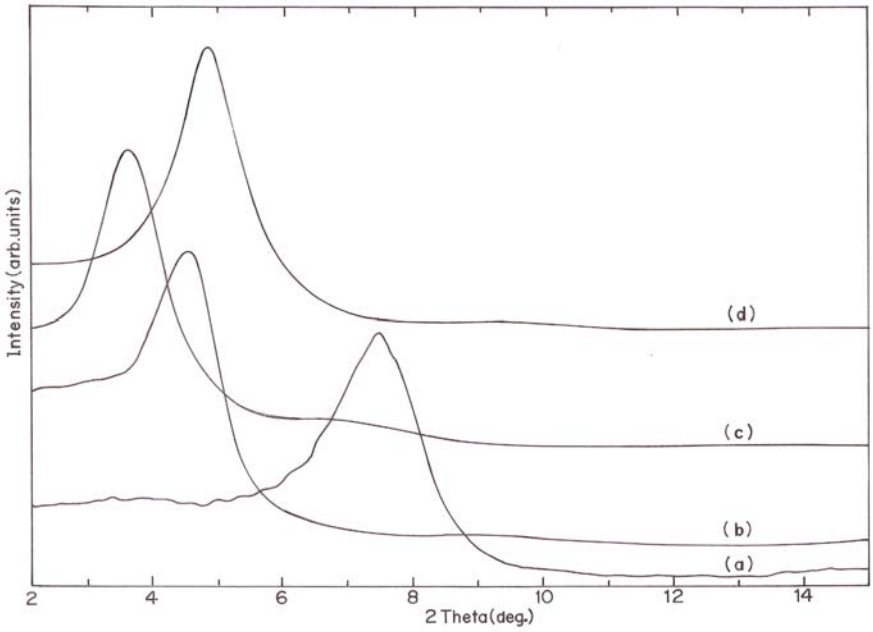

Figure 4.3 X-ray diffraction data for clay and organically modified clays (a) Na^+ montmorillonite, (b) 10A, (c) 93A, and (d) 30B

4.3.1.1 Effect of Concentration of the Intercalant Molecule

The WAXD pattern of PETG6A and org–MMT 6A is presented in Figure 4.4. The nanocomposite shows a slight increase in the gallery height from 3.3 to 3.5 nm as compared to org–MMT 6A. This increase of 0.2 nm can be attributed to the intercalation of the polymer in the silicate layers of 6A. Similar trends are observed in Figure 4.5 and Figure 4.6 where the gallery heights of PETG15A and PETG20A have increased from 3.2 to 3.6 nm and 2.3 to 3.6 nm, respectively. Thus, the PETG15A shows an increment in the gallery height of 0.4 nm while the increase in the interlayer spacing for PETG20A nanocomposite is 1.3 nm, as compared to org–MMTs 15A and 20A, respectively.

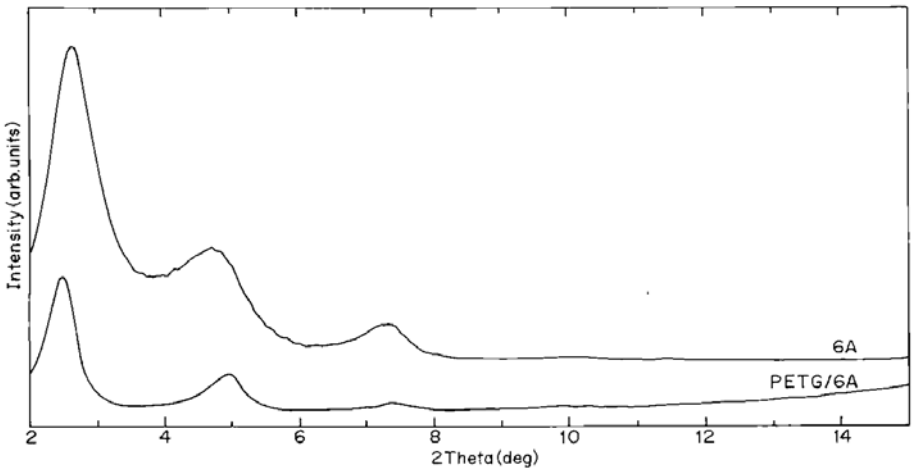

Figure 4.4 WAXD pattern of org–MMT 6A and PETG6A

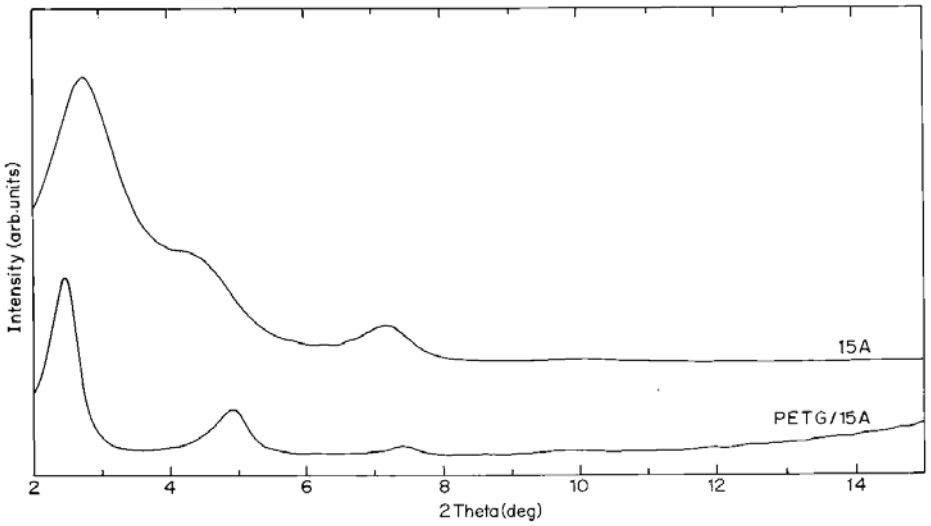

Figure 4.5 WAXD pattern of org–MMT15A and PETG15A

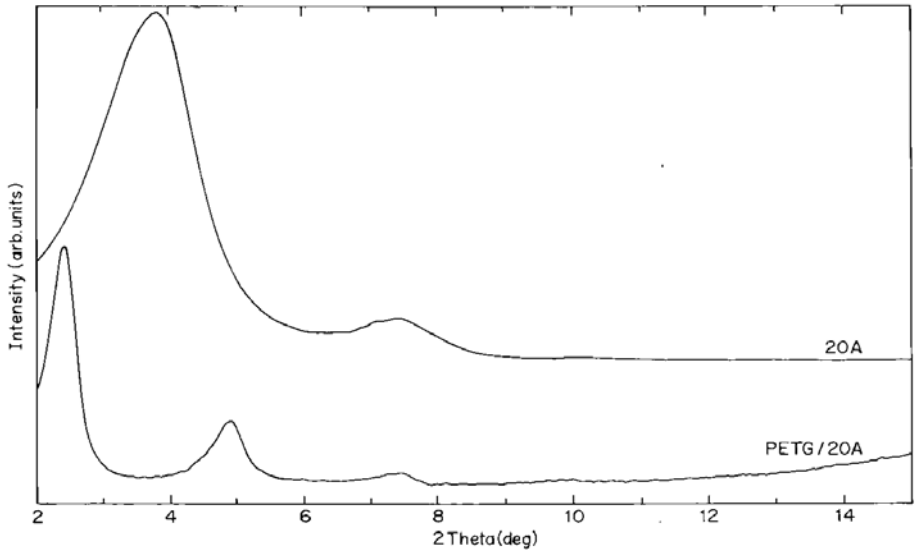

Figure 4.6 WAXD pattern of org–MMT 20A and PETG20A

The d–spacings of the org–MMTs (d_c), those after PETG intercalation (d_{nc}), and the subsequent increase in the interlayer spacing measured using WAXD are summarized in Figure 4.7. The most interesting observation that can be made from the WAXD results is that the trend followed for the nanocomposites is in sharp contrast to that of the org-MMTs. It is expected that org–MMT 6A, which showed highest increase in the interlayer spacing after modification with the tallow compound, should be more organophilic and allow more PETG chains to enter the silicate layers. Thus, PETG6A nanocomposite should show the maximum increase in d–spacing as compared to PETG15A and PETG20A nanocomposites. However, we found that the picture is quite opposite, with PETG20A nanocomposite showing the maximum increase in the interlayer spacing. This could be an effect of the packing density of the modifier in the various org–MMTs, which controls the infiltration of PETG chains in between the clay layers.

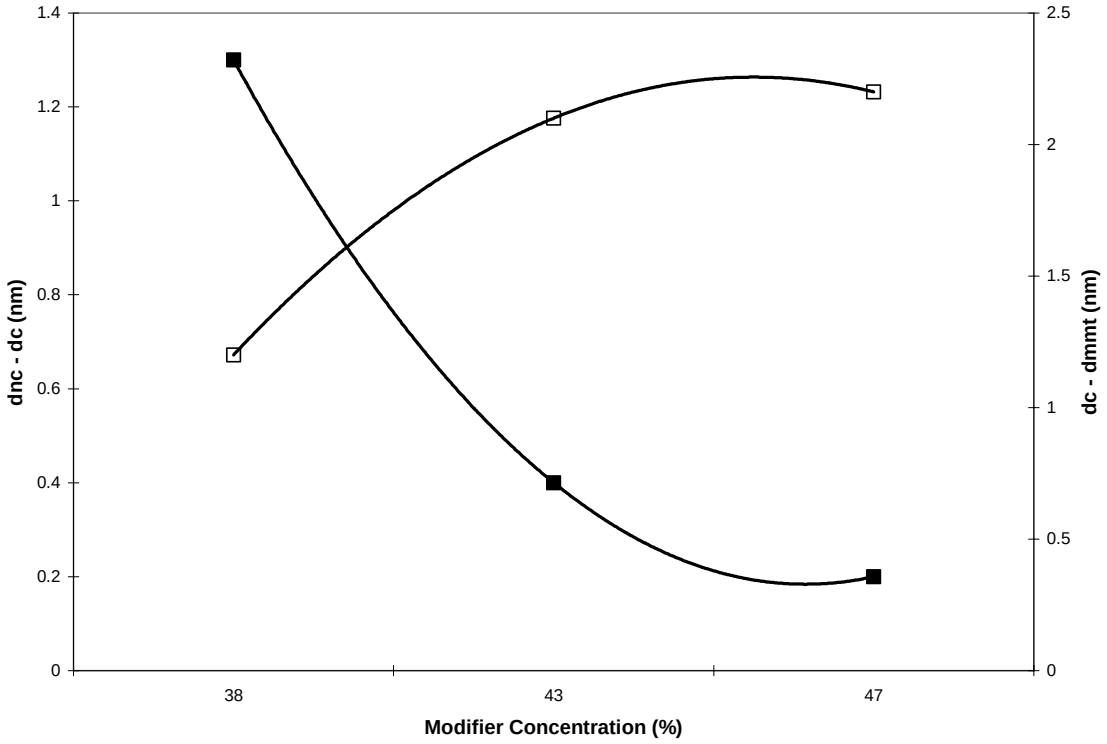

Figure 4.7 A comparison of the increase in interlayer spacing of the org–MMT and that after the formation of the nanocomposites as a function of modifier concentration in the clay. (□) org–MMTs; (■) nanocomposites

The reason for this phenomenon can be explained by considering the thermodynamics of the formation of an intercalated polymer hybrid and the effect of modifier concentration in the clay interlayer. During the process of intercalation, the polymer chains penetrating the clay layers have to overcome a large entropy barrier as a result of the closely packed clay layers. The entropy barrier can be lowered by favorable enthalpic contributions that are possible by modification of the clay using suitable organic moieties such that the polymer–clay interactions are more favorable than the clay–surfactant interactions. Increasing the modifier concentration of the surfactant leads to a more efficient packing and increased interchain contact between the modifier chains resulting in more cohesive van der Waals interactions between the chains and thus giving the interlayer a greater solid–like character. Thus, as the modifier concentration in the clay interlayer increases, making it more dense and reducing the polymer–clay

interactions, it becomes harder for the free polymer chains to infiltrate the clay gallery space.

These qualitative arguments indicate that formation of an intercalated nanocomposite will be favored in systems, which contain org–MMTs with a modifier concentration that is thermodynamically favorable to compensate the loss in conformational entropy by enthalpic gains when it comes in contact with the polymer chain. This is in agreement with the experimental results for the nanocomposites in Table 4.3. The mean field lattice based model developed by Vaia and Giannelis,[1,2] and the self-consistent field theory calculations for interactions between polymers and clay surfaces by Balazs et. al.[3] describe in detail the thermodynamic principals involved in separation of the silicate layers and the infiltration of the polymer chains in between them to form an intercalated hybrid.

Table 4.3 Org–MMT Series Modified using DMDHT

Org–MMT	Modifier Concentration (%)	Effective Concentration of Inorganic Matter [a] (%)	d_{001} (nm)
6A	47	2.65	3.3
15A	43	2.85	3.2
20A	38	3.10	2.3

[a] Effective concentration of Inorganic Matter in the clays is calculated considering 5 wt% clay has been used in each composition

The PETG nanocomposites studied above can be best described as intercalated nanocomposites. Transmission electron microscopy of these nanocomposites confirmed the dispersion of the clay platelets in the PETG matrix. TEM images of PETG6A, PETG15A and PETG20A images at two different magnifications are shown in Figure 4.8. The images clearly show well dispersed clay tactoids throughout the PETG matrix. Furthermore, PETG20A shows a much better dispersion as compared to PETG6A and PETG15A.

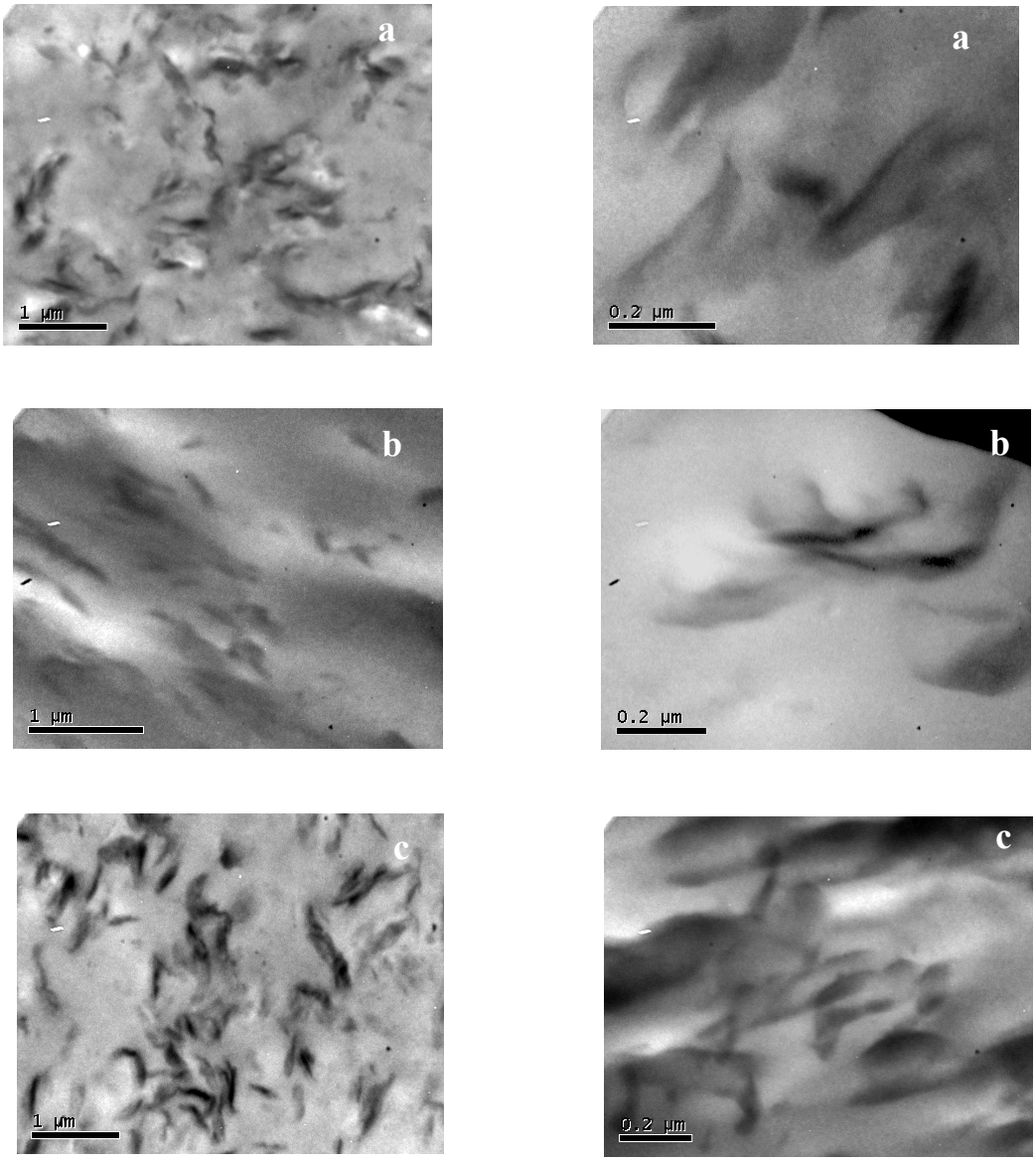

Figure 4.8 Typical TEM images of PETG/clay nanocomposite showing well dispersed clay tactoids throughout the polymer matrix. (a) PETG6A, (b) PETG15A, and (c) PETG20A

4.3.1.2 Effect of Size of the Intercalant Molecule

In Figure 4.9 we compare the angular dependence of the scattering intensity of two nanocomposites viz. PETG10A and PETG15A for the effect of the molecular size of the organic modifier used to increase the wetability of the layered silicate. Both the clays

have a same CEC value of 125 meq/100 g. Hence if an difference is observed in the WAXD data of these two nanocomposites it would be only as a result of the molecular size of the organic modifier used in the particular case.

Both the nanocomposites showed an intercalated structure as was evident from the WAXD data. The d_{001} reflection of PETG10A nanocomposite was placed at a 2θ value of 2.4 ° corresponding to a basal spacing of 3.6 nm. Thus in the nanocomposite the interlayer spacing of org–MMT 10A has increased from 1.9 nm to 3.6 nm. This increase of 1.7 nm can be attributed to the intercalation of the polymer in the silicate layers of org-MMT 10A. A similar trend is observed for the PETG15A, which also shows the d_{001} reflection at $2\theta = 2.4$ ° and a gallery height of 3.6 nm. However, when we compare the increase in the interlayer spacing of org–MMT 15A it can be seen that it has increased from 3.2 to 3.6 nm in case of the nanocomposite, i.e. an increment of 0.4 nm. This difference observed in Δd (see Table 4.2) of the two nanocomposites can be due to different amounts of polymer entering the clay interlayer. We can explain this trend considering the molecular size of the intercalants used in these two nanocomposites. The intercalant in org-MMT 10A has only one 18-numbered hydrocarbon chain, while org–MMT 15A has two 18–member hydrocarbon chains. The bulkiness of the intercalant in 15A as compared to that in 10A is evident from the WAXD data. While org–MMT 15A shows an initial gallery height of 3.2 nm, org–MMT 10A shows 1.9 nm. Thus, the packing density of the organic modifier in case of 15A is higher than that of 10A, thus facilitating less number of polymer chains to infiltrate the clay gallery space. Due to this, we find that although considering the initial interlayer distances in the two layered silicates, one would expect that the nanocomposite PETG15A should show a higher d_{001} reflection than PETG10A nanocomposite, the behavior observed for these two systems is exactly the opposite, and is governed by the difference in the molecular size of the intercalants.

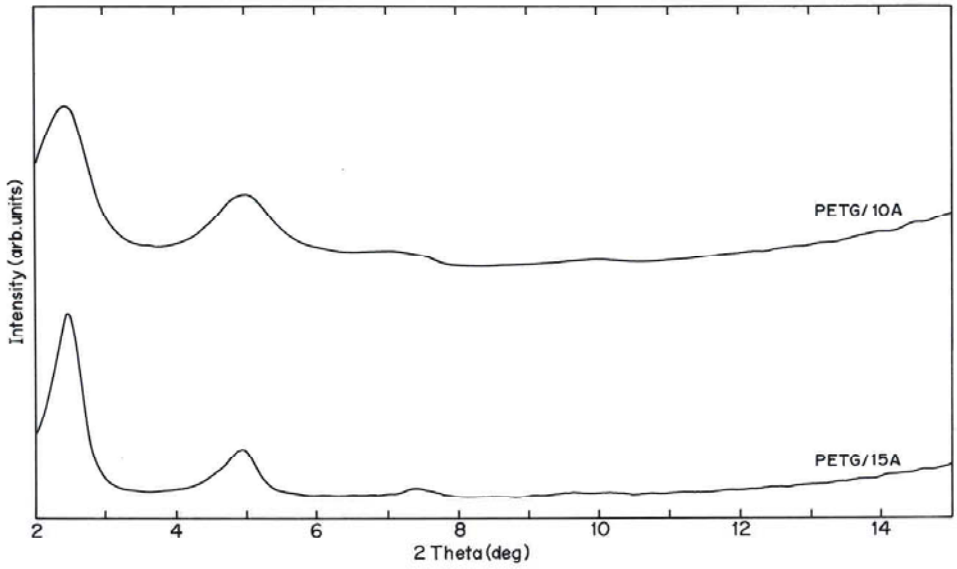

Figure 4.9 WAXD pattern of PETG/10A and PETG/15A

4.3.1.3 Effect of Structure of the Intercalant Molecule

To consider the effect of the molecular structure of the intercalant on the nano-structure of the nanocomposite we prepared two nanocomposites using two different layered silicates containing organic modifiers, which differed in their functionalities. To ensure that the only varying parameter between the two nanocomposites is the functional group in the intercalant molecule we kept remaining parameters the same, including the polymer to layered silicate wt/wt ratio (95/5) and CEC of both the layered silicates (93A and 30B = 90 meq/100g) used. Now we could elucidate the effect of hydroxyl groups on the structure of the nanocomposites. In Figure 4.10 we show the WAXD patterns of these two nanocomposites viz. PETG/93A and PETG/30B. It can be observed from the Figure that PETG93A shows a d_{001} peak at $2\theta = 2.6$ °, corresponding to a basal spacing of 3.3 nm, while PETG/30B showed a d_{001} peak at $2\theta = 2.3$ °, which corresponds to a interlayer spacing of 3.8 nm. If we consider the initial d–spacings of pristine clays 93A and 30B (see Table 4.2), we find that the nanocomposites show respective Δd values of 0.9 nm and 2.0 nm. These results imply that, although layered silicate 30B had a narrower interlayer spacing, more PETG chains infiltrated the gallery space of layered silicate 30B in nanocomposite PETG30B as compared to the amount of PETG chains infiltrating the

gallery space of layered silicate 93A in nanocomposite PETG93A. This increase in the number of polymer chains infiltrating the gallery spaces of the layered silicate can be attributed to the presence of some specific interactions between intercalant functional groups and the functional groups present in the polymer. In the case of PETG30B, nanocomposite there is a strong possibility of formation of hydrogen bonding between the hydroxyls of the intercalant in layered silicate 30B and the carbonyls present in PETG. This hydrogen bond formation facilitates an increased amount of polymer chains to diffuse into the gallery space of the clay. A similar observation was made by Lee et. al. for poly(styrene–co–acrylonitrile)/clay nanocomposites.[4] This type of specific interaction is absent in case of PETG93A nanocomposite. Thus, the amount of polymer molecules diffusing into the interlayer space of the layered silicate 93A is less as compared to those in PETG30B nanocomposites.

On the basis WAXD results, it can be said that the formation of a better-intercalated structure is critically governed by the molecular size and the molecular structure of the intercalant used to increase the wetability of the layered silicate. In the following discussion, we will show how the size and structure of the intercalant molecule plays a critical role in defining the dynamic mechanical properties of polymer/clay nanocomposites.

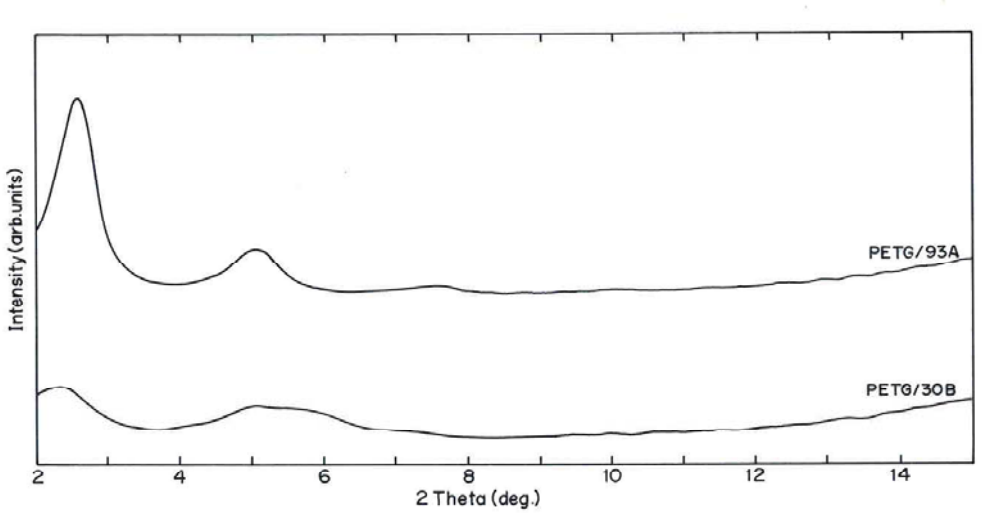

Figure 4.10 WAXD pattern of PETG/93A and PETG/30B

4.3.2 Solid–State Viscoelastic Properties

To obtain an understanding of the viscoelastic properties of PETG/layered silicate nanocomposites and the role of molecular size and molecular structure of the intercalant on them, we perform dynamic mechanical experiments over a temperature range on compression-molded samples. It is now a widely accepted fact that an intercalated nanocomposite shows superior mechanical properties as compared to those of the matrix polymer. All the nanocomposites in this work show an increase in the storage modulus as compared to that of the pristine polymer over the entire temperature range studied (except in the transition region from 68–78 °C), thus following the trend of our earlier studies on PP/clay nanocomposites.[5,6]

Melt processing and montmorillonite are both known to cause molecular weight degradation in polyesters.[7] Therefore, to be certain that our mechanical property results are not compromised by the degradation factor we used melt processed PETG samples as reference. This enabled us to compare the properties of the polymer with its nanocomposites because now both the matrix polymer and the nanocomposites possess similar thermal histories. Some amount of molecular weight degradation might have occurred in PETG/layered silicate nanocomposites as a result of the use of montmorillonite clay. However, when we consider the magnitude of increase in the modulus of PETG after addition of the org–MMT, we can safely deduce that any undesirable deterioration of the dynamic mechanical properties of these nanocomposites has been accounted for by the addition of the nano-clay. Chisholm et. al. have made a similar observation for sulfonated poly(butylene terephthalate)/clay nanocomposites.[8]

4.3.2.1 Effect of Concentration of the Intercalant Molecule

The storage modulus (E') of PETG/layered silicate nanocomposites with clays 6A, 15A, and 20A as a function of temperature is shown in Figure 4.11. The DMTA data shows that the values of storage modulus in the sub–glass regime for all the nanocomposites are almost the same, with an increase of approximately 35 % over that of the pristine polymer. One of the possibilities for no change in the in sub–T_g modulus can be the expelling of the excess surfactant from the clay gallery during extrusion. A similar observation was made by Fornes et. al. from their static mechanical data.[9] If this is the

case, then the amount of polymer entering the gallery space of the clay in these nanocomposites will be the same and thus there would be hardly any difference observed in their mechanical properties. However, from Figure 4.11 a very interesting picture emerges from the storage modulus values in the rubbery plateau. Not only is the increase in the E' values of the nanocomposite much higher than that in the glassy plateau, but also the order of increase varies with the type of org–MMT used. This is possible only if different amounts of polymer had penetrated the clay gallery space. The more polymer present in the constrained gallery space of the clay, the higher will be the modulus of the nanocomposite. These results strongly suggest that the PETG20A nanocomposite, which has the lowest modifier concentration, allowed more polymer chains to infiltrate the clay gallery space as compared to PETG6A nanocomposite. If the excess modifier concentration in 6A clay was expelled from the org–MMT galleries during extrusion this would not have been the case. This indicates that, in contrast to the rubbery regime, the increase in the sub–T_g modulus is more a filler effect. The effective inorganic content in the nanocomposites is around 2.65 to 3.1 %, (see Table 4.3) and hence comparable modulus values are obtained. The nanoscale reinforcement of the clay is more evident in the rubbery regime.

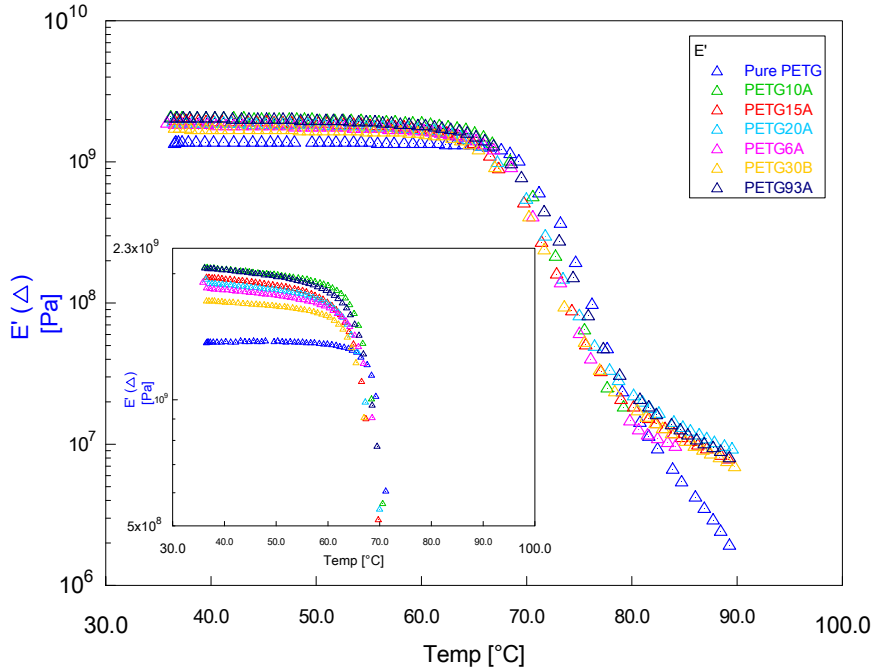

Figure 4.11 Temperature dependence of the storage modulus (E′) for PETG and PETG/layered silicate nanocomposites

To further elucidate the effectiveness of the clay as a reinforcement agent we express the storage modulus of the nanocomposite as relative modulus (E'_r), which is expressed as the ratio of the modulus of the nanocomposite (E'_{nc}) to the modulus of the pristine polymer (E'_p). Table 4.4 represents E'_r at two temperatures. At temperatures above T_g of the polymer, E'_r increases significantly with decreasing modifier concentration of the org-MMTs (1.77 for PETG6A, 2.04 for PETG15A and 2.43 for PETG20A, corresponding to a respective increase of modulus by 77 %, 104 % and 143 % with respect to the pristine polymer). This higher modulus in the rubbery region may be attributed to the reinforcing effect of the clay. Typically, nanofillers have a large effect in raising the modulus above T_g than below it.[10] The main reason for this is the larger relative modulus (E'_r) of the components when the polymer is in the rubbery state compared to the rigid glassy state. Halpin–Tsai have derived theoretical equations, which can be used to calculate the modulus of composites containing uniaxially oriented filler particles dispersed in a continuous matrix.[11] In case of composites, which have fillers with platelet shape, these equations predict a strong dependence of the composite's modulus on the aspect ratio of the filler.[12] As more polymer chains enter the clay interlayer, the particle size of the filler decreases, thus increasing the surface area of the clay. This corresponds to increased modulus as the interactions between the polymer chains and the clay particle increases, forming a network like structure. A more detailed discussion on the effect of apparent aspect ratio on the modulus is described in the later part of the chapter.

Table 4.4 E'_r values for compositions at different temperatures

Sample	E'_r	
	40 °C	**85 °C**
PETG6A	1.32	1.77
PETG15A	1.40	2.04
PETG20A	1.36	2.43

Polymer chains confined between the clay layers are immobilized, increasing the effective volume of the filler. Thus, the higher the amount of intercalated polymer the higher will be the effective volume of the filler. This largely affects the hydrodynamic reinforcement of the filler.[13] The higher storage modulus of the nanocomposite of PETG with org–MMT 20A in comparison to that of the nanocomposite with org–MMTs 6A and 15A can be attributed to a greater hydrodynamic reinforcement. Hydrodynamic reinforcement is also dependent on the shape of the filler, and in turn, its surface area. The higher the surface area the higher will be the hydrodynamic reinforcement.

The reinforcement could also be due to the increased apparent aspect ratio of clay layers dispersed in the polymer matrix. The clay particles exist as clusters or aggregates of montmorillonite platelets. The size of the agglomerates ranges from 100–1000 μm. The primary particles are of the size of 1 to 10 μm. The primary particles consist of compact face-to-face stacking of individual silicate layers. These layers are 0.05 to 0.5 μm in diameter and 1 nm thick. During melt intercalation of the organophilic clay in which the layers are separated by the alkyl ammonium ions, these layers are set apart due to the high shear stresses imposed by the polymer melt. As the amount of polymer molecules intercalating the clay interlayer increases the number of primary particles in each aggregate decreases, which results in the decrease in the size of the aggregate. As a result, even though the thickness of the clay platelets increases due to intercalation, the apparent aspect ratio of the particle also increases. The apparent aspect ratio of clay layers in the polymer matrix can be estimated by using the modified Guth's equation.[14] The shape factor, as described by this equation, is the ratio of the longest dimension of the particle to the shortest i.e. the apparent aspect ratio of the filler. The dependence of the dynamic storage modulus on the volume fraction of the filler can be predicted by taking into account the apparent aspect ratio of the filler and is expressed as:

$$E_c = E_m\left(1 + 0.67 f_g v_f + 1.62 f_g^2 v_f^2\right) \qquad (4.1)$$

where E_c is the storage modulus of the composite, E_m is the modulus of the matrix, f_g is the aspect ratio, and v_f is the volume fraction. Figure 4.12 shows the f_g values for the different nanocomposites as a function of modifier concentration. As the modifier concentration decreases the apparent aspect ratio of the filler increases. Thus, org–MMT

20A shows the highest aspect ratio followed by 15A and 6A, respectively. This could be because of greater intercalation of the polymer in the interlayer of org–MMT 20A. The increased apparent aspect ratio of org–MMT 20A and higher amount of polymer intercalation (as evident from the WAXD results) leads to more interaction between the confined polymer and the clay layers generating more hydrodynamic reinforcement and thus increasing the storage modulus of the nanocomposite. The significant improvement in the rubbery plateau modulus of PETG20A as compared to PETG6A confirms the reinforcing effect of org–MMT 20A.[15] As our study focuses on the comparison of nanocomposites using clays that are modified using the same quaternary ammonium moiety which differ in their modifier concentration we can say that these results give clear evidence that increase in the storage modulus of the nanocomposite is directly proportional to the increased intercalation of the polymer chains in the clay layers.

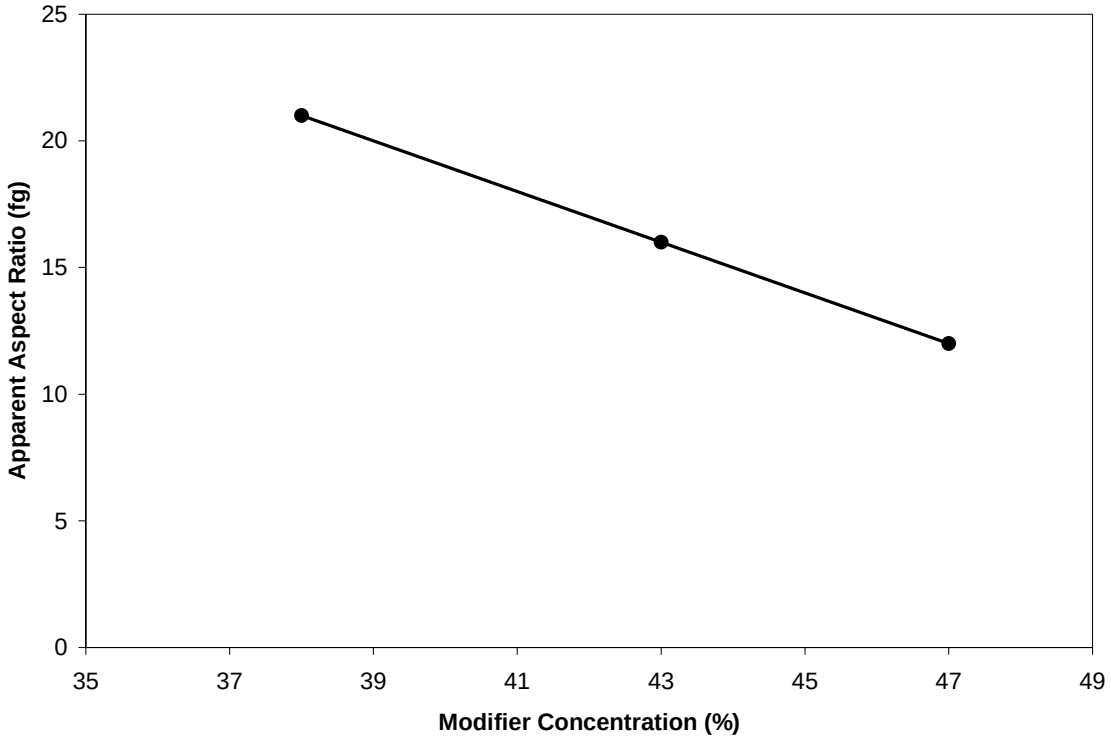

Figure 4.12 Aspect ratio of the filler in the nanocomposite (f_g) as a function of modifier concentration in the clay

The temperature dependence of tan δ of the pristine polymer and its nanocomposites is summarized in Figure 4.13. The values of glass transition temperatures, which were determined from the maximum of the scans of tan δ vs. temperature, are 79 °C for PETG, whereas all the three nanocomposites show T_g at 76 °C. Similar lowering in T_g by about 3 °C was also noted by Chang et. al. for organoclay nanocomposites based on PETN synthesized by a solution intercalation method.[16,17] This lowering of the T_g can be attributed to the plasticizing effect of the low molecular weight DMDHT intercalated in the montmorillonite interlayer. Recently, Lee et. al. reported that reduced T_g in polymer/clay nanocomposites may be due to greatly diminished intermolecular cooperativity.[18] Ideally, a lowering of T_g would lead to an increase in the damping expressed by tan δ. Interestingly, in this work we have observed that even though the nanocomposites show a lower T_g there is a decrease in the damping of the nanocomposites. There could be a plausible hypothesis for this. The interactions that arise between the confined polymer and the clay layers, as explained earlier, could lead to the reduced damping in the nanocomposites. The decrease in the damping may result from reduced friction at the interface between matrix and filler. As the particle size of the filler decreases, its surface area increases, thus more polymer becomes adsorbed onto the filler surface. Adsorption of the polymer onto the clay surface restricts molecular motion, changes the density of the packing of polymer chains, and modifies the conformation and orientation of chain segments in the neighborhood of the surface. Indeed, it has been reported that addition of rigid filler decreases damping.[10] Smaller filler sizes, which are associated with larger surface areas, are more attached to polymer chains leading to reduced internal friction between the polymer and the clay surface, which leads to a decrease in damping.[19] When we compare the three nanocomposites, this fact becomes more evident. PETG20A nanocomposite which showed the maximum Δd (i.e. $d_{nc} - d_c$) and smaller filler size which is evident from higher f_g value (see Figure 4.12) shows the largest decrease in damping followed by PETG15A and PETG6A, respectively. Thus, we can conclude that the higher the concentration of polymer chains present between the clay interlayer the lesser is the internal friction between the polymer chain and modified clay layer, which leads to lesser damping.

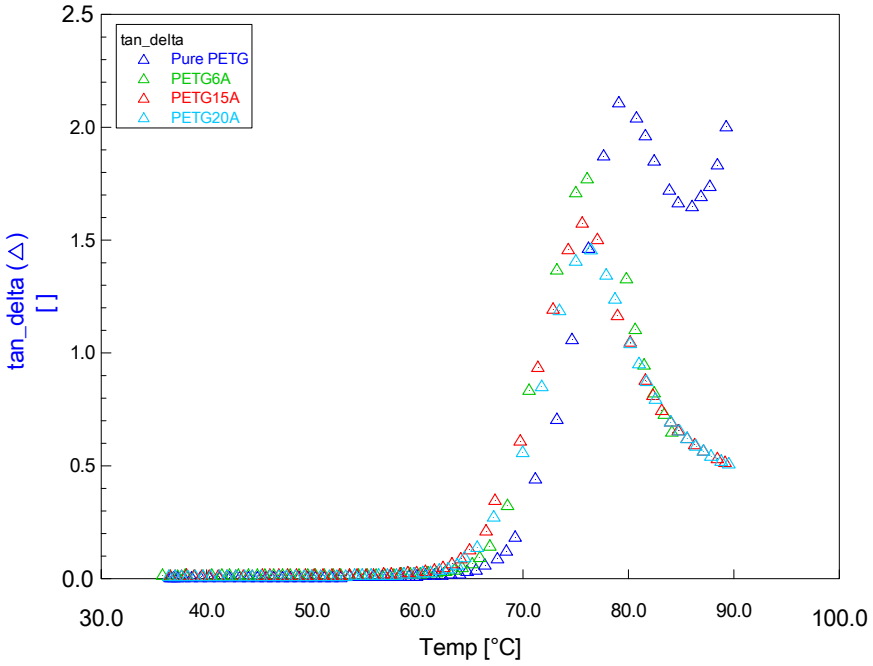

Figure 4.13 Temperature dependence of tan δ for PETG and PETG/clay nanocomposites

4.3.2.2. Effect of Size of the Intercalant Molecule

For the molecular size of the intercalant governing the viscoelastic properties of the nanocomposite, we consider the same pair of nanocomposites, PETG10A and PETG15A as we did in the earlier section. As explained earlier the intercalant molecule in org–MMT 15A is larger in size than that in org–MMT 10A. In Table 4.5, we have shown the relative modulus (E_r') of the nanocomposites at two temperatures one in the sub glassy regime and the other in the rubbery regime. It is observed from Table 4.5 that in the sub–T_g regime the PETG10A and PETG15A nanocomposites show increase of 24 % and 40 %, respectively, over that of pure PETG. This increase may be attributed to the effect of the addition of inorganic filler (effective inorganic matter for PETG10A is 3.05 wt% and that for PETG15A is 2.85 wt%). It is interesting to note that in the rubbery regime the increase in the modulus for the nanocomposites PETG10A shows an increase of 168 %, while PETG15A shows 104 % increase over that of pure PETG. This increase in the rubbery modulus can be explained as follows. Polymer chains in confined environment like that found in clay layers are immobilized, thus increasing the effective volume of the filler. This increase in the filler effective volume is possible when higher

amounts of polymer will enter its gallery space. The hydrodynamic reinforcement of the filler is largely affected by this.[13] Thus, the higher storage modulus of the PETG10A and PETG15A nanocomposites can be attributed to a greater hydrodynamic reinforcement. This difference in the rubbery region storage modulus is a manifestation of the higher Δd value of PETG10A as observed from the WAXD study. Thus, we may attribute this increase in the modulus of PETG10A as compared to PETG15A to the higher amount of polymer chains intercalating the clay gallery.

Table 4.5 E_r' values for comparison at different temperatures one in the sub glassy regime and one in the rubbery regime

Sample	E'_r	
	40 °C	**85 °C**
PETG10A	1.24	2.68
PETG15A	1.40	2.04

4.3.2.3 Effect of Structure of the Intercalant Molecule

Furthermore, to determine the effect of the molecular structure of the intercalant on the viscoelastic properties of PETG/layered silicate nanocomposites we compare E_r' values of PETG93A nanocomposite with those of PETG30B nanocomposites at the same temperatures as in the previous case. These results are shown in Table 4.6. As mentioned earlier the comparison of these two nanocomposites facilitates us to elucidate the effectiveness of hydroxyl groups as an additional contribution. Here we discuss two nanocomposites derived from two different organically modified layered silicates, which differ only in their molecular structure. As observed from Table 4.6 the nanocomposite which is derived from the layered silicate with hydroxyl groups present in the intercalant molecule showed higher E_r' values in both the sub glass and rubbery regimes as compared to the nanocomposite in which the intercalant molecule did not have any hydroxyl groups present in it. As discussed in the WAXD studies the presence of

hydroxyl groups facilitated hydrogen bonding interaction between the hydroxyls of the intercalant molecule and the carbonyls present in the copolyester. These favorable interactions facilitate more polymer chains to penetrate the clay gallery space, which will increase the effective volume of the layered silicate and thus increase its hydrodynamic reinforcement.

Table 4.6 E_r' values for comparison at different temperatures one in the sub glassy regime and one in the rubbery regime

Sample	E'_r	
	40 °C	**85 °C**
PETG93A	1.12	1.91
PETG30B	1.18	2.40

4.3.3 Melt–State Viscoelastic Properties

Linear dynamic oscillatory viscoleastic experiments in melt state were carried out at three different temperatures as mentioned earlier. The rheological behavior followed a similar trend at all the temperatures. For simplicity we present here the data for experiments carried out at 230 °C. The dynamic strain sweeps were first conducted to determine the linear viscoelastic region of the samples.

4.3.3.1 Effect of Concentration of the Intercalant Molecule

The linear rheological data as a function of frequency for pure PETG and PETG/layered silicate nanocomposites containing 5 wt% of 6A, 15A, and 20A are presented in Figure 4.14. It is immediately apparent from Figure 4.14 that the layered silicates have a dramatic effect on the nanocomposite properties as is evident from the storage modulus increase as compared to the pure PETG. Pure PETG shows a liquid like behavior with G'<G″over the entire frequency range studied. Filled polymers normally exhibit a solid–like viscoelastic response with G' >G″ at low frequencies. In an intercalated system this will depend upon the stacks of intercalated silicate layers. In

other words the amount of polymer intercalated in the silicate layers will govern liquid to solid transition in intercalated polymer nanocomposites. As discussed earlier PETG20A nanocomposites have higher amounts of intercalated polymer than that of PETG15A and PETG6A. Thus, the overall effect of the liquid to solid transition will be more in PETG20A as compared to the other two as the number of polymer chains that are in the confined environment, and experience retardation to relaxation, is more than PETG15A and PETG6A. It can be observed from Figure 4.14 that PETG20A show a crossover frequency, ω_c equal to 0.39 rad s^{-1}. Both PETG/15A and PETG6A do not show ω_c over the frequency range studied here. However, note that there is significant reduction in the difference of G' and G″ as compared to pure PETG, i.e. G' and G″ have come closer than in pure PETG.

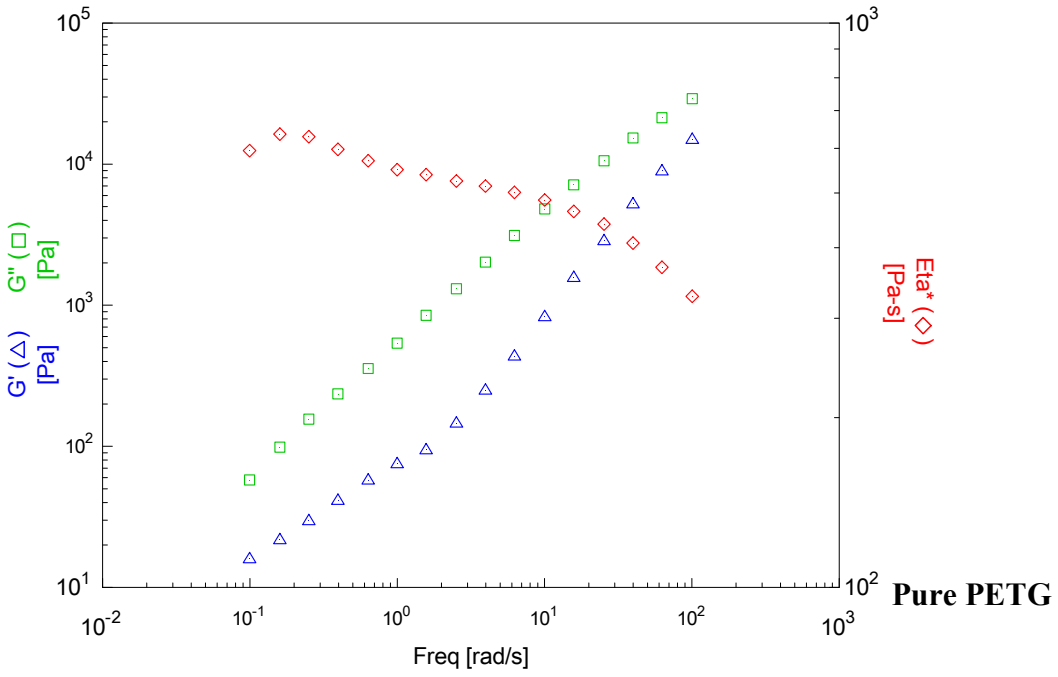

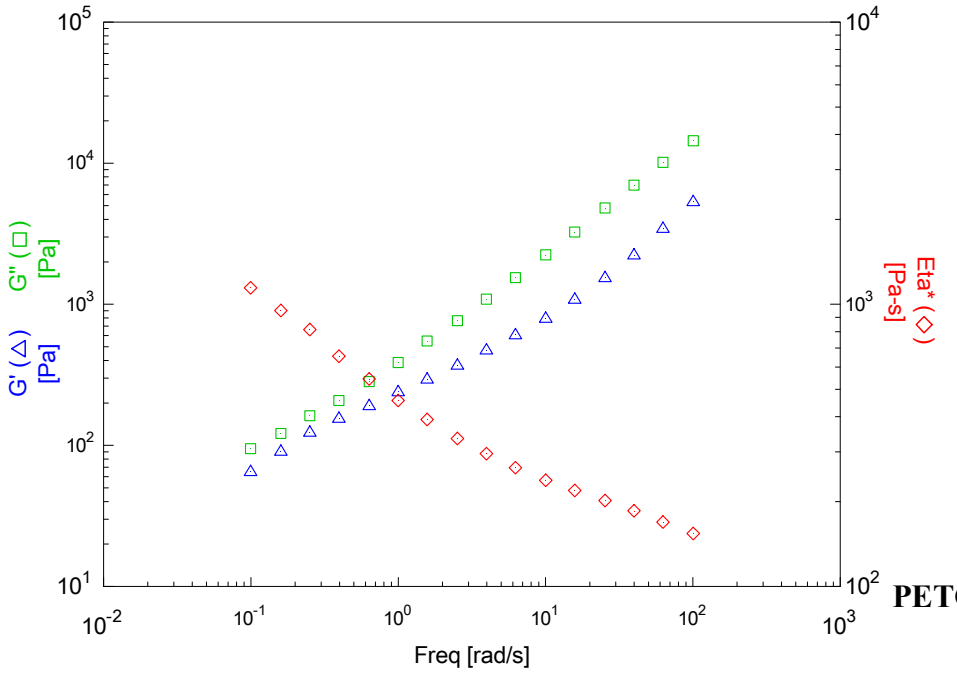

PETG6A

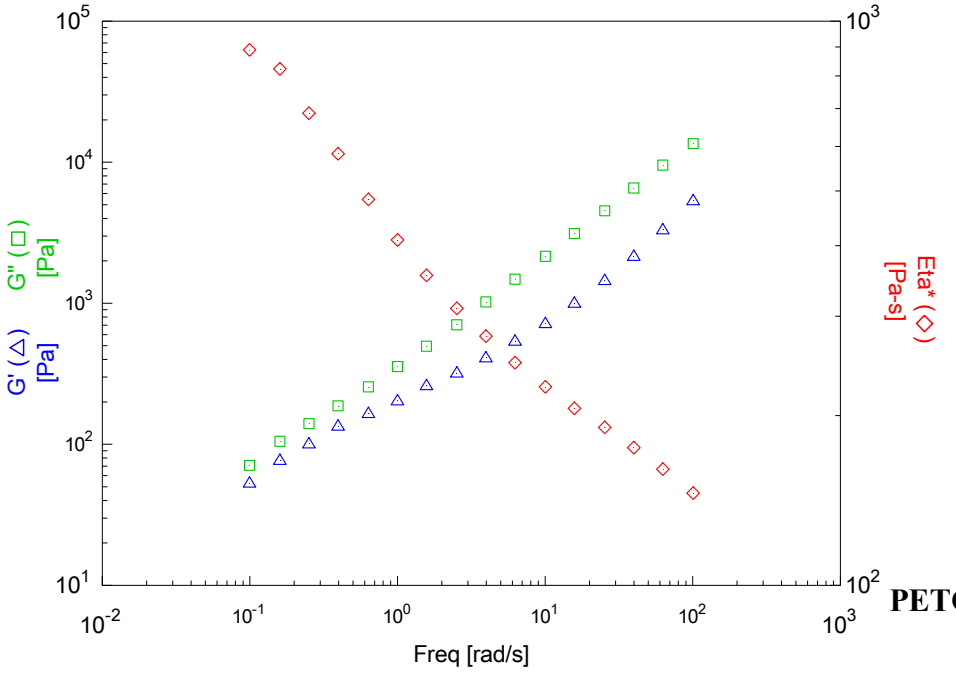

PETG15A

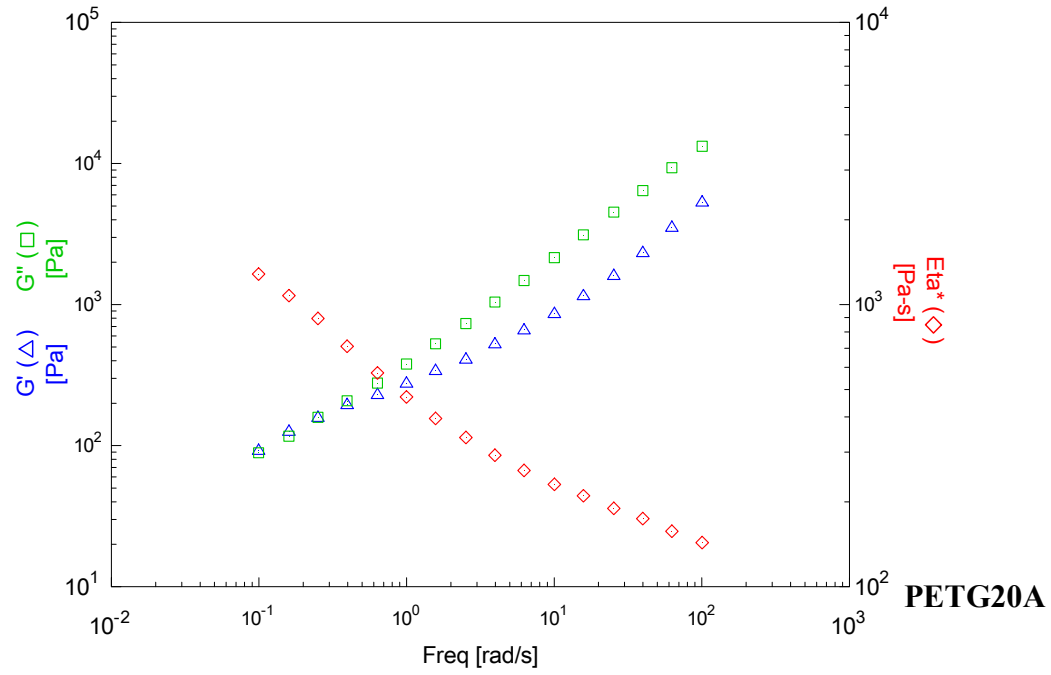

Figure 4.14 Frequency dependence of G', G'', and η^* illustrating effect of concentration of intercalant molecule

Pure PETG shows typical terminal regime, which corresponds to behavior of a Newtonian liquid. However, this terminal behavior goes on reducing from PETG6A to PETG15A and it totally disappears at low frequencies for PETG20A and the dependence of G' and G'' on ω at low frequencies is very weak. This suggests that the polymer chain relaxation in PETG20A is effectively arrested due to polymer chains confined between the silicate layers. A similar effect is observed from PETG6A and PETG15A, which however is less significant than in PETG20A. This difference is attributed to more amounts of polymer chains intercalated in the silicate layers in case of PETG20A.

4.3.3.2 Effect of Size of the Intercalant Molecule

The effect of the size of intercalant molecule is also evident by comparing PETG10A and PETG15A (see Figure 4.15). It is observed that PETG10A shows a clear ω_c at 0.63 rad s^{-1}, whereas, PETG/15A showed a G' and G'' at still lower frequencies (not shown) than those presented here. The shifting of ω_c to higher frequency is a manifestation of more polymer chains present in confined environment. As discussed

earlier org-MMT 10A has only one 18–member hydrocarbon chain, whereas org–MMT 15A has two 18–member hydrocarbon chains. Thus, due to higher effective packing density of org–MMT 15A as compared to org–MMT 10A, less number of PETG chains may `have penetrated the gallery space of the former than the later.

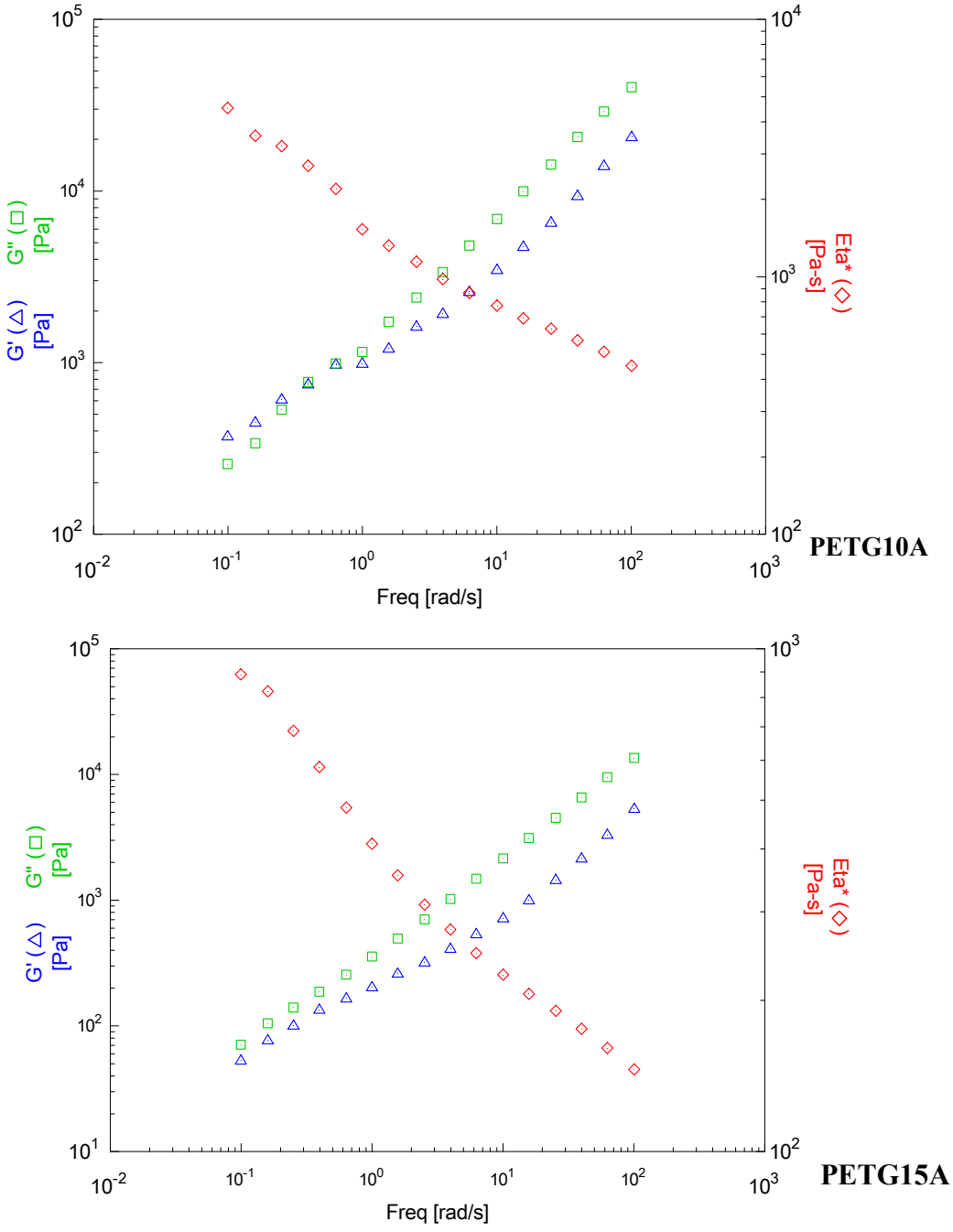

Figure 4.15 Frequency dependence of *G′*, *G″*, and *η illustrating effect of size of intercalant molecule**

4.3.3.3 Effect of Structure of the Intercalant Molecule

A comparison of the linear rheological properties of PETG30B and PETG93A, to study the effect of the structure of the intercalant molecule is shown in Figure 4.15. Better properties of PETG30B as compared to those of PETG93A are immediately apparent from Figure 4.16. PETG30B shows a ω_c value of 1.00 rad s^{-1}, whereas PETG/93A did not show G' and G″ crossover in the frequency range studied. In PETG/30B $G' > G''$ at low frequencies which is indicative of the transformation from liquid like to solid like viscoelastic behavior. From the WAXD and solid–state viscoelastic data presented earlier in the chapter it was shown that, in PETG30B nanocomposite, which is derived from the clay 30B that has hydroxyl groups present in the intercalant molecule, allowed more PETG chains to penetrate the clay gallery space. This is attributed to favorable hydrogen bonding interactions. It is known that the polymer chains in confined environment are unable to completely relax due to geometric constrains. This type of prevented relaxation due to highly geometric constraints of the intercalated silicate layers led to the presence of solid–like behavior as observed in the nanocomposites.[20] The degree of this restricted relaxation was greater in PETG30B nanocomposite because of the higher amount of intercalated polymer chains.

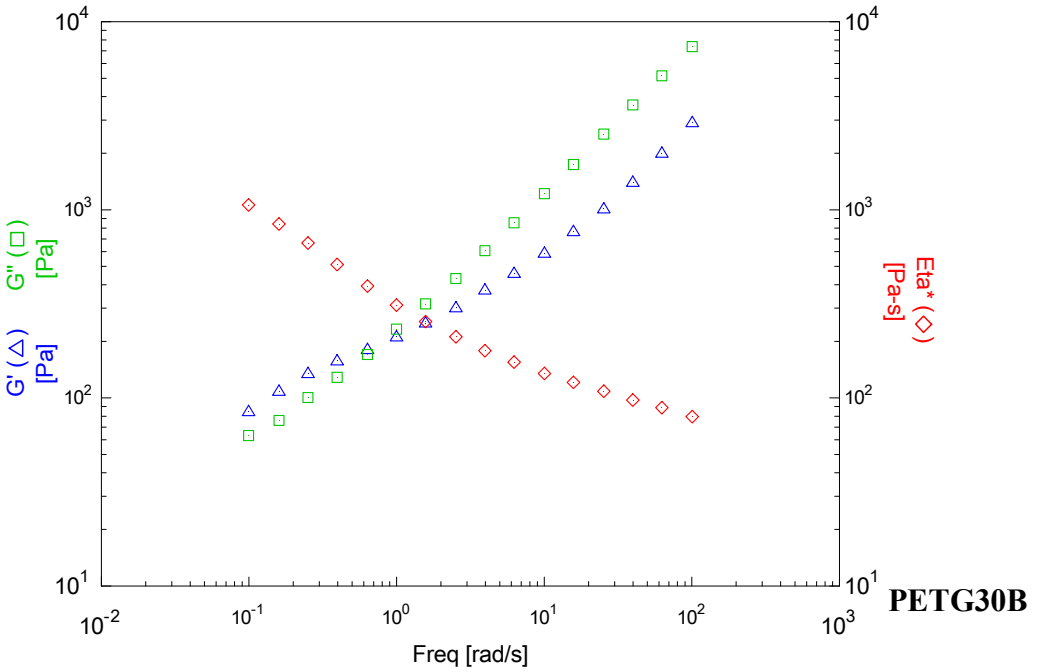

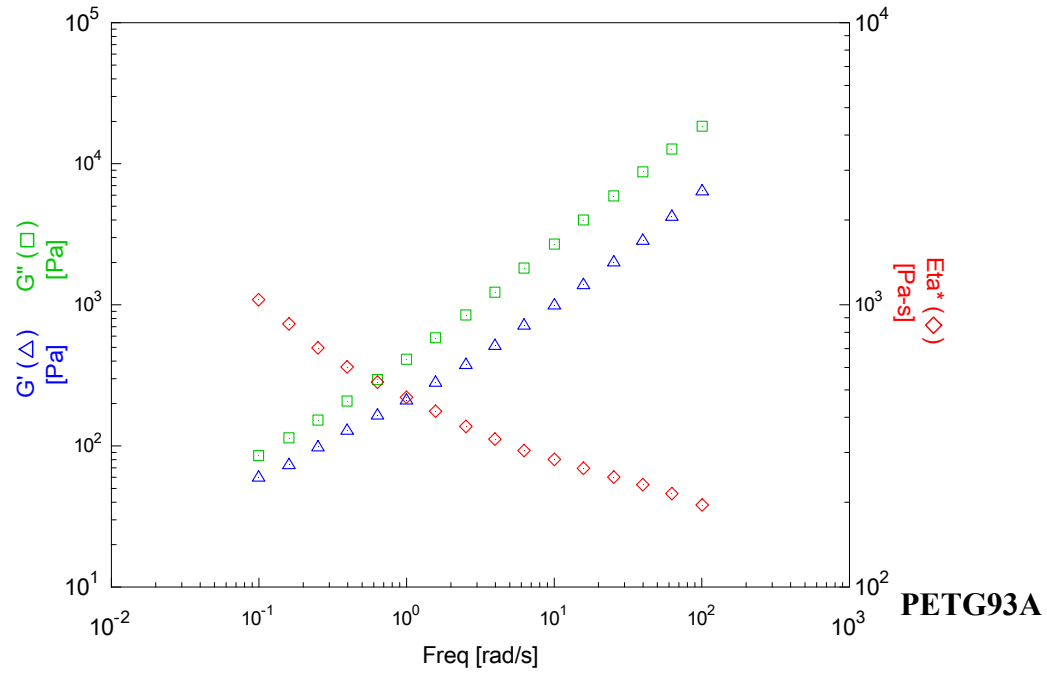

Figure 4.16 Frequency dependence of G', G'', and η^* illustrating effect of structure of intercalant molecule

The dynamic complex viscosity (η^*) for the pure PETG and nanocomposites based on linear dynamic oscillatory shear measurements are also shown in Figures 4.14, 4.15, and 4.16. Pure PETG exhibited almost Newtonian behavior, whereas all nanocomposites exhibited a very strong shear–thinning behavior over the entire frequency range studied. We believe this behavior is as a result of the orientation of the clay particles, which are dispersed in the PETG matrix and is strongly dependent on the shear rate in the dynamic measurements. A more detailed discussion on the rheology of PETG nanocomposites is presented in chapter 6.

4.4 Conclusions

In this chapter, we have demonstrated that the molecular size and the molecular structure of the intercalant molecule in the nanocomposite have a critical role to play in property enhancement of polymer/layered silicate nanocomposites. They govern the extent of intercalation of the polymer in the clay gallery space. It is shown that in nanocomposites derived from layered silicates with larger sized intercalant molecules it is

difficult for the polymer chains to penetrate the clay inter layer as compared to those derived from layered silicates having smaller sized intercalant molecules. We also show that an optimum intercalant concentration is necessary to achieve better intercalation of the polymer chains in the clay interlayer. When organic molecules with hydroxyl functional groups are used as intercalant molecules, higher amount of polymer will infiltrate the clay inter layer in case of polymers, which have functional groups capable of having favorable specific interactions between the intercalant and the polymer. In the present case, hydrogen bonding is formed between the carbonyls of PETG and hydroxyls of org–MMT 30B thus allowing more PETG to enter org–MMT 30B gallery space, as compared to the PETG nanocomposite based on org–MMT 93A in which the hydroxyl groups are absent. We show that the increase in the modulus of the nanocomposite with smaller sized intercalant molecule is greater than that containing a larger sized intercalant molecule. Also, presence of specific interactions between the polymer and the intercalant molecule increases the modulus of the nanocomposite. It is seen that decrease in the T_g of the nanocomposites is rather an effect of plasticization due to the intercalant molecule or reduced intermolecular cooperativity, than as an effect of molecular degradation due to melt processing. It as also observed that the damping decreased which is as a result of confinement of polymer in the clay inter layer. Further it is shown that the amount of polymer present in the confined environment governs the rheological response of the nanocomposite. The liquid–like to solid–like transition in the nanocomposites is strongly dependent of the amount of the intercalated polymer. It is concluded that to achieve better mechanical properties it is necessary to optimize the molecular size and molecular structure of the intercalant used to modify the layered silicate.

REFERENCES

1. R. A. Vaia, E. P. Giannelis, *Macromolecules* **30** 7990 (1997)
2. R. A. Vaia, E. P. Giannelis, *Macromolecules* **30** 8000 (1997)
3. A. C. Balazs, C. Singh, E. Zhulina, *Macromolecules* **31** 8370 (1998)
4. S. Lee, C. Lee, M. Kim, S. Y. Kwak, M. Park, S. Lim, C. R. Choe, J. Kim, *J. Polym. Sci. Part B: Polym. Phys.* **39** 2430 (2001)

5. P. Kodgire, R. A. Kalgaonkar, S. S. Hambir, N. N. Bulakh, J. P. Jog, *J. Appl. Polym. Sci.* **81** 1786 (2001)
6. S. S. Hambir, N. N. Bulakh, P. Kodgire, R. A. Kalgaonkar, J. P. Jog, *J. Polym. Sci. Part B: Polym. Phys.* **39** 446 (2001)
7. J. C. Matayabas, S. R. Turner, Nanocomposite Technology for Enhancing the Gas Barrier of Polyethylene Terephthalate, in: T. J. Pinnavaia, G. W. Beall, (Eds.) Polymer–Clay Nanocomposites, John Wiley & Sons: New York (2000) pp 207 (Chapter 11)
8. B. J. Chisholm, R. B. Moore, G. Barber, F. Khouri, A. Hempstead, M. Larsen, E. Olson, J. Kelley, G. Balch, J. Caraher, *Macromolecules* **35** 5508 (2002)
9. T. D. Fornes, P. J. Yoon, D. L. Hunter, H. Keskkula, D. R. Paul, *Polymer* **43** 5915 (2002)
10. L. E. Nielsen, Mechanical Properties of Polymers and Composites; Marcel Dekker: New York (1974)
11. J. C. Halpin, J. L. Kardos, *Polym. Eng. Sci.* **16** 344 (1976)
12. J. Rexer, E. Anderson, *Polym. Eng. Sci.* **19** 1 (1979)
13. Y. T. Vu, J. E. Mark, L. H. Pham, M. Engelhardt, *J. Appl. Polym. Sci.* **82** 1391 (2001)
14. A. Dufresne, J. Cavaillé, *J. Polym. Sci. Part B: Polym. Phys.* **36** 2211 (1998)
15. L. Priya. J. P. Jog, *J. Polym. Sci. Part B: Polym. Phys.* **40** 1682 (2002)
16. J. Chang, D. Park, *J. Polym. Sci. Part B: Polym. Phys.* **39** 2581 (2001)
17. J. Chang, D. Park, *Polym. Bull.* **47** 191 (2001)
18. Y. –H Lee, A. J. Bur, S. C. Roth, P. R. Start, *Macromolecules* **38** 3828 (2005)
19. N. K. Kalfoglou, *J. Appl. Polym. Sci.* **32** 5247 (1986)
20. B. Hoffman, J. Kressler, G. Stoppelmass, C. Friedrich, G. M. Kim, *Colloid Polym. Sci.* **278** 629 (2000)

CHAPTER 5

PETG20A Nanocomposites

This chapter describes the effect of clay concentration on the structure and properties of PETG/clay nanocomposites prepared using PETG (grade Eastar GN071) and organophilic clay (Cloisite 20A) at different clay loadings. In this study, dynamics of the nanocomposites are investigated over a broad range of temperature and frequency using DRS and DMTA and related to their nanomorphology through WAXD, TEM, and rheology. This chapter also details the effect of processing conditions (nanocomposites prepared at different extruder screw speeds).

5.1 Introduction

We discussed the PETG nanocomposites based on a number of clays and the criteria (with respect to the intercalant used for organically modifying the clay) that affects the properties of these nanocomposites in chapter 4. However, the studies were carried out used only one composition of PETG and clay, viz. 95 : 5 wt % ratio. The concentration of clay or the clay content used in the nanocomposites also governs their property modification. In this chapter we detail the results of our study on the concentration effects of clay content in PETG/Clay nanocomposites. Cloisite 20A (20A) was used for this purpose.

For this study, microstructure of the nanocomposites as WAXD, TEM and rheology is correlated to their dynamics using DMTA and DRS with respect to filler loading. Dynamics of polymer chain relaxation or molecular mobility of polymer main chains and side chains is one of the factors that determine the viscoeleastic properties of polymeric macromolecules. The temperature dependence of molecular mobility is characterized by different transitions in which a certain mode of chain motion occurs.[1] Attempt has been made to fit the data obtained on these nanocomposites using the semi empirical Havriliak–Negami (HN) model. We also discuss the effects of processing conditions on the microstructure and properties of the nanocomposites.

5.2 Experimental

5.2.1 Nanocomposite Fabrication

All the nanocomposites were prepared by melt blending premixed PETG and org–MMT 20A in a co–rotating Berstoff ZE–25 twin screw extruder having screws of 25 mm diameter and L/D ratio of 41.5. Melt compounding was done at 230 °C (temperature profile of the screw increased from 180 °C at the feed to 230 °C near the die). To study the effect of processing parameters PETG20A nanocomposites containing a polymer : clay ratio of 95 : 5 by weight were prepared at varying screw speeds of 100, 200, 300, and 400 rpm. From these results screw speed of 100 rpm was selected for further studies. Four compositions containing 3, 5, 7 and 10 wt% of 20A and coded as PETG20A3, PETG20A5, PETG20A7, and PETG20A10, respectively, were prepared. The

compounded melt was water quenched and pelletized. The pellets were dried in an air circulatory oven at 70 °C for 24 h.

5.2.2 Sample Preparation

Samples of nanocomposite for characterization were prepared by compression molding the extruded pellets at 230 °C in to uniformly thick 0.5 to 1 mm films using a Carver Press model F–15181.

5.2.3 Nanocomposite Characterization

5.2.3.1 Microstructure Characterization

The microstructure of nanocomposites is evaluated by performing wide–angle X–ray Diffraction (WAXD) experiments using a Rigaku model Dmax 2500 X-ray diffractometer. The system consisted of a rotating anode X–ray generator operated at 40 kV and 150 mA and a wide–angle goniometer.

Transmission electron microscopy (TEM) photographs of ultrathin–section PETG20A nanocomposites were taken on a JEOL (JEM 1200 EX) transmission electron microscope with an accelerating voltage of 120 kV.

5.2.3.2 Dynamic Mechanical Thermal Analysis

The dynamic mechanical properties of the samples were studied using Rheometrics dynamic mechanical analyzer, model DMTA IIIE. The samples were analyzed in the tensile mode. To elucidate the solid–state viscoelastic properties, temperature sweep was carried out from 30 to 110 ^{o}C and the sample was heated at a rate of 5 ^{o}C min^{-1}. The frequency was 10 rad s^{-1} and the strain was fixed suitably in the linear region, by carrying out some strain sweep tests and noting that the force lies between the transducer limits. Samples with dimensions of 0.5×6×10 were used. Prior to the tests, all films were dried at least for 6 h in an air circulatory oven at a preset temperature of 70 °C.

5.2.3.3 Dielectric Relaxation Spectroscopy

Dielectric properties of the samples in the film phase were measured using the Novocontrol broadband dielectric spectrometer with the ZGS active sample cell equipped

with temperature controller and WinImp and WinFit software for data analysis. The samples were scanned between frequencies 0.01 Hz and 10 MHz over temperature range of 30 to 120 °C. Bias voltage applied across the sample is 1.0 V. The electrode diameter was 25 mm. Samples having uniform thickness of 0.5 mm were used.

5.2.3.4 Melt Rheology

Dynamic oscillatory frequency sweeps were carried out on a Rheometric Scientific ARES rheometer in the frequency range of 0.01 to 100 rad s^{-1} at 250 ^{o}C. Parallel plate geometry of 25 mm diameter is used for this purpose. The sample specimens having uniform thickness of 1 mm were prepared by compression molding as explained earlier. The strain sweep experiment was carried out to find the region of linear response. The strain was fixed at 1 % ensuring that the measurements are carried out in linear viscoelastic region.

5.3 Results and Discussion

5.3.1 Effect of Processing Conditions

Lot of work on polymer clay nanocomposites has focused on the importance of chemical surface modification of the clay employed (usually montmorillonite) in order to increase the compatibility between the matrix polymer and clay, for the improvement of various properties. Various parameters govern this polymer–clay compatibility, including the organic modifier of the nanoclays, the initial interlayer spacing, the concentration of the organic modifier. In addition to these the operational conditions such as screw configurations of extruders, temperature profile, residence time, rpm, etc. also play a major role in determining the property–performance relationship of nanocomposites. The optimization of operational conditions, which govern the clay dispersion, make the systems, process successfully. In the following the effect of various extruder screw speeds ranging from 100 to 400 rpm on the microstructure and properties of PETG20A5 nanocomposites is discussed.

Figure 5.1 illustrates the WAXD scans for PETG20A nanocomposites prepared by processing at various screw speeds. These results show that an intercalated structure is formed and that the clay still retains an ordered structure after melt compounding.

Further from WAXD curves of PETG20A5 it is observed that the 100 RPM curve shows maximum shift towards lower angles, thereby indicating that the distance between the clay platelets has increased. The results of the nanocomposites analyzed are reported in Table 5.1. Intercalation is dependent on the diffusion time required for the polymer chains to infiltrate the clay gallery space.

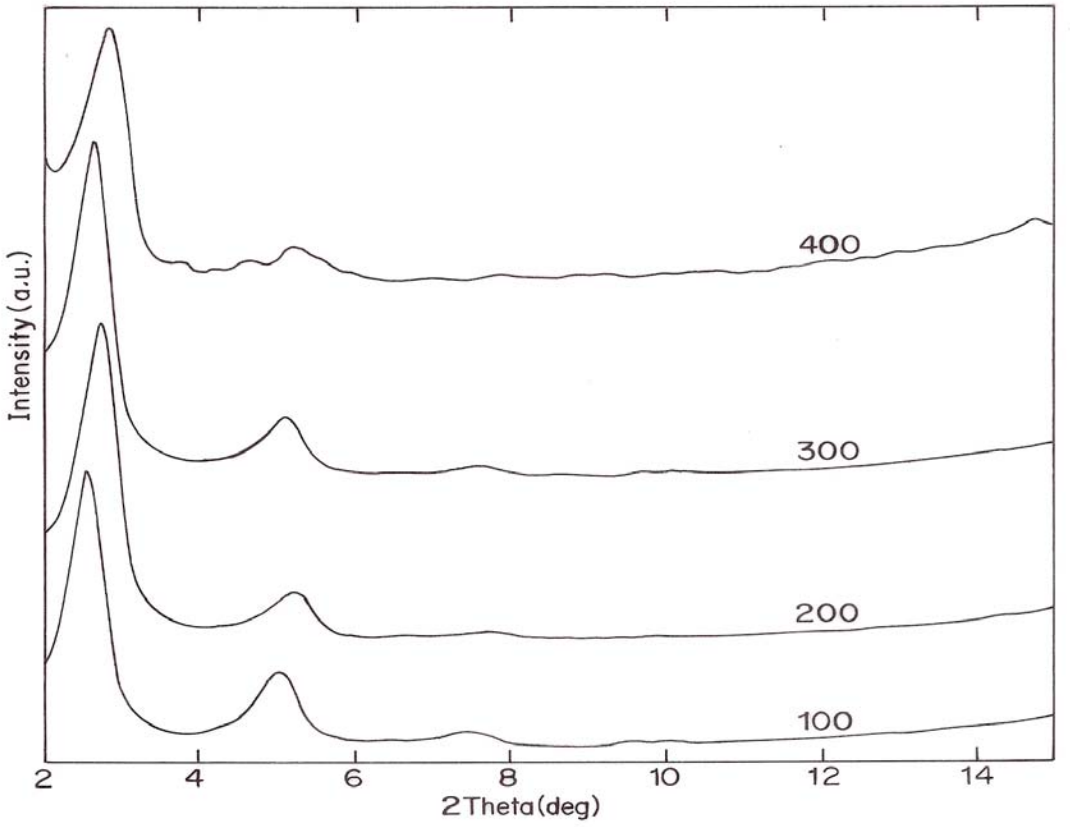

Figure 5.1 WAXD analysis of PETG20A5 nanocomposite processed at various screw speeds (indicated above each scan)

Table 5.1 Interlayer spacing for PETG20A5 nanocomposites processed at various screw speeds

Screw speed (rpm)	100	200	300	400
2θ	2.55	2.75	2.65	2.85
Interlayer spacing (nm)	3.46	3.21	3.33	3.09

In our study it is seen that the nanocomposite obtained by compounding the polymer and clay at 100 rpm shows maximum intercalation. This shows that the short processing time in extrusion is not a limit to achieve a fully intercalated structure. Moreover, it has been reported in the literature that the thermal decomposition of long chain aliphatic quaternary ammonium cations can occur at the processing temperatures equivalent to those used in this study.[2–4] Our results show that this effect is not significantly important in the processing conditions we studied. All the nanocomposites obtained present an interlayer spacing higher than the original 20A clay. This can be explained by the fact that the intercalation process is fast and allows intercalation of the polymer chains in to the silicate galleries within the residence time in the extruder.

Table 5.2 Storage modulus (*E′*) dependence at different temperatures as a function of different screw speeds for PETG20A5 nanocomposites

RPM	Storage Modulus (*E′*) (Pa)	
	70 °C	**100 °C**
100	9.1465×10^{8}	6.7701×10^{6}
200	1.2509×10^{9}	5.9794×10^{6}
300	1.2183×10^{9}	5.5202×10^{6}
400	1.4366×10^{9}	6.3461×10^{6}

Storage modulus (*E′*) dependence at different temperatures as a function of different screw speeds for PETG20A5 nanocomposites is presented in Table 5.2. In the glassy regime the *E′* values for higher screw speed show higher values than that for the nanocomposite processed at 100 rpm. While the picture is reversed in the rubbery regime with PETG20A5 nanocomposite processed at 100 rpm showing higher *E′* values than those observed for the nanocomposites processed at higher screw speeds. As discussed previously in the DMTA section, the reinforcement effect of the nanofiller in a nanocomposite is predominantly observed in the rubbery regime, when the contribution of the bulk matrix towards the stiffness of the nanocomposite is less significant. It is known that increased intercalation of the polymer chains between the silicate galleries

leads to increased aspect ratio of the fillers, thus increasing the storage modulus of the composite.[5,6] From these observations, it is clearly seen that the nanocomposites prepared at 100 rpm show better properties as compared to the rest. Hence, the nanocomposites for further investigations were prepared at 100 rpm.

5.3.2 Transparency Studies

A comparison of the optical clarity of pure PETG, processed PETG, and PETG20A nanocomposites is shown in Figure 5.2. PETG is a material, which possess high optical clarity. On addition of clay this optical clarity is maintained at low clay loadings. However, at higher clay loadings (10 wt%) there is slight decrease in the level of transparency of PETG. Additionally, the nanocomposites develop a distinct color on addition of clay. This color further intensifies with increasing clay content. This color may be due to matrix molecular weight degradation. Paul and coworkers have made similar observations for organoclay nanocomposites based on polycarbonate and nylon–6.[7,8] Note that in spite of development of this color the optical clarity of PETG20A nanocomposites is remarkably high even at higher clay loadings.

Figure 5.2 Comparison of optical clarity of pure PETG, processed PETG, and PETG20A nanocomposites

5.3.3 Matrix Degradation Studies

As reported in chapter 4, melt processing and montmorillonite both cause molecular weight degradation in polyesters.[9] In order to study the matrix degradation PETG20A nanocomposites we measured the inherent viscosities of PETG and PETG20A nanocomposites in a 40 : 60 wt% mixture of 1,1,2,2–tetrachloroethane (TCE) and phenol

at 25 °C using an Ubbelohde viscometer. The inherent viscosity of processed PETG was found to be 0.59 dL/g, which decreased to 0.42 dL/g in PETG20A10. This decrease in the inherent viscosity is due to molecular weight degradation of PETG on addition of clay. However, it is worthwhile mentioning that the viscoelastic and dielectric data obtained for PETG20A nanocomposites clearly indicate significant improvements in properties as compared to pure PETG. Thus, the reinforcement effect of the clay apparently offsets the undesirable property deterioration that would be expected from this molecular weight degradation. Chilsholm and co workers have made similar observations for sulfonated poly(butylenes terephthalate)/clay nanocomposites.[10]

5.3.4 Nanocomposite Microstructure

5.3.4.1 Wide Angle X–ray Diffraction Studies

Wide angle X–ray diffraction (WAXD) gives an idea of the microstructural evolution in polymer clay nanocomposites. Formation of an intercalated or exfoliated hybrid can be elucidated from the diffraction pattern of the nanocomposites. The changes in the WAXD patterns for pristine 20A and PETG20A nanocomposites as a function of different clay loadings are shown in Figure 5.3. The silicate peaks in all compositions of PETG20A nanocomposites shifted to lower 2θ angles. These lower angle clay peaks represent expansion of basal spacing of clay layers in PETG20A nanocomposites. This shift to lower angles and the presence of well defined diffraction peaks in polymer clay nanocomposites is a manifestation of the formation of intercalated structures. The interlayer spacing of each nanocomposite has been determined from the location of the d_{001} basal reflection peaks using the Bragg formula. Pristine 20A shows the d_{001} peak at $2\theta = 3.8°$ corresponding to a basal spacing of 2.3 nm. In all the nanocomposites, the d_{001} peak of the clay shifts to a lower diffraction angle due to intercalation of layered silicates with increasing amount of clay loading. For the PETG20A nanocomposites the calculated inter gallery spacing is approximately 3.4 nm for 3 to 7 wt% clay loading. This independence of gallery height on silicate loading is consistent with the results of Vaia and co workers on model PS based layered silicate nanocomposites.[11,12] Through a simple space filling calculation by assuming the polymer density to be unaffected by confinement and little or no exfoliation of the silicate layers, it was shown that for

nanocomposites with more than 30 % polymer, there exists excess polymer that has not intercalated between the silicate layers. An overall reduction in the intensity of the PETG20A nanocomposites was observed. However, on considering the nanocomposites, the intensity of the d_{001} peak progressively increased with increasing clay loading. This increase in the nanocomposites is related to the increase in concentration of the clay and reflects strong polymer to clay interaction with increasing clay concentration. These changes indicate increase in the coherent order of the clay layers. Furthermore, PETG20A10 shows an inter layer spacing of approximately 3.1 nm. This is expected as in nanocomposites containing higher clay loadings, the tendency of tactoid formation is more as compared to the low clay loading counterparts.[13,14] It may also be noted that presence of higher order peaks in the nanocomposites suggest preservation of long–range order and confirm that these nanocomposites have an ordered structure after melt compounding. The d_{002} peak showed a constant expansion of ~1.7 nm for the compositions up to 7 wt% of clay loading. Table 5.3 summarizes the WAXD results of 20A and PETG20A nanocomposites.

Table 5.3 WAXD data for pristine 20A clay and PETG20A nanocomposites

Sample	2θ (°)	d_{001} (nm)	Δd_{001} (nm)	d_{002} (nm)
20A clay	3.8	2.3	----	1.2
PETG20A3	2.6	3.39	1.09	1.73
PETG20A5	2.55	3.46	1.16	1.74
PETG20A7	2.55	3.46	1.16	1.76
PETG20A10	2.85	3.09	0.79	1.66

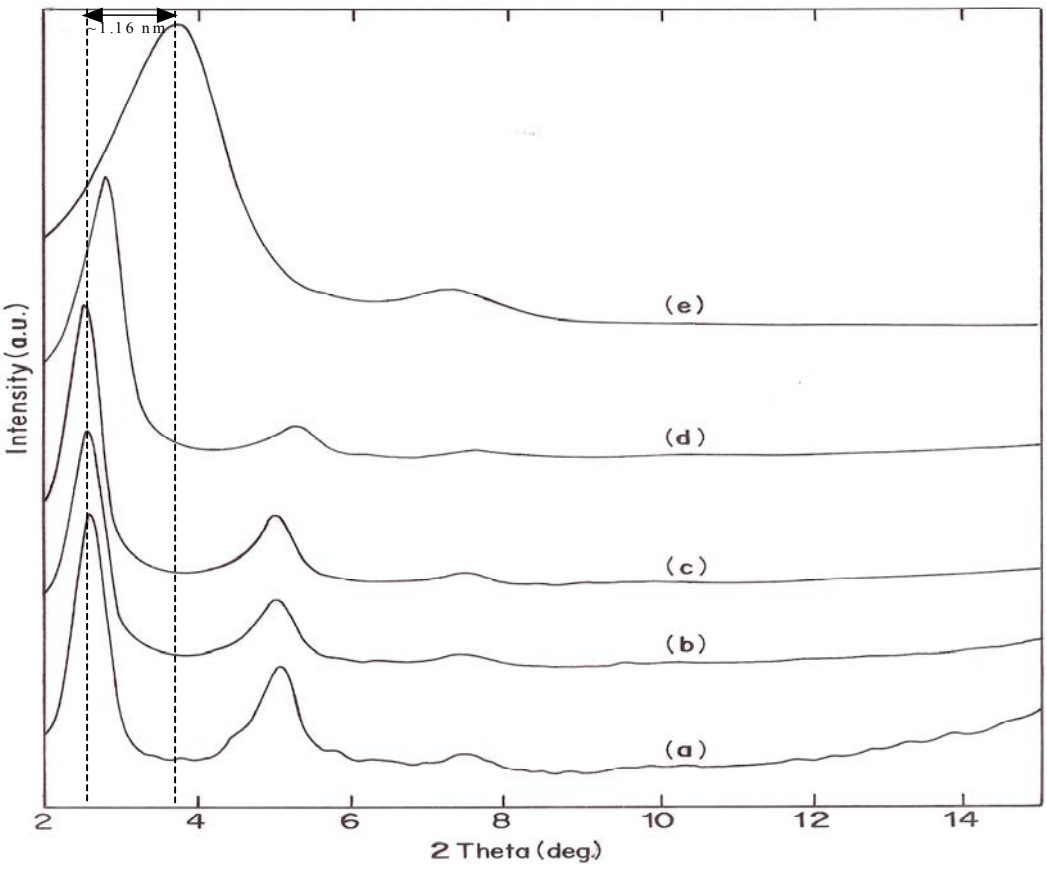

Figure 5.3 Comparison of the WAXD patterns of pristine 20A clay and PETG20A nanocomposites. (a) PETG20A3, (b) PETG20A5, (c) PETG20A7, (d) PETG20A10, (e) pristine 20A

5.3.4.2 Transmission Electron Microscopy

Figure 5.4 represents the TEM images of PETG20A3 and PETG20A10 at two different magnifications in which the dark entities are the cross section of stacked intercalated 20A clay layers and bright area is the PETG matrix. From the TEM image we observe stacked tactoids of clay, which are uniformly distributed in the PETG matrix. Note that the TEM image shows clay tactoids dispersed in the matrix. All the PETG20A nanocomposites studied here possessed an intercalated structure, hence individual clay layers are not observed in the image.

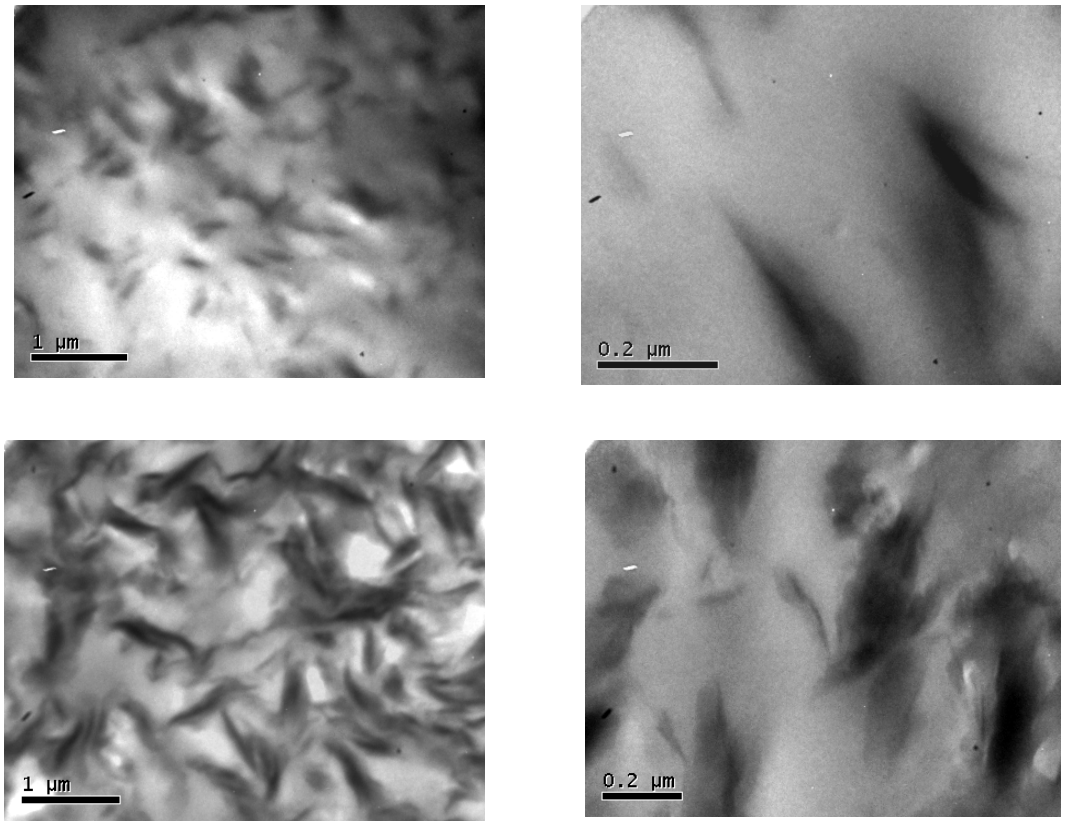

Figure 5.4 TEM images of PETG20A3 (top) and PETG20A10 (bottom) nanocomposite showing well dispersed clay tactoids throughout the PETG matrix

5.3.5 Dynamic Mechanical Thermal Analysis

DMTA was performed on pure PETG and PETG20A nanocomposites in the solid state in order to determine their relaxation properties and investigate how the presence of silicate layers alters the polymer chain mobility. DMTA represents an excellent method of correlating the performance of the nanocomposites and the host matrix with the presence of more or less constrained regions.

5.3.5.1 Modulus

The DMTA data for pure PETG and PETG20A nanocomposites is summarized in Figure 5.5, in which the dynamic storage modulus as a function of temperature is presented. It can be seen that all the nanocomposites show an increased storage modulus than that of the neat polymer (except in the glass–rubber transition region) over the entire

temperature range studied. As discussed in the previous chapter it is known that melt processing and montmorillonite clay may cause some amount of molecular weight degradation in polyesters. This can be clearly seen from Figure 5.6 in which a comparison between as received PETG and melt processed PETG is presented. The melt processed PETG shows lower storage modulus values than those of the as received PETG over the entire temperature range studied. Therefore, to be certain that the mechanical property results are not compromised by the degradation factor, the melt–processed PETG are used as a benchmark for comparison with the nanocomposites as now both the matrix polymer and the nanocomposites posses similar thermal histories. Matrix degradation studies are documented in the later part of the chapter.

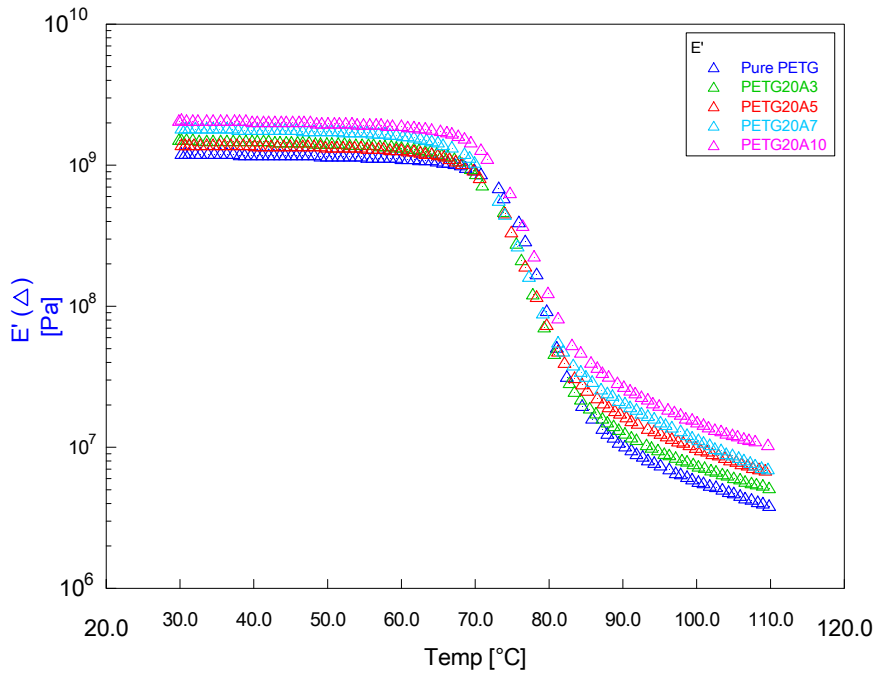

Figure 5.5 Temperature dependence of the dynamic storage modulus (*E′*) of pure PETG and PETG20A nanocomposites at a frequency of 10 rad s^{-1}

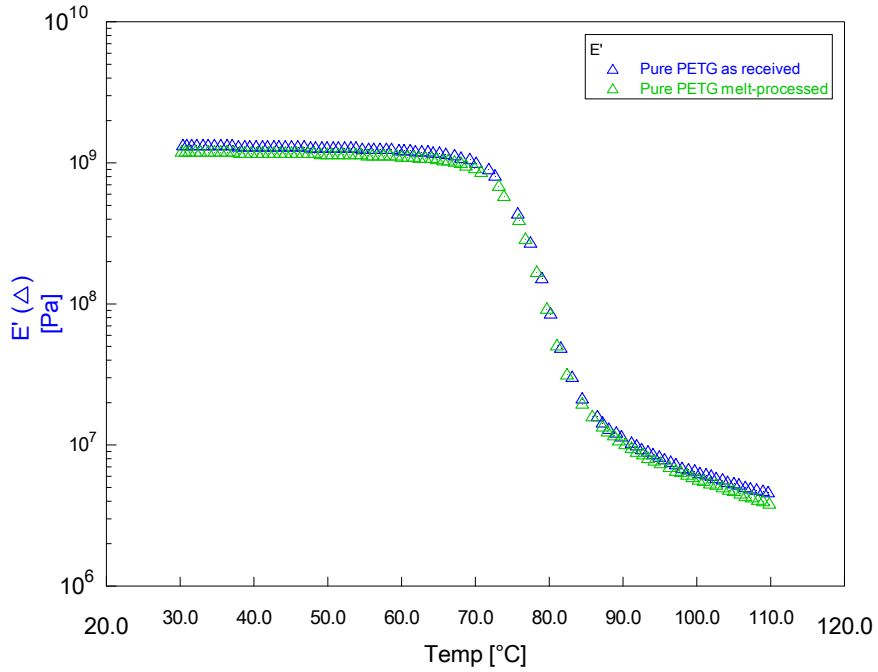

Figure 5.6 Isochronal temperature sweeps for pure PETG as received and melt–processed at a frequency of 10 rad s^{-1}

To elucidate the effect of clay concentration on the dynamic mechanical properties of the nanocomposites relative storage modulus $\left(E_r' = \frac{E_{nanocmposite}}{E_{matrix}} \right)$ of the nanocomposites at two temperatures one in the glassy regime and other in the rubbery regime are listed in Table 5.4. E_r' increased with an increase in clay percentage. In the glassy regime at low filler loading the increase is about 15%, however, in the rubbery regime the increase in relative modulus resulted from the softening of the matrix phase. As the clay percentage increases from 3 to 10%, the relative modulus in the glassy regime significantly increases from 1.15 to 1.70, corresponding to an increase in the modulus from 15 to 70%. In the rubbery regime where the contribution of the nanofiller to the stiffness of the nanocomposite is significant due to the softening of the polymer matrix, the increase in the relative modulus is even more. In this regime the E_r' increases from 1.39 to 2.69, corresponding to an increase of 39 to 169%. This significant improvement

in the storage modulus in the rubbery regime manifests the reinforcement effect of clay in PETG20A nanocomposites. Nanocomposite storage modulus results can be attributed to the confinement of the amorphous PETG chains in the silicate gallery space that partially hinders the molecular motion.

Table 5.4 Relative modulus (E_r') values for PETG20A compositions at different temperatures in glassy and rubbery regime

Sample	E'_r	
	50 °C (T < T_g)	**110 °C (T > T_g)**
PETG20A3	1.15	1.39
PETG20A5	1.22	1.77
PETG20A7	1.50	1.80
PETG20A10	1.70	2.69

5.3.5.2 Tan δ

The loss factor or tan δ scans for pure PETG and PETG20A nanocomposites over a temperature range of –150 to 110 °C are presented in Figure 5.7. Two relaxations are clearly visible from the scans. The high temperature relaxation localized in the vicinity of 81 °C is the segmental glass–rubber transition that is termed as the α relaxation. The low temperature relaxation around –75 °C is the β relaxation, that originates from the motion of polar C=O groups in PETG. It is interesting to note from the figure that no change can be observed in the β relaxation peak of the nanocomposite as compared to pure PETG. In case of the α–process it can be seen that there is a slight lowering of the peak temperature value in the nanocomposites in addition to reduction in damping as compared to the pure polymer. Because the β–processes of pure PETG and PETG20A nanocomposites are almost identical and whatever changes observed from the tan δ scans are for the α–process, we will limit our discussion only to the α–process.

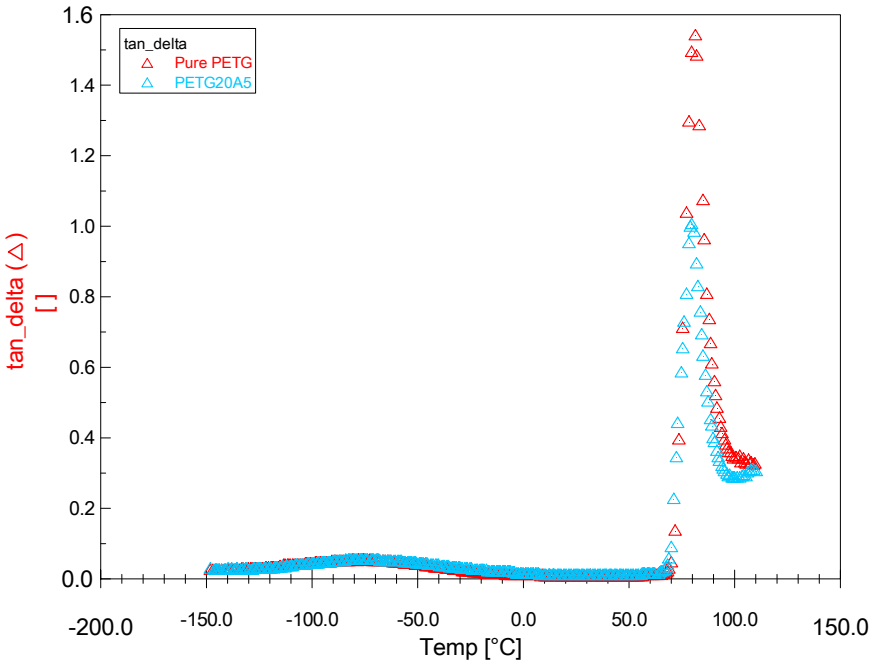

Figure 5.7 Temperature dependence of tan δ for pure PETG and PETG20A5 nanocomposite over a temperature range of –150 to 110 °C

Figure 5.8 displays the variation in the tan δ as function of temperature in the range of 30 to 110 °C for pure PETG and PETG20A nanocomposites containing different filler loadings. An interesting picture that emerges from the loss factor scans is the steady decrease in the glass transition temperature T_g (α relaxation) with increasing concentration of clay to 10 wt%. This behavior is similar to that observed for PETG nanocomposites with different clays (chapter 4), and can be ascribed to the plasticization effect from the low molecular organic intercalant used to modify the clay. There is a steady decrease of about 3 °C in the T_g values up to 7 wt% loading of 20A, however, for 10 wt% 20A loading there is a slight increase in the T_g value. This is probably related to the dispersion of clay in the polymer matrix and the amount of polymer chains intercalated between the clay galleries. Our WAXD results have shown that PETG20A10 has less intercalation as compared to the other nanocomposites.

Another interesting observation that can be made from Figure 5.8 is that even though the nanocomposites show a lower T_g, there is a steady decrease in the damping

with increasing clay concentration in the nanocomposites as compared to the pure polymer. These results are similar to those reported in chapter 4 and may be attributed to favorable interactions between the polymer and the organically modified clay layers resulting in to immobilization of polymer chains. From the WAXD data of PETG20A nanocomposites it can be seen that increasing filler concentration increases the polymer infiltration in the clay galleries up to 7 wt%. Increased intercalation of polymer reduces the filler size and increases its surface area.[5] It has been reported in the literature that decrease in the filler size is associated with a surface area increase, that increases its association with the polymer chains, which results in reduced internal friction leading to a decrease in damping.[15] Therefore, the reduction in damping for PETG20A nanocomposites may be attributed to immobilized polymer chains. Furthermore, this immobilization of polymer chains may be due to the formation of a rigid amorphous phase resulting from the constrained amorphous phase (CAP). The tan δ peak values and the normalized values of tan δ for PETG20A nanocomposites are shown in Table 5.5. The significantly lower values of tan δ than the normalized tan δ values in the nanocomposites indicate the existence of RAP.

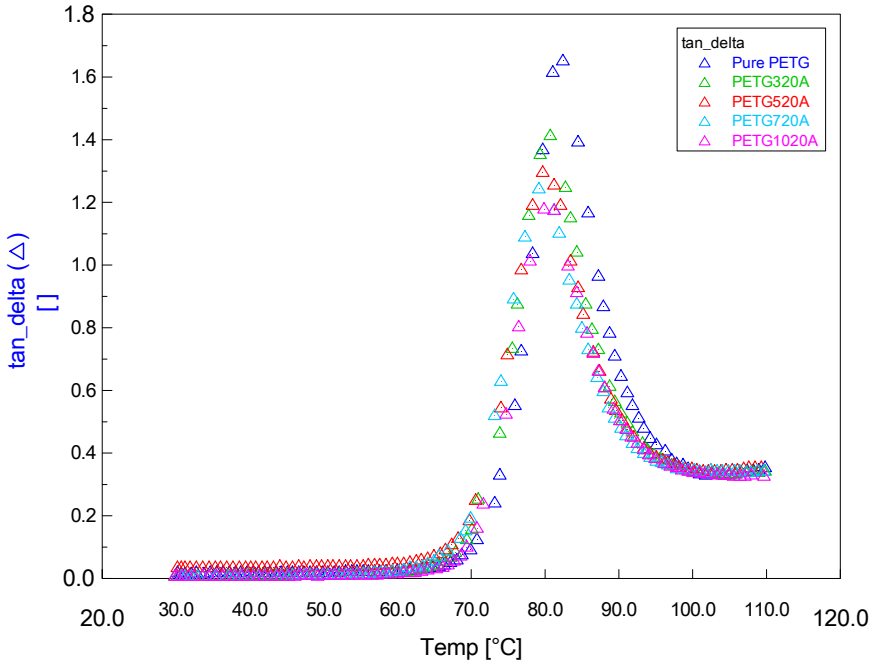

Figure 5.8 Temperature dependence of tan δ for pure PETG and PETG20A nanocomposites over a temperature range of 30 to 110 °C

Table 5.5 Tan δ and normalized tan δ values at peak temperature for PETGCNT nanocomposites

Sample	Tan δ value	Normalized tan δ value
Pure PETG	1.6504	–
PETG20A3	1.4120	1.6008
PETG20A5	1.2962	1.5678
PETG20A7	1.2432	1.5348
PETG20A10	1.1792	1.4853

5.3.5.3 Cole–Cole Plots

The nature of the Cole–Cole plots is reported to be indicative of the homogeneity of the system. Homogeneous polymeric systems are reported to show semicircle diagrams.[16] The Cole–Cole plots of the PETG20A nanocomposites at different clay loading are presented in Figure 5.9. These are skewed semicircles with a kink at higher E' values indicating heterogeneity of the system.

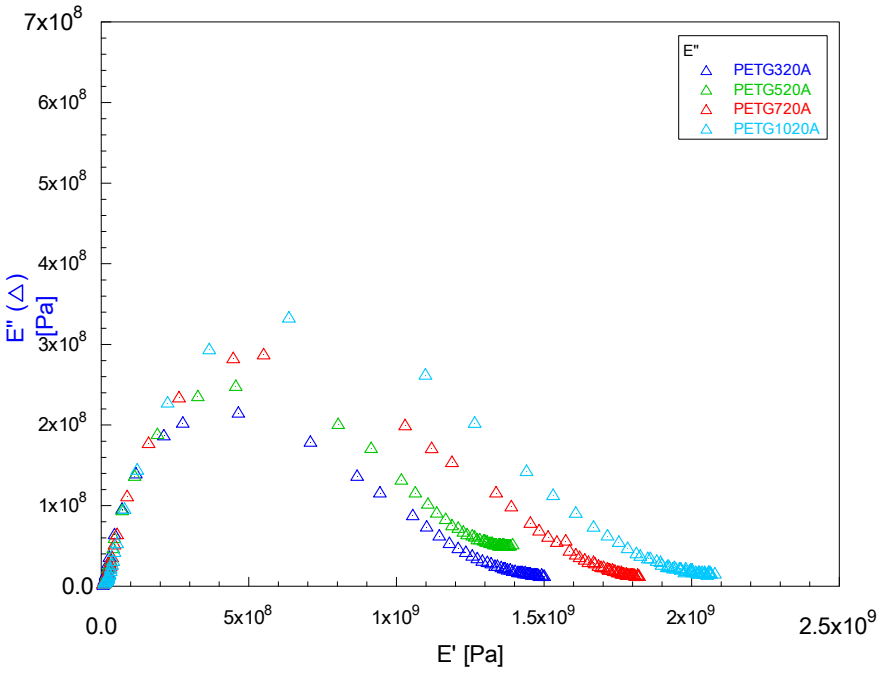

Figure 5.9 Cole–Cole plots of PETG20A nanocomposites at different clay loading

5.3.6 Dielectric Relaxation Spectroscopy

Dielectric relaxation spectroscopy (DRS) is a powerful technique for obtaining molecular dipolar relaxation as a function of temperature and frequency, from which the effect of intermolecular cooperative motion and hindered dipolar rotation can be elucidated. When a nanocomposite is placed in an electric field, it is subjected to ionic, interfacial, and dipole polarization. These polarization mechanisms have considerably different time scales and length scales. This makes dielectric relaxation spectroscopic study a versatile probe to study nanocomposite dynamics. The study can be carried out over a wide range of temperatures and frequencies. In the following the DRS analysis of pure PETG and PETG20A nanocomposites is discussed.

5.3.6.1 DRS of pure PETG

Dielectric measurements on pure PETG in the temperature range of 30 to 120 °C and over frequency from 10^{-2} to 10^{7} Hz were studied. The data is represented as the real part of complex permittivity (ε') and the dielectric loss (ε'') in Figures 5.10 and 5.11, respectively, from which two relaxation processes are visible. It can be observed that for this polar copolyester the dielectric permittivity is a function of frequency and temperature. At low temperatures $T < T_g$ there is slight dependence of permittivity on frequency. However, at $T > T_g$ there is a considerable increase in the permittivity at low frequencies. Most of this high temperature increase in permittivity is due to the electrode polarization effects arising from ionic conduction which show a significant increase at $T > T_g$. Furthermore, the figures also demonstrate the presence of two temperature dependent relaxation processes that are identified by their shouldered response in the ε' data and corresponding peaks and/or shoulders in ε''. These two relaxation processes present in PETG can be characterized as a broad relaxation at $T < T_g$ corresponding to the β relaxation, and then the sharp increase in the permittivity at $T \geq T_g$ that corresponds to the α relaxation due to large scale dipole mobilization at the glass transition of the polymer. This is more clearly demonstrated from the dielectric loss spectra. It can be observed that the relaxation processes of PETG appear as maxima in the frequency dependence of dielectric loss plot (Figure 5.11) which shifts towards higher frequencies

with increasing temperature. This shift in the frequency is because the dissipated thermal energy assists polar groups to follow the motion of the alternating electric field, resulting in reduced relaxation times.

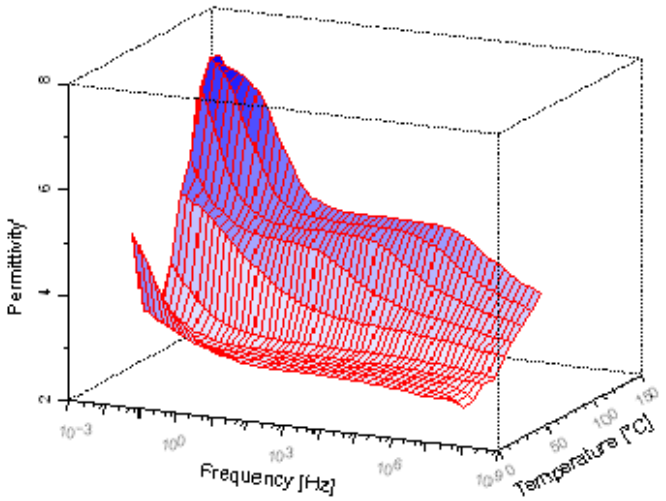

Figure 5.10 Temperature–frequency dependence of the dielectric permittivity (ε') for pure PETG

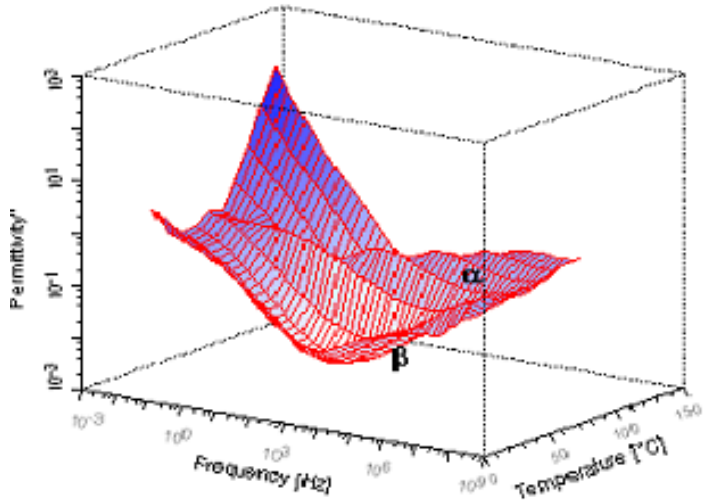

Figure 5.11 Temperature–frequency dependence of the dielectric loss (ε'') for pure PETG

Figures 5.12 and 5.13 illustrate the dielectric loss data for the glass–rubber regime and the sub–glass regime, respectively. The more intense α–process is illustrated above the glass transition temperature of PETG.[17] At elevated temperatures the dielectric loss in the low frequency regime increases continuously as a result of contributions due to conductivity from mobile charge carriers. Note that the faster low temperature sub–glass β–process is rather broad. Furthermore at temperatures near T_g, the α–process appears to be well separated from the β–process. In addition the β–process appears more like a shoulder than as a resolved peak. Our DMA studies have shown that pure PETG shows a β relaxation at –74.84 °C. Thus, the dielectric β–process should appear more resolved in this temperature range. However, instrumental restrictions prevent us to go below the ambient temperature. In this chapter we will focus more on the α–process. The dielectric relaxation processes comprising of the glass rubber (α relaxation) and the sub glass (β relaxation) were analyzed according to the empirical Havriliak–Negami (HN) functional formalism[18,19] that can be phenomenologically described as a combination of the conductivity term with the HN functional form as follows:

$$\varepsilon(\omega) = \varepsilon' - i\varepsilon'' = -i\left(\frac{\sigma_{dc}}{\varepsilon_0 \omega}\right)^N + \sum_{k=\beta,\alpha}\left[\frac{\Delta\varepsilon_k}{\left(1+\left(i\omega\tau_{HN\,k}\right)^{a_k}\right)^{b_k}}\right] \qquad (5.1)$$

where, σ_{dc} is the direct current electrical conductivity, $\omega=2\pi$ is the angular frequency, ε_0 denotes the vacuum permittivity, N is an exponent ($0<N<1$), $\Delta\varepsilon$ is the dielectric of the kth process, τ_{HN} is the most probable value of the central relaxation time distribution function, and a and b are shape parameters related to symmetric and asymmetric broadening of the relaxation peak, respectively. All HN fits reported here were performed using WinFit software program provided with the Novocontrol dielectric analyzer. The solid lines in Figure 5.12 and 5.13 represent the overall best fits according to equation 5.1 considering the sum of two HN functions used to describe the relaxations.

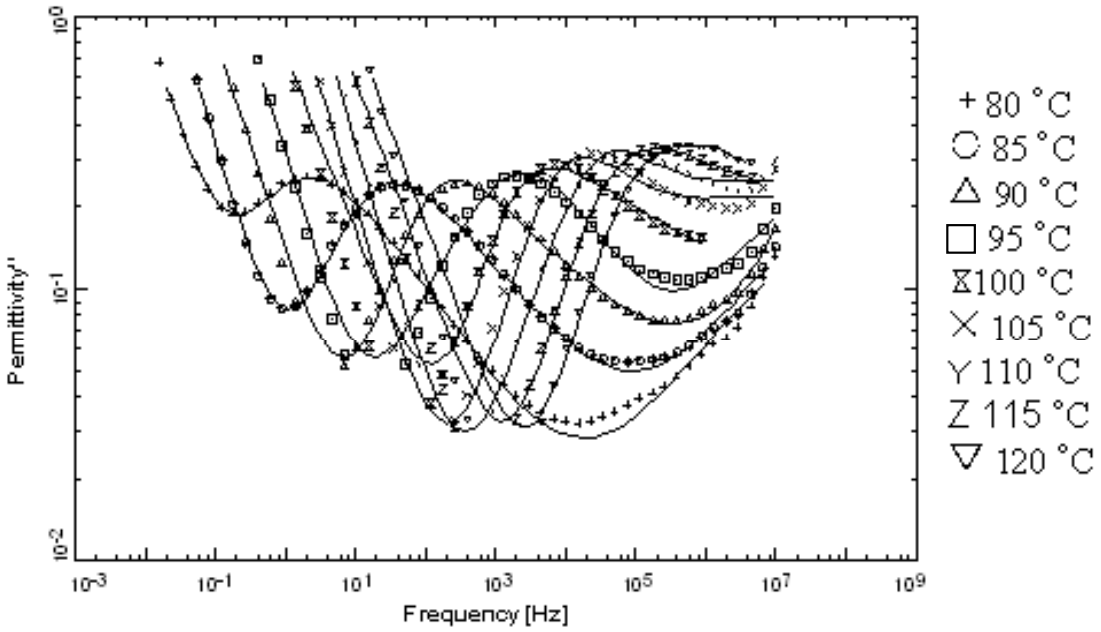

Figure 5.12 Experimental dielectric loss data for pure PETG in glass–rubber regime. Solid line represents best fits according to the HN equation

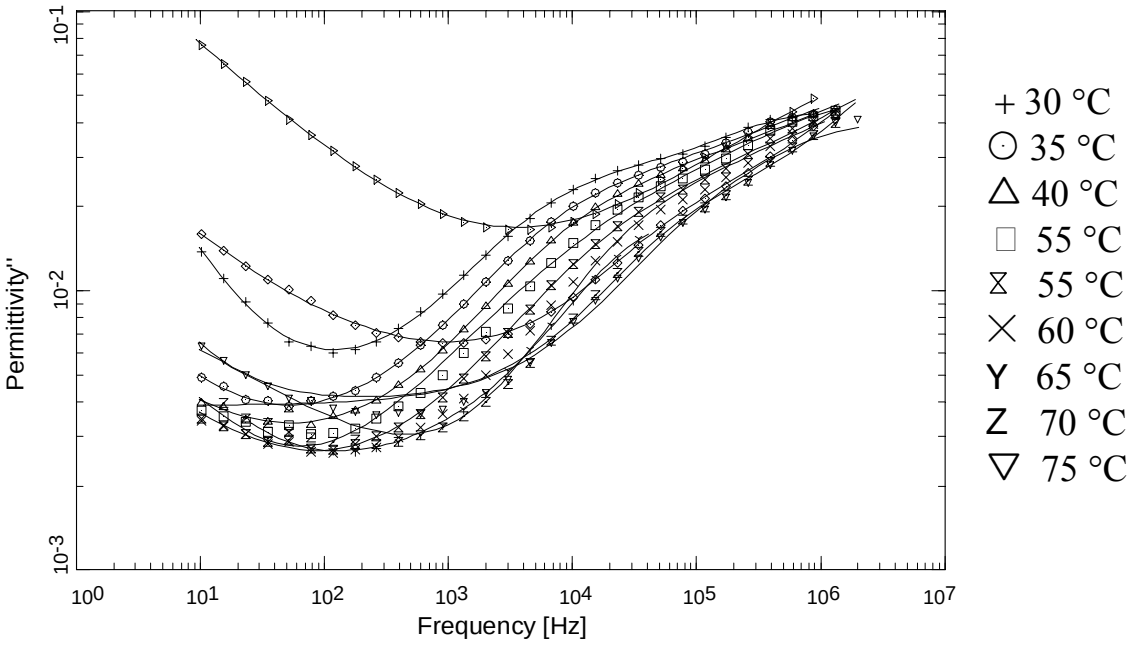

Figure 5.13 Experimental dielectric loss data for pure PETG in the sub–glass regime. Solid line represents best fits according to the HN equation

The frequency maximum peak, F_{max}, as a function of reciprocal of temperature for the α–process is shown in Figure 5.14. As can be seen, the α–process displays a non–Arrhenius type curvature at the higher measured frequencies characteristic of a Vogel–Fulcher–Tamman (VFT) dependence given by:

$$F_{\max} = F_0 \exp\left[\frac{E_a}{T - T_v}\right] \tag{5.2}$$

where, F_0 is a characteristic frequency, T_v is the Vogel Temperature, and E_a is an apparant (temperature–dependent) activation energy.[20] This behavior is characteristic of the cooperative segmental motions appearing above the glass transition temperature. Fitting of the VFT equation to the data is discussed latter in the chapter.

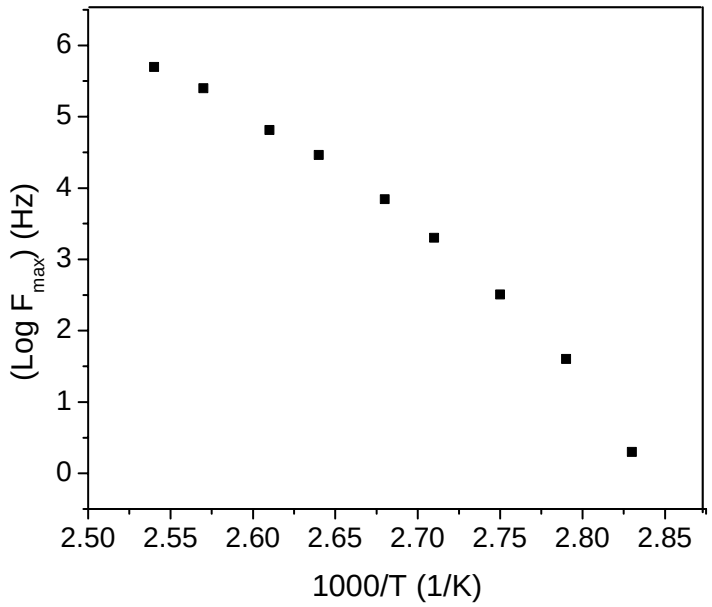

Figure 5.14 Dependence of frequency of maximum loss (F_{max}) with the reciprocal temperature in the α–process regime for pure PETG

The obtained values of the HN–parameters a and b for the α–process of pure PETG are presented in Figure 5.15 The parameter b is related to the asymmetric

broadening. This parameter is often quite low in thermoplastics, with values of 0.29 reported for polycarbonate, 0.3 for poly(vinyl acetal).[21] Similarly, Ezquerra et al. have reported a value of 0.3 for PET and 0.41 for amorphous PET.[22] The values for PETG range between 0.22 and 0.32, which agree well to those, reported in the literature for other thermoplastics. Moreover the narrow range of the values of HN–parameter *b* with temperature is a manifestation of strong asymmetric α relaxation in pure PETG. This behavior is in accordance with previously reported results for PET and amorphous blends of PET and PEN.[23,24]

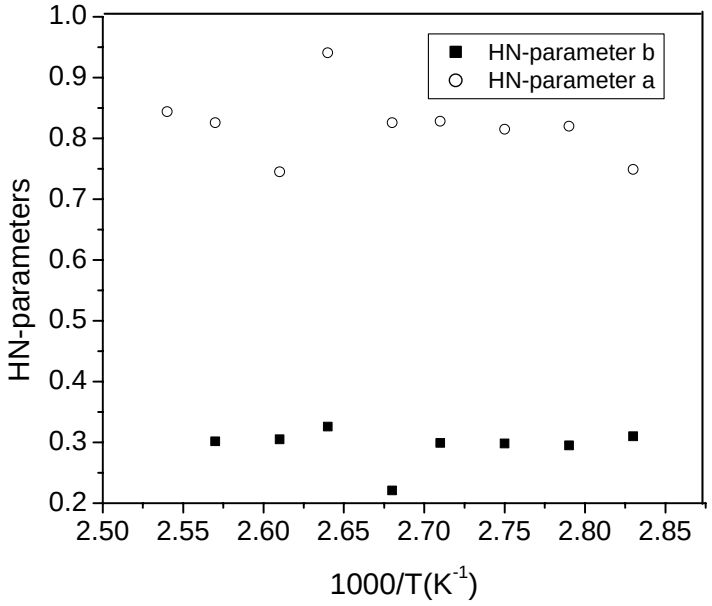

Figure 5.15 Obtained values of HN–parameters a and b as a function of temperature for the α–process of pure PETG

5.3.6.2. DRS of PETG20A nanocomposites

5.3.6.2.1 Dielectric Loss

In the following the dielectric loss, ε'', of the nanocomposites is discussed. Figures 5.16 (a–d) shows the dielectric loss curves for PETG20A nanocomposites in the α relaxation region i.e. at $T > T_g$. In this temperature range the dc conductivity dominates the dielectric loss and its contribution goes on increasing with temperature. Moreover this

high dc conductivity has somewhat dwarfed the α–process. Still it can be observed that the α–process which is associated to the glass–rubber transition is clearly seen for all the nanocomposites. Further in some cases (e.g. PETG20A3 scan at 80 °C) a faint signal due to the β–process which is associated to the local motions of the C=O polar groups can also be observed.

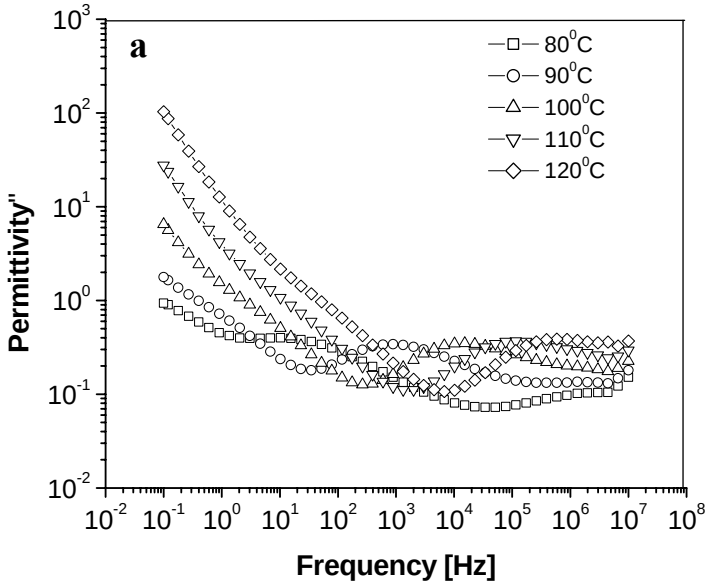

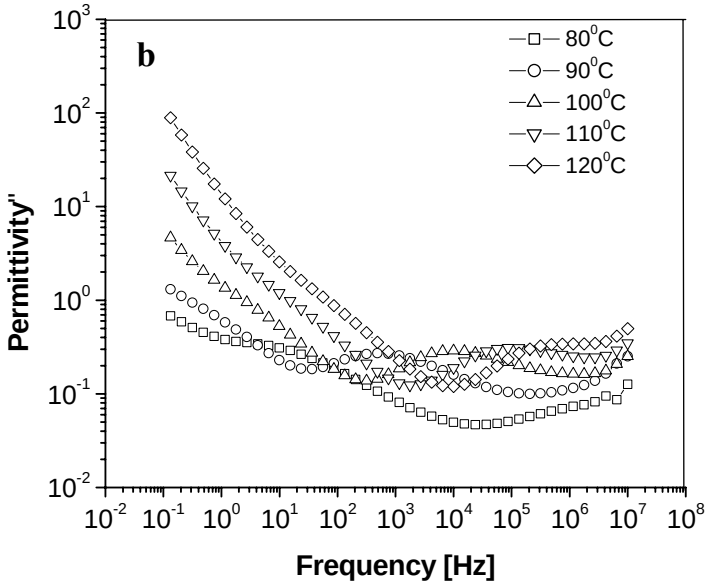
b
80°C
90°C
100°C
110°C
120°C
Permittivity'
Frequency [Hz]

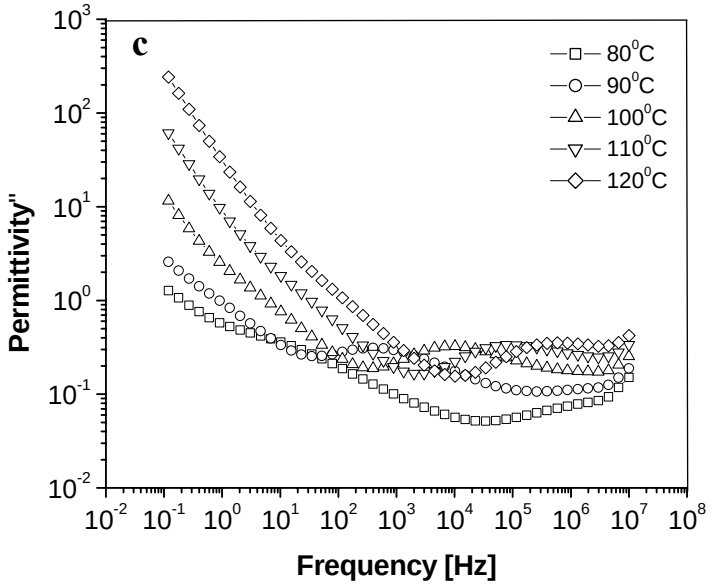
c
80°C
90°C
100°C
110°C
120°C
Permittivity''
Frequency [Hz]

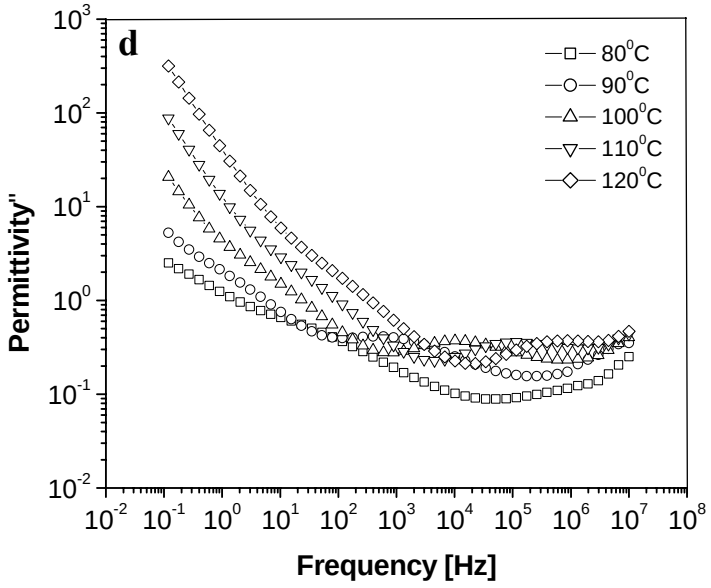

Figure 5.16 Experimental values of the dielectric loss for PETG20A3 (a); PETG20A5 (b); PETG20A7 (c); PETG20A10 (d) as a function of frequency at various temperatures at $T > T_g$

The shapes of the α relaxation curves for PETG20A nanocomposites have been analyzed by the HN equation in combination with the conductivity term (equation 5.1). A representation of the HN fit is presented in Figure 5.17. The values of the HN parameters *a* and *b* for the nanocomposites were found to be similar to those of pure PETG. This suggests that the intermolecular and intramolecular interactions that arise in the polymer and the nanocomposites are almost identical. We have made similar observations in our work based on PETG and clay Cloisite 25A nanocomposites.[25]

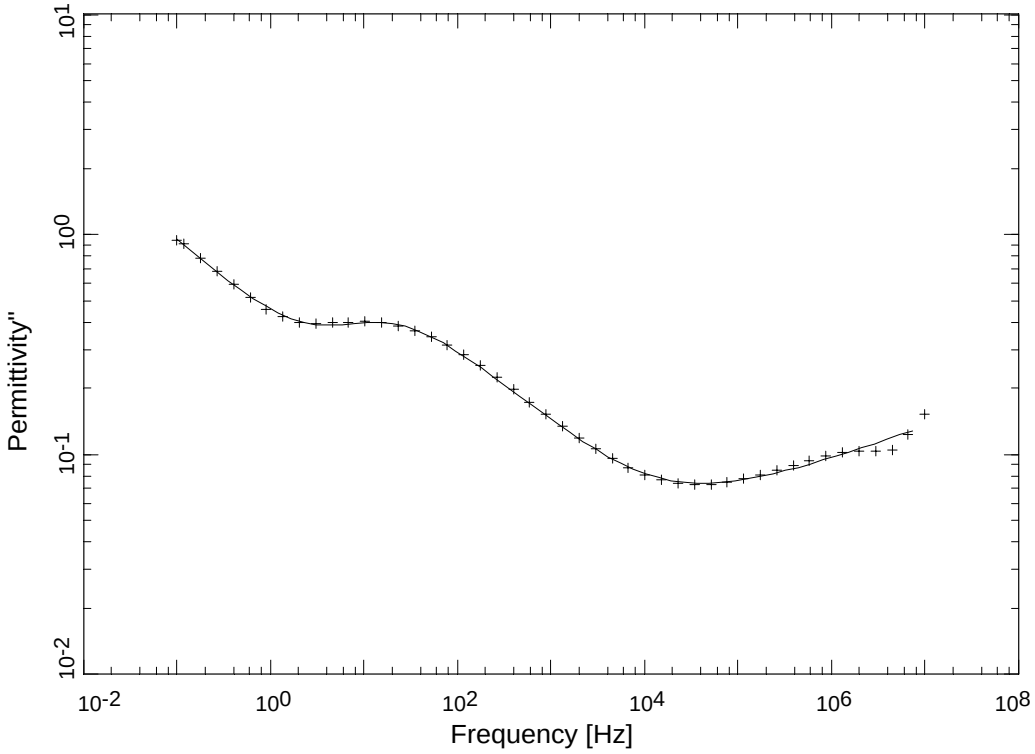

Figure 5.17 Dielectric loss as a function of frequency for PETG20A3 at T = 353 K. The solid line represents the best fit according to equation 5.1. The scan shows the α–process at lower frequencies and the faster β–process at higher frequencies

The relaxation frequencies for the α–process for pure PETG and PETG20A nanocomposites obtained from the frequency maximums are plotted against reciprocal of temperature and presented in Figure 5.18 (for direct comparison between the neat polymer and the nanocomposites the temperature dependence of F_{max} for pure PETG α–process is shown again in Figure 5.18). The solid lines represent fits of the data to the VFT equation (equation 5.2). Addition of clay 20A to PETG increases the α relaxation frequency over that of pure PETG for all the nanocomposite compositions under study over the entire temperature range. In turn, the nanocomposites exhibited lower apparent activation energies as compared to that of the pure PETG. VFT fitting yields values of activation energy between 0.09 to 0.0344 eV and T_v between 293 and 332 K for pure PETG and PETG20A nanocomposites, respectively. Inclusion of nanoclay platelets,

which are flat in shape divide the bulk polymer into smaller domains, thus reducing the intermolecular cooperativity between the polymer chains and accelerating α dynamics. This reduced cooperative motion in the nanocomposites is a result of decreasing glass transition temperature.[26] As discussed in chapter 4 the lowering of T_g may also be due to the plasticizing effect of the low molecular weight organic modifier used to organically modify the clay.

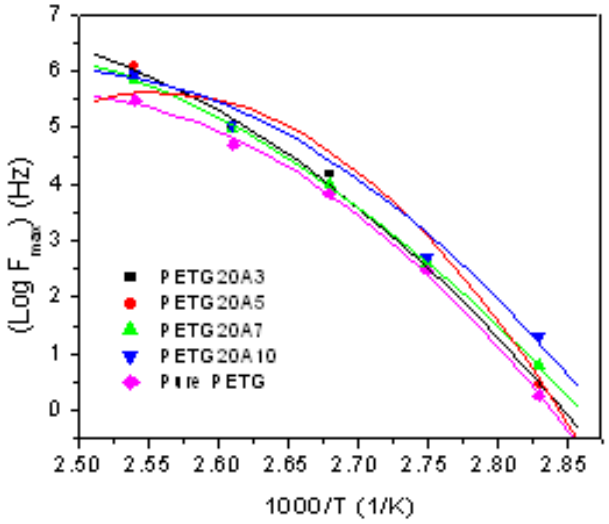

Figure 5.18 Peak frequencies (F_{max}) of the α–process determined from the ε'' plots are plotted against the reciprocal of temperature for pure PETG and PETG20A nanocomposites. Solid lines represent fits of VFT equation

In addition to the two conventional relaxation processes (α and β modes) a third relaxation process can be observed in the nanocomposites in the low frequency region. This process is absent in pure PETG (Figure 5.11). This relaxation mode may be attributed to the Maxwell–Wagner–Sillars (MWS) interfacial polarization, which occurs due to (partial) blocking of mobile charge carriers in inhomogeneous materials on a mesoscopic scale (i.e. due to charge accumulation at matrix–filler interface). This leads to separation of charges which gives rise to a significant contribution to the polarization of the sample.[27–29] MWS dispersion can be distinguished from the α relaxation by its larger intensity ($\Delta\varepsilon_{MWS}$) and a much broader relaxation time distribution (δ_{MWS}). The magnitude

of MWS relaxation derived from the conducting ions is much greater than that for the α relaxation in pure PETG produced by orientation of the molecular dipoles. It may be noted here that the MWS process observed in PETTG20A nanocomposites is a high temperature process and cannot be observed for $T < T_g$. It is worth mentioning that the electric modulus representation gives more robust representation of the of the MWS relaxation. The dc conductivity that was observed in the high–temperature data of Figure 5.16 is associated with the transport of free ions through the softened polymer matrix under action of an electric field. By using the dielectric modulus formalization for the treatment of the raw dielectric data, the contribution of electrode screening and conductivity effects in the low–frequency regime can be minimized.[30,31] As an example Figure 5.19 shows the modulus and the dielectric loss representation of MWS polarization for PETG20A7 at 110 °C. It can be seen that the MWS polarization appears as a part of a broad peak in the dielectric modulus spectrum.

Some interesting features regarding the MWS relaxation are noted below. (1) The relaxation time distribution as determined from the breadth of the relaxation peaks for the MWS interfacial polarization is broader than that for the α relaxations. Note that for MWS relaxation it spans more than 5 orders of magnitude, while for the α process the relaxation time distribution spans only 3 orders of magnitude. This is attributed to the heterogeneous geometry of the polymer–clay interfaces that are responsible for a range of different relaxation times. (2) A much higher dielectric intensity is observed for the MWS relaxation as compared to that for the α relaxation is because of the distinct nature of these two relaxation modes. The higher dielectric magnitude for the MWS mode is produced upon polarization of ions piled up at the polymer–clay interfaces whereas for the α–process, the dielectric intensity results from the alignments of the molecular dipoles.

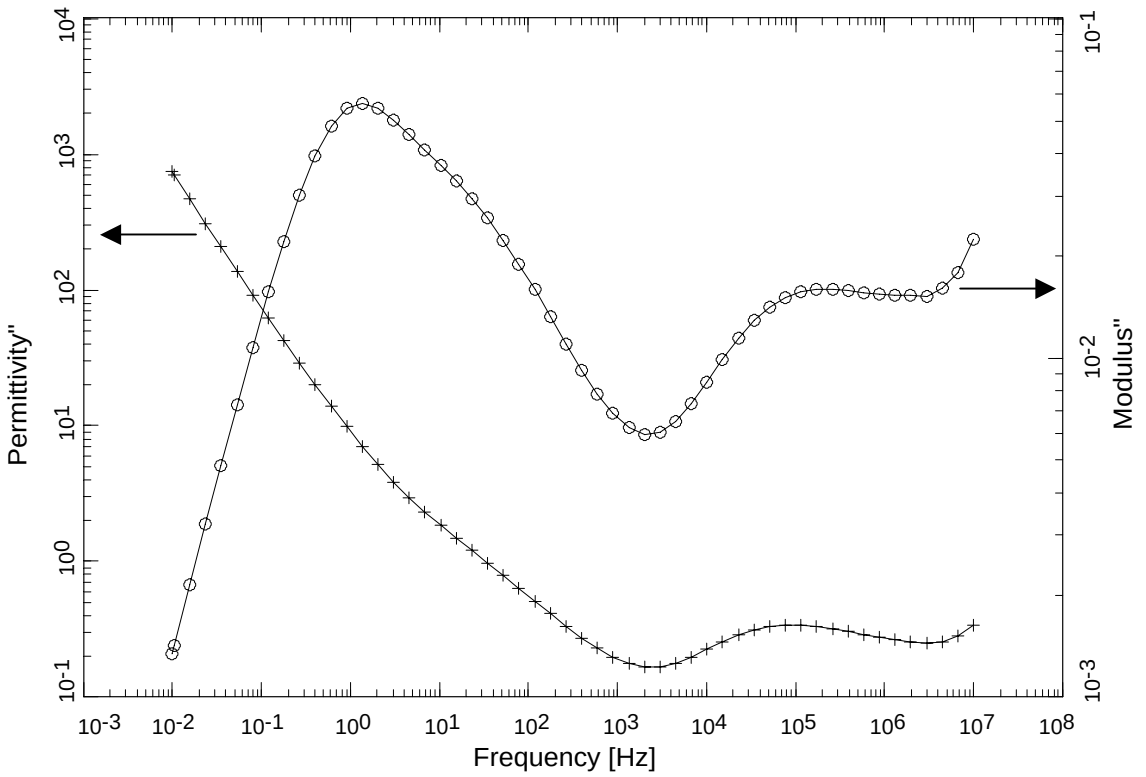

Figure 5.19 Maxwell–Wagner–Sillars and α–process relaxation for PETG20A7 in the frequency domain expressed in two different formalisms: dielectric loss and dielectric loss modulus at T = 383 K

A plot of $F_{\max}$, from the dielectric loss modulus data, as a function of reciprocal of temperature is presented in Figure 5.20. Arrhenius type behavior is observed for all the nanocomposites. The data can thus be fitted via the equation

$$F_{\max} = F^0 \exp\left[-\frac{E_A}{k_B T}\right] \tag{5.3}$$

where F^0 is the pre–exponential factor, E_A is the activation energy, k_B is the Boltzmann constant and T represents the temperature. The obtained values of the activation energy are about 0.9 eV. It has been reported in the literature that $E_{A\text{-MWS}}$ values do not change much with filler content.[32,33]

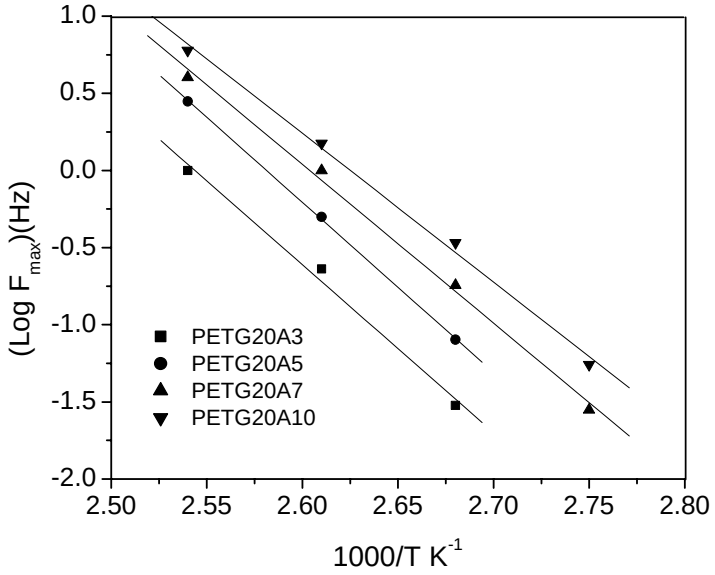

Figure 5.20 Dependence of F_{max} of dielectric loss modulus with the reciprocal of temperature for the MWS relaxation mode in PETG20A nanocomposites

5.3.6.2.2 Dielectric Permittivity

The real part of the dielectric permittvity (ε') for pure PETG as a function of frequency is already presented in Figure 5.10. In Figures 5.21 a–c, isothermal scans of ε' extending over a frequency range of 30 to 120 °C and over frequency from 10^{-2} to 10^{7} HZ are displayed for PETG20A5, PETG20A7 and PETG20A10. For the pure polymer at temperatures above 90 °C, electrode polarization effects can be observed. This effect weakens and/or disappears in case of the nanocomposites. Further the permittivity of the pristine polymer does not increase much over the entire range of temperatures studied. However, there is a marked increase in the permittivity of the nanocomposites with increasing temperature, especially in the low frequency region. For example, the permittivity of the nanocomposites at 10^{-1} Hz is 35, 160, and 70 for PETG20A3, PETG20A5, PETG20A7, and PETG20A10, respectively, at 120 °C. This when compared to the permittivity of the pristine polymer, 7 at 120 °C; this gives increments of 500, 2285, and 1000 % for PETG20A5, PETG20A7, and PETG20A10, respectively. Very interestingly the frequency and temperature dependence of the nanocomposites is quite

significant. Note that without the nanoclay platelets the dielectric permittivity of the pristine polymer is not likely to be affected by either frequency or temperature. This demonstrates that the distributed nanocapacitance, which is hypothetically composed of MMT electrodes and a polymer insert in the clay interlayer, is influenced by the d_{001} distance, and thermal and vibration energies. Furthermore the increase in the permittivity of the nanocomposites is not continuous with PETG20A10 showing a lower increment in permittivity as compared to that shown by PETG20A7. This can be understood in terms of decrease in the gallery spacing for PETG20A10 (see Figure 5.1). The number of polymer chains intercalated in PETG20A10 are less that those between the clay galleries of PETG20A7 nanocomposite. Thus the distributed nanocapacitance for PETG20A10 is lower compared to that for PETG20A7.

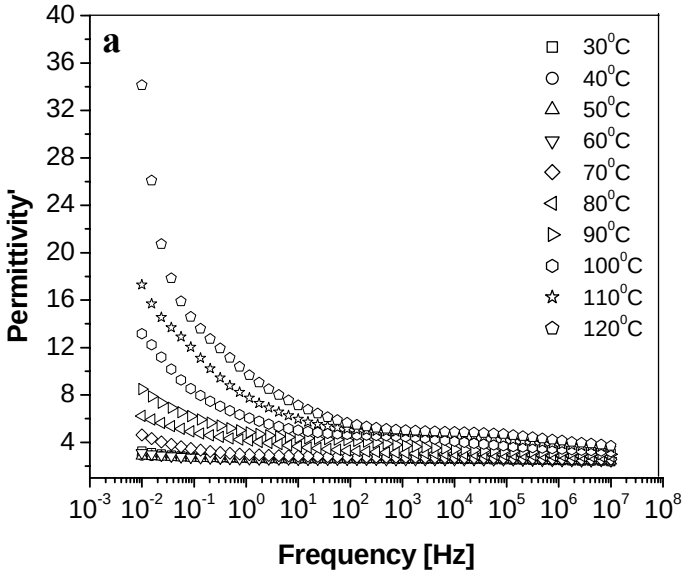

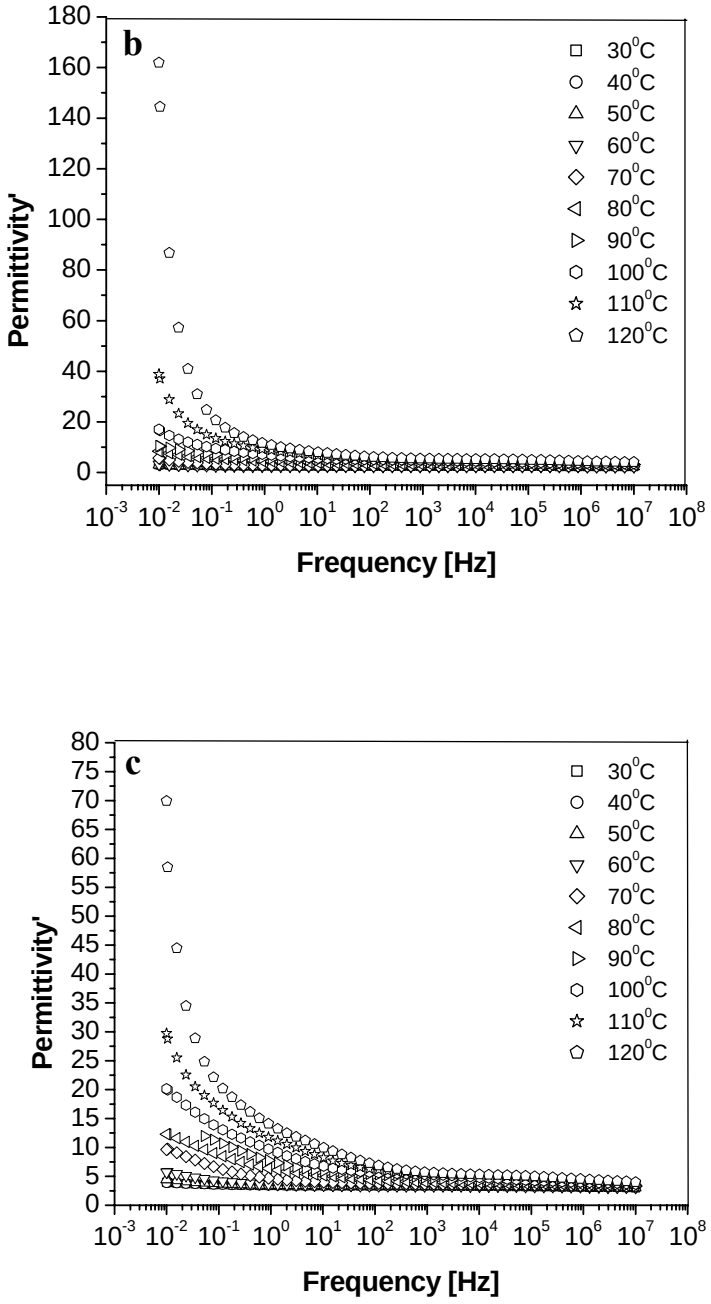

Figure 5.21 Experimental values of dielectric permittivity for (a) PETG20A5; (b) PETG20A7 (c) PETG20A10 as a function of frequency at various temperatures

5.3.6.2.3 Conductivity

The frequency dependence of ac conductivity for pure PETG, PETG20A3 and PETG20A7 nanocomposites over a range of temperatures is depicted in Figure 5.22 (a–c). It can be observed that the ac conductivity shows both frequency and temperature dependence. In the low frequency region (10^{-1} to 10 Hz), σ_{ac} increases by approximately four orders of magnitude with increasing temperature, while with increasing frequency (10^3 to 10^7 Hz) the temperature dependence becomes less evident and conductivity values display proximity, both for the pure polymer as well as the nanocomposites. Considering a single temperature scan, it can be observed that conductivity for all the samples covers a range of almost nine orders of magnitude with increasing frequency. In the same context, in the low frequency regime, the alternating applied field provides sufficient time to charge carriers to drift over larger distances. A tendency to retain almost constant values is observed as the temperature is increased as evident from the low frequency plateau. Increasing the frequency results in a deduction of the mean displacement of the charge carriers and after a certain critical frequency f_c, the real part conductivity follows a power law of the form $\sigma_{ac} \sim \omega^s$, with $0 \leq s \leq 1$. In general at constant temperature the ac conductivity can be expressed as:

$$\sigma(\omega) = \sigma_{dc} + A\omega^s \tag{5.4}$$

where σ_{dc} is the $\omega \to 0$ limiting value of $\sigma(\omega)$ and A and s are parameters which depend upon temperature, morphology, and composition.[34,35] Equation 5.4 represents the frequency independent behavior at low frequencies, which is a characteristic of non–dielectric with a significant direct current (dc) conductivity σ_{dc} and is often described as the so–called universal dynamic response, since it has been found to satisfactorily describe the ac response of numerous different types of materials, which cannot be characterized as crystalline solids.[36,37]. Note that the temperatures where the dc conductivity is recorded are, in all cases, higher than the glass transition temperatures. At temperatures lower than the T_g, the conductivity curve of each system displays only the exponential part of $\sigma(\omega)$.

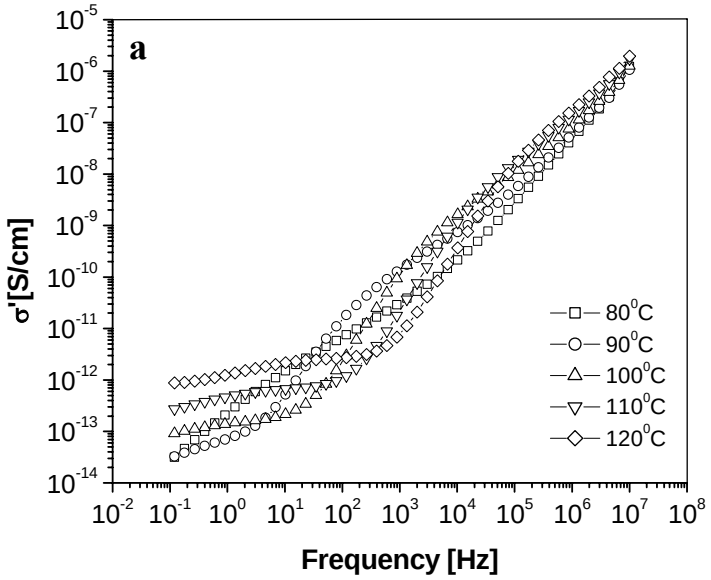
a
σ'[S/cm]
Frequency [Hz]
80°C
90°C
100°C
110°C
120°C

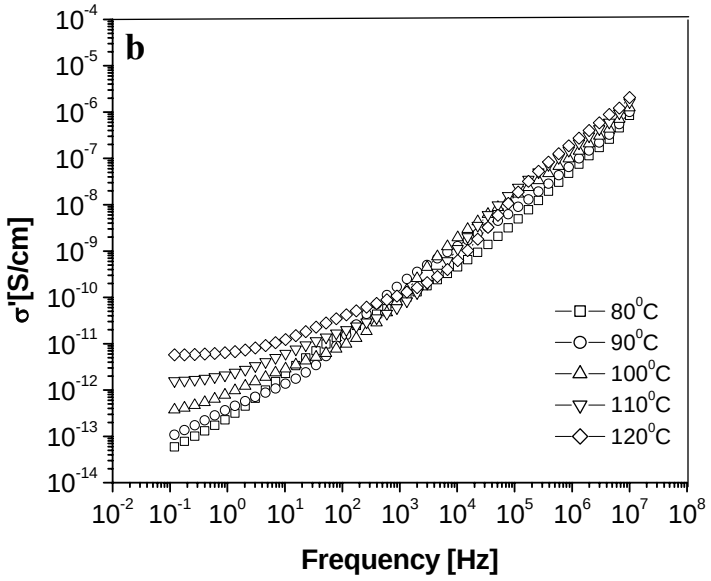
b
σ'[S/cm]
Frequency [Hz]
80°C
90°C
100°C
110°C
120°C

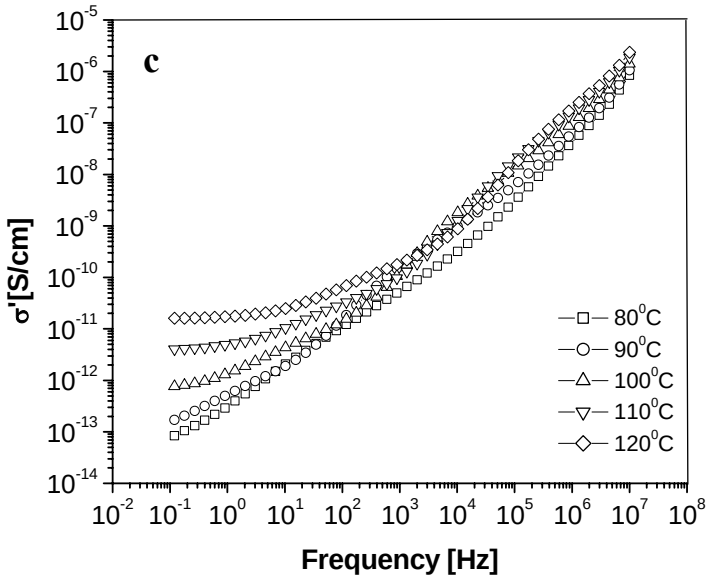

Figure 5.22 Alternating current conductivity for (a) pure PETG; (b) PETG20A3; (c) PETG20A7 as a function of frequency at various temperatures

All the nanocomposites show higher conductivity than that of the pure polymer, which increases with temperature and frequency. It may be observed from Figure 5.22a that pure PETG shows a step in the conductivity data in the frequency region around 10^3 Hz, before the σ_{dc} plateau. In the nanocomposites [Figures 5.22 (b and c)] this step weakens and/or disappears. The presence of this step in the pure polymer is indicative of the so–called conductivity current relaxation (CCR), i. e. to the accumulation of charges at the interfaces between regions of different conductivity under conditions of dc conductivity for a sample as a whole.[38] The presence of CCR suggests a large scale heterogeneity of the structure of PETG matrix.

The electrical conductivity as a function of 20A loading at 110 °C is presented in Figure 5.23. Pure PETG is excellent insulating material with electrical conductivity of 2.5 $\times$ 10^{-13} S/cm. The nanocomposites exhibit an abrupt increase of more than one order of magnitude with the addition of clay. Also the conductivity of the nanocomposites increases with increasing 20A content. This increase in the conductivity of the nanocomposites can be attributed to the nanosized inclusion, which governs the ion–

transport phenomenon, facilitating ion transfer through the inter– and intra–regions of the silicate galleries.[39]

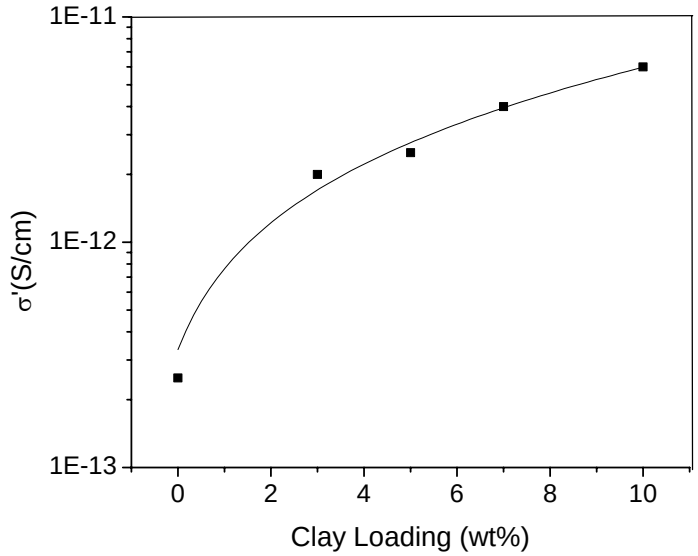

Figure 5.23 Electrical conductivity of pure PETG and PETG20A nanocomposites as a function of 20A loading at 110 °C

The ac conductivity is the sum of all dissipative effects including the contribution of dc conductivity caused by migration of charge carriers, as well as the dielectric loss dispersion.[40] The dc conductivity can be evaluated by extrapolating the constant part of $\sigma(\omega)$ to zero ($\sigma_{dc} = \sigma(\omega) \rightarrow 0$). By convention the dc conductivity is considered to be equal to the value of $\sigma(\omega)$, at the lowest measured frequency, $f = 10^{-1}$ Hz in the present case, in the temperature range where the low frequency plateau occurs. The temperature dependence of dc conductivity for pure PETG and PETG20A nanocomposites is presented in Figure 5.24. An Arrhenius type behavior is observed for both the neat polymer and the nanocomposites. The data in Figure 5.23 can be satisfactorily fitted the equation:

$$\sigma_{dc} = \sigma^0 \exp\left[-\frac{E_A}{k_B T}\right] \qquad (5.5)$$

where σ^0 is the conductivity at infinite temperature, E_A is the activation energy, k_B is the Boltzmann constant and T represents the temperature.

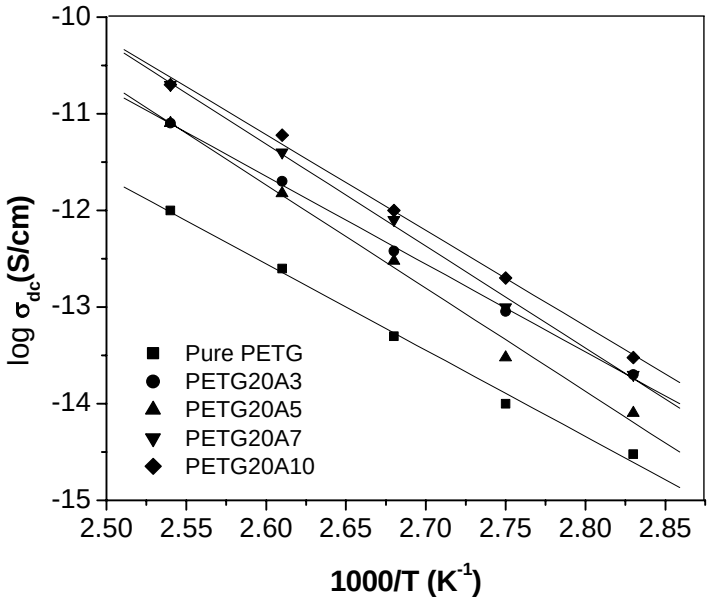

Figure 5.24 Temperature dependence of dc conductivity for pure PETG and PETG20A nanocomposites presented as reciprocal of temperature. Solid lines represent the fits according to equation 5.5

The obtained values of the relevant activation energy for pure PETG and PETG20A nanocomposites are summarized in Table 5.6. The activation energies seem to reach a threshold at 7 wt% of 20A after which there is a slight decrease. This is in line with the structural changes taking place in PETG20A nanocomposites with increasing clay content as evidenced from the structural characterization.

Table 5.6 Activation energy of pure PETG and PETG20A nanocomposites

Sample	Pure PETG	PETG20A3	PETG20A5	PETG20A7	PETG20A10
E_A (eV)	0.76	0.78	0.91	0.90	0.85

5.3.7 Rheology

5.3.7.1 Melt Viscosity

The rheological properties of a polymer are important for the development of the processing–structure–property linkage. The plot of complex viscosity (η^*) as a function of angular frequency (ω) at 250 °C for pure PETG and PETG20A nanocomposites is shown in Figure 5.25. Comparing the rheological curves of the pure polymer with those of the nanocomposites it can be observed that nanocomposites show higher complex viscosity and stronger incremental increases of η^*. Further it is noted that the nanocomposites exhibit a strong frequency dependence (shear thinning non–Newtonian behavior), while the pristine polymer shows almost a frequency independent Newtonian behavior over the entire range of frequencies studies. The increments in complex viscosity observed in this study are comparable to those measured in composite systems having a filler loadings in the range of 40 to 60 wt%.[41,42] The fine dispersion obtained in the nanocomposites, along with the high aspect ratio and the shape of the silicate platelets favors better rheological properties at very low silicate content.

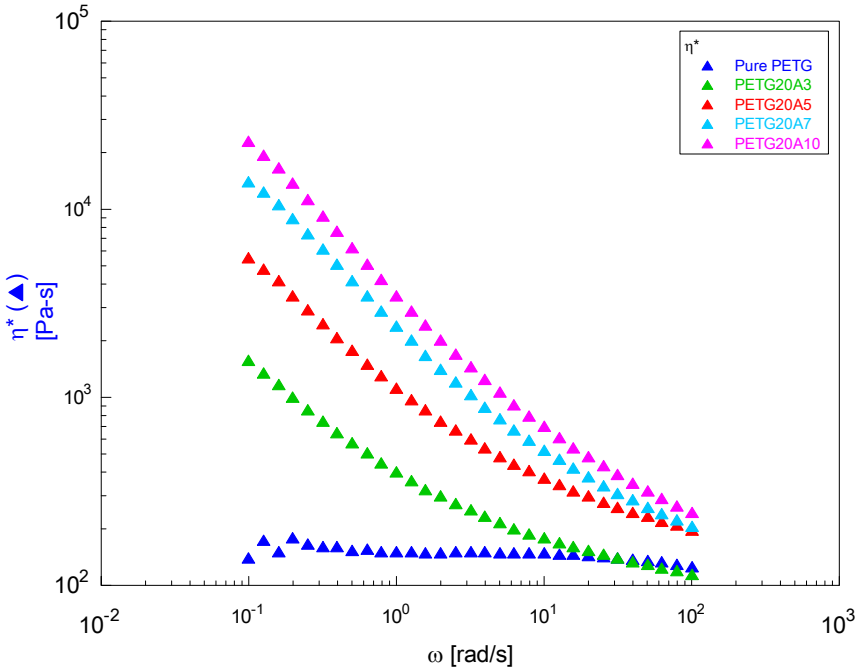

Figure 5.25 Complex viscosity as a function of angular frequency at 250 °C for pure PETG and PETG20A nanocomposites

The increase in the viscosity represents the dispersion quality of filler in a matrix polymer or the intercalation of the polymer into the clay interlayer. In this case the increase in number of polymer chains intercalating the silicate galleries increase up to 7 wt% clay loading. This is reflected in the viscosity data. The increment in viscosity of the nanocomposites between clay loadings of 7 and 10 wt% is smaller as compared to that observed between other clay loadings. From the WAXD results we have shown that for PETG20A10 there is a decrease in the amount of polymer chains intercalating the silicate galleries and formation of clay tactoids. Surprisingly, even though there is a decrease in the intercalation, the viscosity observed for PETG20A10 is higher than that of PETG20A7. This can be attributed to the filler effect that is evident in the case of PETG20A10, which has higher clay content than that in PETG20A7, giving rise to increase in the viscosity.

The viscosity curves in Figure 5.25 were fitted to the power law expression:

$$\eta = k\omega^{(n)} \tag{5.6}$$

where, η is the apparent viscosity, k is a sample specific pre–exponential constant, ω is the oscillation frequency, n is the shear thinning index equivalent to power law index.[35]

In order to determine k and n a plot of log (η^*) vs. log (ω) was made and fitted to a straight line. The shear thinning exponent n is the semi–quantitative measure of nanodispersion of the sample.[43] As in most cases the viscosity data is normally depicted as curved plots. Hence, to determine the shear–thinning exponent, the straight line fit is then carried out for the data at lowest shear rates. This is done because the rheological response at low shear rates is most representative for the composite that does not have oriented fillers particles. At high frequencies the solid–like behavior is not followed due to the filler particle alignment in the direction of the flow. This results in the control of the rheological dynamics by the liquid polymer melt.

Table 5.7 Shear thinning exponent (*n*) for pure PETG and PETG20A nanocomposites

Sample	Pure PETG	PETG20A3	PETG20A5	PETG20A7	PETG20A10
n	-0.05	-0.63	-0.73	-0.78	-0.82

The shear thinning exponent (*n*) for pure PETG and PETG20A nanocomposites are presented in Table 5.7. According to Wagener and Reisinger, the shear thinning exponent can be correlated with independently obtained information on nano and meso–scale structure of the composites.[43] Higher the value of *n* better the nanoclay dispersion in the polymer matrix. In case of PETG20A nanocomposites the increasing values of *n* may be related to WAXD data of PETG20A nanocomposites, which showed strong polymer to clay interaction which can be considered as a measure of better clay dispersion.

5.3.7.2 Modulus

The storage modulus and loss modulus as a function of frequency for pure PETG and PETG20A nanocomposites at 250 °C are compared in Figures 5.26 and 5.27, respectively. Analyzing the graphs it can be observed that both G' and G'' monotonically rise at all the frequencies studies with increasing amount of clay. Moreover, with increasing silicate content, the shape of the G' changes with its frequency dependence decreasing at low frequencies. This behavior manifests pseudo solid–like behavior due to incomplete relaxation of polymer chains in the nanocomposites, as a consequence of intercalation of the polymer. As compared to the increase in G' the corresponding increase observed in G'' is much lower as seen from Figure 5.27.

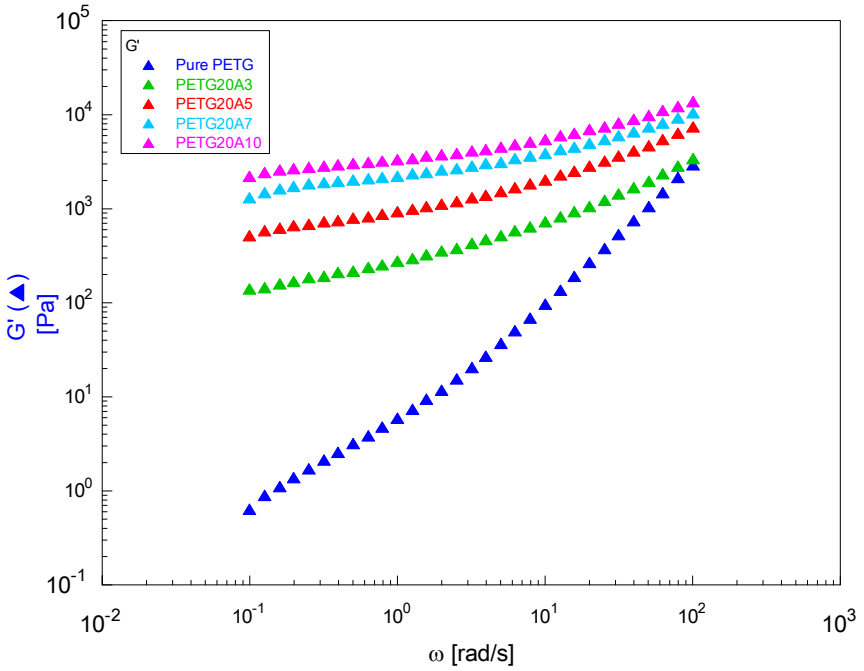

Figure 5.26 Frequency dependence of storage modulus for pure PETG and PETG20A nanocomposites

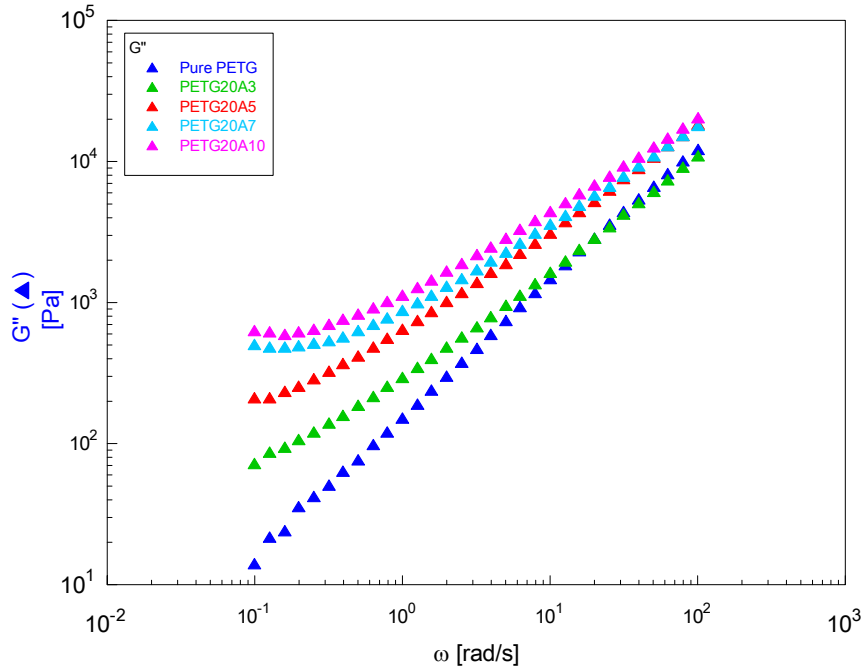

Figure 5.27 Frequency dependence of loss modulus for pure PETG and PETG20A nanocomposites

Note that both the moduli increase with frequency; however the rate of increase becomes less at higher 20A content. Thus, the effect of clay concentration is much higher at low frequencies than that at high frequencies. Figure 5.28 shows plot of storage modulus G' as a function of clay loading at different frequencies. This plot again shows that the increase with clay content is non–linear and in more prominent at low clay concentrations. This observation is especially evident at low frequencies.

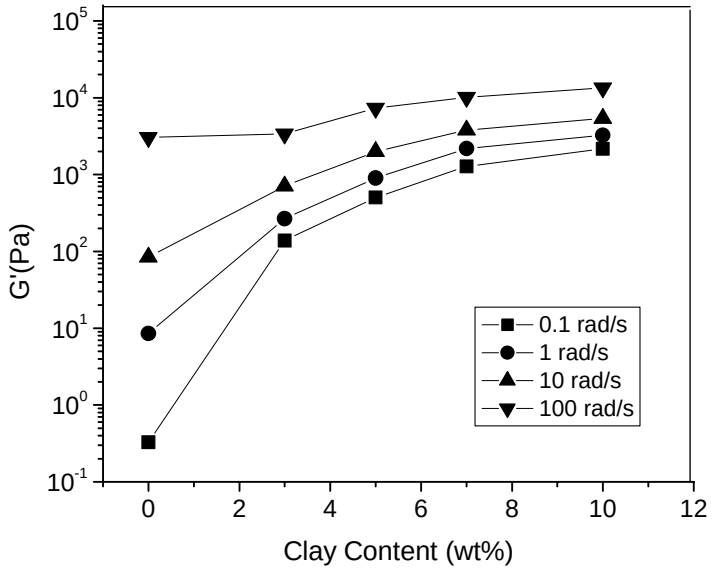

Figure 5.28 Storage modulus as a function of clay loading at different frequencies

Figure 5.29 shows the plot of storage modulus G' versus the loss modulus G'' with frequency as a parameter. This plot is analogous to the Cole–Cole plots used in dielectric spectroscopy.[44,45] These plots were first introduced by Han et. al. to investigate temperature induced changes in the microstructure of homo–polymers, block copolymers, and blends.[46–48] They proposed that if the microstructure does not change with temperature, curves of log of storage modulus versus log of loss modulus at different temperatures should coincide with each other, as observed in case of a homogeneous system. If the microstructure changes with temperatures then the curves for log G' versus log G'' will differ from each other. In heterogeneous systems such plots can be used in a

similar way to indicate structural differences between the matrix polymer and the composites at a given temperature.[49]

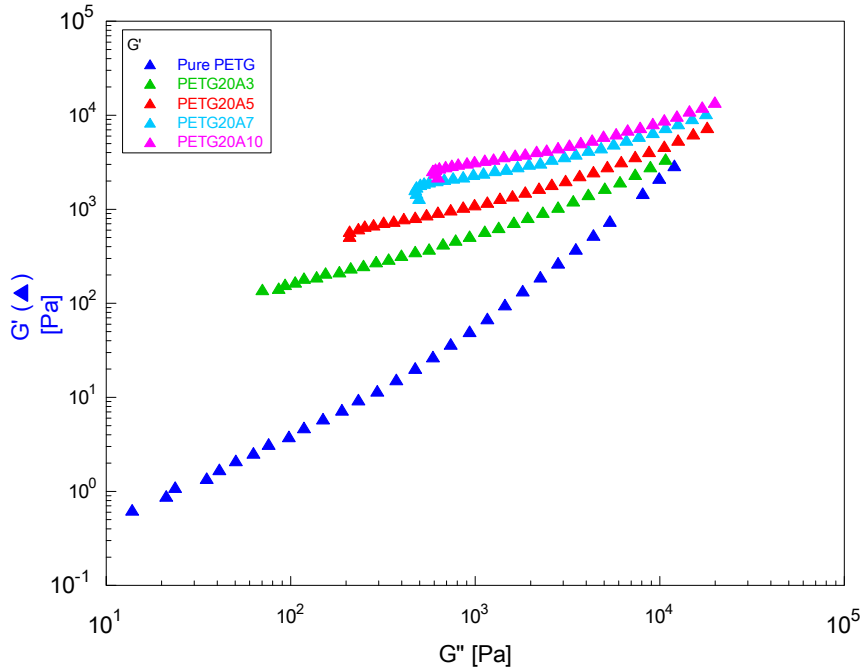

Figure 5.29 Storage modulus *G′* as a function of loss modulus *G″* for pure PETG and PETG20A nanocomposites at 250 °C

From Figure 5.29 it may be observed that the storage modulus, *G′* (for a given loss modulus *G″*) increases significantly with increasing clay content. The slope of the *G′* versus *G″* curve decreases with increasing clay content. Similar response of the first normal–stress difference versus shear stress for glass fiber filled polyethylene composites under steady shear conditions have been reported.[50] It is known in the literature that there is a qualitative similarity between the plots of first normal–stress difference versus shear stress and *G′* versus *G″*. Thus the shift in slope of the *G′* versus *G″* curves indicates that the microstructure of PETG20A nanocomposites changes significantly with the incorporation of clay in PETG matrix.

5.4 Conclusions

In this work nanocomposites of PETG with Cloisite 20A clay were prepared at different clay loadings, viz. 3, 5, 7 and 10 wt% of the organo–MMT by melt–compounding using a twin–screw extruder. Dynamics of the nanocomposites were investigated over a broad range of temperatures and frequencies using DRS and DMTA and related to their nanomorphology through WAXD, TEM, and rheology. The results of processing parameters study showed increased intercalation for the nanocomposite prepared at extrusion screw speed of 100 rpm. Hence, the screw speed of 100rpm was used to prepare PETG20A nanocomposites.

WAXD data of the nanocomposites showed a shift to lower 2θ angles and the presence of well defined diffraction peaks which manifest the formation of intercalated nanocomposites. TGA showed that the thermal stability of the nanocomposites improved by about 25 °C at low clay loadings of 3 wt%. However, this increased relatively slowed down to 5 °C for each increasing clay loading.

DMTA shows that the dynamic storage modulus increases over the entire range of temperatures studied after inclusion of clay in the polymer matrix with increasing clay content. The reinforcement effect of the clay is evident in the rubbery regime with dramatic increase up to 169 % in the storage modulus in comparison to neat PETG. A lowering of T_g is observed in the nanocomposites. Furthermore, addition of clay decreases the damping in the nanocomposites as compared to the pure polymer as a result polymer chains intercalated between the silicate galleries.

Dynamics of pure PETG and PETG20A nanocomposites as studied by DRS showed the presence of two relaxation processes. The low temperature process ($T < T_g$) was termed as β–process while the high temperature was called the α–process which have been assigned to the local motions of the C=O polar groups and the glass–rubber transition or the segmental relaxation associated with the polymer main chain, respectively. We were not able to characterize the β–process in detail due to instrumental limitations. For pure PETG permittivity showed slight dependence on temperature in the sub–glass regime, however, considerable increase in ε' was observed in the rubbery regime. This increase in ε' was attributed to the electrode polarization effects arising from ionic conduction. The reduced relaxation times of the segmental dynamics of this

copolyester were characterized by a shift in the α–process towards higher frequencies with increasing temperature. This behavior was attributed to the dissipated thermal energy that assists the polar groups to follow the motion of the alternating electric field. The dielectric data was fitted reasonably well to the semi–empirical HN equation. The narrow distribution of the values of HN–parameter *b* indicated strong asymmetric α relaxation in pure PETG. The presence of clay platelets accelerated the α relaxation dynamics. Only one relaxation was identified in pure PETG at $T > T_g$, whereas two relaxation modes (α and MWS) were retrieved from the composites data. From the permittivity studies it was shown that addition of clay platelets to the polymer significantly increases the dielectric permittivity of the nanocomposites with increasing clay content up to 7 wt% before attaining a plateau at 10 wt%. This behavior was understood in terms of decreased intercalation of PETG chains in the silicate galleries for PETG20A10 as compared to PETG20A7. A clear effect of clay loading on ac conductivity was observed with significant increase in conductivity which was attributed to the ability of the clay platelets to facilitate ion transfer through the inter– and intra–regions of the silicate galleries.

A direct comparison can be done between the DRS and the DMTA results from the tan δ, which shows excellent agreement between the accelerated α–relaxation dynamics of PETG on addition of 20A clay as studied by DRS and DMTA. The observed accelerated α–relaxation dynamics of PETG20A nanocomposites may be due to the plasticization effect of the low molecular organic intercalant used to modify the 20A clay or by considering that the flat clay platelets divide the bulk polymer into smaller domains reducing the intermolecular cooperativity between the polymer chains. At this point it is not very clear, which is the dominant effect in reducing the T_g in the nanocomposites.

In melt rheology, viscosity and modulii increased with incorporation of clay into PETG. Linear viscoelastic properties of the nanocomposites at different clay loadings show that the filler particles have a stronger effect on the low–frequency response than on the high–frequency response. This result suggests that the clay nanoplatelets influence the relaxation dynamics more than the plateau storage modulus with pronounced deviation from the terminal behavior. A qualitative correlation between rheological and morphological features was obtained from the shear–thinning exponent, which clearly

showed increased levels of dispersion of the clay platelets in the polymer matrix with increasing clay loading. Drastic structural changes were found to exist between pure PETG and PETG20A nanocomposites via a modified Cole–Cole plot.

PETG matrix degradation and color formation in the nanocomposites was also investigated. Optical clarity was maintained in the nanocomposites even at high clay loadings. However, the color deepened with increasing clay content. This change in color was attributed to the polymer degradation. Finally it was shown that the reinforcement effect of the clay apparently offsets the undesirable property deterioration that would be expected from this molecular weight degradation.

REFERENCES

1. M. B. Ahmad, J. O'Mahony, M. Huglin, T. Davis, A. Ricciardone, *J. Appl. Polym. Sci.* **56** 397 (1995)
2. M. Gelfer, C. Burger, A. Fadeev, I. Sics, B. Chu, B. S. Hsiao, A. Heintz, K. Kojo, S. L. Hus, M. Si, M. Rafailovch, *Langmuir* **20** 3746 (2004)
3. W. Xie, Z. Gao, W. P. Pan, D. Hunter, A. Singh, R. Vaia, *Chem. Mater.* **13** 2979 (2001)
4. W. Xie, Z. Gao, K. Liu, W. P. Pan, R. Vaia, D. Hunter, A. Singh, *Thermochim Acta* **339** 367 (2001)
5. R. A. Kalgaonkar, J. P. Jog, *J. Macromol. Sci. Part B – Phys.* **B43** 421 (2004)
6. P. H. Nam, P. Maiti, M. Okamoto, T. Kotaka, N. Hasegawa, A. Usuki, *Polymer* **42** 9633 (2001)
7. P. J. Yoon, D. L. Hunter, D. R. Paul, *Polymer* **44** 5341 (2003)
8. T. D. Fornes, P. J. Yoon, D. R. Paul, *Polymer* **44** 7545 (2003)
9. J. C. Matayabas, S. R. Turner, Nanocomposite Technology for Enhancing the Gas Barrier of Polyethylene Terephthalate, in: T. J. Pinnavaia, G. W. Beall, (Eds.) Polymer–Clay Nanocomposites, John Wiley & Sons: New York (2000) pp 207 (Chapter 11)
10. B. J. Chisholm, R. B. Moore, G. Barber, F. Khouri, A. Hempstead, M. Larsen, E. Olson, J. Kelly, G. Balch, J. Caraher, *Macromolecules* **35** 5508 (2002)
11. R. A. Vaia, E. P. Giannelis, *Macromolecules* **30** 7990 (1997)

12. R. A. Vaia, K. D. Jandt, E. J. Kramer, E. P. Giannelis, *Macromolecules* **28** 8080 (1995)
13. J. Chang, D. Park, *J. Polym. Sci. Part B: Polym. Phys.* **39** 2581 (2001)
14. P. Svoboda, C. Zeng, H. Wang, L. J. Lee, D. L. Tomasko, *J. Appl. Polym. Sci.* **85** 1562 (2002)
15. N. K. Kalfoglou, *J. Appl. Polym. Sci.* **32** 5247 (1986)
16. J. D. Ferry Viscoelastic properties of polymers, Third Edition, Wiley: New York (1980) pp 264
17. The glass transition temperature of PETG grade GN071 is 82 °C as determined from the peak maximum of the DMTA scan
18. S. Havriliak, S. Negami, *J. Polym. Sci. Part C* **14** 99 (1966)
19. S. Havriliak, S. Negami, *Polymer* **8** 161 (1967)
20. R. Richert, C. A. Angell, *J. Chem. Phys.* **21** 9016 (1998)
21. S. Havriliak, D. G. Watts, *Polymer* **27** 1509 (1986)
22. T. A. Ezquerra, F. J. Balta – Calleja, H. G. Zachmann, *Acta Polym.* **44** 18 (1993)
23. C. Alvarez, I. Sics, A. Nogales, Z. Denchev, S. S. Funari, T. A. Ezquerra, *Polymer* **45** 3953 (2004)
24. O. Becker. G. P. Simon, T. Rieckmann, J. Forsythe, R. Rosu, S. Volker, M. O. Shea, *Polymer* **42** 1921 (2001)
25. R. A. Kalgaonkar, S. Nandi, S. S. Tambe, J. P. Jog, *J. Polym. Sci. Part B: Polym. Phys.* **42** 2657 (2004)
26. Y. –H Lee, A. J. Bur, S. C. Roth, P. R. Start, *Macromolecules* **38** 3828 (2005)
27. J. C. Maxwell, Electricity and Magnetism, Clarendon: Oxford (1982)
28. R. W. Sillars, *J. Inst. Electr. Eng.* **80** 378 (1937)
29. K. W. Wagner, *Arch. Elektrotech.* **2** 371 (1914)
30. P. B. Macedo, C. T. Moynihan, J. H. Simmons, R. Bose, *Phys. Chem. Glasses* **13** 171 (1972)
31. A. Kanapitsas, P. Pissis, A. Estrella, *Eur. Polym. J.* **35** 923 (1999)
32. P. D. Aldrich, R. L. McGee, S. Yalvac, J. E. Bonekamp, S. W. Thurow, *J. Appl. Phys.* **62** 4504 (1987)
33. G. Perrier, A. Bergeret, *J. Appl. Phys.* **77** 2651 (1995)

34. G. M. Tsangaris, G. C. Psarras, E. Manolakaki, *Adv. Comput. Lett.* **8** 25 (1999)
35. V. R. Rao, M. H. Shridhar, *Mater. Sci. Eng. A*,73 (35)
36. A. K. Jonscher, *Nature (London)* **267** 673 (1977)
37. A. K. Jonscher Dielectric Relaxation in Solids, Chelsea Dielectrics Press: London (1983)
38. A. Kanapitsas, P. Pissis, R. Kotsilkova, *J. Non–Cryst. Solids* **305** 204 (2002)
39. E. P. M. Williams, J. C. Seferis, C. L. Wittman, G. A. Parker, J. H. Lee, J. –D. Nam, *J. Polym. Sci. Part B: Polym. Phys.* **42** 1 (2004)
40. A. R. von Hippel, Dielectrics and Waves, Artech: Boston (1995) pp 5
41. T. J. Pinnavaia, G. W. Beal, Ed. Polymer–layered silicate nanocomposites, New York: Wiley (2001)
42. C. D. Han, Multiphase flow in polymer processing, New York; Academic Press (1981)
43. R. Wagener, T. J. G. Reisinger, *Polymer* **44** 7513 (2003)
44. K. S. Cole, R. H. Cole, *J. Chem. Phys.* **9** 341 (1941)
45. S. Havrileak, Jr., S. J. Havriliak, Dielectric and mechanical relaxation in materials: analysis, interpretation, and application to polymers, Hanser: Munich, (1997)
46. C. D. Han, K. W. Kem, *Polym. Eng. Rev.* **2** 135 (1983)
47. H. K. Chuang, C. D. Han, *J. Appl. Polym. Sci.* **29** 2205 (1984)
48. C. D. Han, J. Kim, J. K. Kim, *Macromolecules* **22** 383 (1989)
49. C. D. Han, J. Kim, *J. Polym. Sci. Part B: Polym. Phys.* **25** 1741 (1987)
50. T. Kitano, T. Kataoka, Y. Nagatsuka, *Rheol. Acta.* **23** 20 (1984)

CHAPTER 6

PETGCNT Nanocomposites

This chapter focuses on fabrication of PETG based MWCNT nanocomposites using simple melt processing technique, and understanding their viscoelastic properties through a series of experiments performed under various conditions of sinusoidal shear deformations. Both linear as well as non–linear rheological studies are discussed. To gather a better understanding between microstructure–property relationship of the nanocomposites, the electrical conductivity, and complex permittivity of the nanocomposites are also described.

Part of the work presented in this chapter has been accepted for publication:

1) R. A. Kalgaonkar, J. P. Jog, *Polym. Int.* Accepted (April 2007)

6.1. Introduction

In the previous chapters our discussion mainly focused on nanocomposites based on layered silicates, which have one dimension in nanometer size. Nanocomposites based on nanofillers, which have two dimensions in nanometer size, would form the basis of an ideal comparative study. Carbon nanotubes are such materials. Since their discovery polymer nanocomposites based on carbon nanotubes (CNT) have attracted much academic and industrial interest as researchers strive to enhance the polymeric material properties via nanosacle reinforcement.[1] These nanocomposites have the obvious potential as lightweight technological materials having unprecedented mechanical, thermal and electronic properties. Due to their very large surface area per unit volume the properties of the nanocomposites differ extensively than those of the conventional composites. As many important chemical and physical properties are governed by material surface area, these differ considerably in nanocomposites than many larger dimension materials. For fillers having fibrous or foil shapes area per unit volume is inversely proportional to the fiber diameter or foil thickness, respectively. Thus, the smaller these dimensions are, the larger will be the surface area per unit volume of these materials. CNTs have a fibrous shape and very large aspect ratios to the tune of 1000–10000. As reported in chapter 2, the combination of this high aspect ratio, small size, extremely low density and exceptionally high mechanical strength and stiffness, CNT based polymer nanocomposites exhibit uniquely superior physical and mechanical property improvement at very low loadings of CNTs as compared to conventional microcomposites.

A study of polymer nanocomposites that emphasizes the relationships between their structure and their mechanical and rheological properties is of much importance considering their fabrication and final applications. Dynamic mechanical analysis and oscillatory shear rheology are powerful tools, which provide important information on the internal microstructure of the nanocomposites, the state of dispersion of CNTs, their orientation and aspect ratio, as well as the effects of particle–particle interactions in CNTs and particle–polymer interactions on the viscoelastic behavior of the nanocomposites. Therefore, an understanding of the viscoelastic properties of polymer

nanocomposites, both in solid and molten state is essential from processability and structure–property point of view.

Most of the studies based on polymer nanocomposites report increase in the elastic modulus of the nanocomposites and a change of viscoelastic behavior in the nanocomposites to solid-like from the liquid–like behavior observed for the unfilled polymers (see chapter 2 for details). This behavior has been attributed to the formation of interconnected structures of anisometric fillers, or formation of percolated network, or adsorption of polymer molecules on filler surfaces. All these phenomena lead to the immobilization of polymer chains, due to retardation in their relaxation mechanism. Similar observations in property modifications have been reported for polymer/carbon nanotube nanocomposites by various researchers.[2–6] However, some doubts still persist about the origins of the reinforcement effects of CNTs in polymer nanocomposites. It is important from the applications point of view to study the reinforcement effect of the nanocomposites for a better understanding of the mechanisms that underline the property improvement in CNT based polymer nanocomposites.

This chapter focuses on fabrication of PETG based CNT nanocomposites using simple melt processing technique, and understanding their viscoelastic properties through a series of experiments performed under various conditions of sinusoidal shear deformations. The reinforcement effect of CNTs in polymer nanocomposites is estimated by investigating the full spectrum of viscoleastic properties (viz. from solid to melt) of CNT based polymer nanocomposites. Furthermore, the dynamic mechanical and rheological experimental data obtained from this work will be representative of the viscoelastic behavior of amorphous polymer/CNT nanocomposites in the glassy and rubbery regimes as well as in molten state. Another manifestation of the reinforcement mechanism of the polymer nanocomposites is possible by studying the electrical properties of the nanocomposites. The dielectric response of polymer nanocomposites can provide additional insight about the formation of an interconnected filler network at a concentration above the percolation threshold.[7–10] Thus, to gather a better understanding of the microstructure–property interlinks in the nanocomposites, we have also investigated the electrical conductivity, and complex permittivity, as well as the

morphology of the nanocomposites. Finally, the viscoelastic behavior and the dielectric response of the nanocomposites are correlated with respect to their microstructure.

6.2. Experimental

6.2.1. Nanocomposite Fabrication

The nanocomposites were prepared by melt blending in a Haake Polylab internal batch-mixer. The CNTs were mixed with PETG pellets and fed to the batch mixer. The batch mixer was operated at a screw speed of 60 RPM. The batch mixer temperature was 230 °C. The run was carried out till the torque stabilized. This translated in an average residence time inside the batch-mixer of approximately 5.0 min. Before compounding, PETG was dried in an air circulatory oven at a preset oven temperature of 70 °C for 24 h. Five compositions containing a 98 : 2; 97 : 3; 95 : 5; 93 : 7 and 90 : 10 ratio in wt% of polymer to CNTs and coded as PETGCNT2, PETGCNT3, PETGCNT5, PETGCNT7, and PETGCNT10, respectively, were used in this work.

6.2.2. Nanocomposite Characterization

6.2.2.1. Thermogravimetric Analysis

PETGCNT nanocomposites were analyzed by thermogravimetric analysis using a Seiko TG/DTA 32 thermal analysis system. The scans were recorded at a heating rate of 10 °C min^{-1} under nitrogen blanket over a temperature range of 50 to 800 °C.

6.2.2.2. Dynamic Mechanical Thermal Analysis

Dynamic mechanical thermal analysis properties of the nanocomposites were studied using a Rheometrics Dynamic Mechanical Analyzer model IIIE operating in rectangular tension/compression mode. Sample films used in this study had the dimensions of 0.5 mm thickness and 10 mm width and were prepared by compression molding of the batch-mixed lumps at 230 °C for 3 minutes using a Carver press model F-15181. Temperature ramp experiments were carried out to elucidate viscoelastic properties of PETG/CNT nanocomposites. The scans were performed over a temperature range of 30 to 110 °C, heating rate of 5 °C/min, and 0.03 % strain. Each sample was

tested at a constant frequency of 10 rad s^{-1}. Prior to the tests; all sample plates were dried at least for 6 h in an air circulatory oven at a preset temperature of 70 °C.

6.2.2.3. Rheology

Rheological measurements were performed on as processed and annealed samples using an ARES rheometer (Rheometrics Scientific) fitted with 25 mm parallel plates geometry. Sample plates having the dimensions of 1 mm thickness and 25 mm diameter were prepared by compression molding of the processed lumps as explained earlier. Measurements were performed in dynamic oscillatory shear configuration at three different temperatures of 230, 240 and 250 °C, all of which were above the melting temperature of PETG. All measurements were performed in nitrogen atmosphere to avoid oxidative degradation. All sample plates were dried at 70 °C for at least 6 h before the experiments were carried out. Dynamic oscillatory shear experiments are representative of the durability of the sample under various conditions of vibrations and/or external stress. Oscillatory experiments were performed by setting small amplitude sinusoidal shear strain $\gamma(t)$ of the form

$$\gamma(t) = \gamma_0 \sin(\omega t) \qquad (5.1)$$

where, γ_0 is the strain amplitude, ω is the frequency and t is real time. In dynamic oscillatory shear experiments γ_0 was a small constant and frequency dependent elastic modulus $G'(\omega)$, viscous modulus $G''(\omega)$, complex viscosity (η^*) and phase angle (δ) were measured over a frequency range of 10^{-1} to 10^2 rad s^{-1}. Prior to carrying out the frequency sweeps, strain sweep experiments were performed to ascertain the dynamic data was obtained in the linear viscoelastic region. Once the material was mounted sufficient time was given for the sample to stabilize before the run was started. A strain amplitude which was fixed at 1 % was used for all the dynamic experiments reported in this work.

Steady shear experiments were preformed using an ARES rheometer using the parallel plate geometry. Sample plates having similar dimensions as used in the dynamic experiments were used. Experiments were performed over a strain rate range of 10^{-2} to

10^1 s^{-1} at 240 °C under nitrogen blanket. The shear viscosity (η) was recorded as a function of shear rate $(\dot{\gamma})$.

6.2.2.4. Dielectric Relaxation Spectroscopy

Dielectric relaxation spectroscopy was performed as a function of frequency (10^0 to 10^7 Hz) and temperature (30 to 120 °C with increments of 10 °C) using a Novocontrol broadband dielectric spectrometer with the ZGS active sample cell. Samples discs having an uniform thickness of 0.5 mm and 20 mm diameter were prepared by compression molding as explained earlier. Samples discs were sandwiched between circular gold electrodes (20 mm diameter) and placed in the ZGS active sample cell. In this chapter we present the dielectric relaxation spectra of complex dielectric permittivity, $\varepsilon^* = \varepsilon' - i\varepsilon''$ (where ε' represents the real part of complex dielectric permittivity and ε'' the imaginary part or dielectric loss), and electrical conductivity (σ') for pure PETG and PETGCNT nanocomposites.

6.2.2.5 Morphology

The morphology of the CNTs in PETG was investigated with a scanning electron microscope (Leica–440), operating at an accelerating voltage of 20 kV. The specimens were prepared by cryo–fracturing the as compounded lumps in liquid nitrogen. The samples were sputtered with gold to prevent charging.

6.3. Results and Discussion

6.3.1. Thermogravimetric Analysis

Thermogravimetric Analysis (TGA) is used to study the thermal stability of polymeric materials. In Figure 6.1 we show the TGA scans of pure PETG and PETGCNT5 nanocomposite. A remarkable difference can be observed between the two scans. To compare the thermal stability we compare the 50 % weight loss for both the samples. On addition of CNTs the degradation temperature for 50 % weight loss increases from 410 °C in pure PETG to 465 °C in PETGCNT5. This increase of 55 °C in the 50 % weight loss can be attributed to the increased thermal stability of the polymer on addition of CNTs.

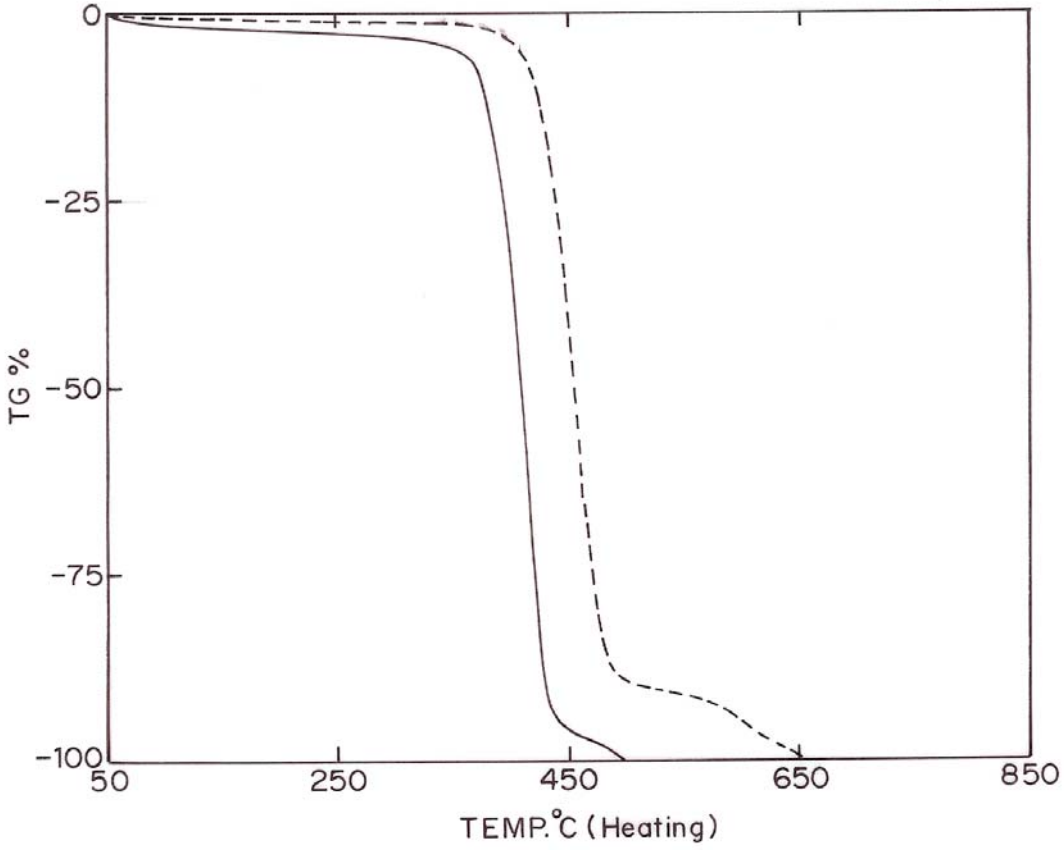

Figure 6.1 TGA scans of pure PETG (—) and PETGCNT5 nanocomposite (----)

6.3.2. Solid–State Viscoelastic Behavior

Dynamic mechanical thermal analysis (DMTA) is an important tool to study the structure–property relationships in polymer composites. DMTA probes essentially the relaxations in polymers, thereby providing a method to understand the mechanical behavior and the molecular structure of these materials under various conditions of stress and temperature. In this study we report the effects of different CNT loadings on the tensile storage modulus E', tensile loss modulus E'', and tan δ as the ratio of loss and storage modulus as a function of temperature between 30 to 110 °C at a constant frequency of 10 rad s^{-1}, using DMTA as a method of quantitative characterization. The

moduli relate to the stiffness of the composite material and tan δ (damping) to the molecular motions under specific conditions of external stress and temperature.

In Figure 6.2 the dynamic storage modulus of pure PETG and its nanocomposites as a function of temperature are summarized. It can be seen from the figure that all the nanocomposites studied here show an increase in the storage modulus over the entire temperature range studied. However, in the glassy regime ($T < T_g$) this increase is minimal with all the nanocomposites having the storage modulus values close to those of the pristine polymer. This shows lesser contribution of CNT towards the stiffness of the composite material at lower temperatures. Moreover, this contribution is almost independent of the CNT loadings. A different picture arises in the rubbery regime ($T > T_g$) with the modulus increase in nanocomposites becoming more prominent as well as composition dependent.

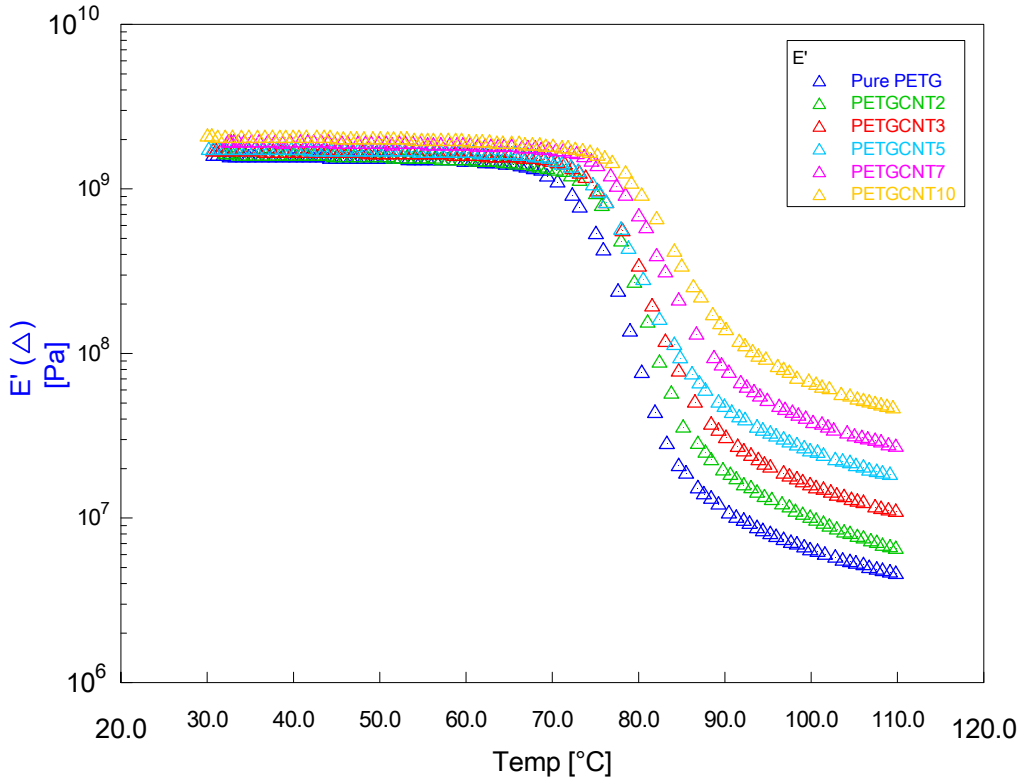

Figure 6.2 Temperature dependence of storage modulus (*E'*) for pure PETG and PETGCNT nanocomposites

Table 6.1: Relative modulus of pure PETG and PETGCNT nanocomposite in the sub glass regime and in the rubbery regime

Sample	E'_r[a]	
	40 °C	**100 °C**
PETGCNT2	1.02	1.56
PETGCNT3	1.07	2.48
PETGCNT5	1.10	4.00
PETGCNT7	1.23	5.90
PETGCNT10	1.31	10.41

[a] Relative modulus was calculated by considering storage modulus of the matrix resin and the nanocomposites at two temperatures: one in the glassy regime and another in the rubbery regime.

The effectiveness of CNTs as nano fillers can be explained by considering the relative modulus $\left(E'_r = \frac{E'_{nc}}{E'_p} \right)$ estimated as a function of temperature. Table 6.1 presents E'_r at two temperatures viz. 40 °C where, $T < T_g$ and 100 °C where, $T > T_g$. It can be observed from the table that in the sub glass-transition regime, PETGCNT2, PETGCNT3, PETGCNT5, PETGCNT7, and PETGCNT10 show increases of 2, 7, 10, 23, and 31%, respectively. Whereas, in the rubbery regime the increase in the modulus of PETGCNT2 is 56 %, that of PETGCNT3 is 148 %, for PETGCNT5 it is 300 %, for PETGCNT7 is 490 %, and that for PETGCNT10 the modulus increase is 941 %. Nielsen and co–workers[11] have observed a similar kind of behavior in the past for polymer composites prepared using rigid fillers and have attributed this phenomenon to filler particle agglomeration. They argued that in rigid agglomerates where relaxation is restricted at particle–particle points of contact, increase the modulus more than in perfectly dispersed systems where filler particles are free from each other. In case of polymer/CNT composites even in well-dispersed composite systems there are evidences of existence of percolated filler network.[12] Thus, the above theory may also be true in case of

polymer/CNT nanocomposites. If the forces on the filler network can overcome the retardation in polymer chain relaxation at the particle–particle and polymer–particle contact points, the modulus will decrease. As, in the glassy regime the modulus of polymer is very high, it can exert large forces on the filler network so as to enable particle–particle motion. Hence, the modulus values observed in this region are more as an effect of the bulk polymer rather than as the reinforcement effect of the filler. However, in the rubbery regime the modulus of the polymer drops significantly (by more than 2 decades in case of PETG). Thus, the deformation forces produced in the material may not be enough to overcome the friction between the CNTs, which form the percolated network. This will result in a much higher modulus in the rubbery regime, which will be characteristic of the reinforcing effect of the filler used. Moreover, if the above discussion is true then the modulus of the composite material in the rubbery regime should increase with increasing filler content. This is exactly what was observed in the DMA experimental data of PETGCNT nanocomposites, with PETGCNT10 showing highest increase in the modulus. Furthermore, this increase in the matrix modulus is more pronounced in case of amorphous polymers as compared to the crystalline or semi–crystalline polymers. This is due to the presence of crystallites in crystalline polymers, which impart higher forces even in the rubbery regime thus hindering the particle–particle motion of the filler network and reducing the reinforcing effect of the filler as compared to that observed in an amorphous polymer composite.

The segmental (α) – relaxation in polymers associates with the glass transition temperature of the polymer and is generally defined as the peak maximum of the viscous modulus E'' curve. The structural arrangements associated with the segmental mobility of the polymeric chains, that produce a dynamic mechanical response, govern the glass transition temperature. The behavior of the viscous modulus as a function of temperature that displays the prominent α- relaxation for PETG and PETGCNT nanocomposites are shown in Figure 6.3. The figure indicates that the T_g of PETGCNT nanocomposites exceeds than that of pure PETG. This can be attributed to the restricted mobility of the polymeric chains in the nanocomposites as an effect of the presence of the filler network. Further, it can also be observed that above the T_g the nanocomposites show slightly

higher loss modulus than pure polymer, which increases with increasing CNT content, because of the friction between the filler particles at points of contact.

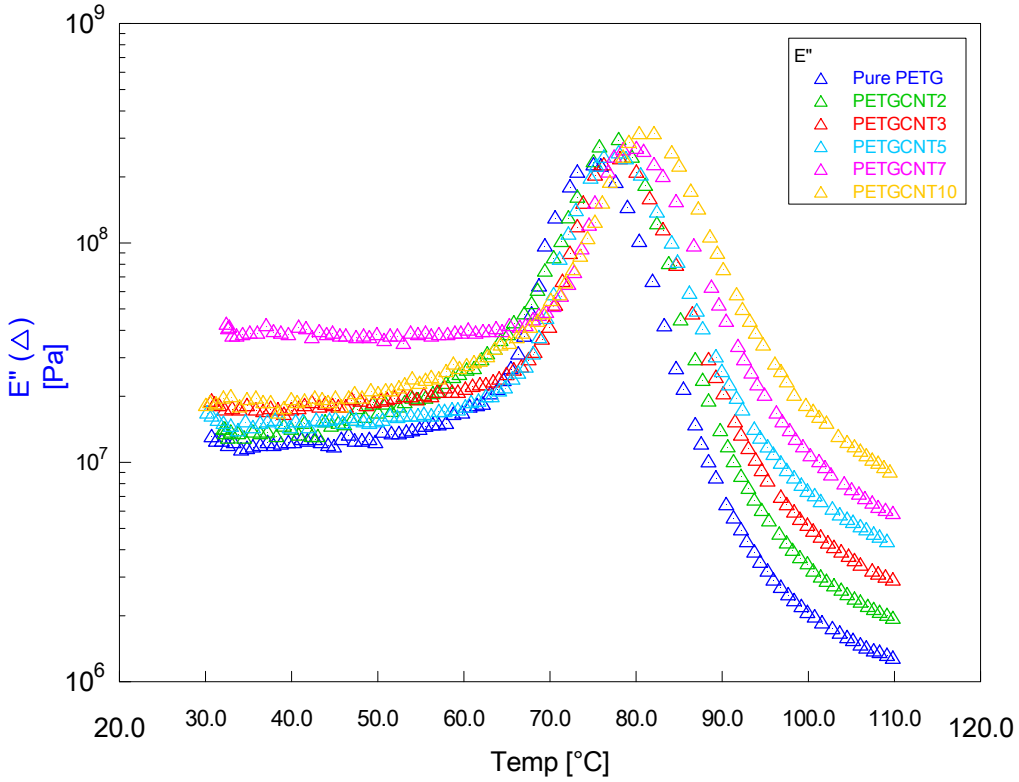

Figure 6.3 Temperature dependence of loss modulus (*E″*) for pure PETG and PETGCNT nanocomposites

The loss factor tan δ is a damping term that can be related to the impact resistance of the polymeric material. It is very sensitive to the structural transformation of the materials and can be calculated as a ratio of the viscous modulus to the elastic modulus (*E″/E'*). Figure 6.4 shows the effect of temperature dependence of mechanical loss factor or tan δ on CNT content for pure PETG and PETGCNT nanocomposites. With the incorporation of CNT in to PETG matrix shifts the tan δ peak values of PETGCNT nanocomposites to higher temperatures. Also the temperature difference increases with increasing CNT content, with PETGCNT7 showing maximum increase in the peak temperature than the pure polymer. Elevation in the tan δ peak temperature can be considered as a measure of favorable interfacial interaction between the polymer and the filler.

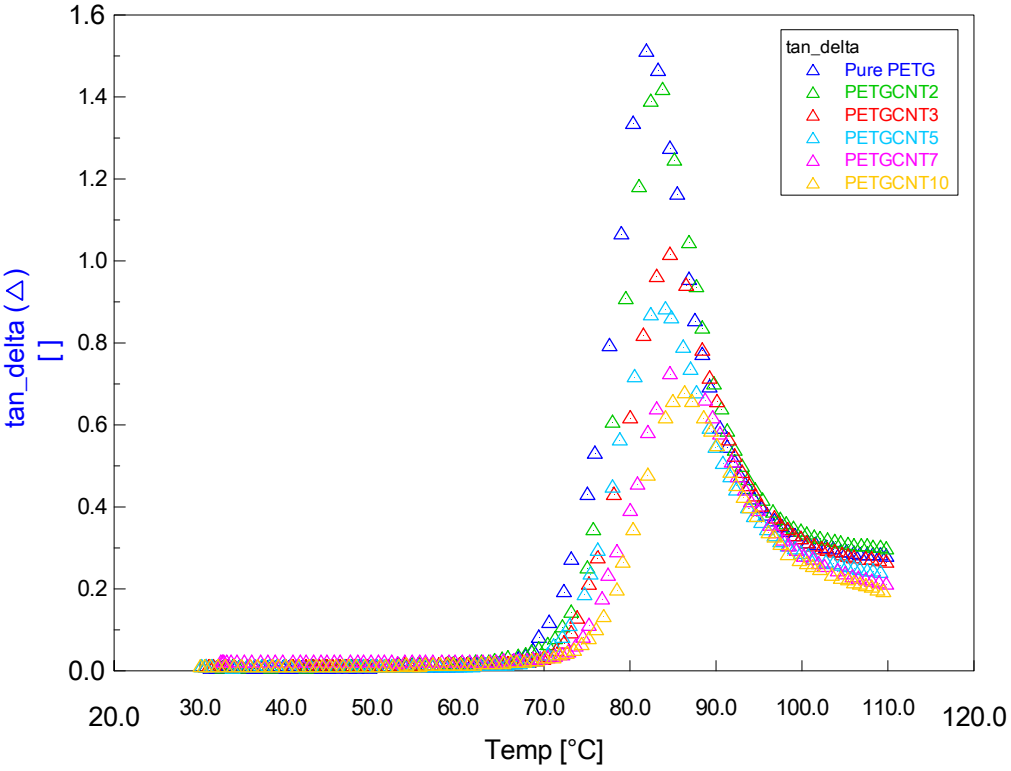

Figure 6.4 Temperature dependence of loss factor tan δ for pure PETG and PETGCNT nanocomposites

In PETGCNT nanocomposites, the incorporation of CNT in the polymer matrix reduces the intensity of tan δ peak. The damping in polymeric materials is sensitive of segmental mobility of the polymer chains. In composites it is indicative of the interfacial interaction between the polymer and the filler as the chain mobility of the polymer close to the filler surface differs from that of the bulk polymer. Strong interfacial interaction between the polymer and the filler tends to restrict the polymer mobility thereby reducing the damping. Moreover, in addition to strong interfacial interaction, presence of a percolated filler network may also reduce the damping as it also leads to retardation of segmental motion of the polymer chains. Both these effects can go hand in hand or individually for the filler to act as an effective reinforcing agent. However, better interfacial interaction between CNTs and the polymer is accompanied by an increase in

the tan δ peak temperature.[13] Importantly, the results shown in Figure 6.4 clearly shows that the reduction in peak intensity effect is more pronounced than the increase in the peak temperature of the nanocomposites with the intensity of the tan δ peak decreases more with increasing CNT content. This could be due to immobilization of polymer chains. Since tan δ value is directly proportional to the amorphous content in the nanocomposite, its decrease indicates decrease in the amorphous content of the nanocomposite. In an ideal case, this decrease should be balanced by an increase in crystallinity. However, PETG being completely amorphous in nature this is increase in crystallinity is not possible PETGCNT nanocomposites. Therefore the decrease in the tan δ peak values with respect to increase in CNT content can be ascribed to the formation of rigid amorphous phase resulting from the constrained amorphous phase (CAP). This suggests that the molecular motions of amorphous chains are restricted due to well–dispersed CNTs in the PETG matrix. The constrained volume of amorphous phase can arise from the formation of the percolated structure of the CNTs in the polymer matrix. Table 6.2 shows the tan δ peak values of PETGCNT nanocomposites and calculated values of the peak normalized with respect to the PETG content. The significantly lower experimental values of tan δ as compared to the normalized tan δ values indicate the existence of the constrained amorphous phase. Similar observations were made by Ogata et. al.[14] on the poly(vinyl alcohol)/montmorillonite nanocomposite system.

Table 6.2 Tan δ and normalized tan δ values at peak temperature for PETGCNT nanocomposites

Sample	Tan δ value	Normalized value of tan δ
Pure PETG	1.51	–
PETGCNT2	1.41	1.48
PETGCNT3	1.01	1.46
PETGCNT5	0.88	1.43
PETGCNT7	0.72	1.40
PETGCNT10	0.67	1.36

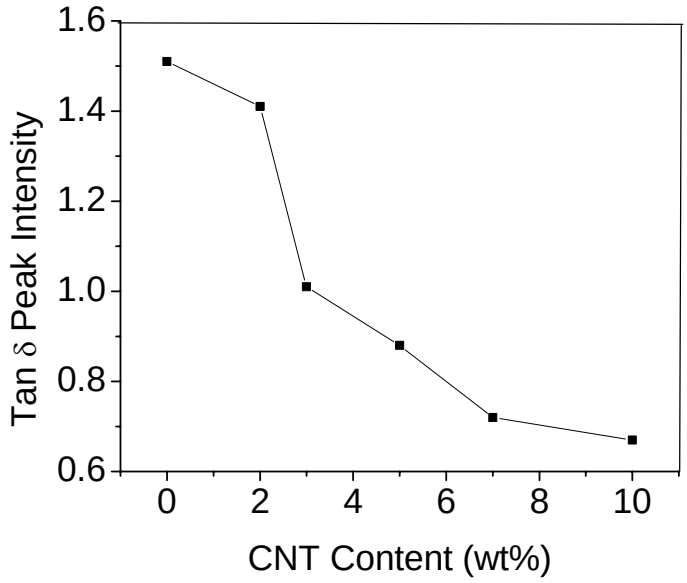

Figure 6.5 Tan δ peak intensity of pure PETG and PETGCNT nanocomposites as a function of CNT loading

Figure 6.5 shows the tan δ peak intensities as a function of CNT loading. Very interestingly, on comparing the tan δ peak intensity of PETGCNT2 and PETGCNT3 with that of pure PETG a clear distinction can be observed. The decrease in the peak intensity is significantly more for PETGCNT3 that that for PETGCNT2. It is reasonably believed that formation of a percolated network of CNTs in PETG matrix is responsible for this sudden drop in the tan δ peak intensity of PETGCNT3.

6.3.3. Melt–State Viscoleastic Behavior

6.3.3.1. Linear Rheology

To determine the linear viscoelastic region, isothermal dynamic strain sweeps were performed on pure PETG and PETGCNT nanocomposites. The linear dynamic oscillatory shear experiments in melt state on pure PETG and PETGCNT nanocomposites were investigated. It was observed that the data of the isothermal oscillatory shear experiments performed at three different temperatures viz. 230, 240, and

250 °C followed a similar trend. Hence, for the sake of simplicity we report here the rheological data for the experiments carried out at 240 °C. The storage modulus (G') and loss modulus (G'') from the isothermal oscillatory shear measurements for PETG and PETGCNT nanocomposites containing various CNT contents are presented in Figures 6.6 and 6.7, respectively.

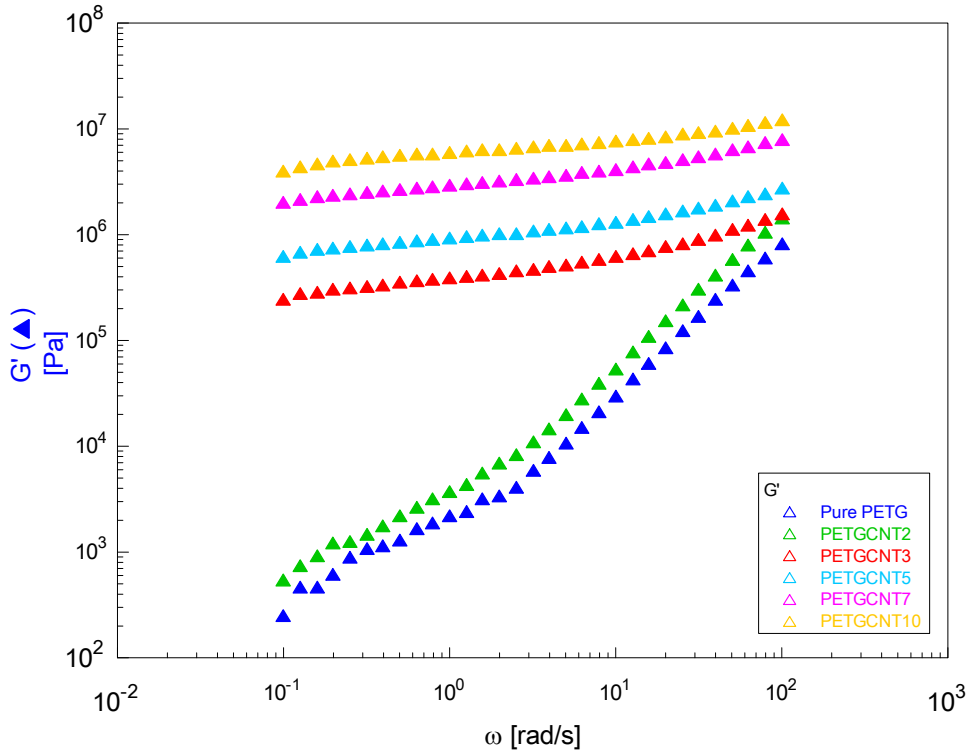

Figure 6.6 Frequency dependence of storage modulus (G') for pure PETG and PETGCNT nanocomposites

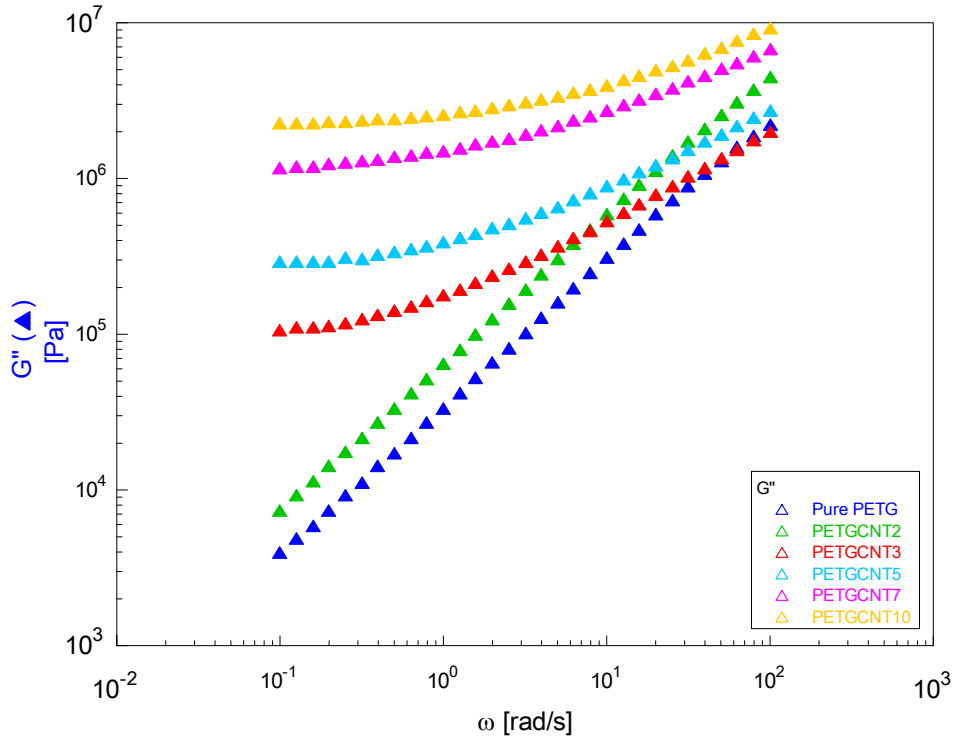

Figure 6.7 Frequency dependence of storage modulus (G'') for pure PETG and PETGCNT nanocomposites

The dramatic reinforcing effect of CNTs as a nanofiller for polymer composites is immediately apparent from Figure 6.6. It can be observed that there is tremendous increase in the (G') of the PETGCNT nanocomposites above 2 wt% CNT loading over that of pure PETG especially at low frequencies. Moreover, the storage modulus increases with increasing CNT content. At 10 wt% loading of CNT the G' changes by more than 4 orders of magnitude. In addition, no significant reduction in the viscous modulus of the nanocomposites relative to pure PETG was observed (see Figure 6.7). At low frequencies the pure PETG has a typical terminal regime as a Newtonian liquid with the viscoelastic behavior following the scaling properties: $G' \propto \omega^2$, $G'' \propto \omega^1$, and $\eta^* \propto \omega^0$, where η^* is the complex viscosity. In PETGCNT nanocomposites when CNT loading exceeds 2 wt% this terminal behavior completely disappears with G' and G'' becoming almost independent of ω. This is a characteristic of typical transition from liquid–like to solid–like behavior in PETGCNT nanocomposites. This suggests that the presence of

CNTs has inhibited the stress relaxation process in PETGCNT nanocomposites and this hindrance systematically increases with increasing CNT loading as is indicative from the G' curves.

The effects are also observed from the slope of the G' and G'' curves. The slopes are listed in Table 6.3. It is expected that the homopolymer–like terminal behavior should be exhibited by the polymer chains at low frequencies with slopes of 2 and 1 for G' and G'', respectively. The slopes of pure PETG G' and G'' are 1.14 and 0.93. PETGCNT2 shows almost similar slopes as those for pure PETG. When the addition of CNTs to PETG exceeds 2 wt% an increase in both the storage and loss modulus is observed, however the effect in the decrease in the slope is more pronounced for G' than for G''.

Table 6.3 Slope of G' and G'' in the terminal region of the modulus curves (Figures 6.6 and 6.7) of PETGCNT nanocomposites compared to pure PETG

Sample	CNT Content (wt %)	Slope G'	Slope G''
Pure PETG	0	1.14	0.93
PETGCNT2	2	0.99	0.92
PETGCNT3	3	0.17	0.44
PETGCNT5	5	0.13	0.33
PETGCNT7	7	0.14	0.25
PETGCNT10	10	0.14	0.21

If the addition of CNTs increases the storage modulus, it means that more energy storage takes place during deformation and decreases the slope of the curve showing almost plateau–like region. The solid–like behavior observed in the nanocomposites can arise as a result of adsorption of polymer chains to the CNT surface or due to the presence of CNT network which can retard the chain relaxations in the bulk polymer.

Indeed, our DMA studies have shown that the solid–like viscoelastic response of PETGCNT nanocomposites is due to the presence of a CNT percolating network.

To further probe whether this hypothesis is true we show in Figure 6.8 the plots of complex modulus (G^*) of pure PETG and PETGCNT nanocomposites as a function of angular frequency (ω).

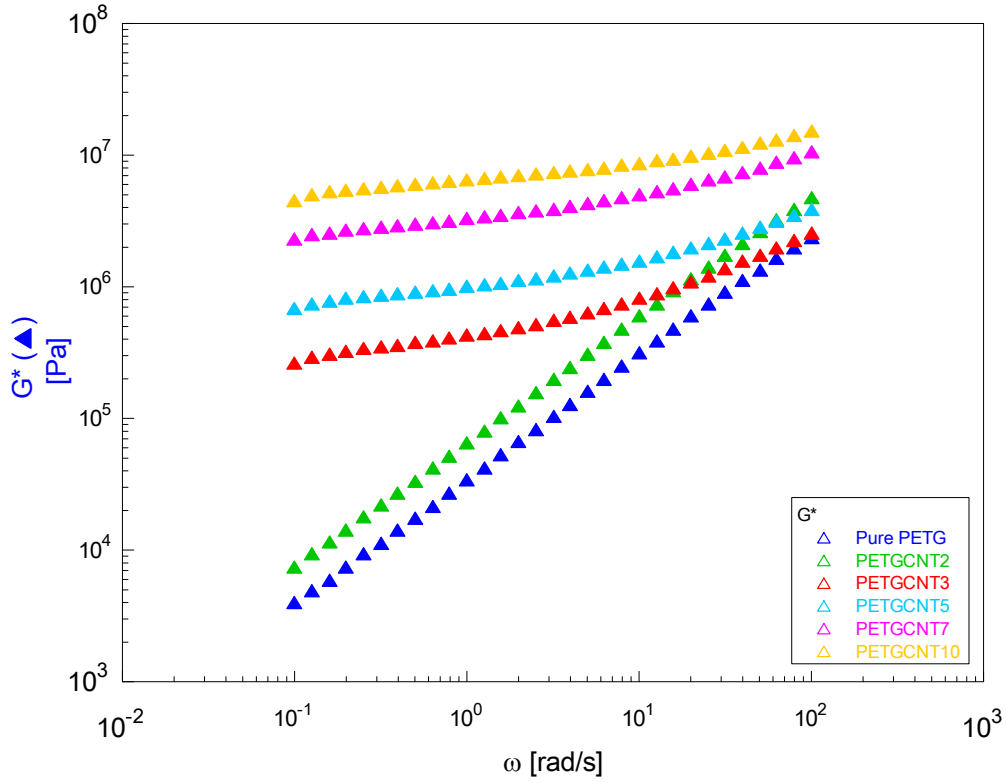

Figure 6.8 Frequency dependence of complex modulus (G^*) for pure PETG and PETGCNT nanocomposites

G^* was calculated from the dynamic measurements on the pure polymer and the nanocomposites. It is well known that pure polymers show flow behavior at almost all applied stresses, i. e. their viscosity is independent of applied stresses. However, in filled systems above the percolation threshold, flow cannot occur below a critical stress. This is termed as yield stress (τ_{yield}). The yield stress may be related to the complex modulus using the following relationship:

$$G^* = \left[\frac{\tau_{yield} + (\omega\eta^*)\gamma_0}{\gamma_0} \right] \qquad (5.2)$$

where, γ_0 is the strain amplitude. Thus, the complex modulus of pure polymers without yield stress will tend to zero at zero shear frequency. However, in presence of a filler network structure the complex modulus will show no or minimal frequency dependence. Note that while the G^* curve of pure PETG and PETGCNT2 converges to zero at $\omega \sim 0$, the complex modulus of the nanocomposites above CNT loading of 2 wt% levels off to a finite value. This shows that the solid–like behavior in PETGCNT nanocomposites is due to the presence of a percolated structure of CNTs, and the rheological percolation threshold of PETGCNT nanocomposites is reached at a CNT loading of 3 wt%.

Further evidence for the presence of a percolated CNT network in PETGCNT nanocomposites can be obtained from the shift in the G' and G'' crossover frequency ω_c. For unfilled polymer G' is much lower than G'' while for composite systems which show solid–like behavior G'>G″. Figures 6.9 (a–f) show the frequency dependence of G' and G'' for pure PETG, PETGCNT2, PETGCNT3, PETGCNT5, PETGCNT7, and PETGCNT10 respectively. From Figures 6.9a and 6.9b it can be observed that for pure PETG and PETGCNT2 G' <G″ over the entire frequency range studied. In the nanocomposites for CNT loadings of 3 and 5 % G'>G″ at low frequencies, following a solid–like viscoelastic response, with ω_c equal to 17.75 and 78.89 rad/s for PETGCNT3 and PETGCNT5, respectively (see Figures 6.9c and 6.9d). For PETGCNT7 and PETGCNT10 (Figures 6.9e and 6.9f) ω_c is not observed as G' >G″ over the entire frequency range studied. This type of rheological behavior in filled polymeric materials is a signature of formation of a percolated filler network.[15] On the basis of the mesoscopic structure, at low CNT concentrations, it is suggested that, beyond a critical CNT loading, the nanotubes are not capable of freely rotating and cannot relax completely when a small amplitude oscillatory shear is applied. This incomplete relaxation is as a result of interconnected filler network or percolation and the critical CNT loading beyond which this phenomenon is observed, is termed as the percolation threshold for the composite material. Note that G'>G″ almost for the entire frequency range studied for PETGCNT3 and PETGCNT5. This confirms the previous observations indicating that the percolation threshold for PETGCNT nanocomposites is reached at 3 wt.% of CNT loading. Moreover, in this study PETGCNT nanocomposites were fabricated using melt-

processing technique. Thus, reaching of the percolation limit at 3 wt% of nanotubes is quite significant. This threshold is little higher than that observed by Potschke et al in polycarbonate (PC)/CNT nanocomposites prepared by melt processing.[16]

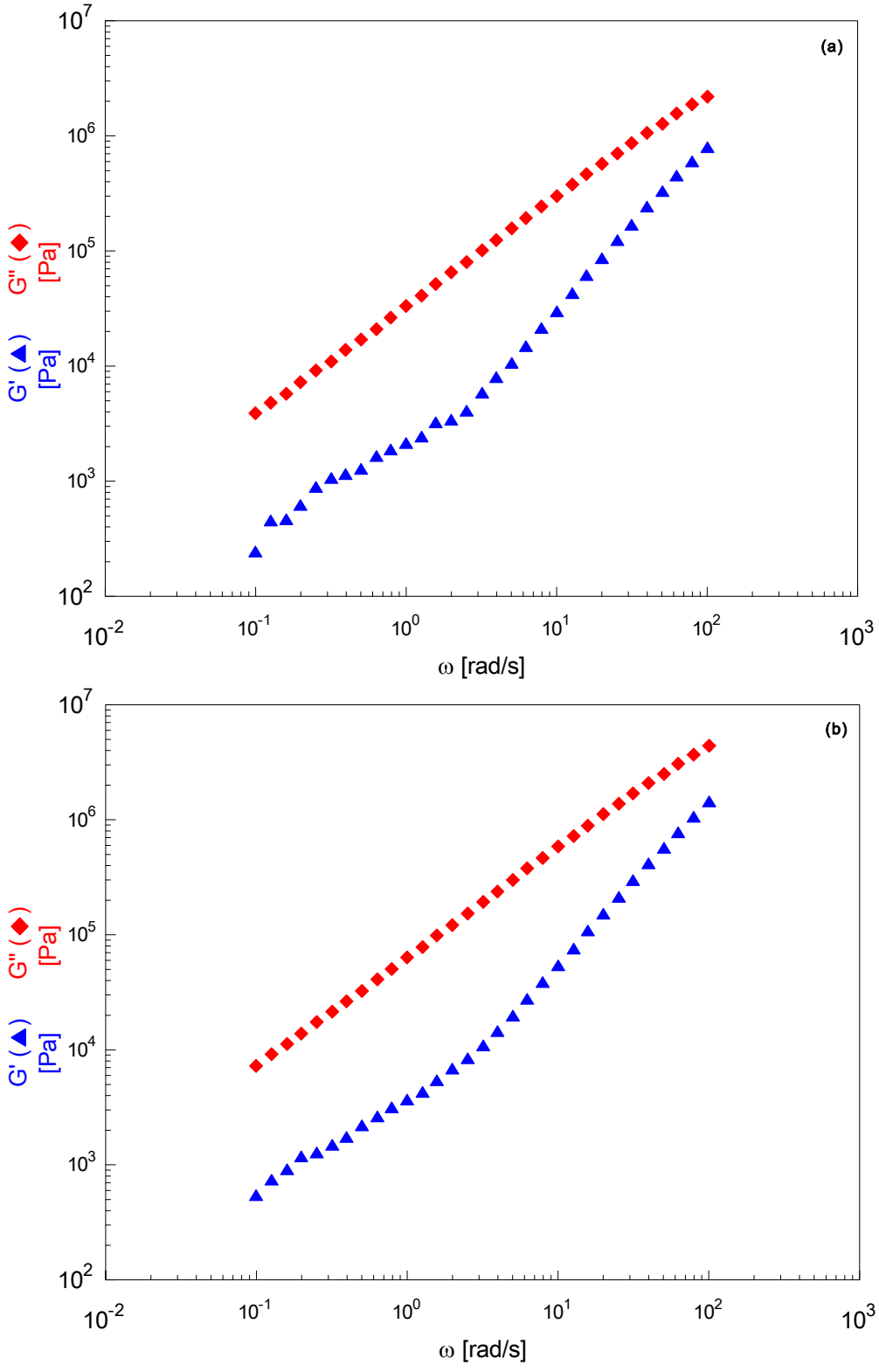

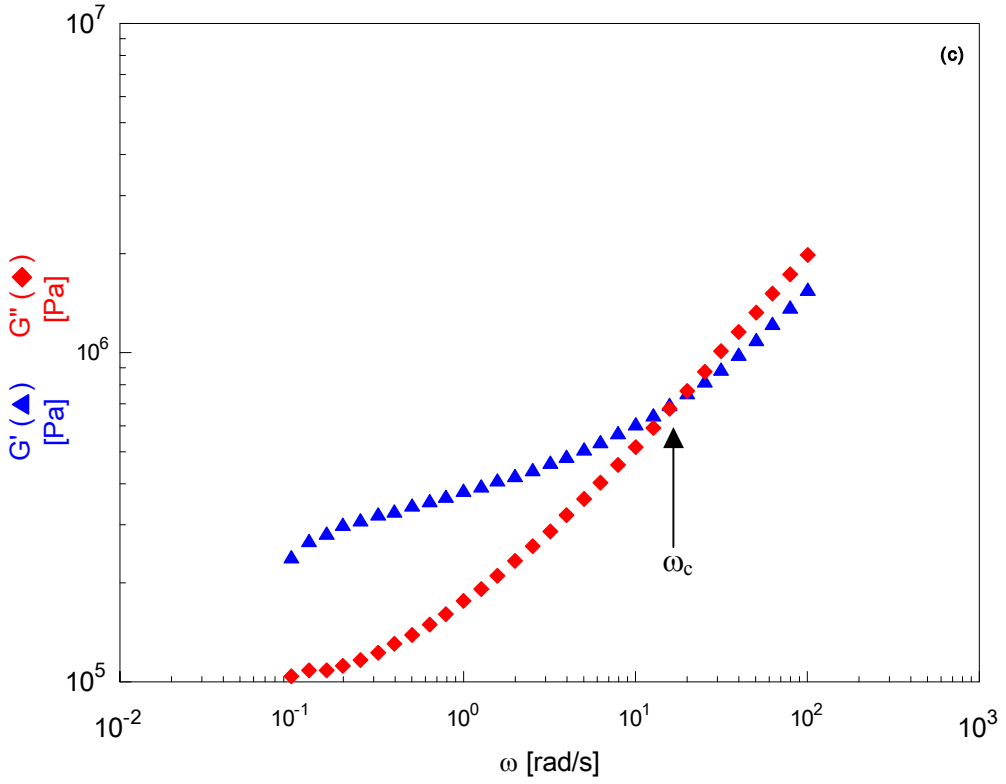
(c)
G' (▲) [Pa]
G" (◆) [Pa]
10^7
10^6
10^5
10^{-2}
10^{-1}
10^0
10^1
10^2
10^3
ω [rad/s]
ω_c

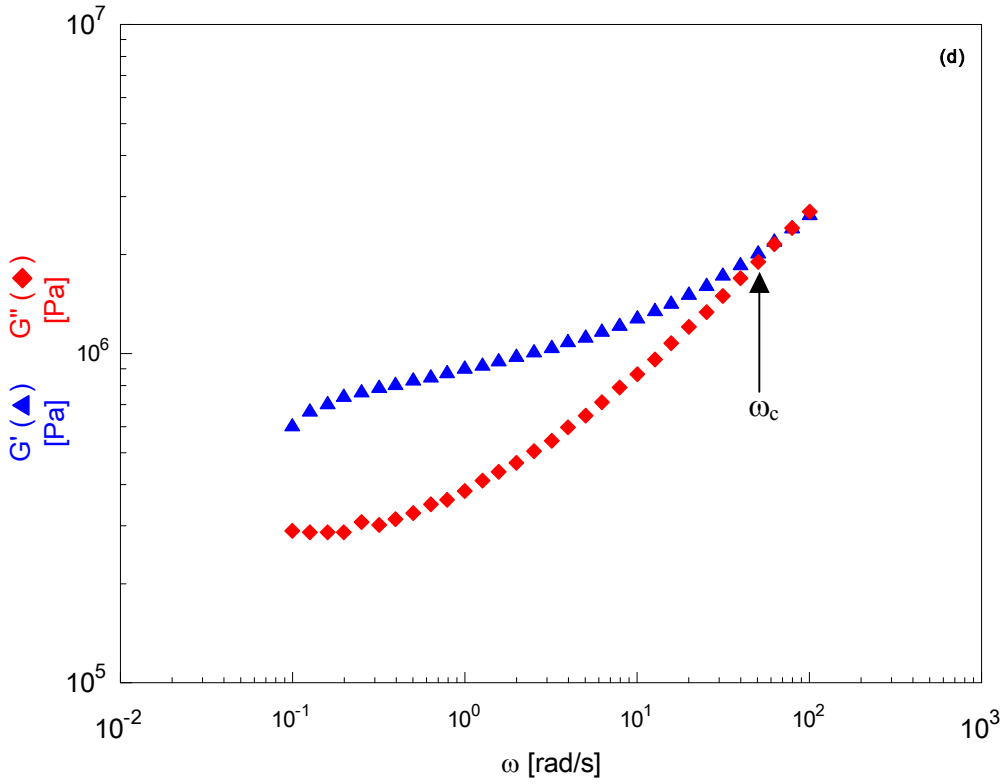
(d)
G' (▲) [Pa]
G" (◆) [Pa]
10^7
10^6
10^5
10^{-2}
10^{-1}
10^0
10^1
10^2
10^3
ω [rad/s]
ω_c

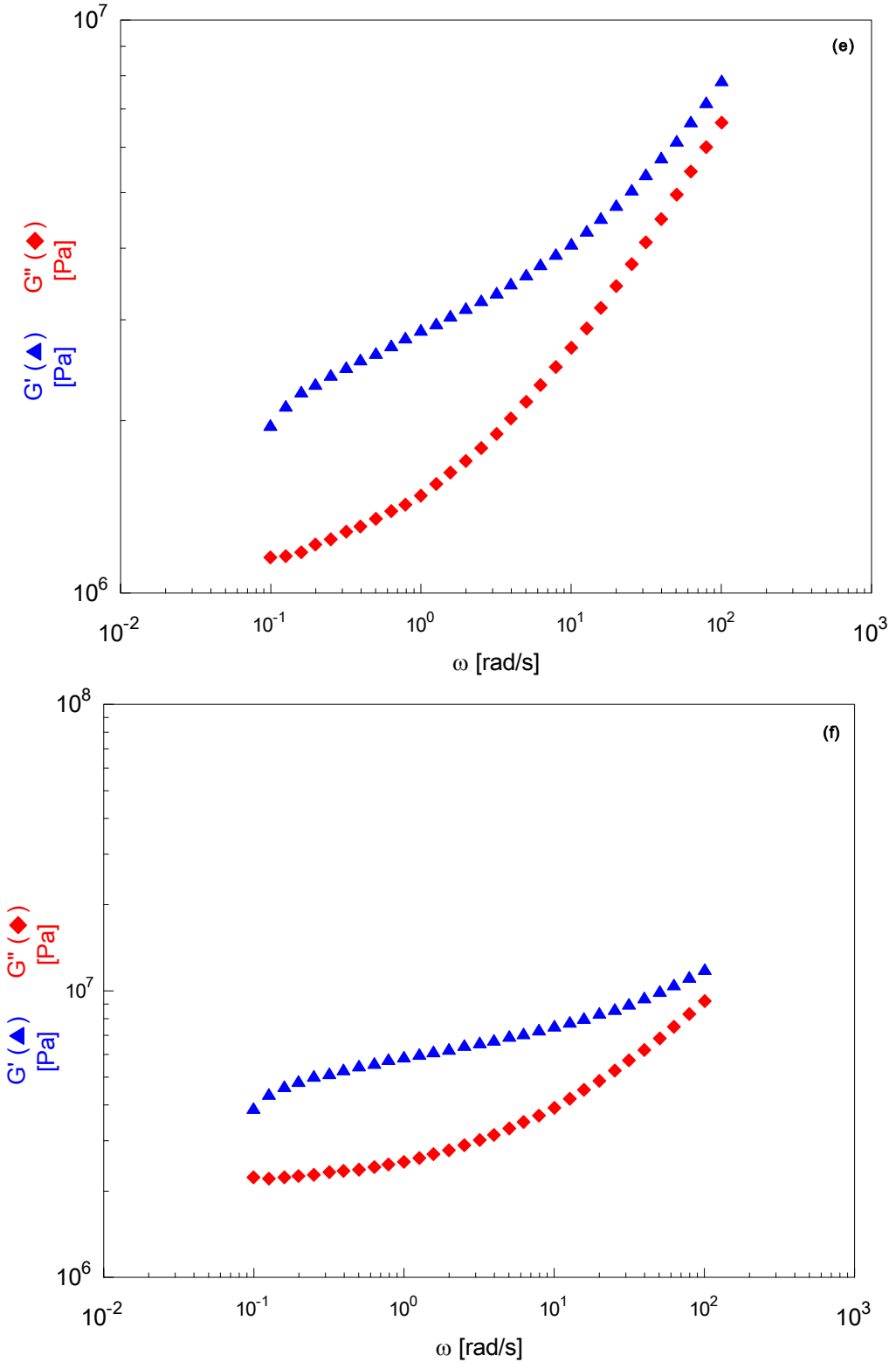

Figure 6.9 Frequency dependence of *G′* and *G″* for (a) pure PETG, (b) PETGCNT2, (c) PETGCNT3, (d) PETGCNT5, (e) PETGCNT7, and (f) PETGCNT10

The complex viscosity (η^*) as a function of the dynamic frequency ω for pure PETG and PETGCNT nanocomposites containing different CNT loadings are presented in Figure 6.10. Pure PETG shows typical Newtonian plateau with very low frequency dependence, and the nanocomposite with CNT loading of 2 wt% shows almost similar behavior as that of the pure polymer. Above CNT loading of 2 wt% a dramatic alteration in this behavior is observed for the nanocomposites. These nanocomposites exhibit a strong shear thinning behavior over the entire frequency range studied. It is interesting to note that the viscosity of the nanocomposites increases by orders of magnitude in the low frequency regime with increasing CNT content. However, with increasing frequency the difference in the viscosity of pure PETG and PETGCNT nanocomposites gradually decreases due to the shear thinning behavior of the nanocomposites. Processability of composites has always been an issue due to their high viscosities. Thus, the shear thinning behavior of PETGCNT nanocomposites, which brings their viscosity down to comparable values to that of pure PETG at high frequencies, which are synonymous to processing frequencies, is advantageous.

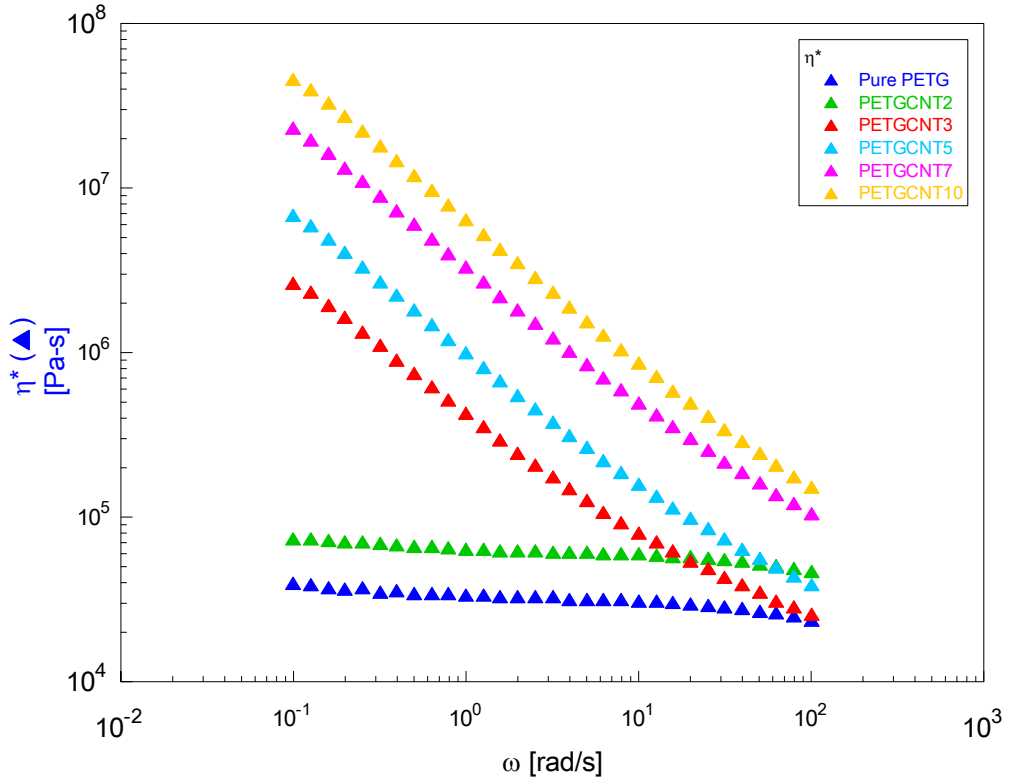

Figure 6.10 Frequency dependence of complex viscosity (η^*) for pure PETG and PETGCNT nanocomposites

Table 6.4 Relative viscosities of PETGCNT nanocomposites at three different frequencies

Sample	CNT Content wt %	Relative Viscosity η_r^*		
		ω = 0.1 rad s^{-1}	**ω = 1 rad s^{-1}**	**ω = 10 rad s^{-1}**
PETGCNT2	2	1.86	1.90	1.51
PETGCNT3	3	66.24	12.56	2.60
PETGCNT5	5	171.40	29.48	5.08
PETGCNT7	7	581.75	97.25	15.95
PETGCNT10	10	1145.46	192.07	27.75

The relative complex viscosity is given by the correlation $\left(\eta_r^* = \frac{\eta_{nc}^*}{\eta_p^*} \right)$, where η_{nc}^* is the complex viscosity of the nanocomposite, and η_p^* is the complex viscosity of the matrix polymer. The relative viscosities of PETGCNT nanocomposites at three frequencies viz. 0.1, 1, and 10 rad s^{-1} are shown in Table 6.4. Relative viscosity data can be indicative of the reinforcement effect of the filler. Higher relative viscosity is indicative of better reinforcement by the filler. It is clearly seen from Table 6.4 that at lower frequencies (0.1 rad s^{-1}) as the percentage of CNT increases from 2 to 10%, η_r^* tremendously increases from 1.86 to 1145.46. This increase by orders of magnitude in the η_r^* values, confirms CNT as an excellent reinforcement agent for polymers. Furthermore, it can be also seen that at higher frequencies (100 rad s^{-1}) the values of η_r^* have decreased significantly, which correspond to typical shear thinning behavior exhibited by filled polymers.

Correlation between the complex viscosity data as a function of CNT loading is shown in Figure 6.11. Although the addition of CNT increases the viscosity at lower as well as higher frequencies for all CNT loadings, it is observed that this increase is more pronounced at the lower frequencies. Further this increase is directly proportional to increasing CNT loading. Thus, the amount of increase in observed in PETGCNT10 is the largest, than the nanocomposites containing lower loadings of CNTs. Moreover, it can

also be observed that at low frequencies 0.1 and 1 rad/s the increase in the viscosity is not linear with composition. The viscosity increases steeply from 2 to 3 wt% loading of CNT. Between 3 to 10 wt% the slope is lower. Note that at high frequencies (10 rad/s) the increase in viscosity is almost linear to the increase in CNT content. This implies the obvious changes in the microstructure of PETGCNT nanocomposites above 2 wt% CNT loading. It can be through increasing filler content, particle–particle interactions become more significant which lead to the formation of a interconnected nanotube structure giving a considerable viscosity increase.

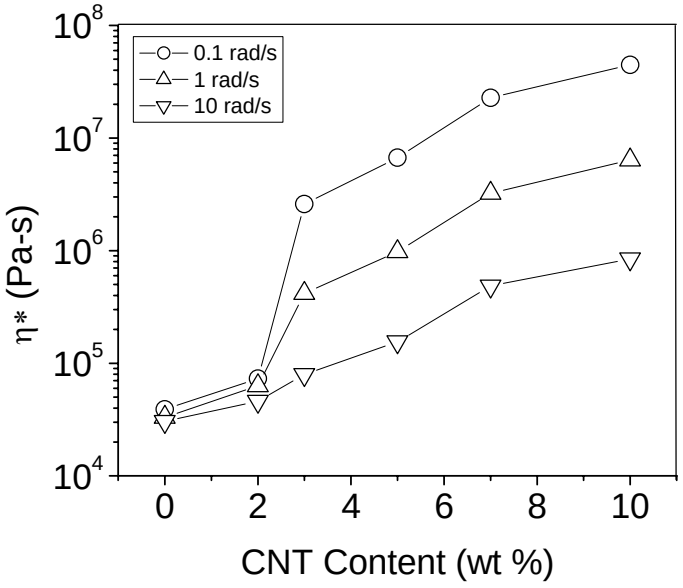

Figure 6.11 Complex viscosity as a function of CNT loadings at three frequencies. Addition of CNT increases the viscosity of all the samples

Cole–Cole diagrams, viz. relationship between dynamic viscosity (η') and loss viscosity (η'') are used extensively to investigate the structure of polymeric materials. These diagrams can also be utilized to get detailed information on filled polymeric melts. Typically, a Cole–Cole plot shows, with linear axes, a semicircular shape for thermoplastic, non–crosslinked polymers. Similar conclusion may be reached for pure PETG and PETGCNT2, which show an identical behavior. With the addition of CNTs

exceeding 2 wt% of CNT loading, η'' (at a given value of η') in the region of long relaxation times (i.e. low ω region) increased with increasing CNT loading (Figure 6.12). The shape of the Cole–Cole plot was significantly affected. The transition from liquid–like to solid–like viscoelastic response made the Cole–Cole plots for the PETGCNT nanocomposites more linear in shape.[17] As explained earlier this transition is as an effect of the formation of the percolated filler network, which retards the polymer relaxation process by increasing the elasticity to viscosity ratio of PETGCNT nanocomposites.

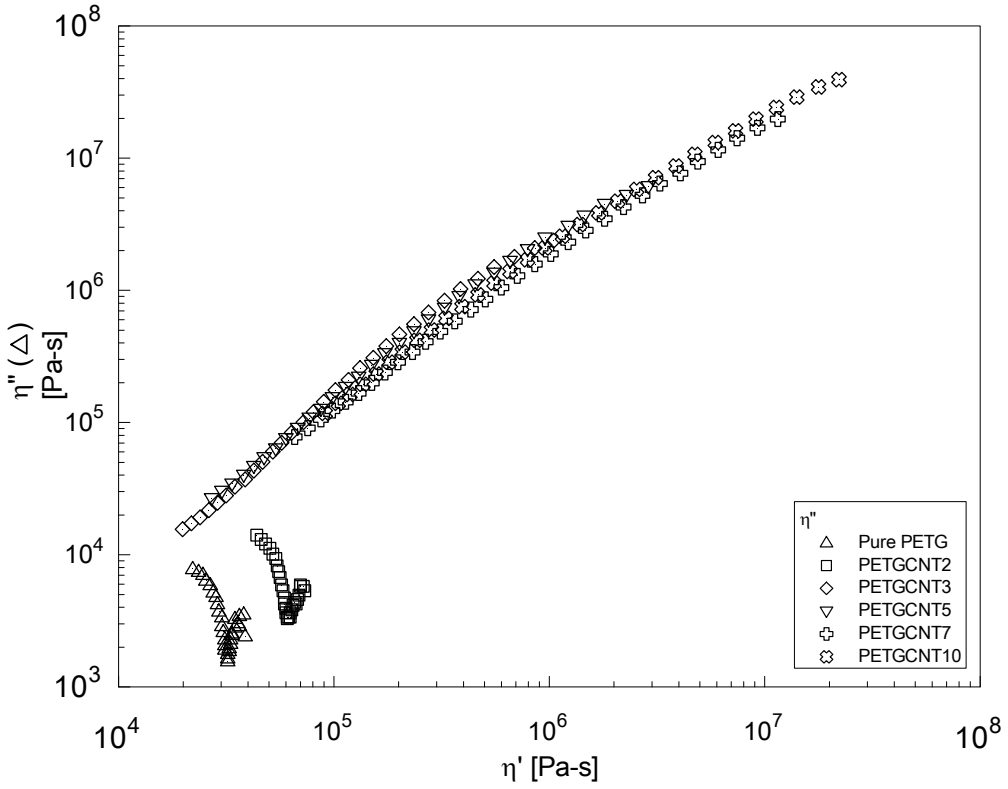

Figure 6.12 Cole–Cole plots of dynamic viscosity (η') versus loss viscosity (η'') for pure PETG and PETGCNT nanocomposites

Discussion of the melt rheology presented in Figures 6.5–6.12 strongly suggests that the liquid–like to solid–like transition observed in PETGCNT nanocomposites is due to the presence of a percolating filler network. To further corroborate our findings we show in Figure 6.13 the plot of frequency dependence of tan δ. The phenomenon of the

formation of a percolated filler network where the rheological properties of the material are dramatically altered in a viscoelastic liquid, may be considered similar to the liquid–like to solid–like transition. A typical example of such a liquid–solid transition is the gelation feature and has been extensively described by Winter and Mours.[18] It is well established that by plotting tan δ as a function of frequency the gel–point can be characterized. At the gel point tan δ is independent of frequency, while for a liquid negative slope is observed and solid material exhibits positive slope. Indeed, it can be seen from Figure 6.13 that the compositions of PETGCNT nanocomposites from PETGCNT3 have become almost frequency independent and may be classified under the so–called pseudo solid–like materials. It can also be seen that pure PETG and PETGCNT2 are showing negative slopes characteristic of a viscoelastic liquid.

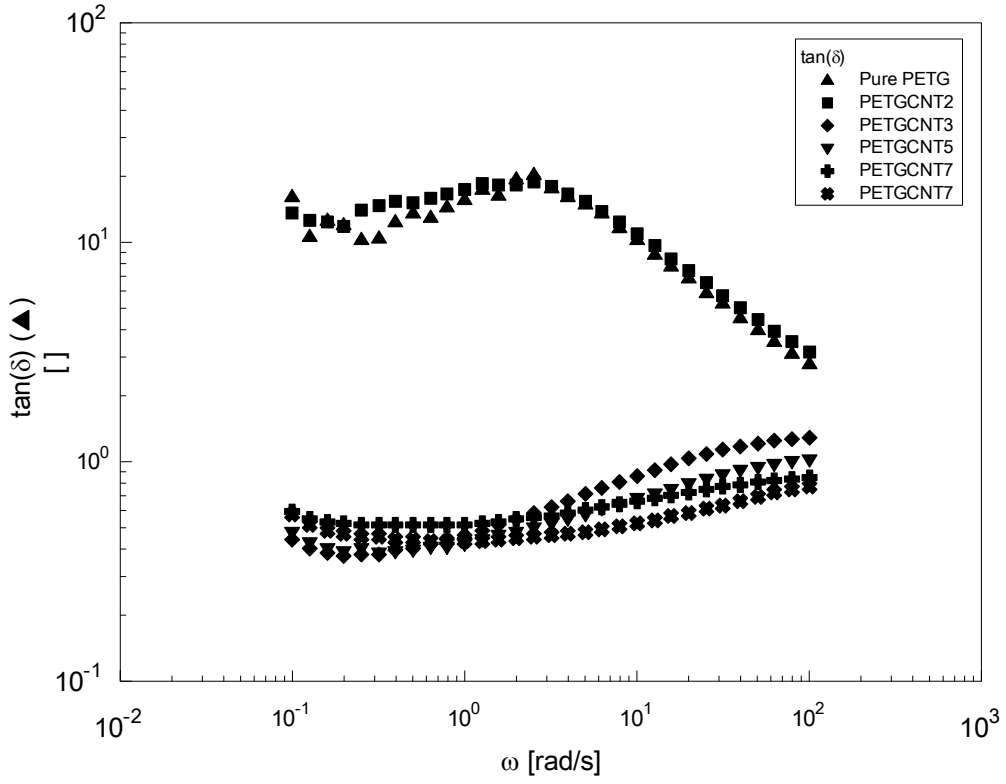

Figure 6.13 Frequency dependence of tan δ for pure PETG and PETGCNT nanocomposites

The van Gurp–Palmer plots, which are the plots of phase angle versus complex modulus, are accepted in literature to be able to identify the rheological percolation threshold.[5] In this plot the percolation threshold is characterized by deviation from the plateau at low complex moduli. The van Gurp–Palmer plots for pure PETG and PETGCNT nanocomposites are plotted in Figure 6.14. Pure PETG and PETGCNT2 show a phase angle of about 90° indicating dominant viscous flow behavior. A dramatic change is observed in PETGCNT nanocomposites above 3 wt% of CNT loading. An increasing elastic behavior with nanocomposite content is observed which is evident from a significant decrease in the phase angle by decreasing modulus. Note that the figure does not show a plateau in any of the G^* curves for the nanocomposites above 3 wt% of CNT loading. This data suggests that the rheological percolation threshold of PETGCNT nanocomposites is at a CNT loading of 3 wt%.

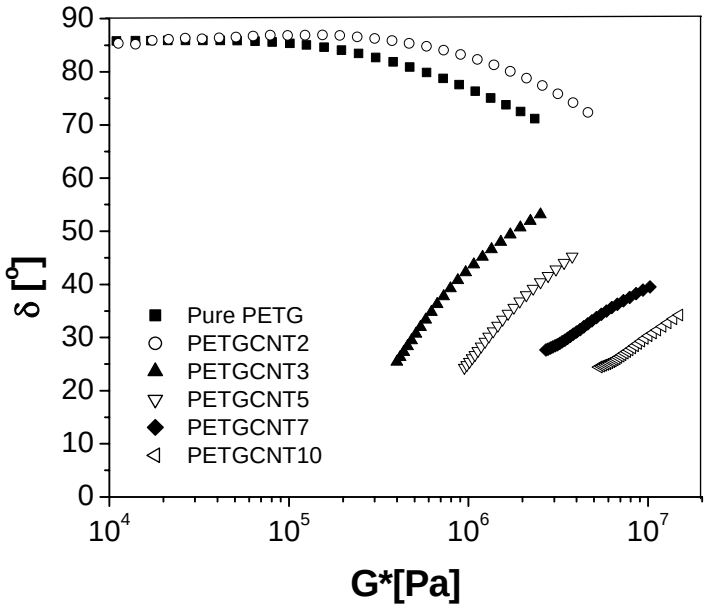

Figure 6.14 Van Gurp–Palmen plots for pure PETG and PETGCNT nanocomposites

6.3.3.2. Non-linear Rheology

Experiments carried out under steady shear conditions provide important information regarding processability of the nanocomposite material. The shear rate $(\dot{\gamma})$

dependence of steady shear viscosity (η) for pure PETG and PETGCNT nanocomposites was investigated.

The samples were subjected to steady shear using parallel plates (25 mm) at 240 °C in the ARES rheometer. Figure 6.15 shows the measured η for pure PETG and PETGCNT2, PETGCNT3, PETGCNT5, and PETGCNT7 nanocomposites. Pure PETG and PETGCNT2 show typical Newtonian behavior with shear viscosity of the shear rates. At low shear rates the viscosities of the nanocomposites from PETGCNT3 are much higher than pure PETG and PETGCNT2. Further as the viscosity of these nanocomposites divergently increases with increasing CNT loadings. This divergence is in agreement with previously discussed liquid–solid behavior of PETGCNT nanocomposites above 3 wt% loading of CNTs, at long times or quiescent conditions. However, the nanocomposites containing CNT loadings of 3 wt% and higher, increasingly shear thin with increasing$(\dot{\gamma})$. The nanocomposites show similar η at high frequencies compared to that of the matrix polymer. This phenomenon is usually associated with retardation in relaxation of polymer chains as a result of hindrance due to formation of filler percolated network structure. Similar behavior was observed by Krishnamoorti and coworkers for polymer/clay nanocomposites.[19] They observed that at low shear rates, the shear viscosity of the nanocomposites increased monotonically with increasing silicate loading, and the intercalated nanocomposites show shear thinning behavior with the silicate loading having relatively small influence on the shear viscosities at high shear rates. Thus, at low shear rates addition of small amounts of CNT results in non–Newtonian behavior and significant increase in shear viscosity as result of formation of a percolated quiescent structure. However, at high shear rates the shear viscosity and the shear thinning behavior of the nanocomposites are comparable with those of the pure polymer with relatively insignificant changes in the polymer dynamics due to strong orientation of the CNT in flow direction. This suggests that at high shear rates the measured viscosity and shear thinning is dominated by the matrix polymer.

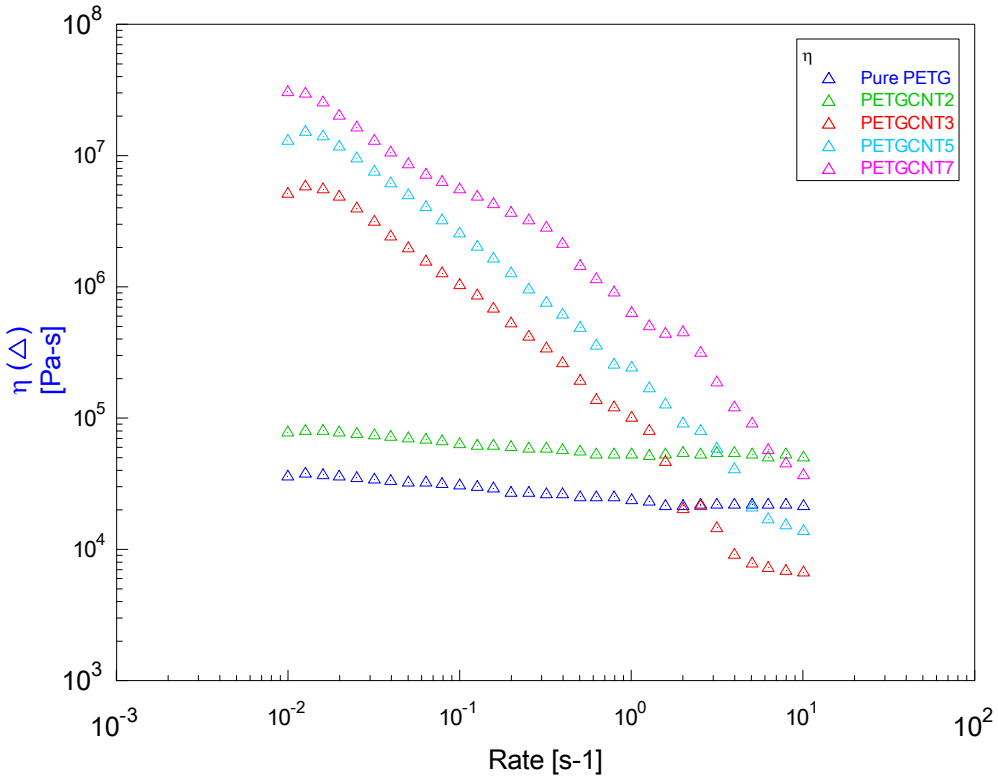

Figure 6.15 Shear rate dependence of steady shear viscosity for pure PETG and PETGCNT nanocomposites

In Figure 6.16 a combined plot of shear viscosity of the nanocomposites obtained via steady shear experiments, and their complex viscosity obtained from the dynamic experiments is shown as functions of $\dot{\gamma}$ and ω, respectively. The empirical Cox–Merz rule states that plotting $\eta(\dot{\gamma})$ versus $\dot{\gamma}$ is almost same as plotting the complex viscosity versus ω and is typically applicable for a wide class of polymer melts and solutions.[20] Thus, for $\dot{\gamma} = \omega$ the viscoelastic data should obey the relationship $\eta^*(\omega) = \eta(\dot{\gamma})$. Interestingly, the shear viscosity and the complex viscosity data for PETG nanocomposites other than that for PETGCNT2 nanocomposite, do not match indicating that the Cox–Merz rule is not valid for PETGCNT nanocomposites from CNT loading of 3 wt% and above. Usually Cox–Merz rule is said to be valid for composite materials below their percolation threshold.[21] This indicates that the percolation threshold of PETGCNT nanocomposites is at 3 wt% loading of CNT.

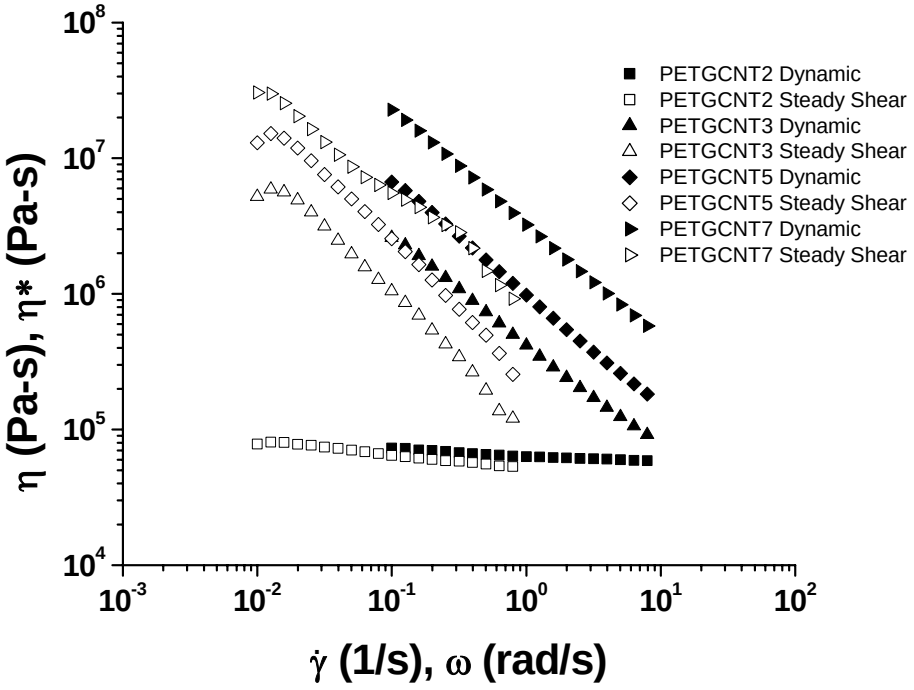

Figure 6.16 η (open symbols) and η* (closed symbols) as functions of $\dot{\gamma}$ and ω for PETGCNT nanocomposites

From Figure 6.16, both η and η* for PETGCNT nanocomposites decrease with increasing $\dot{\gamma}$ and ω and also decrease with decreasing CNT content. Note that the Cox–Merz rule fails for the PETGCNT compositions containing CNT loading of 3 wt% and above, with η* exceeding η at all shear rates. These results suggest that the mesostructural changes experienced by the two samples during these two tests are not of the identical nature and thus the mesostructure as probed by these two tests for the same sample may not be the same. In the dynamic experiments the mesostructure does not change due to small imposed strains and as a result the filler particle–particle interactions remain dominant. On the other hand in steady shear experiments the mesostructure is considerably altered as the CNTs experience much larger strains, which could result in the orientation of the filler particles in the flow direction. Thus, these orientated filler particles will have negligible effect on the viscosity and the net result is only due to the

contribution of the matrix polymer. Additionally, these results also confirm the reinforcement effect of the CNTs as filler. The dynamic viscosity η^* is larger by orders of magnitude than the shear viscosity η. Presence of an interconnected filler network leads to a much larger retardation in the polymer chain relaxation. However, in absence of such a network the effect on viscosity will be more due to the matrix contribution. It may be noted here that the viscosity of a filled system will always be greater than that of an unfilled polymer, but the effect the presence of a filler network will have on the increase in the viscosity will be much more magnified. Indeed, this effect can be clearly observed from our results. PETGCNT2, which lies below the percolation threshold of the nanotubes in PETG, shows reasonable congruence to the Cox–Merz rule. For PETG nanocomposites containing CNT loading of 3 wt% and higher this congruence disappears completely, strongly supporting our arguments on the presence of an interconnected filler network, which is responsible for the dramatic property improvements in PETGCNT nanocomposites.

6.3.4. Dielectric Relaxation Spectroscopy

The real part of alternating current conductivity (σ'), as a function of frequency at 80 °C for different CNT loadings in PETGCNT nanocomposites is presented in Figure 6.17. For CNT content below 5 wt% the spectra show a frequency dependence of conductivity, a behavior which is similar to that of unfilled PETG. However, from 5 wt% of CNT loading the spectra show a frequency independent behavior below a critical frequency, F_c. Above F_c a frequency dependence can be observed. Further the frequency region of constant conductivity extends to higher frequencies with increasing CNT content. This frequency–independent behavior is a characteristic of a non–dielectric behavior as the electron polarization is negligible and is termed as the direct current (dc) conductivity (σ_{dc}). This behavior is similar to the universal dynamic response proposed by Jonscher and was also observed for CNT–epoxy resin nanocomposites.[22,23]

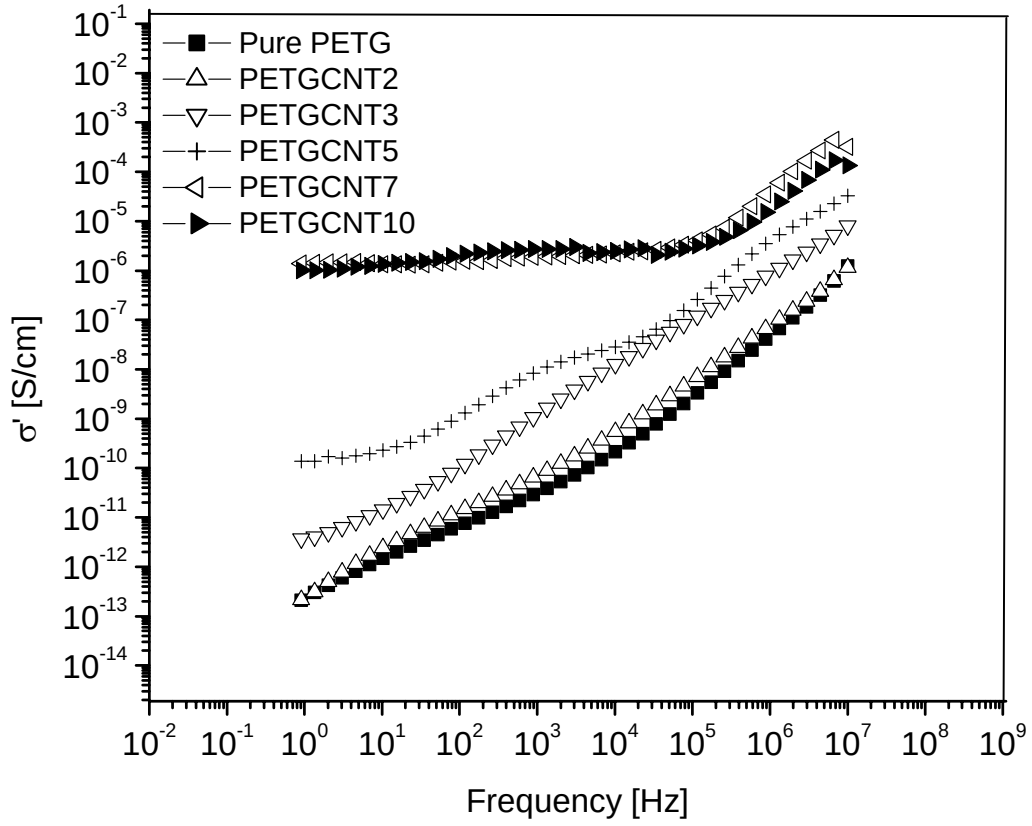

Figure 6.17 Frequency dependence of alternating current conductivity, σ', at 80 °C for pure PETG and PETGCNT nanocomposites

The relationship between σ' and CNT loading at the frequency of 1 Hz is shown in Figure 6.18 in order to emphasize the discontinuous increase in conductivity up on increasing the CNT content. The conductivity percolation concentration is clearly indicated to be between 5 and 7 wt% from the change in the slope. Note the significant change in the conductivity of more than 4 decades. Moreover, above 7 wt% of CNT loading the dc conductivity levels off, indicating that the conductivity percolation threshold of the composite is reached and its conductivity is now controlled by the conducting CNTs which have formed a network of CNTs within the PETG matrix. In other words below this concentration the nanocomposites are resistant to electrical flow, whereas above this value they are conductive.

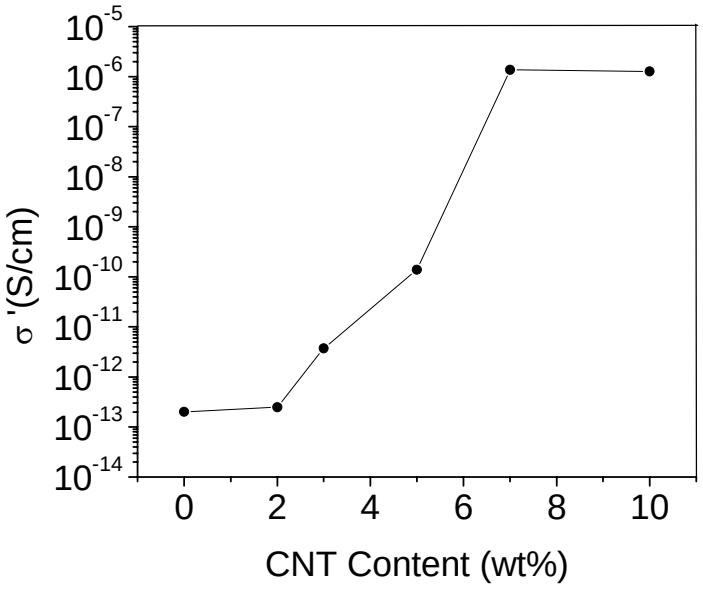

Figure 6.18 Conductivity (σ') at F = 10^0 Hz as a function of CNT content

The frequency dependence of real part of permitivitty (ε') at 80 °C for PETG and PETGCNT nanocomposites is presented in Figure 6.19. The ε' are nearly frequency independent for the unfilled polymer, PETGCNT2, and PETGCNT3. However, from 5 wt% loading of CNT it may be observed that the frequency decreases. This decrease in the ε' is due to mobility decrease in the nanocomposite above the percolation composition as the filler network acts as hindrance to dipole orientation. Thus, charge separation is reduced as a result of decrease in the polymer segmental mobility, which translates in a decrease in the dielectric constant. For PETGCNT10, due to high AC conductivity of the samples, it was not possible to measure reasonable values of ε' for this nanocomposite below $F = 10^4$ Hz.

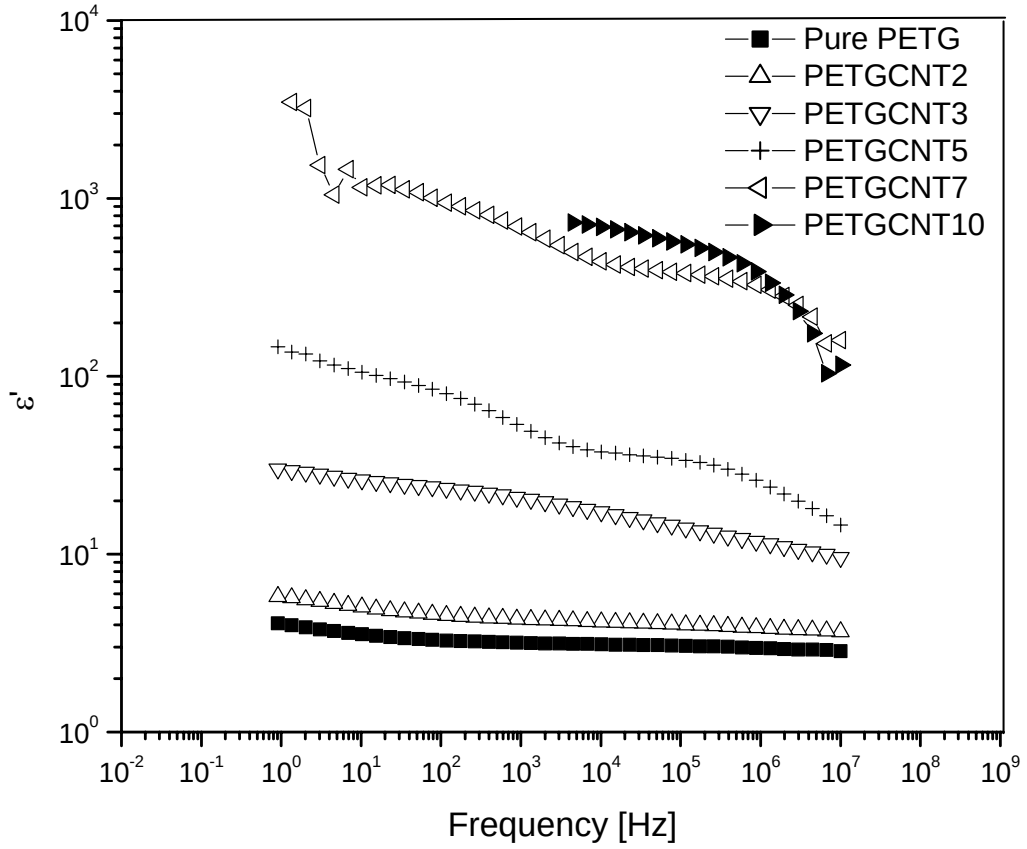

Figure 6.19 Frequency dependence of real part of permitivitty (*ε'*) at 80 °C for PETG and PETGCNT nanocomposites

Figure 6.20 shows the dielectric loss factor as a function of frequency at 70 °C. All the nanocomposites show an increased value over the entire frequency range studied. Significant increase is observed between 5 and 7 wt% reading of the nanocomposite. Furthermore, at CNT loadings of 3 wt% and higher, the spectra show a gradual development of a shoulder which is not observed in pure PETG. The emergence of this shoulder is due to interfacial polarization or more widely termed as Maxwell–Wagner–Sillars relaxation. MWS is a characteristic of heterogeneous systems and is caused by charges blocked at the internal phase boundaries.[24–26]

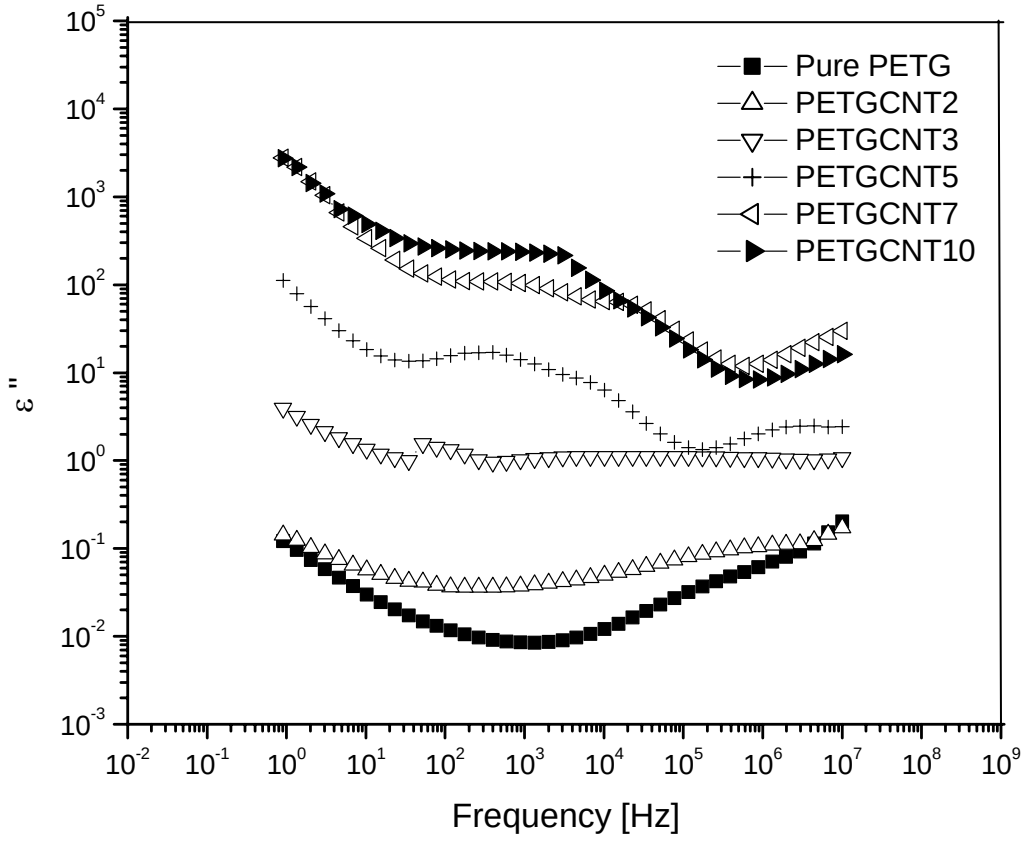

Figure 6.20 Frequency dependence of dielectric loss factor (*ε″*) at 70 °C for PETG and PETGCNT nanocomposites

6.3.5. Morphology

To corroborate the reinforcement mechanism and the state of dispersion the cryo–fractured surfaces of the nanocomposite were investigated by SEM. Figure 6.21 shows typical SEM micrographs of PETGCNT nanocomposites. The micrographs clearly reveal evenly distributed CNTs in the PETG matrix. Note that the CNTs are not aligned, but are randomly oriented in PETGCNT3 and PETGCNT7 (Figure 6.21a and 6.21c). As the SEM specimen was not subjected to unidirectional shear or stretching, no preferred orientation of the CNTs can be observed. In addition, from Figure 6.21c it can be observed that the nanotube network bridges across the microcracks, which permits the

release of stress and absorbs the fracture energy, thus contributing to toughness improvement in the nanocomposites. Furthermore, some orientation to flow direction can be seen in PETGCNT5 (Figure 6.21b) as the SEM specimen was prepared from a compression molded film.

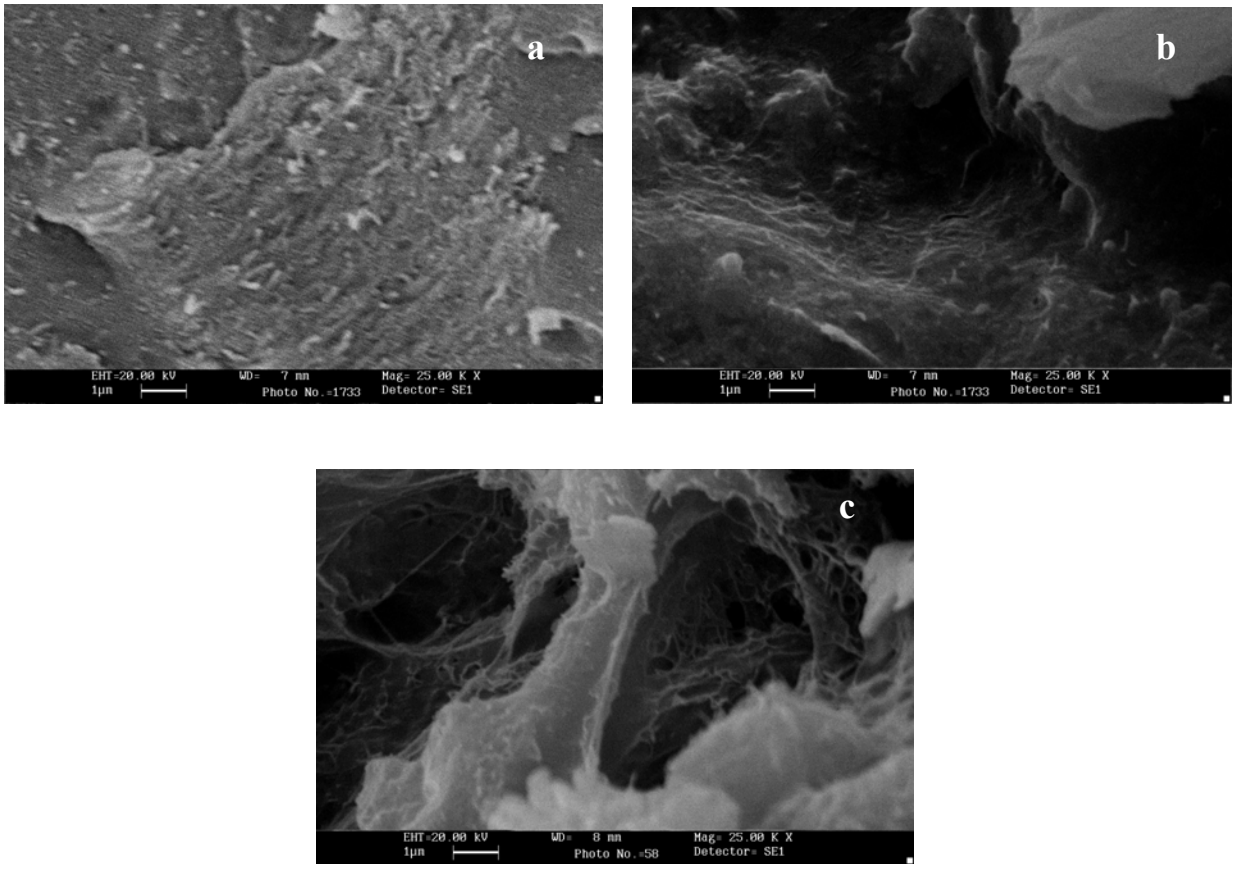

Figure 6.21 Scanning electron micrograph (SEM) image of fracture surfaces of (a) PETGCNT3, (b) PETGCNT5, and (c) PETGCNT7

6.3.6. Comparison Between Rheological and Electrical Percolation Thresholds

From the rheological studies it was observed that the percolation threshold for PETGCNT nanocomposites is at 3 wt% of CNT loading. The dielectric studies suggest that this critical concentration lies between 5 and 7 wt% for these nanocomposites. Du et. al have examined this difference in rheological and electrical percolation thresholds.[6] It is usually accepted that when the CNT loading reaches the electrical conductivity threshold,

a conductive network exists in which the CNTs form a conductive path. However, for this to occur the nanotubes need not be physically in contact to each other, but close enough to allow for the electron hopping mechanism to take place. This distance is less than ~ 5 nm for the nanocomposites to be conductive. Whereas, for the restricted polymer chain mobility to occur it is essential that the gap between the CNTs is less than the radius of gyration of a polymer chain in molten state. This is of the order of several dozens of nanometers. Thus, a larger distance between two nanotubes may suffice the requirement for rheological percolation to occur as compared to that required for electrical percolation. In other word the number of CNTs required to approach the rheological percolation threshold is far smaller than what is required for electrical percolation threshold.

6.4. Conclusions

The results presented in this chapter describe the interlinks between the viscoelastic properties of nanocomposites and their microstucture for nanocomposites based on CNTs. The reinforcement effects of CNTs in PETGCNT nanocomposites by systematically investigating the visocelastic properties both in solid–state and in melt–state are reported. To understand these interlinks better the viscoelastic data was complemented with the dielectric measurements. DMTA results reveal tremendous increase in the storage modulus of the nanocomposites especially in the rubbery regime. The loss factor results showed that in PETGCNT nanocomposites reduction in tan δ peak intensity was more pronounced than the increase in the tan δ peak temperature. The significant decrease in the tan δ values with increase in the CNT content indicates the existence of the CAP. It is suggested that formation of a percolated filler network is responsible for the sudden drop in the tan δ peak intensity at 3 wt% of CNT loading. Linear rheological measurements showed significant increase in storage modulus of up to four orders of magnitude without considerable reduction in the loss modulus. Through a series of rheological representations including presence of a finite yield stress in PETGCNT nanocomposites, and shapes of the Cole–Cole plots, we have shown that the rheological percolation threshold of PETGCNT nanocomposites exists at 3 wt% of CNT loading. Moreover, the transition from liquid–like to solid–like rheological behavior

above a CNT loading of 2 wt% is indicative of the formation of percolated mesoscale CNT network. Non–linear rheological experiments showed a divergent increase in the viscosity of the nanocomposites at low shear rates, however, the nanocomposites shear thinned with increasing $(\dot{\gamma})$ which is attributed to the presence of a percolated structure, which retards the relaxations of the polymer chains. At high shear rates strong orientation of filler particles cause insignificant changes in polymer dynamics, which reflects in the shear thinning behavior of the nanocomposites and comparable shear viscosities to those of a pure polymer. Thus, at low shear rates the reinforcing effect of the CNTs is dominant in controlling the shear viscosities, while the matrix polymer dominates these at higher shear rates. Comparison of the linear viscosity to the steady shear viscosity suggests that due to the presence of a percolated filler network, η^* is larger by orders of magnitude than η. The dielectric measurements indicate an electrical percolation threshold between 5 and 7 wt% of CNT loading at which there is a significant change in the conductivity by more than 4 decades. Microscopy observations clearly indicate the formation of a percolated CNT network in PETG matrix, which is responsible for the remarkable enhancement in the viscoelastic properties of the nanocomposites. Although the changes in the viscoelastic and dielectric properties of the nanocomposites were attributed to the formation of a percolated filler network, it was observed that the rheological percolation threshold was less than the electrical counterpart. This is understood in terms of smaller inter–nanotube distance is required for electrical conduction as compared to the distance required to impede polymer chain mobility.

REFERENCES

1. S. Iijima, *Nature* **354** 56 (1991)
2. M. S. P. Shaffer, A. H. Windle, *Adv. Mater.* **11** 937 (1999)
3. D. Qian, E. C. Dickey, R. Andrews, T. Rantell, *Appl. Phys. Lett.* **76** 2868 (2000)
4. T. V. Sreekumar, T. Liu, B. G. Min, H. Guo, S. Kumar, R. H. Hauge, R. E. Smalley, *Adv. Mater.* **16** 58 (2004)
5. P. Potschke, M. Abdel-Goad, I. Alig, S. Dudkin, D. Lellinger, *Polymer* **45** 8863 (2004)

6. F. Du, R. C. Scogna, W. Zhou, S. Brand, J. F. Fischer, K. I. Winey, *Macromolecules* **37** 9048 (2004)
7. J. N. Coleman, B. E. Kilbride, J. Fraysee, P. Fournet, M. Cadek, A. Drury, S. Hutzler, S. Roth, W. J. Balu, *J. Appl. Phys.* **92** 4024 (2002)
8. P. Potschke, S. M. Dudkin, I. Alig, *Polymer* **44** 5023 (2003)
9. S. Barrau, P. Demont, A. Peigney, C. Laurent, C. Lacabanne, *Macromolecules* **36** 5187 (2003)
10. H. Koerner, W. Liu, M. Alexander, P. Mirau, H. Dowty, R. A. Vaia, *Polymer* **46** 4405 (2005)
11. B. L. Lee, L. E. Nielsen, *J. Polym. Sci. Phys. Ed.* **15** 683 (1977)
12. Y. Song, J. R. Youn, *Carbon* **43** 1378 (2005)
13. X. Gong, J. Liu, S. Baskaran, R. D. Voise, J. S. Young, *Chem. Mater.* **12** 1049 (2000)
14. N. Ogata, S. Kawakage, T. Ogihara, *J. Appl. Polym. Sci.* **66** 573 (1997)
15. J. Ren, A. S. Silva, R. Krishnamoorti, *Macromolecules* **33** 3739 (2000)
16. P. Potschke, T. D. Fornes, D. R. Paul, *Polymer* **43** 3247 (2002)
17. F. Bonemazzi, C. Giavarini, *J. Petrol. Sci. Eng.* **22** 17 (1999)
18. H. H. Winter, M. Mours, Adv. Polym. Sci. 1997, 134: 165 – 234
19. R. Krishnamoorti, R. A. Vaia, E. P. Giannelis, *Chem. Mater.* **8** 1728 (1996)
20. J. M. Dealy, K. F. Wissburn, Melt rheology and its role in plastics processing: theory and applications. The Netherlands, Kluwer Academic Publishers, (1999)
21. R. Krishnamoorti, J. Ren, A. S. Silva, *Chem. Mater.* **114** 4968 (2001)
22. A. K. Jonscher, *Nature (London)* **39** 1222(1977)
23. S. Barrau, P. Demont, A. Peigney, C. Laurent, C. Lacabanne, *Macromolecules* **36** 5187 (2003)
24. P. A. M. Steeman, F. H. J. Maurer, J. V. Turnhout, *Polym. Eng. Sci.* **34** 697 (1994)
25. M. Wubbengorst, E. M. V. Koten, J. C. Jansen, W. Mijs, J. V. Turnhout, *Macromol. Rapid Commun.* **18** 139 (1997)
26. P. A. M. Steeman, C. Gondard, R. L. Scherrenberg, *J. Polym. Sci. Part B: Polym. Phys.* **32** 119 (1994)

CHAPTER 7

CONCLUSIONS AND RECOMMENDATIONS

This chapter details the salient features of the work presented in this thesis and documents the recommendations for future work.

This thesis reports the fabrication of nanocomposites by melt processing technique using two grades of PETG copoylester with two types of nanofillers, viz. layered silicates:– inorganic nanofillers having one dimension at nano level, and CNTs:– organic nanofillers with two dimensions at nano level.

6.1 Conclusions

The main objective of this research was to study the effect of nanofillers having one and two dimensions in nanoscale, on the structure and properties of PETG copolyesters fabricated by melt processing technique. The property performance of polymer nanocomposites greatly depends up on the types of nanofillers used. Overall CNTs provided largest viscoelastic property improvements at fixed filler loadings compared to clays. This is mainly attributed to the large aspect ratio of CNTs (> 1000), high mechanical strength, and stiffness of the nanotubes. Layered silicate platelets which have aspect ratio of ~ 200 also enhance the stiffness of PETG nanocomposites. However, a variety of factors including, concentration of the organic surfactant, its structure and molecular size significantly affect the mechanical property performance. It is shown in this work that these factors influence the amount of PETG infiltration in the silicate gallery, thus controlling the overall structure and morphology of PETG nanocomposites.

Figure 7.1 presents a comparison between the storage modulus enhancements in PETG20A and PETGCNT nanocomposites in solid–state, as a function of the nanofiller loading. Note the significant increase in the storage modulus of PETGCNT as compared to PETG20A. Furthermore, the storage modulus increases with increasing nanofiller loading. These results clearly show that better mechanical performance of polymer nanocomposites is predominantly governed by the nanofiller aspect ratio. As the aspect ratio of CNT >>> Clays, nanocomposites based on CNTs show much better mechanical property enhancement. It is worth mentioning here that the effective inorganic content of clay 20A is 62 % of the total clay loading used in the nanocomposites (see chapter 5). For example, when we consider PETG20A nanocomposites containing 5wt% of 20A clay, the clay content that is actually responsible for enhancing the stiffness of the nanocomposite is only 3.10 %.

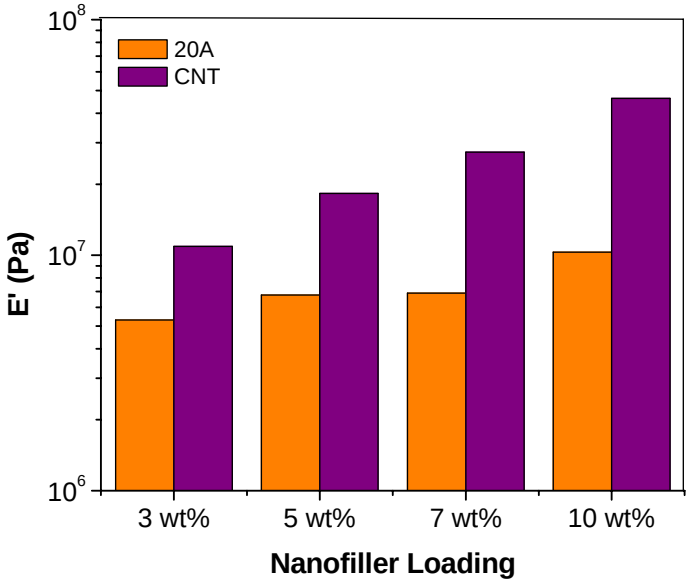

Figure 7.1 Solid–state storage modulus (*E'*) as a function of nanofiller loading for PETG20A and PETGCNT nanocomposites at 110 °C

We compare the α–process dynamics of PETG20A and PETGCNT nanocomposites as a function of the nanofiller loading in Figure 7.2. PETG20A nanocomposites shows an accelerated α relaxation process. It is well documented that with decreasing size of confining geometry results in an enhanced molecular dynamics as well as T_g depression.[1–5] This was attributed to an isolation effect of the silicate layers or micropores that diminish the molecular cooperativity. To gather a general understanding of the relaxation that occurs in nanocomposites a model proposed by Lu and Nutt is considered.[6] It suggests presence of three relaxation domains in nanocomposite based on clays. Domain I is characteristic of slowest relaxation and corresponds to motion of segments located at the interphase, which includes the internal and external surfaces of the nanofiller. The fastest mode (Domain II) corresponds to the relaxation of segments located in the central area of the silicate intergallery. Here, the retardation from the neighbouring segments is shielded by individual layers. The third relaxation mode (Domain III) corresponds to the normal segmental motion of the matrix. No retardation or shielding effects are observed here. Note that fast relaxation dynamics only occur in

intercalated systems as documented in the literature.[4,5] Our results of PETG20A nanocomposites which show an intercalated structure are in good agreement with this. However, PETGCNT nanocomposites an increase in T_g is observed with CNT loading. This increase in T_g is related to the retardation in α–process dynamics in PETGCNT nanocomposites. The overall relaxation behavior of polymer nanocomposites also depends on the fraction of the restricted to unrestricted segments. In systems with nanofillers having higher aspect ratio increase in the extent of nanofiller dispersion results in greater intermolecular cooperativity due to immobilization of the chains at the interface. Thus, in PETGCNT nanocomposites the fraction of immobilized chains (slower relaxation mode:– Domain I) seems to dominate the relaxation dynamics.

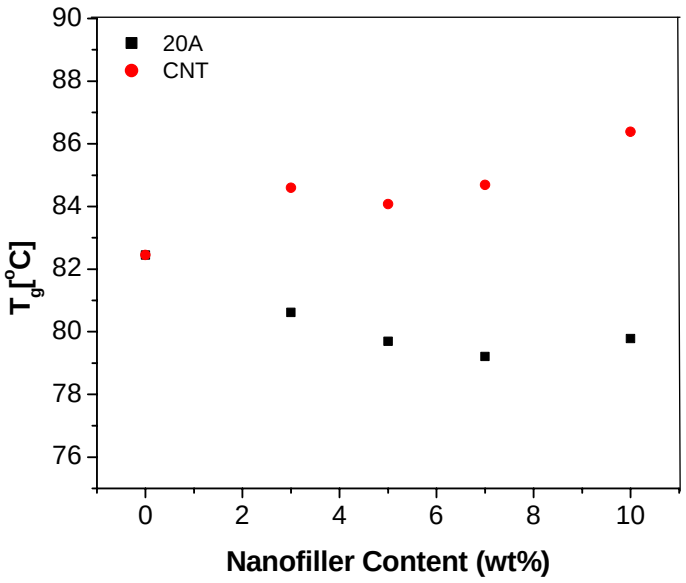

Figure 7.2 A Comparison of variation in glass transition temperature (T_g) as a function of nanofiller loading fro PETG20A and PETGCNT nanocomposites

Through out this thesis it has been described that reduction of particle size is corroborates higher aspect ratio. This is manifested by decrease in damping in the nanocomposites. In Figure 7.3 we compare the tan δ peak intensity for PETG nanocomposites reinforced with 20A clay and CNTs. Note that the decrease in tan δ peak

intensity for PETGCNT nanocomposites is far greater as compared to that for PETG20A nanocomposites. This further reinstates the fact that due to the higher aspect ratio, CNTs posses a larger surface area as compared to that of layered silicates, which facilitates greater attachment to the polymer chains leading to reduced internal friction between polymer and nanofiller surface. This results in greater decrease in the damping in PETGCNT nanocomposites than in PETG20A nanocomposites. Furthermore, the decrease in damping is ascribed to the presence of constrained amorphous fraction (CAF) in the nanocomposites. We show that CAF in PETGCNT is far greater compared to the CAF in PETG20A nanocomposites.

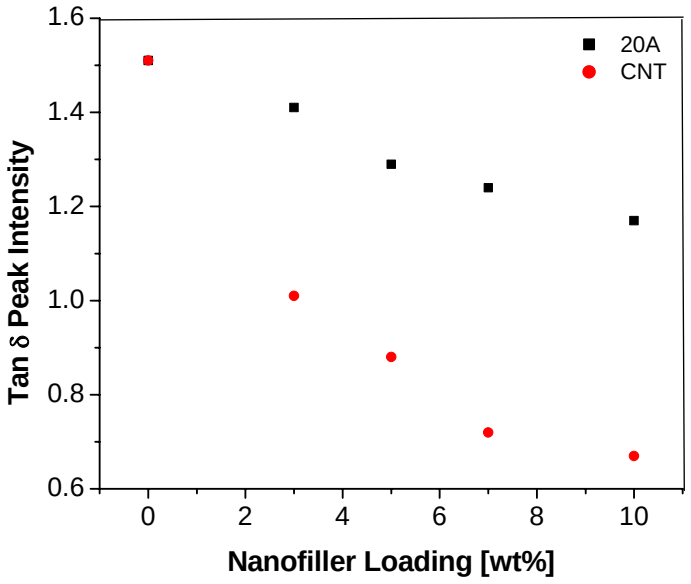

Figure 7.3 A Comparison of tan δ peak intensity of PETG20A and PETGCNT nanocomposites as a function of CNT loading

It was shown that the structural and viscoelastic properties in polymer/clay nanocomposites are strongly governed by the concentration of the modifier. To summarize this effect a comparison of the relative modulus (E'_r) for PETG6A, PETG15A and PETG20A at two temperatures (40°C and 85 °C) is shown in Figure 7.4. In the sub–glass regime all the three nanocomposites show similar reinforcement, which is

attributed to the filler effect. PETG20A nanocomposites derived from clay 20A, which has the lowest amount of modifier present showed maximum reinforcement in the rubbery regime, as compared to PETG6A and PETG15A, derived from 6A and 15A, respectively.

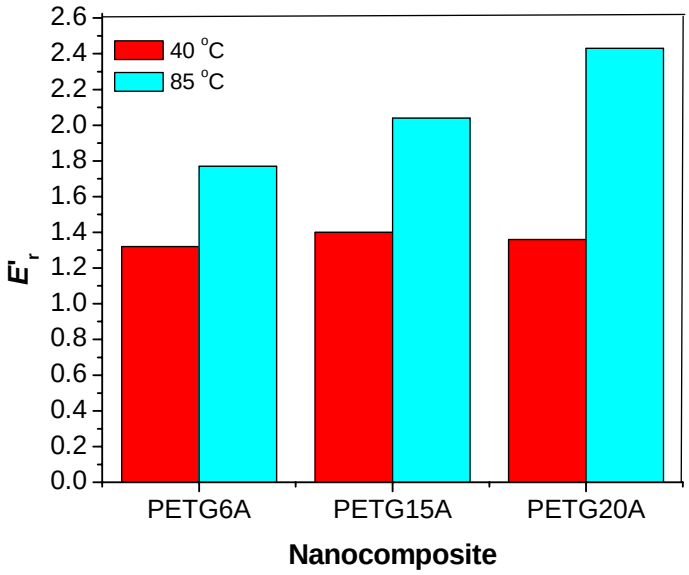

Figure 7.4 A comparison of E_r' for PETG6A, PETG15A, and PETG20A at two temperatures (40°C and 85 °C)

The major results of the present thesis are summarized below:

- PETG nanocomposites based on various layered silicates and multi walled carbon nanotubes were fabricated for the first time.
- It was demonstrated that the concentration, molecular size, and molecular structure of the intercalant molecule in the nanocomposites govern the extent of intercalation of polymer chains between the clay layers and thus have a critical role to play in the property enhancement of polymer/layered silicate nanocomposites.
- The dynamics of PETG20A nanocomposites were studied over a broad range of temperature and frequency using DMTA and DRS and correlated to their

microstructure through WAXD, TEM, and rheology. A direct comparison of DMTA and DRS results on the basis of the polymer chain relaxation processes, showed excellent agreement between the accelerated α–process in the nanocomposites.

- The dielectric data was fitted to the semi–empirical HN equation. The narrow distribution of the values of HN–parameter b indicated strong asymmetric α relaxation in pure PETG.
- A qualitative correlation between rheological and morphological features was obtained from the shear–thinning exponent, which clearly showed increased levels of dispersion of the clay platelets in the polymer matrix with increasing clay loading.
- The interlinks between viscoelastic properties of the nanocomposites and their microstructure for PETG nanocomposites based on CNTs were investigated. To understand these interlinks better the viscoelastic data was complemented with DRS measurements. The enhancement in the properties of the nanocomposites was due to the formation of percolating filler superstructure. However, it was observed that the response of the rheological and dielectric properties differed considerably although both were related to the formation of the percolating network. This was understood in terms of smaller inter–nanotube distance required for electrical conduction as compared to that required to impede polymer chain mobility.

7.2 Recommendations for Future Work

The property improvements in PETG/clay nanocomposites are not limited to intercalated structures. It is a challenge to obtain exfoliated structures using the melt compounding technique. Exfoliated structures in these nanocomposites can be achieved by using proper surfactants to modify the clays and further optimization of the processing conditions. Employing a variety of phosphonium based surfactants, which are thermally more stable than their ammonium counterparts can enhance the clay dispersion in this polar polymer matrix. Furthermore, choosing a suitable surfactant can minimize degradation of PETG in the nanocomposites. Additionally, enhancing the clay layer

dispersion through exfoliation would minimize the light scattering and result in improved optical clarity of the nanocomposites

Effect of orientation of clay and the size of the clay tactoids can be studied using 3-D XRD with possible correlations to the mechanical properties.

One of the major applications of PETG is in packaging industry. Permeability studies on PETG nanocomposites can be carried out to evaluate the transmission rates of various gases.

Enhanced CNT dispersion in PETG matrix, which would further improve the nanocomposite properties, can be explored by functionalization of the nanotubes. Functionalizing the nanotubes with hydroxyl functionality can improve their compatibility with PETG through the formation of hydrogen bonding.

The effect of other inorganic nano fillers such as nanofillers with three dimensions in nanoscale can be explored and effect of the fillers on the structure and properties can be studied.

REFERENCES

1. E. Donth, Glasubergang, Akademic−Verlag: Berlin (1981)
2. N. Tomczak, R. A. L. Vallee, E. M. H. P. van Dijk, L. Kuipers, N. F. van Hulst, G. J. Vansco, *J. Am. Chem. Soc.* **126** 4748 (2004)
3. T. A. Tran, S. Said, Y. Grohens, *Macromolecules* **38** 3867 (2005)
4. S. H. Anastasiadis, K. Karatasos, G. Vlachos, *Phys. Rev. Lett.* **84** 915 (2000)
5. R. A. Vaia, B. B. Sauer, O. K. Tse, E. P. Giannelis, *J. Polym. Sci. Part B: Polym. Phys.* **35** 59 (1997)
6. H. Lu, S. Nutt, *Macromolecules* **36** 4010 (2003)

LIST OF PUBLICATIONS

1. Carbon Nanotube based Copolyester Nanocomposites: Reinforcement Effect of Carbon Nanotubes on Viscoelastic and Dielectric Properties of the Nanocomposites, **Rajendra A. Kalgaonkar** and Jyoti P. Jog, *Polym. Int.* **Accepted for Publication** (2007)
2. Analysis of Viscoelastic Behavior and Dynamic Mechanical Relaxation of Copolyester based Layered Silicate Nanocomposites using Havriliak-Negami Model, **Rajendra A. Kalgaonkar**, Somnath Nandi, Sanjeev S. Tambe, and Jyoti P. Jog, *J. Polym. Sci. Part B: Polym. Phys.* **42** 2657 (2004)
3. Effects of Modifier Concentration on Structure and Viscoelastic Properties of Copolyester/Clay Nanocomposites **Rajendra A. Kalgaonkar** and Jyoti P. Jog, *J. Macromol. Sci. Part B – Phys.* **B43** 421 (2004)
4. Copolyester/Layered Silicate Nanocomposites: Effect of Molecular Size and Molecular Structure of the Intercalant on the Structure and Viscoelastic Properties of the Nanocomposites **Rajendra A. Kalgaonkar** and Jyoti P. Jog, *J. Polym. Sci. Part B: Polym. Phys.* **41** 3102 (2003)
5. PP/Clay Nanocomposites: Effect of Clay Treatment on Morphology and Dynamic Mechanical Properties, Kodgire, P., **Kalgaonkar, R.**, Hambir, S., Bulakh, N., and Jog, J. P., *J. Appl. Polym. Sci.* **81** 1786 (2001)
6. PP/Clay Nanocomposites: A Study of Crystallization and Dynamic Mechanical Behavior, Hambir, S., Bulakh, N., Kodgire, P., **Kalgaonkar, R.** and Jog, J. P., *J. Polym. Sci. Part B: Polym. Phys.* **39** 446 (2001)
7. Molecular Dynamics of Copolyester/Layered Silicate Nanocomposites as revealed by Viscoelastic and Dielectric Properties, **R. A. Kalgaonkar**, J. P. Jog, *under preparation*.

INVITED BOOK CHAPTER

1. Polyolefin/clay nanocomposites: High performance commodity materials, **Rajendra A. Kalgaonkar** and Jyoti P. Jog in Handbook of Nanofiber and Nanotechnology in Textiles, P. J. Brown and K. Stevens Editors, Chapter 13, Woodhead Publishing, Cambridge, UK, In Production, *to be published by Autumn 2007*

PAPERS PRESENTED IN SYMPOSIUMS AND CONFERENCES

1. Copolyester/Layered Silicate Nanocomposites: Effect of Molecular Size and Molecular Structure of the Intercalant on the Structure and Viscoelastic Properties of the Nanocomposites article published in J. Polym. Sci. Part B: Polym. Phys. was presented at Society of Polymer Science in India Symposium held at National Chemical Laboratory, Pune, India and won the second best paper award, July 2003
2. Analysis of Dynamic Mechanical Thermal Analysis Data of Copolyester-Based Layered Silicate Nanocomposites Using Havriliak-Negami Model, **Rajendra A. Kalgaonkar**, Nandi, S., Tambe, S. S., and Jog, J. P. in Polymer Nanocomposites 2003 proceedings, International Conference on Polymer Nanocomposites Science and Technology, Boucherville, Canada, October 6–8, 2003
3. Effects of Modifier Concentration on Structure and Viscoelastic Properties of Copolyester/Clay Nanocomposites, **Rajendra A. Kalgaonkar**, Jog, J. P. in Science Day Symposium proceedings, NCL Research Foundation, February 2003
4. A Study of Static and Dynamic Mechanical Properties of Poly(Butylene Terephthalate)-Layered Silicate Nanocomposites: Effect of Quaternary Ammonium Modified Bentonites, **Rajendra A. Kalgaonkar**, Jog, J. P., in Polymer Nanocomposites 2001 proceedings, International Conference on Polymer Nanocomposites Science and Technology, Montreal, Canada
5. Crystallization Studies of Poly(butylene terephthalate)-Layered Silicate Nanocomposites, **Rajendra A. Kalgaonkar**,Jog, J. P. in International Symposium on Polymer Science and Technology, Eindhoven Technical University, Netherlands, and Society of Polymer Science in India Symposium at National Chemical Laboratory, February 2001